

Synthetic spectra of massive stars as tool for the spectral analysis of stars and stellar clusters

Dissertation

an der Fakultät für Physik

der

Ludwig-Maximilians-Universität München

vorgelegt von

Tadziu Hoffmann

aus Windhoek

München, den 27. Februar 2004

1. Gutachter: Prof. Dr. A. W. A. Pauldrach

2. Gutachter: Prof. Dr. H. Lesch

Tag der mündlichen Prüfung: 26. Mai 2004

Zusammenfassung

Heiße, massereiche Sterne sind in zentraler Hinsicht von großer astrophysikalischer Bedeutung. Grundlegend dafür sind in erster Linie ihre enormen Leuchtkräfte, die das 10^7 -fache der Sonnenleuchtkraft betragen können, und diese Objekte damit zu idealen Beobachtungskandidaten auch in extragalaktischer Hinsicht werden lassen – bis hin zum Virgo- und Fornax-Haufen. Ihre kurzen Lebensdauern, die nur einige 10^6 Jahre betragen, und ihre expandierenden Atmosphären, die in Form von sogenannten Winden dafür verantwortlich sind, daß während der Entwicklung dieser Objekte große Mengen an prozessierter Materie zurück an das Interstellare Medium gegeben werden, ist maßgeblich für die chemische Zusammensetzung ihres Umfelds. Massereiche Sterne prägen somit die Entwicklung der Galaxien in entscheidendem Maße.

Ein grundlegendes Verständnis des damit verbundenen Materiekreislaufs und der galaktischen chemischen Entwicklung setzt somit auch ein tiefgehendes Verständnis der physikalischen Eigenschaften dieser Sterne voraus. Dies betrifft vor allem die genaue Kenntnis der fundamentalen Parameter dieser Sterne wie Masse, Radius, Leuchtkraft, Effektivtemperatur, Windimpuls und chemische Zusammensetzung. Die Bestimmung dieser grundlegenden stellaren Parameter anhand von beobachteten Spektren erfordert zwangsläufig eine detailgetreue Nachbildung der Prozesse, die zur Ausbildung der charakteristischen Merkmale der Spektren heißer Sterne führen. Im Hinblick auf die grundlegende Bedeutung, die massereiche Sterne auf die Entwicklung von Galaxien und auf den Materiekreislauf im Universum haben, stellt eine realistische Simulation der Atmosphären heißer Sterne somit ein bedeutendes Hilfsmittel für den astrophysikalischen Erkenntnisgewinn dar.

In dieser Arbeit wurde der den gegenwärtigen Status Quo repräsentierende Modellatmosphärencode hinsichtlich einer konsistenten Behandlung des Einflusses von Spektrallinien in wesentlichen Punkten verbessert. Das Ziel war dabei zu einer realistischen Beschreibung der ionisierenden EUV-Flüsse und der beobachtbaren UV-Spektren zu gelangen. Die erzielte Qualität der berechneten synthetischen Spektren wurde in einem ersten Schritt durch Einzelsternanalysen überprüft, mit dem Befund, daß der Status Quo realistischer Modelle sichergestellt werden konnte.

In einem weiteren Schritt wurden die berechneten Massenverlustraten und Endgeschwindigkeiten mit Vorhersagen der sogenannten Windimpuls-Leuchtkraft-Relation verglichen. Wesentliches Merkmal dieser auf Beobachtungen basierenden Relation ist, daß ein signifikanter Unterschied in den jeweiligen Korrelationen von Hauptreihensternen und Überriesen vorliegt. Dieser Befund konnte anhand unserer Modellserien nicht verifiziert werden. Als Erklärung wurden jedoch zwei Möglichkeiten herausgearbeitet. Die erste Möglichkeit hat Bezug zu einer Fragmentierung in den abströmenden Atmosphärenteilern – sogenannte Klumpung –, wohingegen die zweite Möglichkeit sich auf systematische Fehler in den stellaren Radien der Überriesensterne bezieht. Eine weiterführende Untersuchung anhand von Objekten bekannter Entfernung (massereiche Sterne in den Magellanschen Wolken) wird in diesem Punkt Klärung schaffen.

Ein weiteres wichtiges Ergebnis dieser Arbeit basiert auf einem großen Modellgitter, das den beobachteten Parameterbereich der massereichen Sterne des Spektraltyps O umfaßt. Resultat dieses Gitters waren emergente EUV-Strahlungsflüsse, die für die Simulation der Emissionslinienspektren von H-II-Regionen (durch die Strahlung der Sterne ionisierte Wolken interstellaren Wasserstoffs) in Sternentstehungsgebieten und Starbursts benützt werden. Die in zeitlicher Abhängigkeit für instantane und kontinuierliche Starbursts berechneten kumulativen EUV-Spektren zeigten in Abhängigkeit der diesbezüglich verwendeten IMF (initial mass function) und SFR (star formation rate) große Unterschiede hinsichtlich der Form und der Stärke der SEDs (spectral energy distributions). Dementsprechende Unterschiede resultieren darauf basierend in den Emissionslinienspektren der die Sterncluster umgebenden H-II-Regionen. Es wurde somit eine Methode bereitgestellt, den zeitlichen Ablauf der Sternentstehung hinsichtlich der IMF, der SFR, und der Bursteigenschaften zu analysieren. Dies wird das Verständnis der individuellen chemischen Entwicklung von Galaxien in entscheidendem Maße vertiefen.

Contents

1. Introduction: the astrophysical importance of hot stars	1
2. The basics: fundamentals of radiation-driven wind theory	5
2.1. Radiative energy and radiation transfer	6
2.2. Interaction of matter and light; opacities and emissivities; rate equations and occupation numbers	8
2.2.1. Radiative transitions	9
2.2.2. Collisional transitions	12
2.2.3. Opacities and emissivities	13
2.3. Kinetic temperature and energy balance	14
2.4. Hydrodynamics and radiative driving	16
3. The models: numerical methods and implementation details	19
3.1. General procedure	19
3.2. The NLTE model	21
3.2.1. The treatment of line blocking	24
3.2.1.1. Method I — the opacity sampling method	24
3.2.1.2. Method II — the detailed radiative line transfer	33
3.2.2. Treatment of line blanketing	36
3.2.3. Atomic data	38
3.2.4. Treatment of shock radiation	38
3.3. Interstellar lines	43
4. UV spectral analysis as a constraint for the SEDs of massive stars	47
4.1. α Cam	48
4.2. AV 232	48
5. Investigation of stellar parameters as a constraint for the SEDs of massive stars	57
5.1. Dependence of \dot{M} and v_∞ on $\log g$ and R	58
5.2. Dependence of wind momentum on metallicity	61
5.3. Models for a sample of Galactic O stars	62
5.4. Summary	66
6. Spectral energy distributions (SEDs) for massive stars and evolving stellar clusters	67
6.1. Basic parameters of the grid models	68
6.2. SEDs and ionizing photon emission rates	70
6.3. Evolving cluster calculations	73
7. Summary, conclusions, and future work	79
References	82
Appendix	85
List of Publications	163

1

Introduction: the astrophysical importance of hot stars

Massive hot stars play a decisive role in modern astrophysics by constituting the link between major areas of astrophysical research. Understanding the properties of hot stars and obtaining precise measurements of their fundamental parameters from the observed spectra is therefore of crucial importance not only for stellar physics per se, but also for a host of interrelated fields. Among the most important of these subjects are:

Stellar evolution: The evolution of massive stars is severely affected by mass loss (the high mass-loss rates cause them to lose a significant fraction of their total mass already during the hydrogen-burning phase). Accurate measurements of the stellar parameters of massive main-sequence stars and supergiants, as well as CSPNs, are required not only for testing evolutionary models, but also to provide the necessary input to these models with regard to the mass loss rates.

Chemical evolution of galaxies: Although massive stars are rare compared to low-mass stars, they are the ones primarily responsible for chemical evolution of their host galaxies: not only do massive stars produce heavy elements much faster than low-mass stars, but their short lifetimes, coupled with efficient “mechanisms” for recycling of the stellar matter (winds during main-sequence and supergiant phases; supernova at end of lifetime) lead to a quick enrichment of the interstellar medium (ISM) with heavy elements. Apart from carrying nuclear processed material back to the ISM, the stellar winds (and supernova explosions as the final state of these objects) also have a significant *dynamic* impact on the interstellar environment (“wind-blown bubbles” and “superbubbles”), by compressing surrounding material into denser filaments and thus likely triggering new star formation (e.g., Oey and Massey 1995). Abundance measurements from the spectra of stars not only help

constrain the evolution histories of observed galaxies or stellar clusters, but accurate knowledge of the winds of massive hot stars as function of their stellar parameters is also a required input for realistic models for the evolution of galaxies.

Extragalactic distance measurements: One of the fundamental results of the spectroscopic analysis of radiation-driven winds is the existence of a wind-momentum–luminosity relation for massive stars (e.g., Lamers and Leitherer 1993; Kudritzki et al. 1995). This relation makes it possible, in principle, to determine the absolute luminosity of these stars from the observed spectra alone. In combination with measured apparent magnitudes and knowledge of the interstellar extinction this allows determination of the distances to these objects even out to the Virgo and Fornax clusters, beyond the local group. However, a calibration of the relation by means of stars with accurately known parameters is essential for its reliable application to distance measurements. In particular the dependence on metallicity is of fundamental relevance.

Cosmology: The EUV radiation from Population III stars, the very first generation of very massive stars with extremely low to zero metallicity, is suspected to have played a significant role in the reionization of the universe at redshifts ≥ 6 (cf. Bromm et al. 2001). As observations are not yet available (these will hopefully become possible with the Next Generation Space Telescope, NGST), computer models are currently the only way to study in detail the properties of these objects.

Analysis of starburst galaxies: The integrated spectra of starburst galaxies and stellar clusters too distant to resolve individual stars can be analyzed via population synthesis models, in which spectra for representative points along the evolutionary tracks of stars are added up with the appropriate weights to represent the integrated spectrum of an evolving stellar population. (For a recent paper see Leitherer et al. 2001.) Different star formation histories and/or metallicities are tried to determine the one that best fits the observed spectrum. Here the advantage of using synthetic spectra is immediately obvious: whereas individual observed spectra, used heretofore in this kind of calculation, can only represent the metallicities of our own and the neighboring galaxies, the Magellanic Clouds, synthetic spectra can in principle be computed for arbitrarily low (and high) metallicities, and can thus also be used for the analysis of starburst galaxies at high redshifts, where significantly lower metallicities are expected. Again, this requires that the synthetic spectra accurately represent those of the real physical objects with the given stellar parameters.

Photoionization calculations of H II regions: This type of analysis attempts to derive information about abundances and star formation histories by simulating the ionized material surrounding hot stars or star clusters (Galactic as well as extragalactic) and comparing the strength of calculated and observed emission lines. A critical input to these simulations are the spectral energy distributions (SEDs) of the ionizing sources. Because these ionizing fluxes are not directly observable due to absorption by interstellar hydrogen, they must be provided by stellar atmospheric models (optionally augmented by a population synthesis model). In this regard it is very encouraging that by using recent sophisticated stellar atmosphere models the observed emission line strengths of the ionized gas can be much better reproduced than with earlier models (e.g., Giveon et al. 2002).

Although stellar winds are a direct consequence of the high radiation densities in the atmospheres of hot stars, from a purely observational standpoint they can be considered a fortuitous circumstance, for the following two reasons: (1) Hot stars are intrinsically bright (luminosity scales with the temperature as T_{eff}^4), and can thus be observed as individual objects even at extragalactic distances up to the Virgo and Fornax clusters. In **starburst galaxies** at even farther distances the light of the most massive stars dominates that of the entire galaxy, so that the integrated spectrum of the galaxy still carries the spectral signatures of the winds of these massive stars. (2) The characteristic spectral features introduced by the stellar winds allow (provided that adequate tools are available) to extract a wealth of physical information from the spectra alone, not only about the mass loss rates and the chemical composition, but also about the stellar parameters. (Thus, the spectra of starburst galaxies at high redshift can yield, in principle, information about stellar populations in the early universe.)

The crucial issue here are the tools needed to extract that information. These must by necessity be based on computer models that mimic as realistically as possible the physical conditions present in the atmospheres of hot stars. This, however, represents a formidable task, since modelling the atmospheres

of hot star involves replicating a tightly interwoven mesh of physical processes — the equations of radiation hydrodynamics including the energy equation, the rate equations for all important ions (from H to Zn) including accurate atomic physics, and the radiative transfer equation at all transition frequencies have to be solved simultaneously.

In view of the enormous astrophysical potential, as outlined above, of hot stars as diagnostic tools, it is a continuing effort of several groups worldwide to develop suitable computer codes to tackle this problem. (Recent basic papers of the different groups describing the various approaches taken and methods used are: Abbott and Hummer 1985; Drew 1989, 1990; Pauldrach et al. 1994, 1998; Schaerer and de Koter 1997; Aufdenberg et al. 1998; Hamann and Koesterke 1998; Hillier and Miller 1998; and Pistinner et al. 1999.) Whereas the need of a non-thermodynamic-equilibrium treatment in hot stars is generally recognized, it is still not a standard procedure to treat all related aspects consistently; for adequate models used in *quantitative* analyses, however, a consistent treatment of all required effects is essential, as the resulting synthetic spectra used in spectral analysis depend critically on such a consistent treatment.

Chapter 2 will give an overview of the basic physics of radiation-driven winds and chapter 3 will discuss details of the model code, in particular with regard to modifications and enhancements. The quality of the results from the model code will then be verified in chapter 4 via a detailed comparison of synthetic and observed UV spectra of individual O stars. In Chapter 5 we will compare the wind parameters predicted by the models to those derived from an analysis of optical spectra, and illustrate how the synthetic UV spectra allow a determination of the stellar parameters. Finally, the improved model atmosphere code will be used in chapter 6 to compute EUV spectral energy distributions to be used as input for photoionization simulations employed for the analysis of the H II regions surrounding massive hot stars and starbursts.

Parts of this thesis have already been published in Pauldrach, Hoffmann, and Lennon (2001); Hoffmann and Pauldrach (2001); Pauldrach, Hoffmann, and Méndez (2001); Hoffmann, Pauldrach, and Puls (2003); and Sternberg, Hoffmann, and Pauldrach (2003).

2

The basics: fundamentals of radiation-driven wind theory

As foundation for (and to introduce the terminology of) the following chapter describing the numerical models, this chapter will review briefly the basic physical processes that define the state of matter and radiation in the atmospheres of hot stars, and which are ultimately responsible for the emergent spectral energy distributions that we observe. By adjusting the parameters of a computer model of these processes until the simulated spectrum resembles the observed one, we deduce information about the physical properties of the observed object. Figure 2-1 gives an overview of the physics to be treated, which are discussed in more detail in the following sections. Chapter 3 will then focus on the computer models used in simulating these processes.

The theory of expanding stellar atmospheres as employed in this work is based on the assumptions that the atmosphere is *homogeneous*, *spherically symmetric*, and *stationary*, and that the expansion is *radiatively driven*. The last assumption, that the atmospheres are driven by the transfer of momentum from the radiation field via the absorption in hundreds of thousands of atomic spectral lines, is by now well established for O stars (Abbott 1980, 1982; Abbot and Lucy 1985; Pauldrach et al. 1986; Pauldrach 1987; Pauldrach et al. 1994; Kudritzki et al. 1995; Puls et al. 1996). The first three assumptions, however, are quite restrictive, and, given the sophistication of stellar atmosphere modelling as presented in this work, are perhaps the the most severe approximations¹ present in the current models, but the

¹ Observations of the characteristic P Cygni profiles of spectral lines in the UV reveal drifting absorption features (“narrow line components”, “discrete absorption components” (DACs), Snow 1977; Henrichs 1984; Prinja and Howarth 1986; Massa et al. 1995) which are believed to result from higher-density inhomogeneities in the wind. The currently favored explanation for these inhomogeneities is instabilities in the driving mechanism (Lucy and

promising results from detailed comparisons of models and observations justify continuing this approach of stationary, spherically symmetric models, and improving instead on the description of the inherent physics.

2.1. Radiative energy and radiation transfer

Radiation and radiation transfer is described in terms of the so-called *specific intensity* $I = I(\vec{r}, \vec{n}, \nu)$, defined as the amount of energy dE at frequency ν streaming per unit time dt and frequency interval $d\nu$ in a direction \vec{n} through a unit area dS (normal to \vec{n}) at \vec{r} into a solid angle $d\omega$:

$$dE = I_\nu dS d\omega dt d\nu, \quad (2.1)$$

where the index ν emphasizes the explicit frequency dependence. In spherically symmetric geometry, the independent variables are reduced to radius r , an angle θ (where $\theta = 0$ is chosen to be the outward direction at the currently considered location), and frequency ν .

It is often helpful to consider angular-weighted integrated quantities, the *moments* of the radiation field,

$$X_\nu^{(n)} = \frac{1}{2} \int_{-1}^1 I_\nu \mu^n d\mu \quad (2.2)$$

with $\mu = \cos \theta$ the directional cosine with respect to the outward direction. (In spherically symmetric geometry, these moments are dependent only on frequency and radius.) The zeroth-order moment

$$J_\nu = \frac{1}{2} \int_{-1}^1 I_\nu d\mu \quad (2.3)$$

is simply the *average intensity*, and the first-order moment

$$H_\nu = \frac{1}{2} \int_{-1}^1 I_\nu \mu d\mu, \quad (2.4)$$

the so-called *Eddington flux*, is related to the energy flux F_ν (the angular integral over the intensity weighted with $\cos \theta$) as $H_\nu = F_\nu/4\pi$. The *luminosity* of the star, $L = 4\pi r^2 \int_0^\infty F_\nu d\nu$, the total energy output per unit time, is an important quantity due to the fact that it must be conserved throughout the atmosphere as all energy is generated in the stellar core and the atmosphere contains no energy sources or sinks (see also section 2.3). The second- and third-order moments are denoted by K_ν and N_ν , respectively.

The propagation of radiation through matter is described by the radiation-transfer equation

$$\frac{dI_\nu}{dz} = -\chi_\nu I_\nu + \eta_\nu \quad (2.5)$$

where z is the geometrical coordinate along the direction considered. χ is the *opacity* and describes (per unit length) processes proportional to the intensity (absorption and stimulated emission; the latter is

Solomon 1970, Owocki et al. 1988) that compress the wind into narrow “shells”, collisions of which are also believed to be the cause of the observed X-ray emission from the winds (e.g., Harnden et al. 1979, Seward et al. 1979). Although a full time-dependent, selfconsistent treatment of the hydrodynamics is still outstanding, Lucy (1982) has shown that the mean local velocity of a phenomenological model with a multiply non-monotonic velocity field wind is described by the same equation of motion as that of the stationary model (since the maximum amplitude of the variations is small compared to the velocity of the outflow). Concerning spherical symmetry, although some O and B stars are known to possess relatively fast equatorial rotation speeds of around 50 to 300 km/s at the surface (Conti et al. 1977) which theory shows can lead to a latitude-dependent mass loss rate (wind compressed disk effect, Bjorkman and Cassinelli 1993; Owocki et al. 1994; Petrenz and Puls 1996), no detailed analysis of the influence of this asymmetry on the UV spectra exists to date. Pauldrach, Puls, and Kudritzki (1986) conclude that the influence of rotation on the wind is minimal for $v_{\text{rot}} < 200$ km/s.

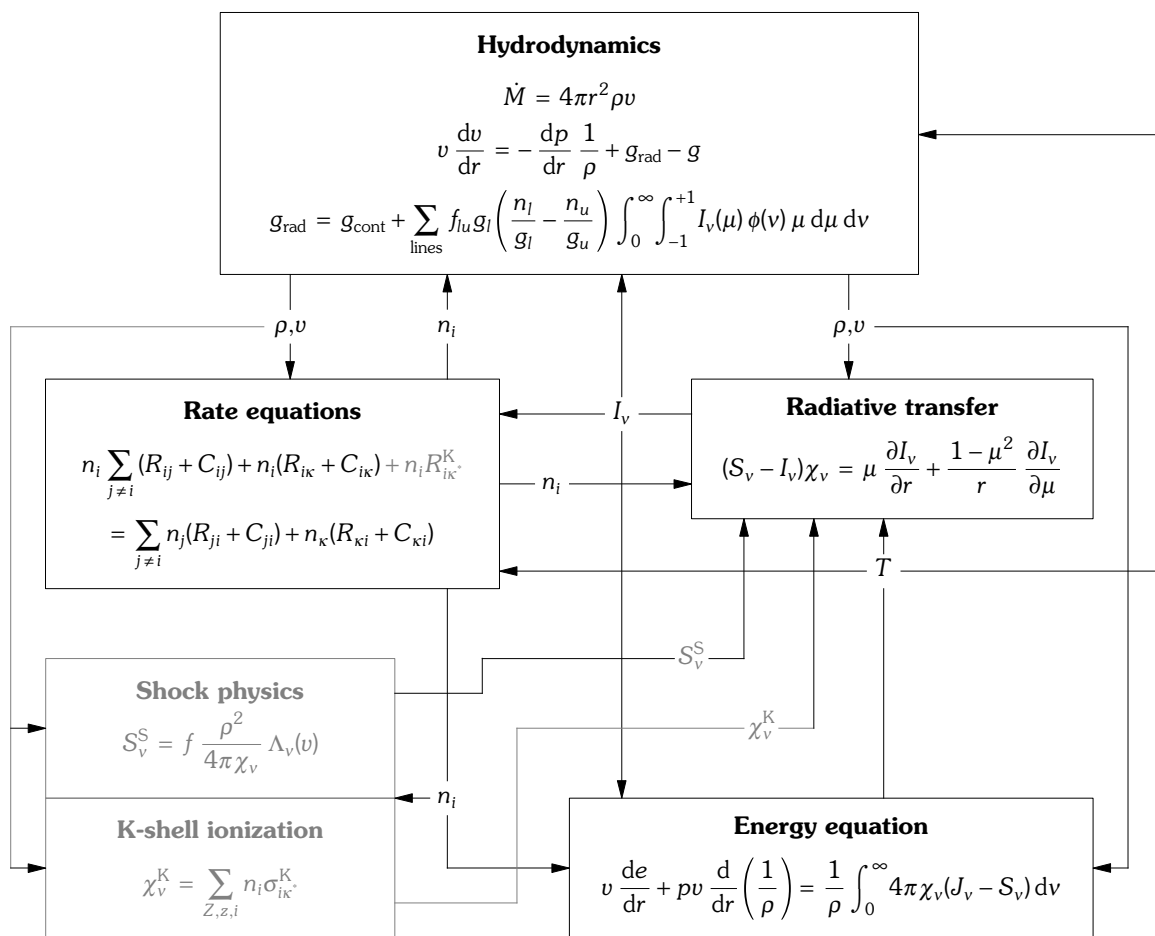


FIGURE 2-1. — The basic physical equations of the theory of radiatively-driven stellar atmospheres.

treated as negative opacity). η is the *emissivity*² of the material resulting from spontaneous emission. As the intensity itself also enters into the processes governing the atomic level populations, and thus the number density of absorbers and emitters (the microscopic processes will be discussed in the next section), both χ and η will be functions of the spatial and angular coordinates (and the frequency), and a *consistent* solution of the radiation transfer can, in general, only be obtained numerically (e.g., by an iteration scheme). Solution of the radiation-transfer equation for given opacities and emissivities is known as a *formal solution* or *formal integral*.

In spherical coordinates the radiation transfer equation takes the form

$$\mu \frac{\partial I_\nu}{\partial r} + \frac{1 - \mu^2}{r} \frac{\partial I_\nu}{\partial \mu} = -I_\nu \chi_\nu + \eta_\nu, \quad (2.6)$$

but as this represents a (numerically much more difficult to solve) partial differential equation, the preferred method to compute the radiative transfer involves a ray-by-ray solution using cartesian coordinates in so-called (p, z) -geometry as illustrated in figure 3-8 on page 27.

It is customary to write the radiation transfer equation using as the spatial coordinate the dimensionless *optical depth* τ_ν , defined by $d\tau_\nu = \chi_\nu dz$, or equivalently, by $\tau_\nu = \int_{z_0}^z \chi_\nu(z') dz'$,³

² The dimensions are intensity per unit length, i.e., erg/sr/s/Hz/cm³.

³ The terms *optically thin* and *optically thick* refer to the condition that $\tau \ll 1$ resp. $\tau \gg 1$.

$$\pm \frac{dI_v^\pm}{d\tau_v} = S_v - I_v^\pm, \quad (2.7)$$

where I_v^+ and I_v^- are the intensity in positive resp. negative z direction along the ray considered and $S_v = \eta_v/\chi_v$ is known as the *source function*. The physical significance of the source function is that at large optical depths (deep in the atmosphere) it approaches the universal *Planck function*

$$B_v(T) = \frac{2h\nu^3}{c^2} \frac{1}{e^{h\nu/kT} - 1}, \quad (2.8)$$

as the mean free photon path lengths ($\sim 1/\chi_v$) then become small and the radiation field becomes dominated by *local* processes, i.e., the conditions approach *local thermodynamic equilibrium* (LTE). In these cases of great optical depths the transport of radiation becomes *diffusive*, and the flux can be approximated as

$$H_v = -\frac{1}{3} \frac{\partial B_v(T(\tau))}{\partial \tau} = -\frac{1}{3} \frac{1}{\chi_v} \frac{\partial B_v}{\partial T} \frac{dT}{dz} \quad (2.9)$$

(for a detailed discussion see, e.g., Mihalas 1978, chapter 3). We use this *diffusion approximation* as the inner boundary for the radiative transfer in the model atmospheres.

Of special relevance in this context is the *Rosseland mean* of the opacity, a weighted average defined by

$$\frac{1}{\chi_{\text{Ross}}} = \frac{\int_0^\infty \frac{1}{\chi_v} \frac{\partial B_v}{\partial T} dv}{\int_0^\infty \frac{\partial B_v}{\partial T} dv}. \quad (2.10)$$

The *Rosseland optical depth* τ_{Ross} is analogously defined by $d\tau_{\text{Ross}} = \chi_{\text{Ross}} dz$. In regions where the diffusion approximation is valid, it can be used to derive the temperature structure (a so-called *gray atmosphere*, as only frequency-integrated quantities are considered), since the total flux $\int_0^\infty H_v dv$ must be conserved. In plane-parallel geometry this yields (for spherical geometry see section 3.2.2)

$$T_{\text{gray}}^4 = \frac{3}{4} T_{\text{eff}}^4 \left(\tau_{\text{Ross}} + \frac{2}{3} \right). \quad (2.11)$$

The stellar radius R is customarily defined as the radius where $\tau_{\text{Ross}} = 2/3$, so that $T_{\text{gray}}(R) = T_{\text{eff}}$. The effective temperature T_{eff} is defined such that $4\pi R^2 \sigma T_{\text{eff}}^4 = L$, with σ being the Stefan-Boltzmann constant.

The radiation transfer equation can be solved numerically both in its differential form as given above, as well as in an integral formulation,

$$I_v^+(\tau) = \int_{\tau_0}^{\tau} S(\tau') e^{-(\tau-\tau')} d\tau' + I^+(\tau_0) e^{-(\tau-\tau_0)}. \quad (2.12)$$

Both approaches will be used in the course of this work.

2.2. Interaction of matter and light; opacities and emissivities; rate equations and occupation numbers

To determine the opacities and emissivities, the occupation numbers of all contributing atomic levels have to be known. Since the densities of expanding atmospheres in regions still affecting the emergent spectrum⁴ can become small enough that collisions can no longer establish LTE⁵ against the dominating

⁴ This is by necessity the region where the material becomes optically thin and the radiation field therefore non-locally determined.

⁵ Note that at the densities and temperatures considered here, deviations from LTE only regard the radiation field

radiative processes, the occupation numbers must be explicitly computed considering all relevant atomic transitions. (In LTE, the occupation numbers simply follow a Boltzmann distribution at the local kinetic temperature.) Given stationarity, the sum of all rates $n_i P_{ij}$ depopulating any particular level i must be balanced by the sum of all transitions $n_j P_{ji}$ populating that level (statistical equilibrium):

$$n_i \sum_{j \neq i} P_{ij} = \sum_{j \neq i} n_j P_{ji} \quad (2.13)$$

where n_i is the occupation number (number density) of atoms in state i and P_{ij} is the *rate coefficient* giving the probability per unit time of a transition from level i to level j . As molecules need not be considered here (they only become important in cool stars of spectral type G or later), these equation systems can be considered on a per-element basis. The summations are carried out over all levels of all considered ionization stages, including excitation and de-excitation processes (i and j within the same ionization stage) as well as ionization and recombination processes (i and j in different ionization stages). The redundant system of equations is closed by replacing one of the equations by the requirement of particle conservation, $\sum_i n_i = n$, where $n = \rho Y/A$ is the number density of the element in question (ρ is the local mass density, and A and Y are the atomic mass and abundance (mass fraction) of the element). Finally, the electron density is computed by summing over the contributions of the ionization stages of all elements considered (charge conservation).

The transition probabilities P_{ij} comprise radiative (R_{ij}) and collisional (C_{ij}) transitions. For clarity, the upper level in ionization and recombination processes (bound-free transitions) will in the following be denoted by κ . This is usually the ground state of the next-higher ionization stage plus a mean over the free-electron distribution. (Where the ionization cross-sections to excited states of the next ionization stage are also relevant, these are considered as well.)

2.2.1. Radiative transitions

The photoionization rate coefficients are given by

$$R_{i\kappa} = \int_{\nu_{i\kappa}}^{\infty} \frac{4\pi\alpha_{i\kappa}(\nu)}{h\nu} J_\nu d\nu \quad (2.14)$$

where $\nu_{i\kappa}$ is the ionization threshold frequency. In this work, the photoionization cross-sections $\alpha_{i\kappa}(\nu)$ are parametrized in the *Seaton approximation*

$$\alpha_{i\kappa}(\nu) = \alpha_{i\kappa} \left(\beta_{i\kappa} \left(\frac{\nu}{\nu_{i\kappa}} \right)^{-s_{i\kappa}} + (1 - \beta_{i\kappa}) \left(\frac{\nu}{\nu_{i\kappa}} \right)^{-s_{i\kappa}-1} \right) \quad (2.15)$$

with values for $\alpha_{i\kappa}$, $\beta_{i\kappa}$, and $s_{i\kappa}$ fitted to best reproduce the cross-sections from detailed calculations (cf. section 3.2.3). Resonances in the cross-sections (autoionization, dielectronic recombination) are treated as line transitions to the ionized state κ , in a similar manner as described by Mihalas and Hummer (1973). The radiative recombination rate coefficient is

$$R_{\kappa i} = \left(\frac{n_i}{n_\kappa} \right)^* \int_{\nu_{i\kappa}}^{\infty} \frac{4\pi\alpha_{i\kappa}(\nu)}{h\nu} \left(\frac{2h\nu^3}{c^2} + J_\nu \right) e^{-h\nu/kT} d\nu \quad (2.16)$$

where g_i and g_κ are the statistical weights of the two levels and

$$\left(\frac{n_i}{n_\kappa} \right)^* = n_e \frac{g_i}{g_\kappa} e^{h\nu_{i\kappa}/kT} \frac{1}{2} \left(\frac{h^2}{2\pi m_e kT} \right)^{3/2} \quad (2.17)$$

is the *Saha-Boltzmann factor*, the ratio of the occupation numbers that would be reached in LTE.

and the atomic level populations. As elastic collisions between particles (mostly electrons) are much more common than other processes, the kinetic thermal energies here still conform to a Boltzmann distribution (i.e., a Maxwellian distribution for the velocities).

For radiative bound-bound (line) transitions we have (i is the lower, j the upper level of the transition)

$$R_{ij} = B_{ij} \int_0^\infty \phi_{ij}(v) J_\nu dv \quad (2.18)$$

$$R_{ji} = A_{ji} + B_{ji} \int_0^\infty \phi_{ij}(v) J_\nu dv \quad (2.19)$$

where A_{ji} , B_{ji} , and B_{ij} are the *Einstein coefficients* of the transition and $\phi_{ij}(v)$ is the line-profile function, normalized such that $\int_0^\infty \phi_{ij}(v) dv = 1$. (Note that $\phi_{ij}(v)$ has dimensions of 1/frequency). For the line profile function we use a Gaussian with a Doppler width given by the local thermal velocity v_{therm} (m is the mass of the ion) and a local microturbulent velocity v_{turb} (see section 3.2.1.2)

$$\phi_{ij}(v) = \frac{1}{\Delta v_D \sqrt{\pi}} e^{-\frac{(v-v_{ij})^2}{\Delta v_D^2}}, \quad \Delta v_D = \frac{v_{ij}}{c} \left(v_{\text{therm}}^2 + v_{\text{turb}}^2 \right)^{1/2}, \quad v_{\text{therm}}^2 = \frac{2kT}{m}. \quad (2.20)$$

Since the line width is much smaller than the transition frequency, the expressions for the rate coefficients can be written in a form analogous to those of the bound-free transitions,

$$R_{ij} = \int_0^\infty \frac{4\pi\alpha_{ij}(v)}{hv} J_\nu dv \quad (2.21)$$

and

$$R_{ji} = \left(\frac{n_i}{n_j} \right)^* \int_0^\infty \frac{4\pi\alpha_{ij}(v)}{hv} \left(\frac{2hv^3}{c^2} + J_\nu \right) e^{-hv/kT} dv \quad (2.22)$$

with the *Boltzmann factor*

$$\left(\frac{n_i}{n_j} \right)^* = \frac{g_i}{g_j} e^{hv_{ij}/kT} \quad (2.23)$$

that (like the Saha-Boltzmann factor) describes the LTE occupation number ratio. The cross-section $\alpha_{ij}(v) = \alpha_{ij}\phi_{ij}(v)$, the *oscillator strength* f_{ij} , and the Einstein coefficients A_{ji} , B_{ji} , and B_{ij} are related via

$$\alpha_{ij} = \frac{\pi e^2}{m_e c} f_{ij}, \quad \alpha_{ij} = \frac{hv_{ij}}{4\pi} B_{ij}, \quad g_i B_{ij} = g_j B_{ji}, \quad A_{ji} = \frac{2hv_{ij}^3}{c^2} B_{ji}. \quad (2.24)$$

One of these quantities (in addition to line frequency v_{ij} and the level indices i and j) is sufficient to characterize the transition. In astrophysics, it is customary to use the “*gf-value*” $gf = g_i f_{ij} = g_j f_{ji}$.

Contrary to the bound-free rate coefficients, which can be computed to sufficient accuracy by straightforward numerical integration⁶ if the continuum is described with about 1000 frequency points (see section 3.2.1.1), such a simple integration is not possible for the bound-bound rate coefficients, since the line profile cannot be resolved on this scale. (Using a finer frequency grid which resolves the line profiles is impractical, since this would require on the order of 10^7 frequency points.) For computing the bound-bound rate coefficients we therefore make use of the Sobolev Approximation (Sobolev 1957) generalized to include interaction with the continuum by Hummer and Rybicki (1985) and Puls and Hummer (1988).

As Sellmaier et al. (1993) and Santolaya-Rey et al. (1997) have shown, the Sobolev-with-continuum formalism represents an excellent approximation to the time-consuming, “exact” comoving-frame calculations. Deviations only appear for some weak second-order lines in the subsonic region of the atmosphere, which, however, are inconsequential in establishing the ionization structure of the atmosphere (Santolaya-Rey et al. 1997).

We write the integrals in equations 2.18 and 2.19 as

$$\bar{J} = \int_0^\infty \phi_{ij}(v) J_\nu dv = \frac{1}{2} \int_{-1}^1 \int_0^\infty \phi_{ij}(v) I_\nu(\mu) dv d\mu = \frac{1}{2} \int_{-1}^1 \bar{I}(\mu) d\mu, \quad (2.25)$$

where $\bar{I}(\mu)$ is the frequency-integrated intensity in the line (weighted with the line-profile function). In Sobolev-with-continuum approximation, this is given by (cf. Puls and Hummer 1988)

⁶ Integration with weights taking into account the v^{-s} and v^{-s-1} dependence of the cross-section.

$$\bar{I} = I_{\text{inc}}(r, \nu(\mu), \mu) \frac{1 - e^{-\tau_S(r, \mu)}}{\tau_S(r, \mu)} + S_{ij} \left(1 - \frac{1 - e^{-\tau_S(r, \mu)}}{\tau_S(r, \mu)} \right) + (S_C - S_{ij}) U(\tau_S(r, \mu), \beta) \quad (2.26)$$

where I_{inc} is the intensity incident on the interaction region of the line, S_{ij} is the source function of the line (equation 2.36), S_C is the continuum source function,

$$\tau_S(r, \mu) = \frac{\chi_{ij}}{v_{ij}/c} \frac{1}{\mu^2 \frac{dv}{dr} + (1 - \mu^2) \frac{v}{r}} \quad (2.27)$$

is the *Sobolev optical depth* of the interaction region of the line (where χ_{ij} is the frequency-integrated line opacity (see section 2.2.3), with dimensions opacity times frequency),

$$U(\tau, \beta) = \tau \int_{-\infty}^{\infty} dx \varphi(x) \int_x^{\infty} dy \varphi(y) e^{-\tau \int_x^y ds \varphi(s)} \left(1 - e^{-\beta \tau(y-x)} \right), \quad \varphi(x) = \Delta v_D \phi(\Delta v_D x) \quad (2.28)$$

is the “*interaction function*”, and β is the ratio of continuum opacity to line opacity.

The rate coefficients are then given by

$$R_{ij} = B_{ij} \bar{J} \quad (2.29)$$

$$R_{ji} = A_{ji} + B_{ji} \bar{J}. \quad (2.30)$$

where $\bar{J} = \frac{1}{2} \int_{-1}^1 \bar{I} d\mu$ (equation 2.25) is obtained by integrating the intensity (equation 2.26) over all solid angles. The angular integrals

$$P_S = \frac{1}{2} \int_{-1}^1 \frac{1 - e^{-\tau_S(r, \mu)}}{\tau_S(r, \mu)} d\mu \quad (2.31)$$

$$\bar{U} = \frac{1}{2} \int_{-1}^1 U(\tau_S(r, \mu), \beta) d\mu \quad (2.32)$$

can be pre-calculated for a series of values of τ and β and interpolated at runtime from the tables. Given a suitable analytic parametrization of the functional dependence of I_{inc} on μ , the integral

$$P_1 = \frac{1}{2} \int_{-1}^1 I_{\text{inc}}(r, \nu(\mu), \mu) \frac{1 - e^{-\tau_S(r, \mu)}}{\tau_S(r, \mu)} d\mu \quad (2.33)$$

can also be pre-computed as a function of the coefficients of the parametrization, as described by Taresch et al. (1997). For this purpose we represent I_{inc} as a piecewise linear function in μ (in the two intervals $-1 \leq \mu < \mu_c$ and $\mu_c \leq \mu \leq 1$, where $\mu_c = (1 - (R/r)^2)^{1/2}$ represents the angular extent of the photosphere (“core”) as seen from point r), chosen such that this linear approximation yields the same moments J , H , K , and N as derived from the solution of the radiation transfer. (However, in contrast to Taresch et al., who used a continuous piecewise linear representation in the three intervals $-1 \leq \mu < 0$, $0 \leq \mu < \mu_c$, and $\mu_c \leq \mu \leq 1$, our parametrization is possibly discontinuous at $\mu = \mu_c$, as this better describes the change in intensity at the edge of the stellar disk.)

For the angular dependence of the frequency Doppler shift

$$\nu(\mu) = v_{ij} \cdot \left(1 + \frac{\mu v(r)}{c} \right) \quad (2.34)$$

of the incident intensity in the angular integral we make the approximation of representing $I_{\text{inc}}(r, \nu(\mu), \mu)$ by $I_{\text{inc}}(r, \nu(\mu = 1), \mu)$, i.e., we use

$$I_{\text{inc}}(r, \nu(\mu), \mu) \approx I_{\text{inc}} \left(r, v_{ij} \cdot \left(1 + \frac{v(r)}{c} \right), \mu \right). \quad (2.35)$$

(Note that this approximation concerns only the angle-dependence of the frequency argument. The explicit angle-dependence of the incident intensity is properly considered in the angular integral.) This is not a bad approximation, because if the continuum is optically thick, the radiation field will be nearly isotropic and vary only slowly with frequency, so that the approximation is sufficiently accurate. In the opti-

cally thin case, on the other hand, the largest contribution to the integral will be by the radiation from the stellar disk (around $\mu = 1$), for which our approximation gives the correct Doppler shift.

Finally, since

$$S_{ij} = \frac{n_j A_{ji}}{n_i B_{ij} - n_j B_{ji}} \quad (2.36)$$

the rate coefficients can be simplified to

$$R_{ij} = B_{ij} (P_1 + S_C \bar{U}) \quad (2.37)$$

$$R_{ji} = B_{ji} (P_1 + S_C \bar{U}) + A_{ji} (P_S + \bar{U}), \quad (2.38)$$

which gives the same net rates as equations 2.29 and 2.30.

2.2.2. Collisional transitions

The rate coefficients for collisional excitation by electrons are given by

$$C_{ij} = n_e \int_0^\infty v \sigma_{ij}(v) f(v) dv, \quad \sigma_{ij}(v) = \frac{\pi \hbar^2}{v^2 m_e^2} \frac{\Omega_{ij}(E)}{g_i} \quad (2.39)$$

where $f(v)$ is the electron velocity distribution, $\sigma_{ij}(v)$ is the collisional excitation cross-section from level i to level j , and $\Omega_{ij}(E)$ is the energy-dependent *collision strength*. As the electron velocity distribution $f(v)$ is known (Maxwellian), the integrals can be performed in advance for a series of temperatures to give a temperature-dependent collision strength $\Omega_{ij}(T)$, so that

$$C_{ij} = n_e \left(\frac{2\pi}{kT} \right)^{1/2} \frac{\hbar^2}{m_e^{3/2}} \frac{\Omega_{ij}(T)}{g_i} e^{-h\nu_{ij}/kT} = n_e \frac{8.629 \times 10^{-6}}{T^{1/2}} \frac{\Omega_{ij}(T)}{g_i} e^{-h\nu_{ij}/kT}. \quad (2.40)$$

The collisional de-excitation rate coefficient is

$$C_{ji} = \left(\frac{n_i}{n_j} \right)^* C_{ij}. \quad (2.41)$$

In this work, tabulated collision strengths for $T = 20000$ K are used, along with a coefficient describing a (linear) temperature dependence of Ω_{ij} . Where no data are available for Ω_{ij} , for radiatively allowed transitions we employ van Regemorter's (1962) approximate formula (as given by Mihalas 1978) relating the collision strength to the photoionization cross-section

$$C_{ij} = 5.465 \times 10^{-11} n_e T^{1/2} (14.5 f_{ij}) \bar{g} \left(\frac{E_H}{h\nu_{ij}} \right)^2 \frac{h\nu_{ij}}{kT} e^{-h\nu_{ij}/kT} \quad (2.42)$$

where E_H is the ionization energy of Hydrogen and \bar{g} takes the value 0.7 if the main quantum numbers of levels i and j are equal, 0.2 otherwise. For the remaining transitions we use equation 2.40 with a representative value $\Omega_{ij} = 1$ (cf. Pauldrach 1987).

For collisional ionization we use an approximate formula from Seaton as given by Mihalas (1978),

$$C_{i\kappa} = n_e \frac{1.55 \times 10^{13}}{T^{1/2}} \bar{g} \alpha_{i\kappa} \frac{e^{-h\nu_{i\kappa}/kT}}{h\nu_{i\kappa}/kT} \quad (2.43)$$

where $\alpha_{i\kappa}$ is the photoionization cross-section at the ionization threshold. \bar{g} takes the value 0.1, 0.2, or 0.3 for initial ionic charge of 0, 1, or ≥ 2 , respectively. Finally, the collisional recombination rate coefficient is

$$C_{\kappa i} = \left(\frac{n_i}{n_\kappa} \right)^* C_{i\kappa}. \quad (2.44)$$

Note that since the electron velocity distribution is Maxwellian, collisions tend toward establishing LTE occupation numbers.

2.2.3. Opacities and emissivities

The opacities and emissivities are closely related to the radiative transitions as they are in fact a different aspect of the same microphysical processes. For bound-free transitions we have (cf. equations 2.14 and 2.16)

$$\chi_{ik}(v) = n_i \alpha_{ik}(v) - n_\kappa \alpha_{ik}(v) \left(\frac{n_i}{n_\kappa} \right)^* e^{-hv/kT} = \alpha_{ik}(v) \left(n_i - n_\kappa \left(\frac{n_i}{n_\kappa} \right)^* e^{-hv/kT} \right) \quad (2.45)$$

$$\eta_{ik}(v) = n_\kappa \alpha_{ik}(v) \left(\frac{n_i}{n_\kappa} \right)^* \frac{2hv^3}{c^2} e^{-hv/kT}. \quad (2.46)$$

For bound-bound transitions the opacities and emissivities are (cf. equations 2.21 and 2.22)

$$\chi_{ij}(v) = \chi_{ij}\phi(v) = n_i \alpha_{ij}\phi_{ij}(v) - n_j \frac{g_i}{g_j} \alpha_{ij}\phi_{ij}(v) = \alpha_{ij}\phi_{ij}(v) \left(n_i - \frac{g_i}{g_j} n_j \right) = \frac{hv_{ij}}{4\pi} (n_i B_{ij} - n_j B_{ji}) \phi_{ij}(v) \quad (2.47)$$

$$\eta_{ij}(v) = \eta_{ij}\phi(v) = n_j \frac{g_i}{g_j} \alpha_{ij} \frac{2hv_{ij}^3}{c^2} \phi_{ij}(v) = \frac{hv_{ij}}{4\pi} n_j A_{ji} \phi_{ij}(v). \quad (2.48)$$

The opacity and emissivity from free-free transitions (Bremsstrahlung) is

$$\chi_{ff}(v) = n_e n_+ \alpha_{ff}(v, T) (1 - e^{-hv/kT}) \quad (2.49)$$

$$\eta_{ff}(v) = n_e n_+ \alpha_{ff}(v, T) \frac{2hv^3}{c^2} e^{-hv/kT} \quad (2.50)$$

where n_+ is the number density of the particular ionic species ($n_+ = \sum_i n_i$, where the summation runs over all levels of this ionization stage). Note that we must have $S_{ff} \equiv \eta_{ff}/\chi_{ff} = B_v$ since our electron gas is in thermal equilibrium. The coefficient⁷ α_{ff} is computed from tabulated gaunt-factors g_{ff} as

$$\alpha_{ff}(v, T) = \frac{4e^6 Z^2}{3ch} \left(\frac{2\pi}{3kTm_e^3} \right)^{1/2} v^{-3} g_{ff} \quad (2.51)$$

where Z is the ionic charge (cf. Mihalas 1987). Note that we do not consider free-free transitions in the rate equations because we treat all unbound states of an ionization stage as a single, but temperature-dependent, “level” (which is possible since the electron velocity distribution is Maxwellian). (Thus, free-free transitions do not change our level occupations n_i .) For reasons of energy conservation this temperature dependence must be taken into consideration by accounting for the transfer of energy to the plasma via the free-free heating and cooling rates (see next section).

The opacity from Thomson scattering is independent of frequency and is given by

$$\chi_{Th}(v) = n_e \sigma_{Th} \quad (2.52)$$

with the Thomson scattering cross-section

$$\sigma_{Th} = \frac{8\pi}{3} \frac{e^4}{m_e^2 c^4} = 6.652 \times 10^{-25} \text{ cm}^2. \quad (2.53)$$

The Thomson emissivity (assuming *complete redistribution* over angles) is

$$\eta_{Th}(v) = \chi_{Th} J_v \quad (2.54)$$

where J_v is the average intensity.

⁷ α_{ff} is technically not a cross-section as it has dimensions of cm^5 , but we use the same symbol (α) in analogy to the formulae for the bound-free and bound-bound transitions; however, $n_+ \alpha_{ff}$ and $n_e \alpha_{ff}$ are cross-sections.

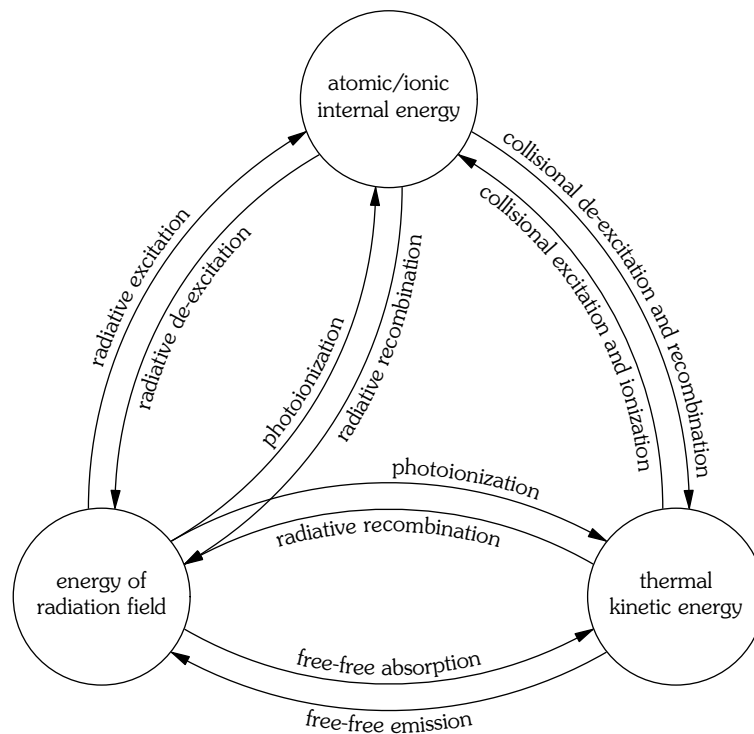


FIGURE 2-2. — Sketch illustrating the transfer of energy by microphysical processes to and from the major “energy pools” in the atmosphere.

2.3. Kinetic temperature and energy balance

The temperature at each point in the atmosphere results from the requirement that the energy absorbed per unit time by any particular volume element be equal to the energy emitted per unit time by that volume element (radiative balance).⁸ Microphysically speaking, any imbalance in the absorption/emission of radiative energy will result in a heating resp. cooling of the gas (see figure 2-2), and in the stationary case the balance of the heating and cooling rates (cf. Hummer and Seaton 1963) is completely equivalent to the balance of radiation absorption and emission, although depending on the physical conditions either description can be more advantageous for numerical modelling (see below).

In the outer parts of the atmosphere where the continuum becomes optically thin the opacity is dominated by lines. These mostly have a scattering characteristic, meaning that most of the radiative energy absorbed in a particular transition is also reemitted in that transition. Radiative bound-bound transitions, however, do not directly affect the thermal kinetic energy of the gas, and thus the processes dominating the radiative balance actually become unimportant for determining the temperature. Only the numerically much smaller *differences* between the absorbed and emitted radiation determine the energy balance of the gas (via radiative bound-free and free-free processes and collisional processes coupling to the levels dominated by the line transitions). In these cases it is therefore numerically advantageous to determine the temperature by balancing the heating and cooling rates. (See also Hoffmann 1995; Pauldrach et al. 1998; Kubát et al. 1999.)

Heating⁹ (in $\text{erg}/\text{cm}^3/\text{s}$) by radiative bound-free transitions (photoionization) is given by

⁸ We will disregard very minor effects such as dissipative processes (for example, frictional heating, cf. Springmann and Pauldrach 1992) and adiabatic cooling.

⁹ Heating rates will be denoted by Γ (“gain”), cooling rates by Λ (“loss”).

$$\Gamma_{ik}^R = n_i \int_{v_{ik}}^{\infty} \frac{4\pi\alpha_{ik}(v)}{hv} J_v h(v - v_{ik}) dv \quad (2.55)$$

which corresponds to the radiative bound-free rate with an additional term $h(v - v_{ik})$ in the integrand, since only the difference to the ionization energy will remain as kinetic energy for the released electron. The analogous expression for cooling by radiative recombination is

$$\Lambda_{ki}^R = n_k \left(\frac{n_i}{n_k} \right)^* \int_{v_{ik}}^{\infty} \frac{4\pi\alpha_{ik}(v)}{hv} \left(\frac{2hv^3}{c^2} + J_v \right) e^{-hv/kT} h(v - v_{ik}) dv. \quad (2.56)$$

Radiative bound-bound transitions (lines) couple the atomic internal energy to the radiation field but do not influence the kinetic energy of the electrons (cf. figure 2-2). Collisional (bound-bound and bound-free) processes release or consume a fixed amount of kinetic energy corresponding to the excitation resp. ionization energy of the transition. Their contribution to heating and cooling of the gas is given by

$$\Lambda_{ik}^C = n_i C_{ik} h v_{ik} \quad (2.57)$$

$$\Gamma_{ki}^C = n_k C_{ki} h v_{ik} \quad (2.58)$$

$$\Lambda_{ij}^C = n_i C_{ij} h v_{ij} \quad (2.59)$$

$$\Gamma_{ji}^C = n_j C_{ji} h v_{ij} \quad (2.60)$$

where the Cs are the rate coefficients as described in section 2.2.2. Finally, the heating and cooling by free-free transitions from a particular ionic species is given by

$$\Gamma^{ff} = n_e n_+ \int_0^{\infty} 4\pi\alpha_{ff}(v, T) J_v dv \quad (2.61)$$

$$\Lambda^{ff} = n_e n_+ \int_0^{\infty} 4\pi\alpha_{ff}(v, T) \left(\frac{2hv^3}{c^2} + J_v \right) e^{-hv/kT} dv \quad (2.62)$$

where n_+ is the number density of the ions and $\alpha_{ff}(v, T)$ is the corresponding ‘‘cross-section’’ (equation 2.51). Like the bound-free heating and cooling, the evaluation of these expressions by numerical integration over frequency is straightforward. For numerical reasons, it is convenient to express equations 2.61 and 2.62 as a net rate

$$\Gamma^{ff} - \Lambda^{ff} = n_e n_+ \int_0^{\infty} 4\pi\alpha_{ff}(v, T) \left(\frac{J_v}{B_v} - 1 \right) \frac{2hv^3}{c^2} e^{-hv/kT} dv. \quad (2.63)$$

An analogous expression for the radiative bound-free heating and cooling rates is

$$\Gamma_{ik}^R - \Lambda_{ki}^R = n_k \left(\frac{n_i}{n_k} \right)^* \int_{v_{ik}}^{\infty} 4\pi\alpha_{ik}(v) \left(1 - \frac{v_{ik}}{v} \right) \left(\frac{J_v}{S_{ik}(v)} - 1 \right) \frac{2hv^3}{c^2} e^{-hv/kT} dv \quad (2.64)$$

where $S_{ik}(v) \equiv \eta_{ik}(v)/\chi_{ik}(v)$ is the corresponding bound-free source function. Note that approaching LTE, $S_{ik} \rightarrow B_v$, and if also $J_v \rightarrow B_v$, the integrand becomes zero, i.e., the heating and cooling rates also go into detailed balance.

In the inner parts of the atmosphere where collisions begin to dominate the rate equations and the occupation numbers approach LTE, the balancing of the heating and cooling rates becomes less sensitive to the temperature. In this case it is advantageous to determine the temperature via radiative balance, in particular since in the inner parts the continuum (bound-free and free-free processes) becomes optically thick, and absorption and emission is no longer dominated by line processes. Here we therefore employ a variant of the radiative-balance scheme based on conservation of the flux (see section 3.2.2).

2.4. Hydrodynamics and radiative driving

In the stationary case assumed here, the density and velocity structure of the wind are governed by the equation of continuity

$$4\pi r^2 \rho(r)v(r) = \dot{M} = \text{const} \quad (2.65)$$

where \dot{M} is the *mass loss rate* of the star (i.e., the total amount of mass carried off per unit time by the expanding atmosphere), and by the competing forces of gravity and gas and radiation pressure in the equation of motion

$$v \frac{dv}{dr} = -\frac{1}{\rho} \frac{dp}{dr} - g + g_{\text{rad}} \quad (2.66)$$

where ρ and v are the density and velocity of the outflow at radius r in the wind, $g = GM/r^2$ is the local gravitational acceleration (M is the mass of the star and G is the gravitational constant), and $p = a^2/\rho$ is the local gas pressure with the isothermal sound speed a .

The radiative acceleration

$$g_{\text{rad}} = \frac{2\pi}{c} \frac{1}{\rho} \int_0^\infty \int_{-1}^1 \chi_\nu I_\nu \mu \, d\mu \, d\nu \quad (2.67)$$

accounts for the transfer of momentum from the radiation field to the matter. (Note that only absorptive processes (and stimulated emission) contribute to the radiative acceleration; spontaneous emission is treated as isotropic in the comoving frame and does not provide a net transfer of momentum to the material.) The radiative acceleration consists of contributions by Thomson scattering, continuous opacities, and line opacities.

The contribution by Thomson scattering is given by

$$g_{\text{rad}}^{\text{Th}} = \frac{1}{c} \frac{n_e \sigma_{\text{Th}}}{\rho} F = \frac{1}{c} \frac{n_e \sigma_{\text{Th}}}{\rho} \frac{L}{4\pi r^2} \quad (2.68)$$

as the Thomson opacity $\chi_{\text{Th}} = n_e \sigma_{\text{Th}}$ is frequency-independent. (n_e is the volume density of free electrons, σ_{Th} is the Thomson scattering cross-section, and $F = L/4\pi r^2$ is the frequency-integrated flux at radius r .) Since $g_{\text{rad}}^{\text{Th}}$ has the same dependence on radius as the gravitational acceleration (provided the number of free electrons per unit mass remains roughly constant), the two are often combined to give an “effective gravity”

$$g_{\text{eff}} = g - g_{\text{rad}}^{\text{Th}} = (1 - \Gamma)g \quad (2.69)$$

where $\Gamma = g_{\text{rad}}^{\text{Th}}/g$ is the ratio of Thomson acceleration to gravity (typical values for O stars lie in the range of 0.2 to 0.6). $\Gamma = 1$ defines the so-called *Eddington limit*, at which pressure from Thomson scattering alone would cancel gravitational attraction and thus make the existence of a star impossible.

For frequency-dependent opacities, the Doppler shift due to the velocity field of the expanding atmosphere must principally be considered in the integral. For free-free and bound-free opacities this can be disregarded due to the slow variation of χ with ν . Even the Doppler shift $\Delta\nu = \pm v_{\text{ik}} \nu/c$ of ionization edges can usually be neglected, since it is small compared to the frequency range over which the opacity is effective. Thus, we can evaluate the contribution of continuous opacity to the radiative acceleration by numerical integration over opacity times flux:

$$g_{\text{rad}}^{\text{cont}} = \frac{2\pi}{c} \frac{1}{\rho} \int_0^\infty \chi_\nu \int_{-1}^1 I_\nu \mu \, d\mu \, d\nu = \frac{4\pi}{c} \frac{1}{\rho} \int_0^\infty \chi_\nu H_\nu \, d\nu = \frac{1}{c} \frac{1}{\rho} \int_0^\infty \chi_\nu F_\nu \, d\nu, \quad (2.70)$$

where χ_ν is the sum over all contributing continuous (bound-free and free-free) opacities.

Analogous to the bound-bound (line) rate coefficients, such a simple integration is not possible for the line radiative force. As with the bound-bound rate coefficients, we must therefore evaluate the line radiative acceleration in Sobolev approximation. For a single line we have

$$g_{\text{rad}}^{\text{line}} = \frac{2\pi}{c} \frac{1}{\rho} \chi_{ij} \int_{-1}^1 I_{\text{inc}}(r, v(\mu), \mu) \frac{1 - e^{-\tau_s(r, \mu)}}{\tau_s(r, \mu)} \mu d\mu, \quad (2.71)$$

where τ_s is the optical thickness of the resonance zone of the line (equation 2.27). However, as there can be several hundred thousand lines contributing to the radiative acceleration, repeatedly evaluating this expression while solving the hydrodynamics is impractical. Furthermore, depending on the quality of the initial values, the correspondence between r , v , and dv/dr may shift significantly during the iteration of hydrodynamics and the calculation of the radiative acceleration. As any particular NLTE model can only evaluate the line force for a given velocity field, it is therefore expedient to use an expression for the line force which explicitly accounts for the primary dependence on the hydrodynamic variables, namely the velocity gradient, which through the Doppler shift influences the amount of stellar radiation a single spectral line can absorb, and the radial coordinate, which determines the geometrical dilution of the flux and the angular extent of the photospheric disk.

We use the ingenious parametrization suggested by Castor, Abbot, and Klein (1975) and elaborated by Abbot (1982) and Pauldrach, Puls, and Kudritzki (1986),

$$g_{\text{rad}}^{\text{lines}} = g_{\text{rad}}^{\text{Th}} M(t, r, v) C(r, v, dv/dr), \quad (2.72)$$

which expresses the total line acceleration in terms of the Thomson acceleration. The quantity

$$M = kt^{-\alpha} (\tilde{n}_e/W)^\delta \quad (2.73)$$

is known as the *force multiplier*; k , α , and δ are the *line force parameters*¹⁰ (see below for details), $W = (1 - \mu_c)/2$ is the geometric dilution factor for the average intensity, and $\tilde{n}_e = n_e/(10^{11} \text{ cm}^{-3})$. The *depth parameter* t , defined by

$$t = n_e \sigma_{\text{Th}} v_{\text{therm}} \left(\frac{dv}{dr} \right)^{-1}, \quad (2.74)$$

represents the optical depth of the resonance zone of a line assumed to have a strength corresponding to the Thomson opacity; t is a useful scaling parameter, and the thermal velocity of hydrogen will be used in its definition. (Note that the line radiative force (equation 2.71) is actually independent of the thermal velocity; v_{therm} cancels in equation 2.76.) The *finite disk correction factor*

$$C(r, v, dv/dr) = 2 \left(\frac{r}{R} \right)^2 \int_{\mu_c}^1 \left(\mu^2 \frac{dv}{dr} + (1 - \mu^2) \frac{v}{r} \right)^\alpha \left(\frac{dv}{dr} \right)^{-\alpha} \mu d\mu \quad (2.75)$$

accounts for the fact that any point r in the atmosphere receives radiation not from a point source, as would be implicitly assumed (“radial streaming approximation”) in equations 2.73 and 2.74, but from the photosphere that subtends the finite angular extent μ_c .

As the angular integral is already accounted for by the correction factor C , we also compute the force multiplier from the NLTE model in radial-streaming approximation:

$$M = \sum_{\text{lines}} \frac{v_{ij}}{c} v_{\text{therm}} \frac{H(r, v_{ij}(1 + v(r)/c))}{H(r)} \frac{1 - e^{-\tau_r}}{t}, \quad (2.76)$$

where $H(r)$ is the frequency-integrated Eddington flux at radius r and $\tau_r = \chi_{ij} c/v_{ij} (dv/dr)^{-1}$ is the radial ($\mu = 1$) Sobolev optical depth of the line (χ_{ij} is the frequency-integrated opacity of the line and has dimensions of opacity times frequency, cf. equations 2.47 and 2.20). Although the line force parameters k , α , and δ can be interpreted as being related to the line strength distribution function (for a very detailed discussion see Puls et al. 2000), they are simply parameters to fit the functional dependence of M (equation 2.73) to the actual computed force multiplier (equation 2.76). For the sake of completeness, we mention that k is proportional to the total number of lines driving the wind; δ accounts for variation of k with changes in the ionization balance (recombination rates are proportional to n_e ; photoionization rates are proportional to W). Finally, α is the ratio of line force from optically thick lines to the

¹⁰ The line force parameter k and the force multiplier M are not to be confused with the Boltzmann constant k and the stellar mass M ; the meaning of the symbols should be clear from the context.

total line force. (In the limit of an optically thick line ($\tau_r \gg 1$), the last factor in equation 2.76 yields $1/t = t^{-1}$, while in the limit of an optically thin line ($\tau_r \ll 1$) it yields $\tau_r/t \sim t^0$; the average over the actual distribution is represented by $t^{-\alpha}$, where $0 \leq \alpha \leq 1$.)

3

The models: numerical methods and implementation details

This chapter describes the numerical methods used to simulate the physical processes outlined in the previous chapter. Figure 3-1 gives an overview of the modelling procedure, illustrating the interdependence of the major components of the computer code. This consists of three main blocks,

- ▷ the solution of the hydrodynamics,
- ▷ the solution of the NLTE-model (calculation of the radiation field and the occupation numbers),
- ▷ the computation of the synthetic spectrum,

that interact with each other.

3.1. General procedure

A model calculation (see figure 3-1) begins with the computation of the hydrodynamic structure (velocity $v(r)$ and density $\rho(r)$) of the atmosphere. (The solution method of the hydrodynamics is described in detail by Pauldrach, Puls, and Kudritzki (1986).) Apart from the stellar parameters (effective temperature T_{eff} , surface gravity $\log g$, and stellar radius R), this requires, in a first step, a suitable guess for the parametrization of the line force: the line force parameters k , α , and δ are chosen so that the hydrodynamics yields the mass loss rate \dot{M} and terminal velocity v_{∞} expected for this particular star. A constant temperature $T(r) = T_{\text{eff}}$ is assumed, and for the continuum force only that due to Thomson scattering is considered.

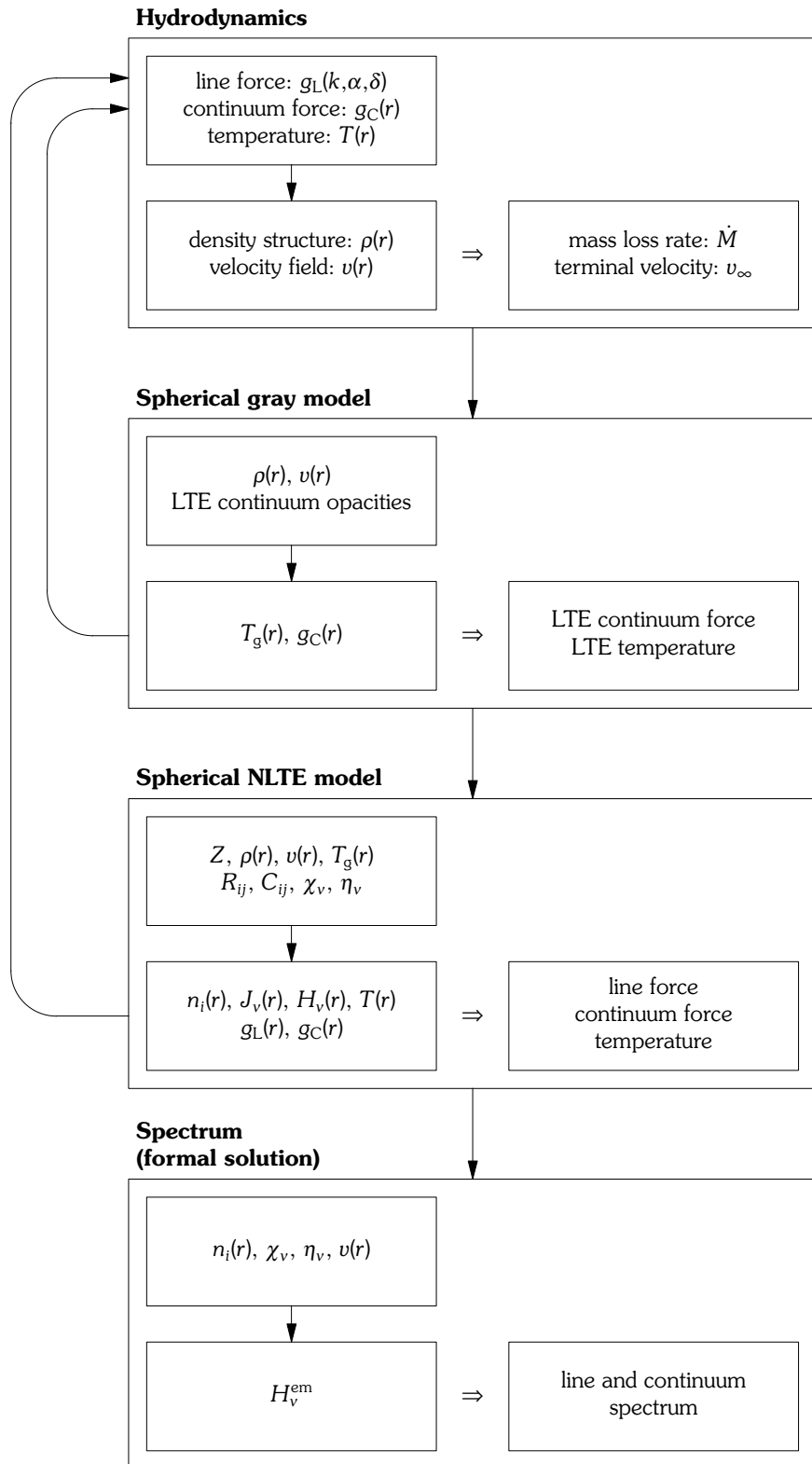


FIGURE 3-1. — Sketch of the modelling procedure for a complete model atmosphere calculation, showing the interdependence of the major components of the computer code.

In a second step, an improved continuum force is computed using the continuum opacities of all important ions, along with an updated temperature structure, using a spherical gray LTE model. Hydrodynamic structure and gray LTE model are iterated to convergence (typically 6 iterations). (This step is not essential, as the NLTE model computes continuum opacities without the approximations of the LTE model. However, the computing time for the LTE model is negligible compared to that of the NLTE model, and the number of necessary iterations between hydrodynamics and NLTE model is reduced considerably by this step.)

The main part of the computation consists of the NLTE model, which will be described in detail in the next section, and which forms the focus of the technical part of this thesis. In addition to the continuum opacities, the opacity due to spectral lines is taken into account, as well as the back-reaction of these opacities on the temperature structure, and a *consistent* solution of radiation field, occupation numbers, opacities and emissivities, and temperature is computed. From these, the radiative acceleration due to lines is calculated, and new line force parameters are derived. If necessary, a new hydrodynamic structure is then computed and the NLTE model re-run with the new velocity and density structures. Hydrodynamics and NLTE model are iterated until consistency is reached.

Finally, for comparison with the observations, a synthetic spectrum is computed from the converged hydrodynamic structure and the calculated continuum opacities and emissivities and the occupation numbers, using a detailed formal integral solution of the transfer equation in the observer's frame (see section 3.2.1.2).

By adjusting the parameters of the models until a good fit to the observed features is reached, one thus obtains not only the stellar parameters and the abundances, but also the ionizing fluxes (i.e., the spectral parts blueward of the hydrogen Lyman edge, which due to absorption by interstellar hydrogen cannot normally be observed directly, but knowledge of which is necessary for the quantitative analysis of H II regions), and the mass loss rates (which are of interest for stellar evolutionary calculations and models of the interstellar environments in galaxies).

3.2. The NLTE model

The main part of the simulation consists of the NLTE model for computing a selfconsistent solution of radiation field and occupation numbers. A consistent treatment is necessary here because the opacities determining the radiation transfer depend directly on the ionic level populations and the ionization balance, whereas the excitation and ionization rates which determine the level populations are in turn strongly dependent on the intensity of the radiation field.

Of particular concern in this context is the influence of hundreds of thousands of spectral lines on the radiation field. The huge number of metal lines present in hot stars in the EUV and UV attenuate the radiation in these frequency ranges drastically by radiative absorption and scattering processes, an effect known as *line blocking*. The example in figure 3-2 shows that in supergiants with high mass loss rates this blocking by lines can reduce the emergent flux by up to two orders of magnitude over a significant wavelength range, compared to the case when only continuum opacities are considered. Only a small fraction of the radiation is re-emitted and scattered in the outward direction; most of the energy is radiated back to the inner layers (*backwarming*). This leads to an increase of the temperature in the deeper layers of the atmosphere (*line blanketing*) and, consequently, to an enhanced flux in the spectral regions with lower opacities, such that the total flux is conserved.

With regard to a proper treatment of the line blocking effects in the model atmosphere code used here, a first step had been done by Sellmaier (1996) by implementing an opacity sampling method¹¹ (cf. Peytre-

¹¹ A simple straightforward approach would require considering approximately 10^7 frequency points to resolve the spectral lines in the spectral range affected by line blocking, since the thermal width of a UV metal line covers just a few mÅ. Such a procedure would lead to a severe problem concerning the computational time. An alternative method using *opacity distribution functions* (ODFs) (cf. Labs 1951; Kurucz 1979), where the opacities are rearranged within a rough set of frequency intervals in such a way that a smoothly varying function is obtained which

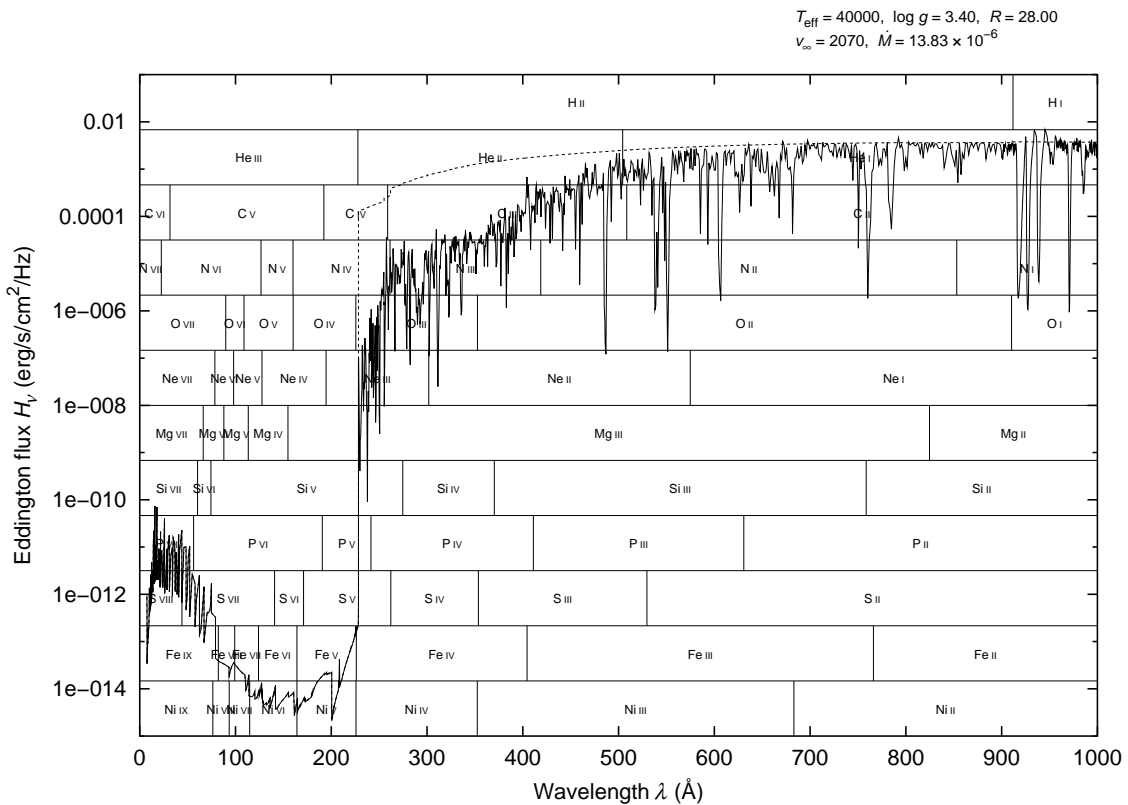


FIGURE 3-2. — Emergent EUV spectral energy distribution (solid line) of a 40000 K supergiant model. For comparison, the dashed line represents the emergent flux when only continuum opacities are taken into account in the radiative transfer. The emission blueward of the He II ionization threshold ($\lambda < 227 \text{ \AA}$) is due to shock emission also considered in this model. The vertical bars indicate the ionization thresholds of the most important ions; the ionization balance depends almost entirely on the ionizing flux, and this influence can be traced by the spectral lines in the observable part of the UV spectrum.

mann 1974; Sneden et al. 1976; Anderson 1991) to account for the line opacities in the radiative transfer. Although some technical problems which had led to spurious results in Sellmaier’s work have been overcome by Pauldrach et al. (1998), the method still suffered from a major approximation, namely that the angular dependence (in the observer’s frame) of the line opacities and emissivities (due to the angular dependence of the Doppler shift) was not considered, and thus in particular line emission was not correctly reproduced. (The characteristic P Cygni line profiles in expanding atmospheres are a direct result of this angular-dependent Doppler shift.) A major objective of the present work therefore was to improve on the procedure so as to also properly take this aspect into account. The method best suited for this purpose is a detailed formal integral on a spatial microgrid capable of resolving individual spectral lines (see section 3.2.1.2), similar to the method used for computing the high-resolution synthetic spectrum for comparison with observations.

This improved treatment, however, is computationally much more costly than the opacity sampling method, and performing the complete NLTE iteration cycle with this detailed method is impractical. To save computation time we therefore revert to the opacity sampling method (“method I”) for the bulk of the iteration cycle (“pre-iteration”), switching to the detailed radiative transfer (“method II”) only for the

conserves the statistical distribution of the opacities, often used in modelling the *hydrostatic* atmospheres of cooler stars, is not applicable for *expanding* atmospheres, since there is no appropriate way to treat the lineshift in the wind, and due to the rearrangement of the opacities the frequential position of the lines is changed. This, however, prevents a correct computation not only of the bound-bound transitions used for the solution of the statistical equilibrium equations, but also of the radiative line force, which depends crucially on this Doppler shift.

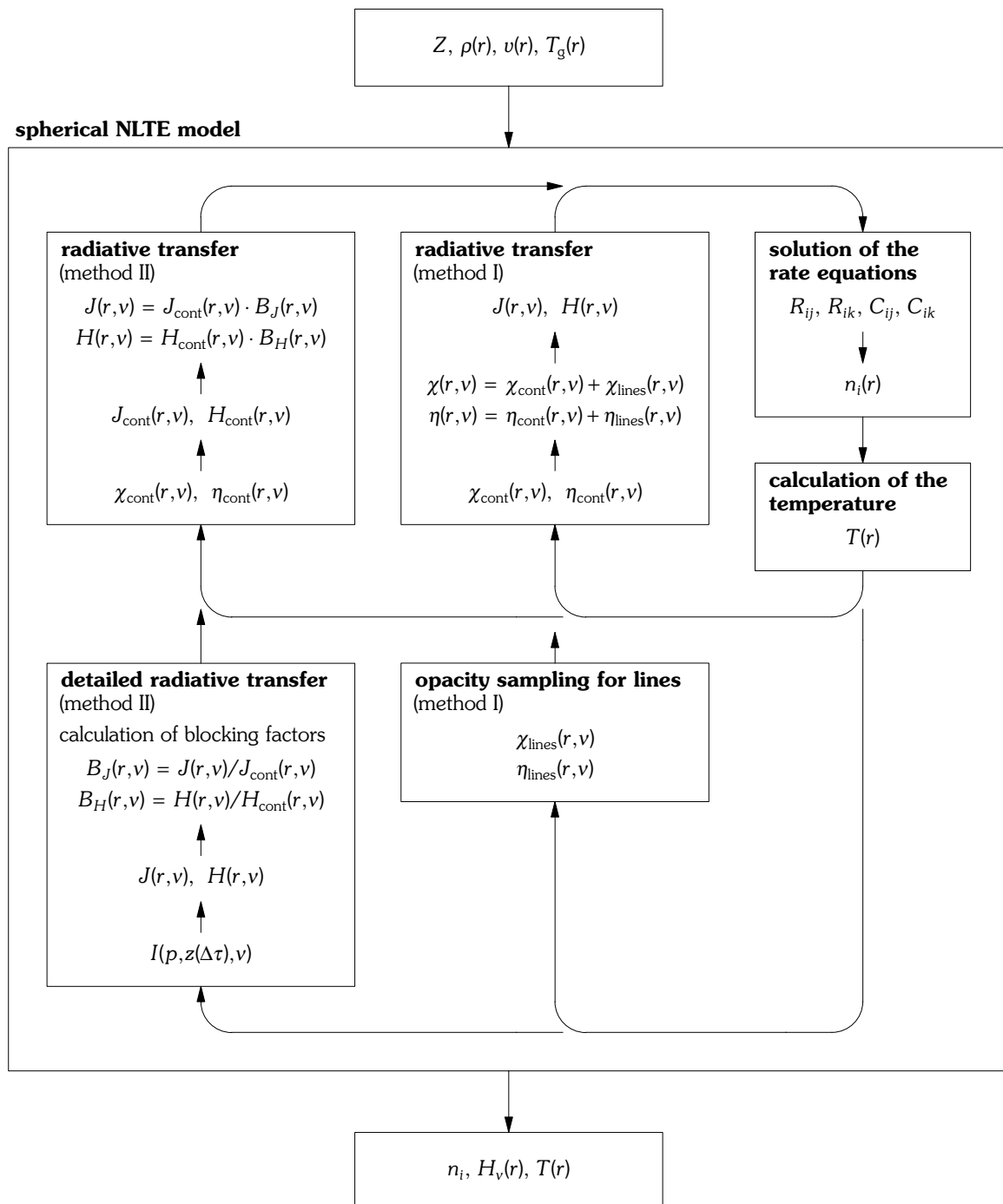


FIGURE 3-3. — Sketch of the NLTE model code for computing selfconsistent occupation numbers and radiation field involving an accelerated lambda iteration (ALI). Two different methods are used to deal with line opacities in the radiative transfer: an exact, detailed method (method II) used for the final iteration blocks and a faster, approximate opacity sampling method (method I) used in a pre-iteration cycle. To decrease the total time needed for a model run, the computationally expensive quantities shown in the bottom part of the loop are computed not in every iteration cycle, but only once per iteration block (ca. 30 iteration cycles).

final iterations. Both methods are based on the same radius and frequency grids and take into account the same lines. The purpose of using method I is to give good starting values for the final (real) iteration using method II, so that only very few iteration cycles using this method are needed, since the pre-iteration has already converged near the final solution. As will be shown below, despite its intrinsic limitation, method I is well suited for this purpose.

A sketch of the solution procedure used in the NLTE model is shown in figure 3-3. Consistency of occupation numbers, radiation field, and temperature is achieved in an iteration scheme in which these quantities are alternately computed. To circumvent the normal convergence problems of this type of iteration, an accelerated lambda iteration (ALI; cf. Cannon 1973, Werner and Husfeld 1985) according to Pauldrach and Herrero (1988) is used. Occupation numbers are computed by explicitly solving the rate equations including all relevant processes (as described in section 2.2), using a comprehensive atomic database (cf. section 3.2.3) including a total of about 5000 levels for the most important 149 ionization stages of the 26 elements considered (H to Zn, apart from Li, Be, B, and Sc) (see Pauldrach et al. 1994, 1998). The radiative transfer is solved in spherical geometry at up to 2500 frequency points and at every depth point, including the layers where the radiation is thermalized and the diffusion approximation can therefore be used as a proper boundary condition. The solution includes all relevant opacities. In particular, the effects of wind and photospheric EUV line blocking on the ionization and excitation of levels are treated on the basis of 4 million lines, with proper consideration of the influence of the velocity field on the line opacities and emissivities and on the radiative rates.

In total, almost 1000 ALI iterations are required by the complete NLTE procedure, divided into blocks of 30 iterations each. (One iteration comprises calculation of the occupation numbers and the radiation field.) Up to 31 of these iteration blocks are performed using the opacity sampling method (method I), computing the total line opacities and emissivities at the beginning of each iteration block, and updating the temperature structure and the Rosseland optical depth every third ALI-iteration within a block. All following iterations are then performed using method II, calculating the blocking factors with the detailed radiative transfer before each iteration block and updating temperature, optical depth, and continuum opacities and emissivities as before. (Several iteration blocks using method II can be executed, but 1 is usually sufficient — see below.) In this phase the radiative transfer solved in the ALI-iterations within one iteration block is just based on continuum opacities and emissivities, and the blocking factors are applied to get the correct radiative quantities used for calculating the radiative rates.

As a final result of the complete iteration cycle, the converged occupation numbers, the emergent flux, and the final NLTE temperature structure are obtained. In order to illustrate the behavior of convergence of the iteration, figure 3-4 shows the ionization fractions of N III, N IV, and N V versus density and iteration block number for a 29000 K supergiant model. (The steep increase of N V in the outer part results from the EUV and X-ray radiation from shock-heated matter included in this model.)

3.2.1. The treatment of line blocking

To put the newly implemented improved line transfer in perspective, we will in the following review the main features of our treatment of line blocking effects, beginning with a description of the opacity sampling method (method I), used in the first stages of an NLTE model calculation (and to which a number of enhancements have been made), before discussing the improved treatment (method II, section 3.2.1.2), used in the final iteration cycles.

3.2.1.1. Method I — the opacity sampling method

Following the general idea of opacity *sampling*, a representative set of frequency points is distributed in a logarithmic¹² wavelength scale over the relevant spectral range, and the radiative transfer equation is

¹² The advantage of using a regular frequency grid for sampling is that the correspondence between the (Doppler-shifted) frequency of any particular line to the index numbers of the bordering frequency grid points — e.g., to obtain the intensity at these frequency points, used in calculating the radiative rate coefficients for the line — can be trivially *computed* and no wavelength search has to be performed.

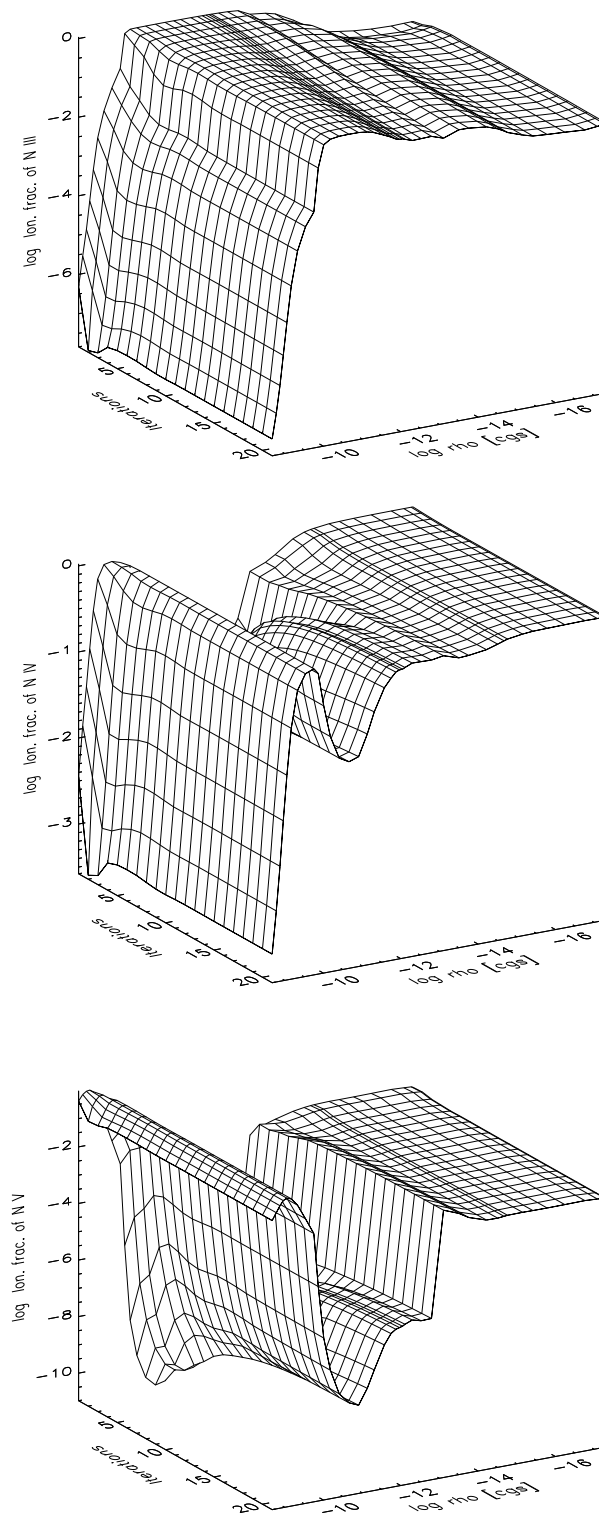


FIGURE 3-4. — Logarithm of the ionization fractions of N III, (top) N IV, (center) and N V (bottom) versus density and iteration block number for an O supergiant model ($T_{\text{eff}} = 29\,000\text{ K}$, $\log g = 3.0$, $R = 27 R_{\odot}$), illustrating the convergence of the model. The region between two successive contour lines (one iteration block) corresponds to 30 iterations. The steep increase of N V in the outer part results from the EUV and X-ray radiation from shock-heated matter included in this model.

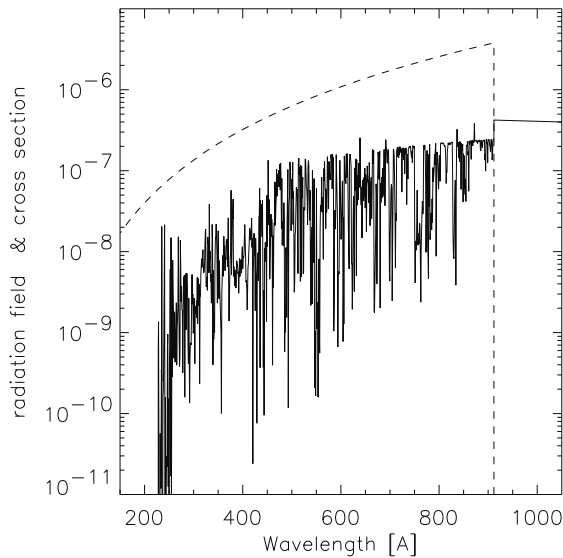


FIGURE 3-5. — Typical mean radiation field J_ν (solid line) together with the photoionization cross-section $\alpha_{ik}(\nu)$ (dashed) of the ground state of hydrogen (in arbitrary units) (cf. Sellmaier 1996; Pauldrach, Hoffmann, and Lennon 2001).

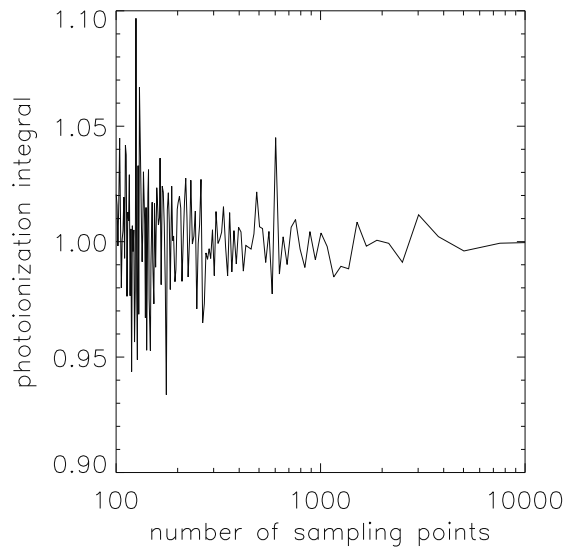


FIGURE 3-6. — Accuracy of the normalized photoionization integral R_{ik} of the ground state of hydrogen in dependence of an increasing number of sampling points within the Lyman continuum (cf. Sellmaier 1996; Pauldrach, Hoffmann, and Lennon 2001).

solved for each point.¹³ (The method is described in more detail in Pauldrach, Lennon, Hoffmann, et al. 1998.) In this way the exact solution is reached by increasing the number of frequency points. A smooth transition is obtained when the number of frequency points is increased up to the number — about 10^7 — which is required to resolve the thermal width of the UV lines. However, convergence can be achieved already with significantly less points (see below). Furthermore, special blocking effects on selected bound-bound transitions can in principle be investigated more thoroughly by spreading additional frequency points around the line transition of interest.

The most important effect of line blocking is its influence on the ionization structure via the photoionization integrals (equation 2.14)

$$R_{ik} = 4\pi \int_{\nu_{ik}}^{\infty} \frac{J_\nu}{h\nu} \alpha_{ik}(\nu) d\nu.$$

This is illustrated by figure 3-5, which shows that the mean radiation field J_ν changes rapidly over the frequency interval (several 100 Å) covered by a typical smooth bound-free cross-section $\alpha_{ik}(\nu)$. The accuracy of the photoionization rates thus depends crucially on how accurately the radiation field in the relevant frequency range is rendered by the model. This is in turn dependent on the number of frequency points used.

To determine the number of sampling points required for an accurate description of the bound-free (photoionization) and bound-bound (line) radiative rates, Sellmaier (1996) has performed empirical tests by calculating models with an increasing number of sampling points. Representative for the behavior of the radiative rates, and thus the occupation numbers, figure 3-6 shows the dependence of the normalized photoionization integral of the ground state of hydrogen on the number of frequency points. For small numbers of sampling points there is no systematic trend, and the rates converge for higher numbers of

¹³ For O stars the relevant wavelength range depends on T_{eff} ; for hot objects the lower value is at ≈ 90 Å and for cooler objects the upper value is at 2000 Å; note that accurate ionization calculations require extending the line blocking calculations to the range shortward of the He II edge (cf. Pauldrach et al. 1994).

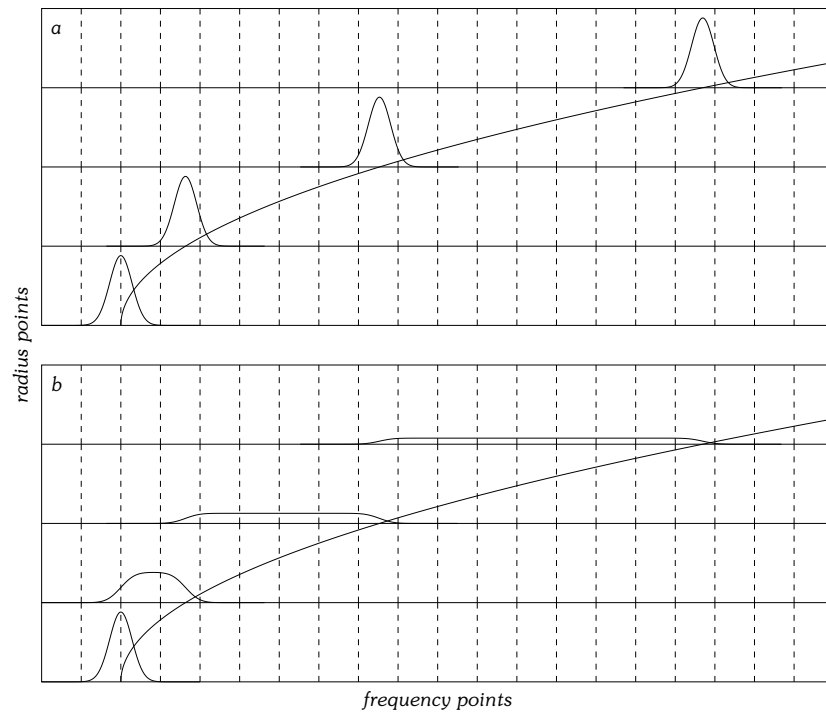


FIGURE 3-7. — Simply shifting the line profile along $v_{\text{CMF}} = v_{ij}(1 + u(r)/c)$ (represented by the thin curve) at each radius grid point (standard opacity sampling, upper panel) causes the line to be missed at most frequency points. This problem is solved by convolving the line profiles with a normalized boxcar profile with a width corresponding to the difference in Doppler shift between two successive radius points (“Doppler-spread opacity sampling”, lower panel).

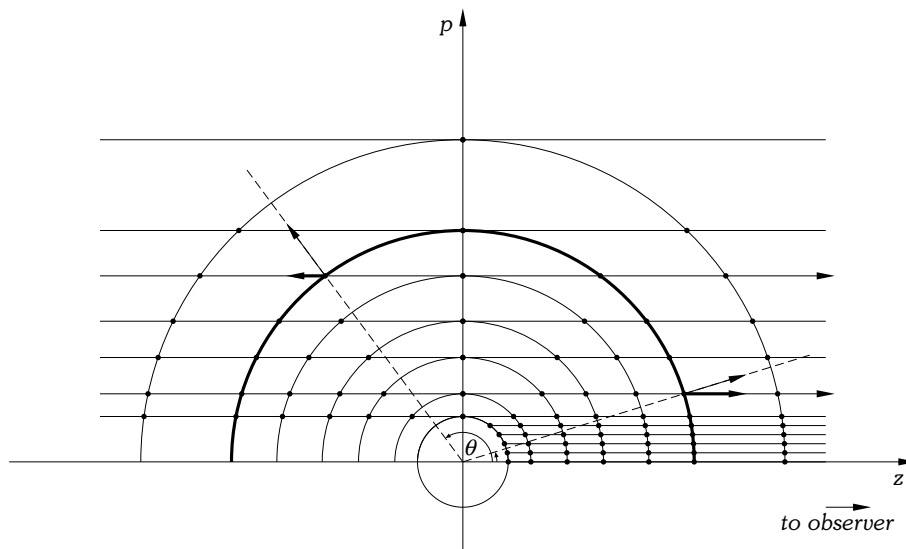


FIGURE 3-8. — (p,z) -geometry for the spherically symmetric radiative transfer. For any given depth point (for instance, the one marked with the thick line), a different Doppler shift must in principle be considered for every p -ray, since the projected velocity varies with $\cos \theta$. However, as no analogy to the boxcar method exists in this case, in the opacity sampling method the Doppler shift of the central ray is taken as being representative for all other rays. The detailed radiative line transfer, however, correctly accounts for these different Doppler shifts. Angular integrals of radiative quantities at a particular radius point are computed by summing up, with appropriate weights, the contributions of each p -ray intersecting that radius shell.

sampling points. The conclusion is that 1000 sampling points within the Lyman continuum on a logarithmic wavelength scale guarantee a sufficient accuracy of about 1 to 2 percent. By means of a separate investigation, Sellmaier (1996) has also shown the given number of sampling points to be reasonable, since the lines thus sampled represent the actual line-strength distribution function quite well.

Treatment of the lineshift. In the static, inner part of the atmosphere a line's opacity covers with its (thermal and microturbulent) Doppler profile ϕ only a very small interval around the transition frequency ν_{ij} (this inner region is represented in figure 3-7 by the lower edge in both panels; with regard to our frequency grid about 40 percent of the available lines are treated in this part). The effect of these lines on the radiation field is nevertheless considerable (cf. figure 3-5), if the lines are strong enough to become saturated.

In the expanding atmospheres of hot stars the effect of line blocking is enhanced considerably in the supersonic region due to the nonlinear character of the radiative transfer. A velocity field $v(r)$ enables the line to block the radiation also at other frequencies $\nu = \nu_{ij}(1 + v(r)/c)$, i.e., the Doppler shift increases the *frequency interval* which can be blocked by a single line to a factor of ≈ 100 . On the other hand, the velocity field reduces the *spatial area* where a photon can be absorbed by a line. If a line is optically thick, however, the effect of blocking will ultimately be *increased* compared to a static photosphere.

The total opacity at a certain sampling frequency ν is given by adding the line opacity χ_l to the continuum opacity χ_c ,

$$\chi(r, \nu) = \chi_l(r, \nu) + \chi_c(r, \nu), \quad (3.1)$$

where χ_l is the sum over all single line opacities at the current radius and frequency,

$$\chi_l(r, \nu) = \sum_{\text{lines}} \chi_{ij}(r) \phi_{ij}(r, \nu). \quad (3.2)$$

(The emissivity is treated analogously.) The lineshift due to the velocity field is applied to the individual line opacities before the summation in equation 3.2 is carried out at each sampling and depth point. However, in method I this is done by applying the Doppler shift of the radial ray to all p -rays (see figure 3-8), i.e., we use

$$\phi_{ij}(r, \nu) = \frac{1}{\Delta\nu_D \sqrt{\pi}} e^{-\frac{(\nu - \nu_{ij}(1 + v(r)/c))^2}{\Delta\nu_D^2}}, \quad (3.3)$$

ignoring the angular dependence of the Doppler shift (this is what we call the *single-p-ray approximation* for the sampling opacities). Apart from the intrinsic character of the sampling method this is the most restrictive approximation in the first part of the iteration cycle. Nevertheless, the main effect of the frequency shift due to the expanding wind — increase of the frequential range of line absorption — is included, and as will be shown below, the approximation is sufficient to provide a good starting point for the final iterations using the detailed line transfer.

The upper panel of figure 3-7 shows that if the line opacity is simply shifted along the comoving frame frequency $\nu_{\text{CMF}} = \nu_{ij}(1 + v(r)/c)$ to every radius point successively, many frequency points will miss the line, since the radius grid is too coarse to treat large lineshifts in the observer's frame. This is remedied by convolving the intrinsic Doppler profile of the line with a boxcar profile $\phi_{\Delta\nu}$ representing the velocity range of a radial interval (figure 3-7, lower panel).

The boxcar profile is the mean profile obtained by considering the velocity shifts $\Delta\nu$ of the two radius grid points bordering the interval, such that the gaps in the frequency grid are closed. This can be expressed in terms of the Heaviside step function Θ :

$$\phi_{\Delta\nu}(\nu) = \frac{\Theta(\nu_2 - \nu) - \Theta(\nu_1 - \nu)}{2(\nu_2 - \nu_1)}, \quad (3.4)$$

where ν_1 and ν_2 are the observer's frame frequencies corresponding to the Doppler shift of the line at the two successive radius points r_1 and r_2 , i.e., $\nu_{1,2} = \nu_{ij}(1 + v(r_{1,2})/c)$. Assuming thermal Doppler broadening for the intrinsic line profile,

$$\phi_D(v) = \frac{1}{\Delta v_D \sqrt{\pi}} e^{-\frac{(v-v_{ij})^2}{\Delta v_D^2}} \quad (3.5)$$

where Δv_D is the thermal Doppler width, the convolution $(\phi_D * \phi_{\Delta v})(v)$ results in the final profile function

$$\phi(v) = (\phi_D * \phi_{\Delta v})(v) = \frac{\operatorname{erf}\left(\frac{v_2 - v}{\Delta v_D}\right) - \operatorname{erf}\left(\frac{v_1 - v}{\Delta v_D}\right)}{2(v_2 - v_1)}. \quad (3.6)$$

This profile can be used for the entire sub- and supersonic region: in the limit of small velocity differences, $v_2 - v_1 \ll v_D$, it yields the intrinsic Doppler profile corresponding to the standard opacity sampling, as indicated in figure 3-7; and for sufficiently high velocity gradients, $v_2 - v_1 \gg v_D$, the integration over a radius interval represents the Sobolev optical depth $\tau_{\text{Sob}}(r)$ of a local resonance zone for a radial ray ($\mu = 1$):

$$\Delta\tau = \int_{r_1}^{r_2} \chi_{ij} \phi(v) dr \approx \chi_{ij} \frac{1 - (-1)}{2(v_2 - v_1)} (r_2 - r_1) = \chi_{ij} \frac{r_2 - r_1}{v_2 - v_1} \frac{c}{v_{ij}} \approx \chi_{ij} \frac{c}{v_{ij}} \left(\frac{dv}{dr}\right)^{-1} = \tau_{\text{Sob}}(r). \quad (3.7)$$

At sufficiently high velocity gradients all lines are included in the radiative transfer if the sampling grid is fine enough (see also Sellmaier 1996). In this case, therefore, the *Doppler-spread opacity sampling method* becomes an *exact solution*.

In summary, the Doppler-spread sampling technique

- ▷ makes opacity sampling usable even at large velocity gradients where the standard sampling would miss a line at many frequency points. The *statistical character* inherent in opacity sampling is greatly diminished, since at high velocity gradients *all available lines* are considered.
- ▷ does not overestimate the line blocking effect, since the convolution (equation 3.6) preserves the frequency-integrated line strength. Rather, the Sobolev optical depth (equation 3.7) is the upper limit for the optical thickness of a blocking line as broadened with the boxcar profile.
- ▷ leads neither to an increased nor a decreased line overlap, since the broadening only spreads a line over the frequencies corresponding to the Doppler shifts between one depth point and the next one. If lines overlap through this broadening at a certain radius grid point, they must also overlap in reality (see figure 3-12) in the interval between that radius point and the adjacent one, because *the basic relationship between frequency shift and radius* (via the velocity field) is independent of the resolution of the radius grid.

Essentially, the broadening projects the sharply peaked line opacities and emissivities inside a radial interval, which would otherwise be overlooked in the radiation transfer in the discretized scheme (see below), onto a point at the edge of that interval so that the radiation transfer on the discretized radius grid can be performed correctly. For any particular radius interval and spectral line, this affects all frequencies in the interval determined by the Doppler shifts corresponding to the velocities at the edges of the radial interval in question, irrespective of the number of frequency points that actually lie in that frequency interval. Increasing this number of frequency points does not influence this geometric configuration, whereas increasing the radial resolution improves the quality of this procedure, finally converging to the exact solution (exactly this is being done in the detailed radiative transfer).

In principle, one would have to account for the angular variation (see figure 3-8) of the Doppler shift in a similar manner, but as no analogy to the boxcar profile method exists in this case, the (correctly calculated, radially dependent) opacities $\chi_l(r, v)$ of the *central p-ray* are simply applied to the other p-rays, regarding these opacities as *representative*. A welcome result of this simplification is the fastness of the method, a very important consideration in this part of the iteration cycle.

However, by making use of this method it soon became clear that with respect to realistic models some additional problems had to be solved.

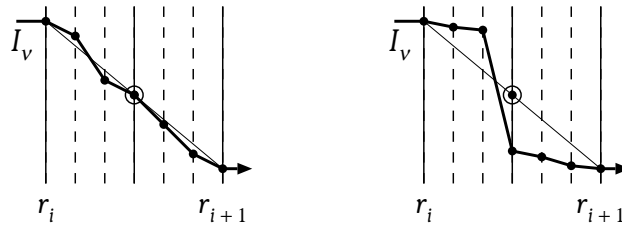


FIGURE 3-9. — Schematic sketch to illustrate the artificial effect of self-shadowing (see text).

One problem regards the artificial effect of *self-shadowing* which occurs because the intensity used in the Sobolev-with-continuum method for the calculation of the bound-bound transition rates in the rate equations is not truly the intensity *incident* on the interaction zone of the line, but instead an “average” value resulting from the solution of the radiation transfer accounting for a multitude of lines in the interval between two radius points. If the lines contained in the interval are of almost similar strength (figure 3-9, left panel), this is no problem, because in a statistical sense the calculated intensity at the sampling point (denoted with a circled dot) represents a fair *mean value* for the true incident radiation of the individual lines in the interval.

If, however, a strong line dominates the opacities in the interval (figure 3-9, right panel), then the intensity taken at the sampling point is much smaller than the *true incident radiation* for this line, because in the solution of the radiative transfer the line opacity has already influenced this value considerably. In consequence the source function of this line is underestimated and the radiative processes — the scattering part is mostly affected — are not correctly described in the way that the line appears systematically too weak.

The solution to this problem is rather simple: in calculating the bound-bound rates of the dominating lines we use an incident intensity which is independent of the lines in the considered interval (cf. Pauldrach et al. 1998). This is done by suitably interpolating between the previous and next radius points the coefficients of the piecewise linear representation of the intensity (cf. section 2.2.1) used in the Sobolev-with-continuum method.

Another problem involves the discretization of the transfer equation in its differential form, for computing the radiative quantities (Feautrier method). In the standard approach (see, for example, Mihalas 1978) the equation of transfer is written as a second-order differential equation with the optical depth τ as the independent variable:

$$\frac{d^2 u}{d\tau^2} = u - S, \quad (3.8)$$

where S is the source function and $u = \frac{1}{2}(I^+ + I^-)$, with I^+ and I^- being the intensities in positive and negative τ direction along the ray considered.

This differential equation is then converted to a set of difference equations, one for each radius point i on the ray,

$$\left. \frac{d^2 u}{d\tau^2} \right|_{\tau_i} \approx \frac{\left. \frac{du}{d\tau} \right|_{\tau_{i+1/2}} - \left. \frac{du}{d\tau} \right|_{\tau_{i-1/2}}}{\tau_{i+1/2} - \tau_{i-1/2}} \approx \frac{\frac{u_{i+1} - u_i}{\tau_{i+1} - \tau_i} - \frac{u_i - u_{i-1}}{\tau_i - \tau_{i-1}}}{\frac{1}{2}(\tau_{i+1} + \tau_i) - \frac{1}{2}(\tau_i + \tau_{i-1})}, \quad (3.9)$$

resulting in a linear equation system

$$a_i u_{i-1} + b_i u_i + c_i u_{i+1} = S_i \quad (3.10)$$

with coefficients

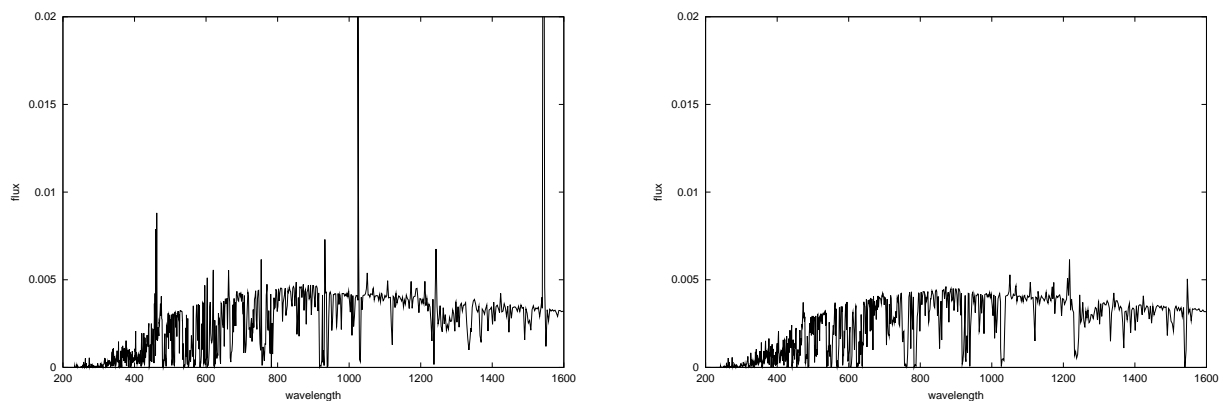


FIGURE 3-10. — Part of the synthetic EUV spectrum (200–1600 Å) of the S-45 supergiant model ($T_{\text{eff}} = 45000 \text{ K}$, $\log g = 3.6$, $R = 18.0 R_{\odot}$) calculated with the opacity sampling method and the differential form of the transfer equation. The left panel shows the spectrum obtained with the standard Feautrier coefficients, which produces several strong artificial emission lines. The right panel shows the correct spectrum resulting with the modified Feautrier coefficients.

$$a_i = -\left(\frac{1}{2}(\tau_{i+1} - \tau_{i-1})(\tau_i - \tau_{i-1})\right)^{-1} \quad (3.11)$$

$$c_i = -\left(\frac{1}{2}(\tau_{i+1} - \tau_{i-1})(\tau_{i+1} - \tau_i)\right)^{-1} \quad (3.12)$$

$$b_i = 1 - a_i - c_i, \quad (3.13)$$

(and appropriate boundary conditions). This linear equation system has a tridiagonal structure and can be solved economically by standard linear-algebra means.¹⁴ Note that the equations contain only *differences* in τ , which can easily be calculated from the opacities and the underlying z -grid (cf. figure 3-8) as

$$\tau_{i+1} - \tau_i = \frac{1}{2}(\chi_{i+1} + \chi_i)(z_{i+1} - z_i), \quad (3.14)$$

with χ_i being the opacity at depth point i .

The equation systems are well-behaved if the opacities and source functions vary only slowly with z . Caution must be taken if this cannot be guaranteed, for example, *whenever a velocity field is involved* at strong ionization edges or with the opacity sampling method at strong lines, since the velocity field shifts the lines in frequency, causing large variations of the opacity from depth point to depth point for a given frequency. In particular, a problematic condition occurs if a point with a larger-than-average source function S_i and low opacity χ_i borders a point with a high opacity χ_{i+1} (and low or average source function S_{i+1}). In reality, this large source function should have little impact, since it occurs in a region of low opacity, and thus the emissivity is small. However, the structure of the equations is such that the emission is computed to be on the order of

$$\Delta I \approx \bar{S} \cdot \Delta\tau \approx \frac{1}{2}(S_{i+1} + S_i) \cdot \frac{1}{2}(\chi_{i+1} + \chi_i)(z_{i+1} - z_i), \quad (3.15)$$

where, if the other quantities are comparatively small (in accordance with our assumptions), the term $S_i\chi_{i+1}$ dominates,¹⁵ leading to artificially enhanced emission. Figure 3-10 (left panel) shows the exaggerated emission of the strongest spectral lines in the emergent flux of a stellar model computed using this standard discretization, leading to false results.

¹⁴ In practice, a Rybicki-type scheme (cf. Mihalas 1978) is used for solving the equation systems for all p -rays simultaneously, since the source function contains a scattering term which redistributes the intensity at each radius shell over all rays intersecting that shell.

¹⁵ The physical reason for the failure of the system is that the source function only has meaning relative to its corresponding opacity. Multiplying the source function from one point with the opacity at another point is complete nonsense.

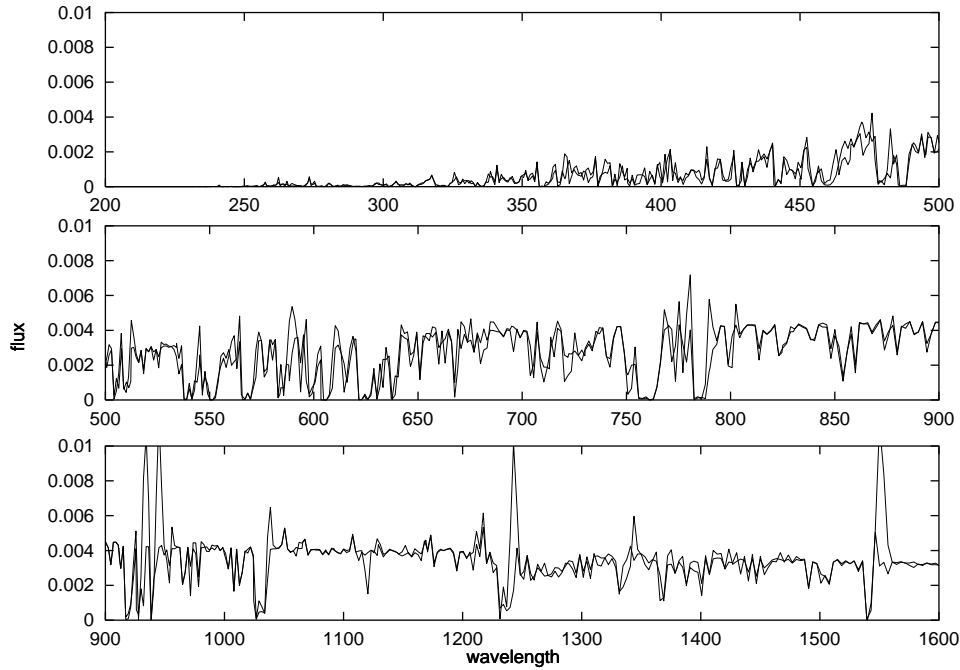


FIGURE 3-11. — Comparison of the synthetic EUV spectrum (200–1600 Å) of the S-45 supergiant model ($T_{\text{eff}} = 45000 \text{ K}$, $\log g = 3.6$, $R = 18.0 R_{\odot}$) calculated with the Doppler-spread opacity sampling method (thick line) and the detailed method (thin line) on the same frequency grid. Due to simplifications in the implementation the sampling method cannot produce P Cygni emission; nevertheless it provides an extremely good basis for the final iterations using the detailed method.

However, with a subtle modification of the equation system coefficients the method can nevertheless be salvaged. This involves writing the transfer equation as an equation not in τ , but in z for derivation of the coefficients, since only this formulation treats correctly the z -dependence of χ :

$$\frac{1}{\chi} \frac{d}{dz} \left(\frac{1}{\chi} \frac{du}{dz} \right) = u - S. \quad (3.16)$$

Again approximating the differential equation with a system of differences we obtain

$$\frac{1}{\chi_i} \left(\frac{d}{dz} \left(\frac{1}{\chi} \frac{du}{dz} \right) \right) \Big|_i \approx \frac{1}{\chi_i} \frac{\left(\frac{1}{\chi} \frac{du}{dz} \right) \Big|_{i+1/2} - \left(\frac{1}{\chi} \frac{du}{dz} \right) \Big|_{i-1/2}}{z_{i+1/2} - z_{i-1/2}} \quad (3.17)$$

$$\approx \frac{1}{\chi_i} \frac{\frac{1}{\bar{\chi}_{i+1,i}} \frac{u_{i+1} - u_i}{z_{i+1} - z_i} - \frac{1}{\bar{\chi}_{i,i-1}} \frac{u_i - u_{i-1}}{z_i - z_{i-1}}}{\frac{1}{2}(z_{i+1} + z_i) - \frac{1}{2}(z_i + z_{i-1})}, \quad (3.18)$$

so that

$$a_i = - \left(\frac{1}{2} \chi_i (z_{i+1} - z_{i-1}) \cdot \bar{\chi}_{i,i-1} (z_i - z_{i-1}) \right)^{-1} \quad (3.19)$$

$$c_i = - \left(\frac{1}{2} \chi_i (z_{i+1} - z_{i-1}) \cdot \bar{\chi}_{i+1,i} (z_{i+1} - z_i) \right)^{-1} \quad (3.20)$$

$$b_i = 1 - a_i - c_i. \quad (3.21)$$

Even though these coefficients seem not too different from those of the standard method, their impact on the computed radiation field is significant, as witnessed by the drastic improvement in the emergent flux shown in the right panel of figure 3-10. The crucial difference in the coefficients is that the first factor in a and c now contains only the *local* opacity.

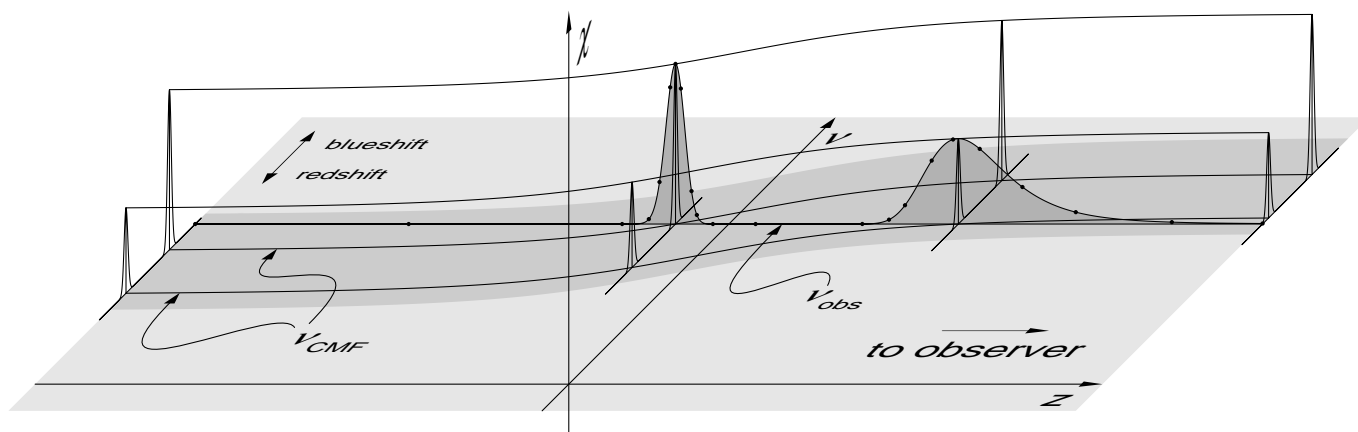


FIGURE 3-12. — Diagram (not to scale) illustrating the basic relationship of the rest-frame frequencies of spectral lines (v_{CMF}) to observer's frame frequency (v_{obs}) for one particular (non-core) p -ray in the spherically symmetric geometry (cf. Figure 3-8). Shown are two spectral lines which get shifted across the observer's frame frequency by the velocity field in the wind. The dots represent the stepping points of the adaptive microgrid used in solving the transfer equation in the detailed radiative line transfer.

Test calculations have shown that for the second factor in the coefficients the geometric mean (an arithmetic mean on a logarithmic scale)

$$\bar{\chi}_{i+1,i} = (\chi_{i+1} \cdot \chi_i)^{1/2} \quad (3.22)$$

gives good results, as demonstrated in figure 3-11, where a spectrum computed with the opacity sampling method is compared to one computed with the detailed radiative line transfer (method II), described in the next section. Considering the relative coarseness of the opacity sampling method, and the fact that the detailed line transfer suffers none of the approximations of the sampling method, the agreement is remarkable; however, it is this agreement that allows using only few iterations of method II (see below) for full convergence of the model. Note again that through the *single-p-ray approximation* for the sampling opacities (see above), method I (opacity sampling) *cannot* produce P Cygni profiles, since the P Cygni emission is a direct result of the different Doppler shifts of a particular spectral line along different rays.

3. 2. 1. 2. Method II — the detailed radiative line transfer

The detailed radiative line transfer (method II), implemented for the final iterations, is an exact solution of the transfer equation in the observer's frame, and is completely equivalent to a comoving frame solution. It removes the two most significant simplifications of the opacity sampling method (method I), i.e., it accounts for:

1. correct treatment of the angular variation of the opacities (cf. figure 3-8),
2. spatially resolved line profiles¹⁶ (implying correct treatment of multi-line effects).

Whereas in method I the former is completely ignored, the lack of spatial resolution was already compensated for to a large extent through the use of the Doppler-spread sampling. (Multi-line interaction is partly included in method I, but without regard for the sign of the Doppler shift (using just that of the central ray), and without regard for the order of the lines along the ray within a radius interval, as the Doppler-spread sampling effectively "maps" the lines to the nearest radius point.)

¹⁶ Note that this will not by itself solve our problem of self-shadowing, since that is an intrinsic property of any method (such as the Sobolev-with continuum method) using an "incident radiation" in solving for the bound-bound radiative rates with the radiation field already affected by the transition being considered. As the Sobolev-with-continuum method is also used for computing the radiative line transition rates in the final iteration cycle using method II for the radiative transfer, the correction for self-shadowing has to be applied here as well.

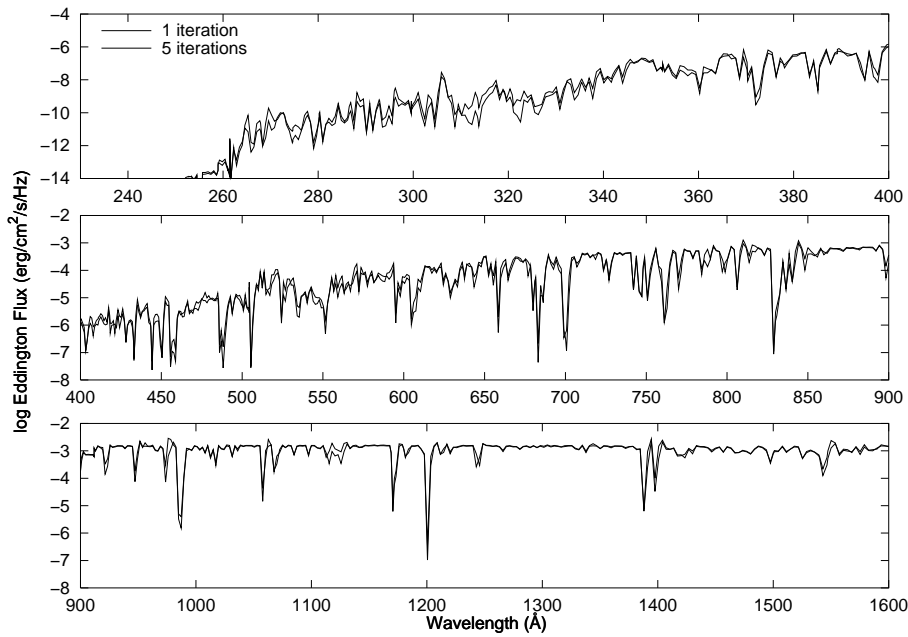


FIGURE 3-13. — Flux of the S-29 supergiant model ($T_{\text{eff}} = 29000$ K, $\log g = 3.0$, $R = 27.0 R_{\odot}$) after 1 and 5 iteration blocks of method II.

In contrast to method I, where the symmetry and our assumption of only radially (not angular) dependent Doppler shifts allowed solving the transfer equation for only one quadrant, a correct treatment of the both red *and* blue Doppler-shifted line opacities (see figure 3-8) requires a solution in two quadrants (corresponding to, from the observer’s viewpoint, the front and back hemispheres; the rotational symmetry along the line-of-sight is taken care of through the angular integration weights).

The method employed is an adaptation of the one described by Puls and Pauldrach (1990), using an integral formulation of the transfer equation and an adaptive stepping technique which ensures that the optical depth in each step (“microgrid”) does not exceed $\Delta\tau = 0.3$, so that the radiation transfer in each micro-interval can be approximated to high accuracy by an analytical formula assuming a linear run of opacity and emissivity between the micro-interval endpoints:

$$I(\tau_0) = I(\tau_n)e^{-(\tau_n-\tau_0)} + \int_{\tau_0}^{\tau_n} S(\tau)e^{-(\tau-\tau_0)} d\tau, \quad (3.23)$$

where the integral is performed as a weighted sum on the microgrid

$$\int_{\tau_0}^{\tau_n} S(\tau)e^{-(\tau-\tau_0)} d\tau = \sum_{i=0}^{n-1} \left(e^{-(\tau_i-\tau_0)} \int_{\tau_i}^{\tau_{i+1}} S(\tau)e^{-(\tau-\tau_i)} d\tau \right), \quad (3.24)$$

each “microintegral” being evaluated as

$$\int_{\tau_i}^{\tau_{i+1}} S(\tau)e^{-(\tau-\tau_i)} d\tau = w_i^{(a)} S(\tau_i) + w_i^{(b)} S(\tau_{i+1}) \quad (3.25)$$

with weights

$$w_i^{(a)} = 1 - \frac{1 - e^{-\Delta\tau_i}}{\Delta\tau_i}, \quad w_i^{(b)} = \frac{1 - e^{-\Delta\tau_i}}{\Delta\tau_i} - e^{-\Delta\tau_i} \quad (3.26)$$

where $\Delta\tau_i = \tau_{i+1} - \tau_i$. To accurately account for the variation of the line opacities and emissivities due to the Doppler shift, all line profile functions $\phi_{ij}(\nu)$ are evaluated correctly for the current microgrid- (z, p) -coordinate on the ray, thus effectively resolving individual line profiles. Only the slowly-varying occupation numbers (or equivalently, the integrated, frequency-independent line opacities χ_{ij} and emissivities η_{ij}) and the velocity field are interpolated between the regular radius grid points.

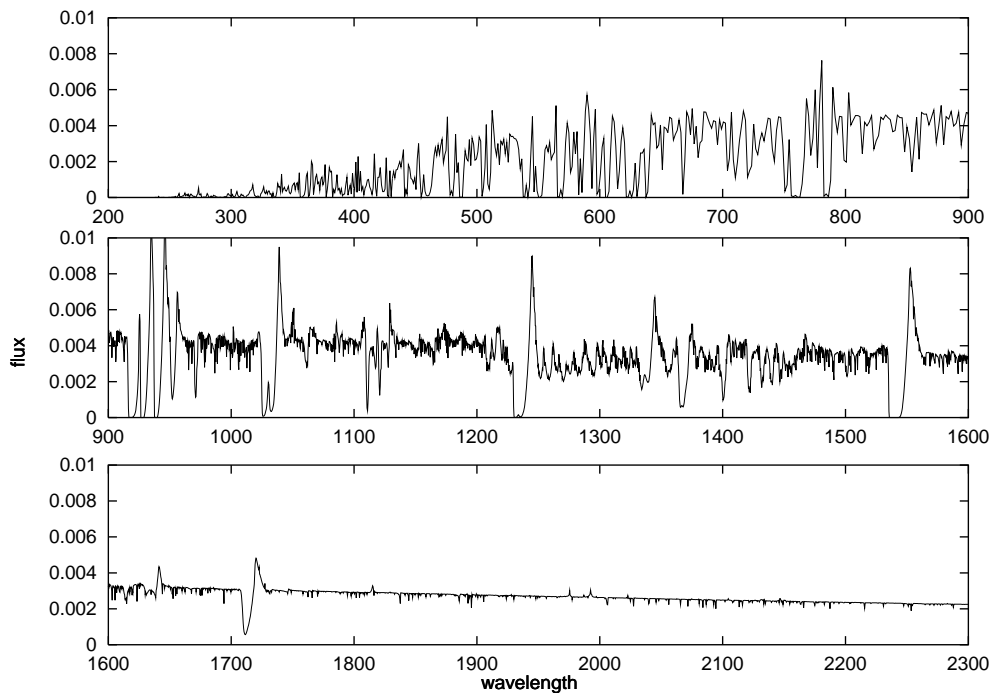


FIGURE 3-14. — The final spectrum from 200 to 2300 Å of the S-45 supergiant model. The observable UV region redward of the Lyman edge has been computed with a high resolution (for comparison with observed spectra).

The radiative transfer is solved twice for each frequency, once including all opacities and emissivities (lines and continuum) and a second time using only continuum opacities and emissivities, and blocking factors (cf. Pauldrach et al. 1996) $B_J(r, \nu) = J(r, \nu)/J_{\text{cont}}(r, \nu)$ and $B_H(r, \nu) = H(r, \nu)/H_{\text{cont}}(r, \nu)$ are computed as the ratio of the radiative quantities calculated in the two passes. These blocking factors are then applied to the solution of the radiative transfer computed in the iterations within one iteration block, involving only continuum opacities and emissivities during method II, to obtain the correct radiative quantities used for calculating the radiative rates (see figure 3-3). The advantage of this scheme (as opposed to using the calculated J_ν and H_ν from the detailed radiative transfer directly) is that it allows occupation numbers and radiation field to be iterated within one iteration block using only the computationally comparatively cheap continuum transfer while retaining the characteristic of the full radiative transfer solution.

Figure 3-12 depicts schematically the relationship between the Doppler-shifted frequencies of spectral lines (which are constant in the comoving frame) and the observer's frame frequency for which the radiative transfer is being calculated. The figure also illustrates the *line overlap* in accelerating, expanding atmospheres: lines clearly separated in the comoving frame (slices parallel to the (ν, χ) -plane) overlap in the observer's frame (slice parallel to the (z, χ) -plane at ν_{obs}) due to large Doppler shifts many times the intrinsic (thermal and microturbulent) linewidth. The areas shaded in dark gray correspond to the spatially resolved Sobolev resonance zones of the two lines for this particular observer's frame frequency and p -ray. Note that the dimensions are not to scale, i.e., the intrinsic width of the lines, and consequently the thickness in z of the resonance zones, has been greatly exaggerated in relation to the total velocity shift.

All lines whose maximum Doppler shift $\Delta\nu = \pm v_{ik} v_\infty / c$ puts them in range of the observer's frame frequency for which the radiative transfer is being calculated are considered for that frequency point. In figure 3-12, these correspond to those lines whose rest frequencies lie in the gray band in the (ν, z) -plane at $z = 0$.

Broadening of the lines includes thermal and microturbulent contributions. For every atomic species and depth point, the correct thermal Doppler broadening based on atomic weight and local temperature is used. Microturbulence as a function of radius or outflow velocity can be specified; default values are 10 km/s in the photosphere and a linear increase with the outflow velocity to a maximum of $0.1 v_\infty$ in the outer regions of the wind, which is generally in good agreement with the observations.¹⁷

After the occupation numbers have converged in the iteration cycle using method I, one iteration block with method II is usually sufficient for full convergence of the model, as demonstrated by figure 3-13, where the emergent spectrum of the S-30 model after 1 iteration block of method II is compared to the spectrum resulting from 5 iteration blocks of method II.

A high-resolution spectrum is computed for the purpose of comparison with observations (wavelength range usually from 900 to 1800 Å) after full convergence of the model. This spectrum is generated with the same procedure as used for the detailed line blocking calculations. The high-resolution spectrum is then merged with the (usually) lower-resolution blocking flux for the final flux output (figure 3-14).

3.2.2. Treatment of line blanketing

Line blanketing refers to the back-reaction of line blocking onto the temperature structure. Qualitatively, the increased opacities due to lines result in a steeper temperature gradient to “drive” the flux (cf. diffusion approximation, equation 2.9). As the diffusion approximation, however, is not fully valid in the regions of interest here (the regions where the emergent UV spectrum and ionizing flux is formed), the temperature structure must be computed explicitly to satisfy the constraint of energy conservation.

▷ In the inner, optically thick parts of the atmosphere ($\tau_{\text{Ross}} \geq 0.1$), this is done by using an “NLTE Hopf function” (see Santolaya-Rey et al. 1997) as a parametrized “correction function” to the gray atmosphere:

$$T^4 = \frac{3}{4} T_{\text{eff}}^4 \frac{\tilde{\tau}_{\text{Ross}}}{\tau_{\text{Ross}}} (\tau_{\text{Ross}} + q_{\text{N}}(\tilde{\tau}_{\text{Ross}})). \quad (3.27)$$

(This is possible since at these depths τ_{Ross} is still the major factor determining the temperature.) Here $\tilde{\tau}_{\text{Ross}}$ is the Rosseland optical depth accounting for sphericity, defined by

$$d\tilde{\tau}_{\text{Ross}} = \chi_{\text{Ross}}(r) \left(\frac{R}{r} \right)^2 dr, \quad (3.28)$$

and

$$q_{\text{N}}(\tilde{\tau}_{\text{Ross}}) = q_\infty + (q_0 - q_\infty) e^{-\gamma \tilde{\tau}_{\text{Ross}}} \quad (3.29)$$

is a parametrized approximation to the spherical NLTE Hopf function. The parameters q_∞ , q_0 , and γ are adjusted to yield an overall good conservation of the flux (see Pauldrach et al. 1998). Specifically, the algorithm proceeds as follows:

1. Suitable starting values for all three parameters are chosen from tabulated values derived from previous models. (This is done to save computing time).
2. The parameter q_0 is adjusted until the flux at a depth of $\tau_{\text{Ross}} \approx 3$ is conserved to about 0.5%.
3. The parameter q_∞ is adjusted to conserve the flux at a depth of $\tau_{\text{Ross}} \approx 0.1$. If during the iteration the deviation of the flux at $\tau_{\text{Ross}} \approx 3$ again becomes larger than 0.5%, q_0 is adjusted again.
4. Finally, γ is adjusted to conserve the flux at a depth of $\tau_{\text{Ross}} \approx 1$.

▷ In the outer parts of the atmosphere ($\tau_{\text{Ross}} \leq 0.1$), where scattering processes start to dominate, a linearized Newton-Raphson method has been implemented to extrapolate a temperature (at every depth point) that balances the local heating and cooling rates (cf. section 2.3).

¹⁷ It should be noted, however, that it is not yet clear whether the slopes of the blue edges of the P Cygni absorption troughs, which are normally fitted with this assumed supersonic turbulence in the outer regions, are actually the result of real turbulent motion or rather of a multiply non-monotonic velocity field (Lucy 1982, 1983).

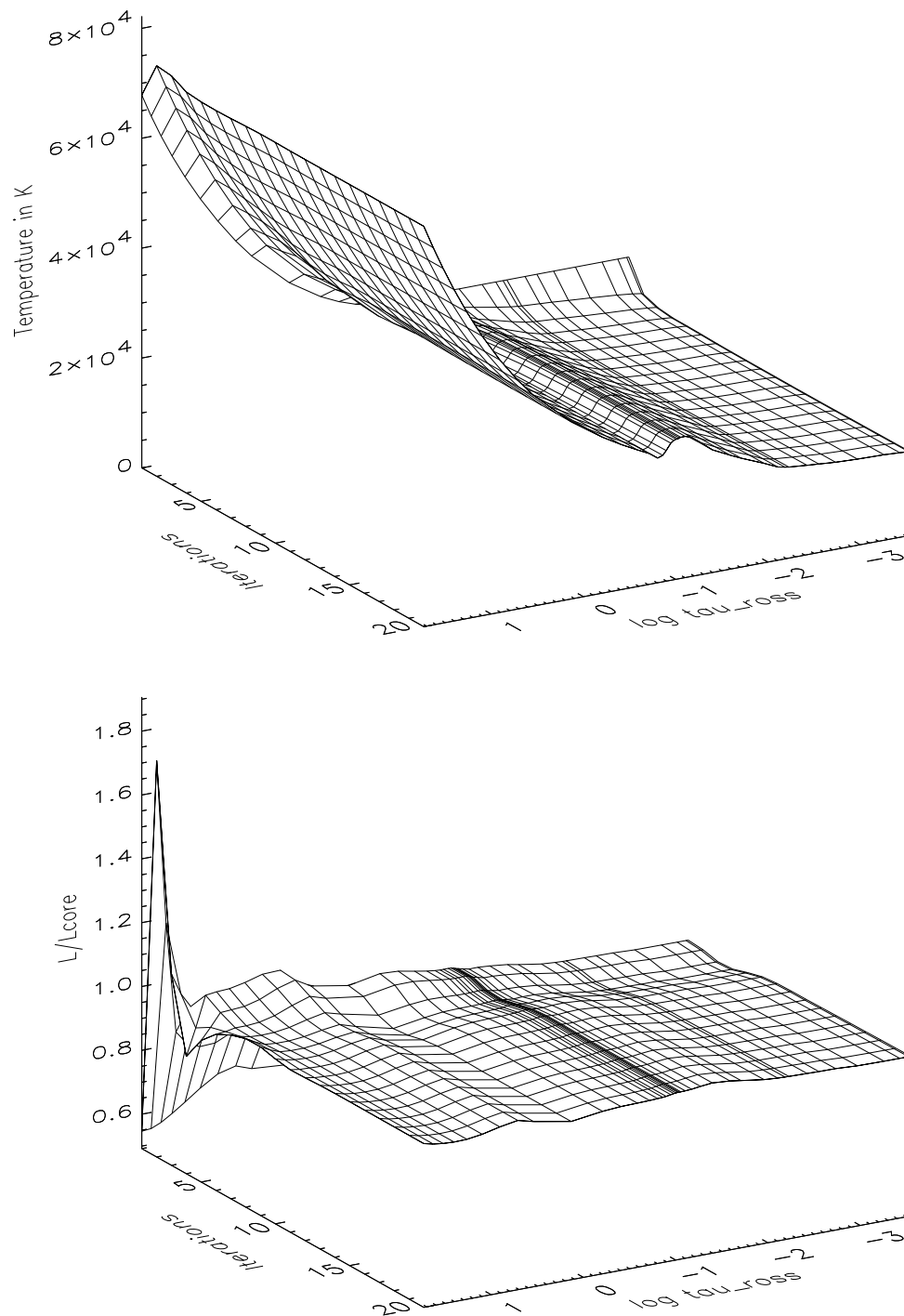


FIGURE 3-15. — Temperature structure $T(r)$ (top) and flux conservation $L(r)/(4\pi R^2 \sigma T_{\text{eff}}^4)$ (bottom) as function of optical depth and iteration block number for a cool O supergiant model ($T_{\text{eff}} = 29\,000$ K, $\log g = 3.0$, $R = 27 R_{\odot}$). The flux is conserved on the 1% level for the final iteration blocks.

Figure 3-15 shows the resulting temperature structure $T(r)$ and the flux conservation $L(r)/(4\pi R^2\sigma T_{\text{eff}}^4)$ as function of optical depth and iteration block number for a cool O supergiant model ($T_{\text{eff}} = 29\,000\text{ K}$, $\log g = 3.0$, $R = 27 R_{\odot}$). The suitability of this two-part method for computing the temperature structure in O-star atmospheres is manifested by the fact that the resulting flux conservation in the final iterations is at the 1% level.

It is worthwhile noting at this point that conservation of flux is not directly enforced anywhere in the model. Instead, it is a consequence of the dependence of the opacities and emissivities on the temperature. The fact that the temperature structure that conserves the flux also balances the heating and cooling rates is an indication that the microscopic processes involved are treated consistently in the models.

3.2.3. Atomic data

The accuracy of the calculated occupation numbers and of the synthetic spectrum will obviously depend directly on the quality of the atomic data used in the NLTE computations. Thus, accurate atomic models are a prerequisite for realistic atmospheric models. The atomic models used here have been computed in our working group (mainly by M. Lennon) using the *Superstructure* program (Eissner et al. 1974; Nussbaumer and Storey 1978), which employs the configuration-interaction approximation to determine wave functions and radiative data. The data comprise the most important 149 ionization stages of the 26 elements considered (H to Zn, apart from Li, Be, B, and Sc), with a total of about 5000 levels (where the fine-structure levels have been “packed” together) for which the occupation numbers are explicitly computed, and more than 30 000 corresponding radiative bound-bound transitions as well as 20 000 individual transition probabilities of low-temperature dielectronic recombination and autoionization used in the rate equations. For the blocking, line-force, and spectrum calculations the individual lines of each multiplet are considered, with a total of over 4 000 000 lines.¹⁸

Additional line data were taken from the Kurucz (1992) line list: approximately 20 000 lines have been added to the Superstructure data for ions of Mn, Fe, Co, and Ni. These concern transitions to even higher levels than those having been calculated with Superstructure, but which might nonetheless be of significance in the blocking calculations. From the Opacity Project (cf. Seaton et al. 1994; Cunto and Mendoza 1992) another 4466 lines have been included, as well as photoionization cross-sections (almost 2000 data sets have been incorporated). Collisional data have become available through the IRON project (Hummer et al. 1993), from which almost 1300 data sets have been included.

Table 3-1 gives a summary of the recently revised atomic data (cf. Pauldrach et al. 1998; Pauldrach, Hoffmann, and Lennon 2001) for the most important metal ions used in the models.

3.2.4. Treatment of shock radiation

The generally accepted explanation today for both the observed X-ray emission from O stars as well as the EUV radiation needed to theoretically account for the observed presence of high ionization stages (O VI, N V) is radiation from shock instabilities in the wind flow (Cassinelli and Swank 1983; Lucy and White 1980; Lucy 1982). Although considerable progress has been made in the last years in modelling these instabilities (e.g., Feldmeier et al. 1997b) a consistent theory predicting *quantitatively* from first principles the strength and distribution of these shocks in the atmosphere is not yet available. Theoretical investigations of time-dependent radiation hydrodynamics (e.g., Owocki, Castor, and Rybicki 1988; Feldmeier 1995), however, favor the picture of a stationary “cool wind” with embedded randomly distributed shocks, where the shock distance is much larger than the shock cooling length in the accelerating part of the wind. They also indicate that only a small amount of high velocity material appears with a filling factor not much larger than $f \approx 10^{-2}$ and jump velocities of about $u = 300$ to 700 km/s , corresponding to immediate post-shock temperatures of approximately $T_S = 1 \times 10^6$ to $8 \times 10^6\text{ K}$.

¹⁸ The Superstructure calculations involve many more excited levels than actually used in the NLTE calculation. The line list, however, does include transitions to such highly excited levels above the limit of considering the level structure; occupation numbers of these upper levels are estimated using the two-level approximation on the basis of the (known) occupation number of the lower level.

Ion	levels		lines		Ion	levels		lines	
	packed	unpacked	rate eq.	blocking		packed	unpacked	rate eq.	blocking
C II	36	73	284	11005	S VI	18	32	59	142
C III	50	90	520	4406	S VII	14	26	39	1031
C IV	27	48	103	229	Ar V	40	86	328	3007
C V	5	7	6	57	Ar VI	42	93	400	1335
N III	40	82	356	16458	Ar VII	47	87	483	2198
N IV	50	90	520	4401	Ar VIII	15	27	41	111
N V	27	48	104	229	Mn III	50	141	364	175593
N VI	5	7	6	57	Mn IV	50	124	467	131821
O II	50	117	595	39207	Mn V	50	124	508	61790
O III	50	102	554	24506	Mn VI	13	25	35	87
O IV	44	90	435	17933	Fe II	50	148	405	227548
O V	50	88	524	4336	Fe III	50	126	246	199484
O VI	27	48	102	231	Fe IV	45	126	253	172902
Ne IV	50	113	577	4470	Fe V	50	124	451	124157
Ne V	50	110	534	2664	Fe VI	50	138	452	60458
Ne VI	50	112	343	1912	Fe VII	22	62	91	10123
Mg III	50	96	529	2457	Fe VIII	42	96	300	4777
Mg IV	50	117	589	3669	Co III	50	141	469	200637
Mg V	50	100	547	3439	Co IV	41	97	70	146252
Mg VI	21	44	54	305	Co V	45	126	253	182780
Al IV	50	96	529	2523	Co VI	43	113	317	124053
Al V	50	117	588	18317	Co VII	34	80	246	50270
Al VI	19	37	41	153	Ni III	40	102	281	131508
Si III	50	90	480	4044	Ni IV	50	146	528	183267
Si IV	25	45	90	245	Ni V	41	97	70	179921
Si V	50	98	531	3096	Ni VI	45	126	253	186055
Si VI	50	116	596	3889	Ni VII	43	113	317	123386
P V	25	45	90	245	Ni VIII	34	80	246	43778
P VI	14	26	41	1096	Cu IV	50	124	477	17466
S V	44	78	404	903	Cu V	50	146	527	30457
					Cu VI	50	126	246	10849

TABLE 3-1. — Summary of recently revised atomic data used in the models (cf. Pauldrach et al. 1998; Pauldrach, Hoffmann, and Lennon 2001). Column 2 lists the number of levels used in the calculation of the occupation numbers, where the fine-structure levels have been “packed” together; column 3 gives the number of corresponding fine-structure levels. The number of line transitions between packed levels (i.e., all lines of a multiplet treated as a single line) used in the rate equations is given by column 4, and column 5 lists the number of corresponding individual lines, used in the blocking, line-force, and spectrum computation.

On this basis Pauldrach et al. (1994) had developed a semi-empirical approximate treatment which describes the shocks via four adjustable parameters (and which we have also used in our analysis of α Cam (see below)). This description assumes that the shocked material is smoothly distributed (with a filling factor f) and that the shock emission is mostly characterized by the immediate post-shock temperature T_S . This post-shock temperature at each radius point in the wind is calculated via the Rankine-Hugoniot relation from the local sound speed in the unshocked medium and the jump velocity $u(r)$, for which a functional dependence

$$\frac{u(r)}{u_\infty} = \left(\frac{v(r)}{v_\infty} \right)^\gamma \quad (3.30)$$

is assumed, where u_∞ is taken to be approximately the turbulent velocity v_{turb} in the outer regions of the wind. (This turbulent velocity can be determined from the slope of the blue edge of the absorption

TABLE 3-2. — Stellar and wind parameters of ζ Pup and shock parameters used in the test calculations for the revised treatment of shock emission. The abundances of He, C, N, and O are given as a factor relative to the solar value; for the other elements solar abundances have been used.

$\log \frac{L}{L_{\odot}}$	T_{eff} (10^3 K)	$\log g$ (cm/s^2)	R (R_{\odot})	v_{∞} (km/s)	\dot{M} ($10^{-6} M_{\odot}/\text{yr}$)	Y_{He}	Y_{C}	Y_{N}	Y_{O}	$\log \frac{T_{\text{S}}}{\text{K}}$	$\frac{f}{10^{-3}}$	$\log \frac{N_{\text{H}}}{\text{cm}^{-2}}$
6.006	42	3.625	19	2250	5.9	1.2	0.35	8.0	0.75	6.75	4.3	20.00

troughs of the strong P Cygni profiles, and is normally on the order of $0.1 v_{\infty}$. However, see also footnote 17 on page 36.) The exponent γ is a parameter determined empirically via comparison of synthetic and observed UV spectrum. The minimal radius at which shocks are assumed to begin to form is controlled by another empirical parameter, m , defined such that $u_{\text{min}} = ma$, with a the local adiabatic sound speed of the unshocked medium.

The emission coefficient due to shocks,

$$\eta_{\nu}^{\text{S}}(r) = \frac{f}{4\pi} n_{\text{p}} n_{\text{e}} \Lambda_{\nu}(T_{\text{S}}(r), n_{\text{e}}), \quad (3.31)$$

incorporated in the radiative transfer, is then obtained from the volume emission coefficient Λ_{ν} of the shock-heated matter computed using the thermal X-ray emission code developed by Raymond and Smith (1997), Cox and Raymond (1985), and Raymond (1988). The filling factor f is adjusted within the framework of the NLTE iteration cycle until the emergent X-ray luminosity of the model equals some pre-specified value L_{X} (on the order of the values observed in O stars, $L_{\text{X}}/L \approx 10^{-7}$, cf. Chlebowski et al. 1989).

Although this description, with properly adjusted parameters, could correctly account for the strengths of the lines of high ionization stages (O VI, N V) in the observed UV spectra (cf. Pauldrach et al. 1994), it was not quite satisfactory, as the observed ROSAT spectra could not be reproduced with the same set of parameters. We have therefore begun implementing a revised treatment of shock radiation, for which we here present results of test calculations (cf. Pauldrach, Hoffmann, and Lennon 2001). The major improvement consists of considering the *cooling zones* of the shocks, i.e., in contrast to the above description which assumes that all shock-heated matter of a shock front radiates at the same temperature (non-stratified, isothermal shocks), we now account for the fact that the shocks have a cooling structure with a certain *range* of temperatures that contribute to the EUV and X-ray spectrum.

With regard to these cooling structures, two limiting cases exist. In the inner region of the wind, where the cooling time can be regarded to be shorter than the flow time, the approximation of *radiative shocks* can be applied for the cooling process (cf. Chevalier and Imamura 1982). In the outer region, where the stationary terminal velocity is reached, the radiative acceleration is negligible, and the flow time is therefore large. Here radiative cooling of the shocks is of minor importance, and the cooling process can be approximated by *adiabatic expansion* (cf. Simon and Axford 1966, who investigated a pair of reverse and forward shocks that propagate through an ambient medium under these circumstances).

To account for the cooling structures, we have followed the modified concept of isothermal wind shocks presented by Feldmeier et al. (1997a), in which the volume emission coefficient Λ_{ν} of the shock-heated matter in equation 3.31 is replaced by the corresponding integral over the cooling zone,

$$\hat{\Lambda}_{\nu}(T_{\text{S}}(r)) = \pm \frac{1}{x_{\text{S}}} \int_r^{r \pm x_{\text{S}}} \hat{f}^2(r') \Lambda_{\nu}(T_{\text{S}}(r') \hat{g}(r')) dr'. \quad (3.32)$$

Here r is the location of the shock front and r' is the cooling length coordinate (with a maximum value of x_{S}); the plus sign corresponds to forward and the minus sign to reverse shocks. $\hat{f}(r')$ and $\hat{g}(r')$ denote the normalized density and temperature structures with respect to the shock front; for these we have presently adopted the analytical approximations given by Feldmeier et al. (1997a), based on the above two limiting cases of radiative and adiabatic cooling layers behind the shock fronts.

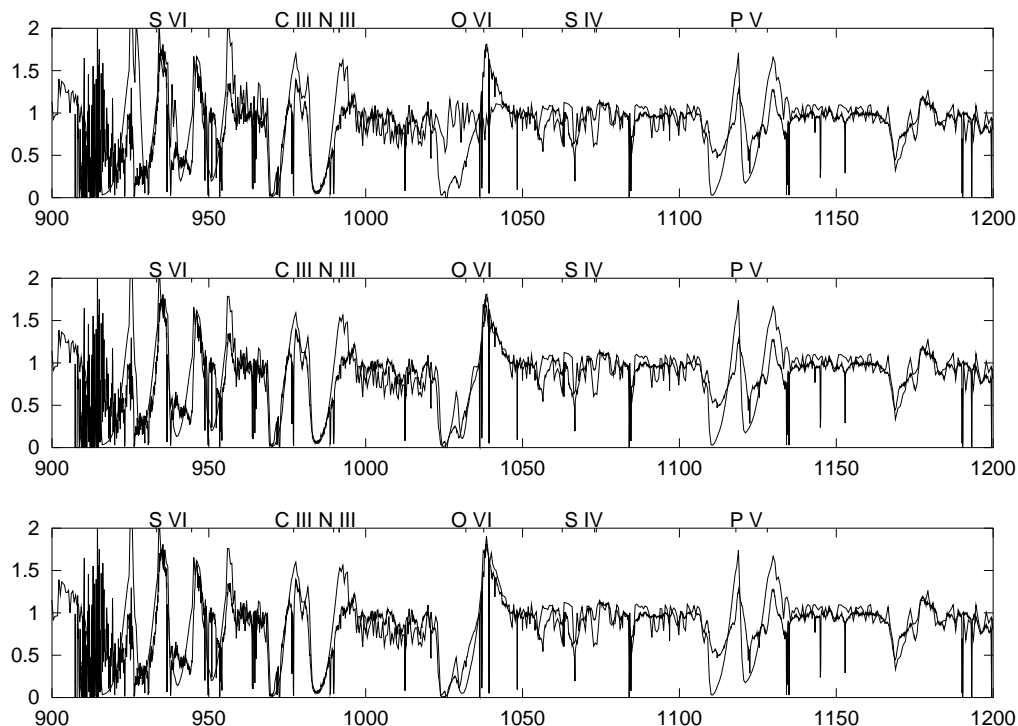


FIGURE 3-16. — Comparison of observed and synthetic UV spectra for a series of models for ζ Puppis. Top: model for which shock radiation has not been considered. Center: model where the influence of shock radiation has been treated in the approximation of isothermal shocks (model 1). Bottom: model with new treatment including cooling zones (model 2).

As test object for the revised treatment we have selected the O4 supergiant ζ Puppis, for which a high-signal-to-noise ROSAT observation exists, and which was also subject of the analyses of Pauldrach et al. (1994) and Feldmeier et al. (1997a). The stellar parameters and abundances (cf. table 3-2) have been adopted from Pauldrach et al. (1994). For the purposes of comparison we have also adopted for the test calculations the maximum post-shock temperature T_{ζ} and the filling factor f from the analysis of Feldmeier et al. (1997a), although of course the ultimate objective for future work is to determine these parameters from a fit to the observed X-ray spectra. These values are also given in table 3-2, together with the column density ($\log N_{\text{H}}$) of interstellar hydrogen (Shull and van Steenberg 1985) along the line of sight to ζ Puppis, used to compute the interstellar absorption of the X-ray flux.

In figure 3-16 we compare the observed UV spectrum of ζ Puppis to that resulting from a model using the earlier description of isothermal shocks (“model 1”, center panel), as well as one using the modified treatment (“model 2”, bottom). Both models reproduce the observed O VI resonance lines quite well, apart from minor differences. For reference we also show a model for which shock emission has not been included (top panel), and which clearly demonstrates that such a model does not reproduce the strong observed O VI lines.

That model 1 does not entirely describe the physics correctly is shown by a comparison to the observed ROSAT spectrum (figure 3-17): it produces too much radiation in the harder energy bands and too little in the soft X-ray part (shortward of 0.7 keV the spectrum is more likely characterized by a cooler shock component of $\log T_{\zeta} \approx 6.30$). The model with structured cooling zones (model 2), however, quite well reproduces the ROSAT spectrum, and the comparison shown is at least of the same quality as that obtained by Feldmeier et al. (1997a) with their best fit (see also Stock 1998). Actually, it is the fact that, compared to the non-stratified isothermal shocks, the post-shock cooling zones with their temperature stratifications radiate much more efficiently in the soft spectral band which leads to the improved fit.

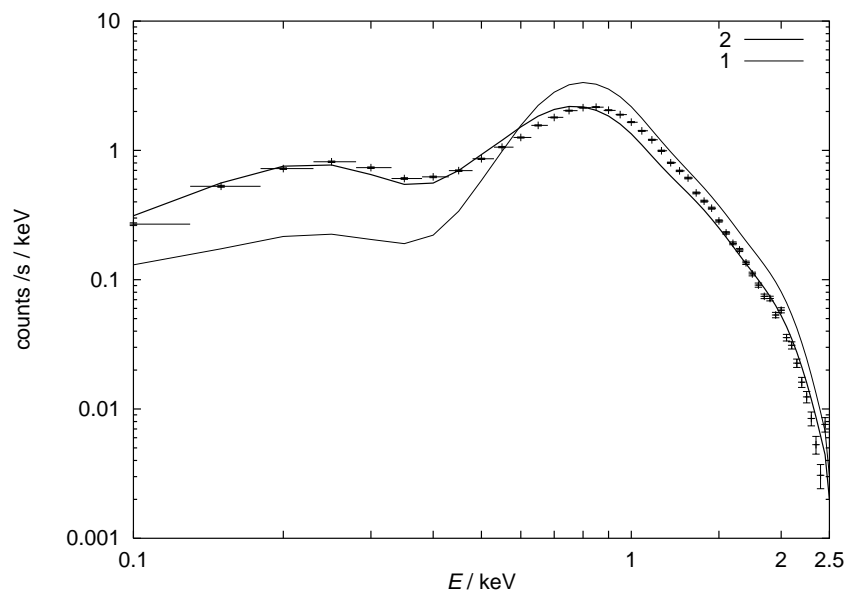


FIGURE 3-17. — Comparison of the ROSAT-observations (error bars) with the results of model 2 (thick line) and model 1 (thin line) for ζ Puppis. Note that the maximum shock temperatures are identical for both models. (Figure from Stock 1998.)

Hunsinger (1993) and Stock (1998) have shown that in the relevant energy range of ROSAT the wind is optically thick up to large radii, especially in the soft X-ray band, and consequently most of the observed X-ray radiation stems from the outermost regions of the wind only. This fact reduces the significance of the fit of the ROSAT spectrum somewhat, because it allows only the properties of the radiation produced in this outer region to be determined from the observed X-ray spectrum. This, however, is not the case for the EUV and X-ray radiation which populates the levels connected with the resonance lines of N v and O vi, since due to their P Cygni structure these lines provide information about the complete wind region, and the properties of the influencing radiation produced also in the inner wind region can therefore be analyzed by means of spectral line diagnostics.

For the significance of our improved treatment accounting for the structured cooling zones behind the shocks it is therefore extremely convincing that model 2 reproduces not only the observed X-ray spectrum, but also simultaneously the observed resonance lines of N v and O vi (the latter is shown in figure 3-16). (That both model 1 and model 2 yield a good fit of the P Cygni lines shows, on the other hand, that distinguishing between two different models from the profiles alone is not always possible.) Considering the greater importance, as discussed above, of a fit of the UV resonance lines of the highly ionized species compared to a fit of the Rosat spectrum, and the fact that the X-ray spectrum from model 1 is nonetheless a fair approximation to the observed spectrum, we conclude that the old treatment of isothermal shocks remains a workable description as long as the ROSAT observations are not required to be fitted perfectly (see also Pauldrach, Hoffmann, and Lennon 2001).

This conclusion is also supported by a comparison of the emergent X-ray emission from our final model for α Cam using the simplified treatment of isothermal shocks (cf. section 4.1 and appendix D) to the corresponding ROSAT observation (figure 3-18). The count rate in the ROSAT spectrum is comparatively low (only 226 counts total) and several ROSAT channels have been combined to “superchannels” with a minimum count. The model flux has been artificially degraded to that of the observation by applying the corresponding ROSAT PSPC (position sensitive proportional counter) detector response matrix (cf. Briel et al. 1997) and binned to the same “superchannels”. Interstellar continuous absorption (Morrison and McCammon 1983) with a hydrogen column density of $\log N_{\text{H}} = 21.08$ (Shull and van Steenberg 1985) has been included in the model flux, and a distance to α Cam of 0.95 kpc (Markova et al. 2003) has been assumed.

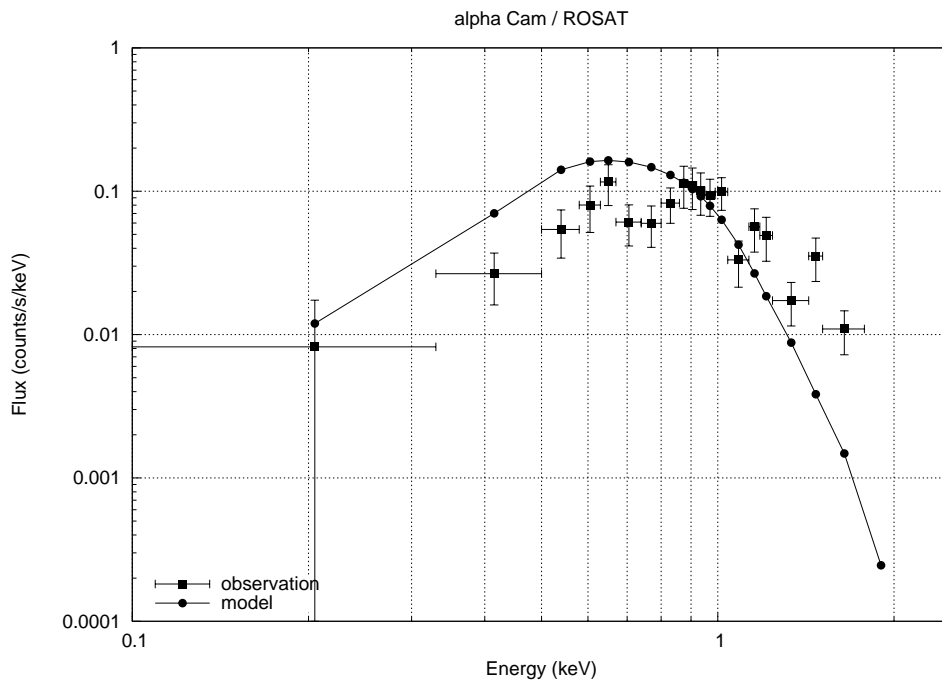


FIGURE 3-18. — Comparison of the X-ray spectrum of α Cam observed by ROSAT (errorbars) with the flux from our final model (curve) degraded to the same resolution. Considering the fact that the shock parameters have been constrained on basis of the shock influence on the UV spectrum alone, the agreement can be regarded as excellent.

The agreement between the model spectrum and the observation can be considered excellent in view of the fact that the shock parameters have been constrained on basis of the shock influence on the UV spectrum alone. This again indicates that the semi-empirical shock parametrization used provides a useful description despite its simplifying assumptions. The disagreement at higher energies is attributed to neglecting the lower temperatures of the shock cooling zones (and thus we determine different maximum shock temperatures from the UV fit than would be the case if these were properly considered), and we expect the fit to improve with the more sophisticated description which is currently being implemented (see the discussion of ζ Pup above).

3. 3. Interstellar lines

In spectral regions with overlapping interstellar lines we may run the risk of misinterpreting an observed stellar spectrum, as it is not a priori clear to what extent certain features are of stellar or of interstellar origin. (Primarily the wavelength region shortward of 1150 \AA is affected.) To account for this we can optionally compute an interstellar absorption spectrum which is applied to the synthetic spectrum of the stellar model before comparison with the observed stellar (and interstellar) spectrum. The interstellar matter can be described with a simple absorption-only model (since the average intensity J in the interstellar medium is much smaller than the intensity of the stellar disk, and thus the probability of a photon being scattered *into* the line of sight is negligible), and as absorbers only ground states and levels with very low excitation potential need be considered.

In constructing our interstellar absorption model we assume that the interstellar matter exists in “clouds”, each with a radial velocity v and a velocity dispersion b .¹⁹ Furthermore, for every cloud the effective

¹⁹ A “cloud” must not necessarily be connected or confined to a comparatively small volume. The only requirement is that the bulk motion of the absorbers can be described this way.

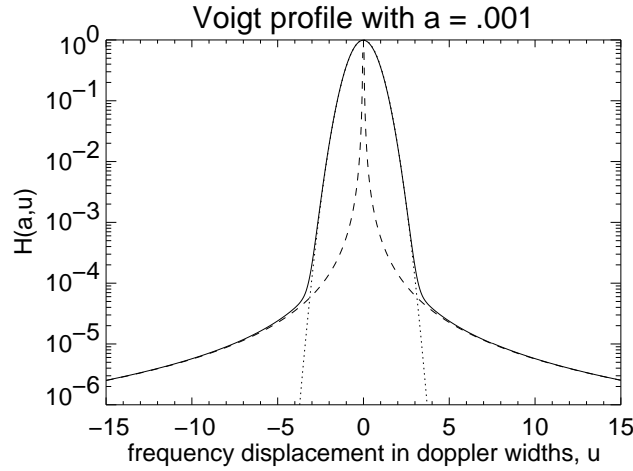


FIGURE 3-19. — Voigt profile (solid line) as convolution of Lorentz (dashed) and Doppler (dotted) profiles.

number of absorbers of each type (i.e., atomic/ionic or molecular energy level) will be specified by a column density N . These numbers are varied²⁰ until the best fit to the observed spectrum is achieved. (This way we can also derive information about the composition and excitation state of the interstellar material.) To ensure that our interstellar absorption spectrum is in itself consistent the absorption profiles of all lines originating from a particular level will of course be computed using the same column density.

The absorption line profiles (with ν_0 the center frequency of the transition) depend on the velocity dispersion b , for which we will assume a Gaussian

$$\varphi_{\text{Doppler}}(\nu) = \frac{1}{\nu_0 b/c\sqrt{\pi}} e^{-\frac{(\nu-\nu_0(1+\nu/c))^2}{(\nu_0 b/c)^2}} \quad (3.33)$$

and on the natural broadening profile (radiative damping) given by a Lorentzian (γ is the damping constant of the transition)

$$\varphi_{\text{damping}}(\nu) = \frac{\gamma/4\pi^2}{(\nu - \nu_0(1 + \nu/c))^2 + (\gamma/4\pi)^2} \quad (3.34)$$

(Radiative damping is considered here because due to the potentially very large column densities in the interstellar medium a significant optical depth can also be reached in the line wings.) The convolution of these yields the final profile

$$\varphi(\nu) = \frac{1}{\nu_0 b/c\sqrt{\pi}} H(a,u), \quad a = \frac{\gamma/4\pi}{\nu_0 b/c}, \quad u = \frac{\nu - \nu_0(1 + \nu/c)}{\nu_0 b/c} \quad (3.35)$$

where

$$H(a,u) = \frac{a}{\pi} \int_{-\infty}^{\infty} \frac{e^{-y^2}}{a^2 + (u-y)^2} dy \quad (3.36)$$

is the Voigt function (figure 3-19). The total optical depth at any frequency is then given by summing up the contributions of all lines from all levels

$$\tau(\nu) = \sum_{\text{clouds}} \sum_{\text{levels } i} \sum_{\text{lines } j} N_i \frac{\pi e^2}{m_e c} f_j \varphi_j(\nu) \quad (3.37)$$

(f_j is the oscillator strength of transition j originating from level i). From this we finally obtain our com-

²⁰ Computing the interstellar absorption spectrum is fairly fast, and this “line fitting” can be done interactively on any modern personal computer. An IDL program for the interactive modelling of interstellar lines has been developed and made available to the community by the author of this thesis.

binned synthetic stellar and interstellar spectrum,

$$H(\nu) = H^*(\nu) e^{-\tau(\nu)} \quad (3.38)$$

where $H^*(\nu)$ is the flux of the stellar atmosphere model. Transition wavelengths, oscillator strengths, and damping coefficients are taken from the atomic resonance line list of Morton (1991) and the molecular line list compiled by Taresch et al. (1997).

In figure 3-20 we show the observed spectrum of α Cam compared to the synthetic spectrum of our best model (cf. section 4.1 and appendix D) with (top) and without (bottom) inclusion of an interstellar absorption line model. (The column densities²¹ giving the best fit to the observed interstellar features are listed in table 3-3.) As the Copernicus spectrum of α Cam does not show multiple components in the interstellar lines (at least not outside the instrumental resolution) we have used a single cloud which can be adequately fitted with a radial velocity $v = 0$. Following Taresch et al. (1997) we have also assumed a velocity dispersion of $b = 20$ km/s. As can be seen from the figure, the overall agreement with the observed spectrum is obviously much improved. However, with regard to the constraints for the shock parameters derived from the fit of the synthetic stellar O VI resonance line to the observed one, the important point is that we can verify that this has not been influenced by the interstellar lines present in the spectrum, and the small discrepancy in the O VI emission that remained in our model is not made significantly worse by inclusion of the interstellar features.

TABLE 3-3. — Column densities used in modelling the interstellar absorption lines in the observed spectrum of α Cam (figure 3-20).

level	$\log N$ (cm ⁻²)	level	$\log N$ (cm ⁻²)
H ₂ ($J = 0$)	20.0	N I	15.0
H ₂ ($J = 1$)	19.9	Si II	14.0
H ₂ ($J = 2$)	15.5	C I	14.0
H ₂ ($J = 3$)	15.0	S II	15.0
H ₂ ($J = 4$)	14.5	O VI	14.0
		O I	15.5

²¹ Interstellar hydrogen Lyman lines are not included in the interstellar spectrum here since these were already taken into account in the rectification of the observed spectrum, cf. Haser 1995.

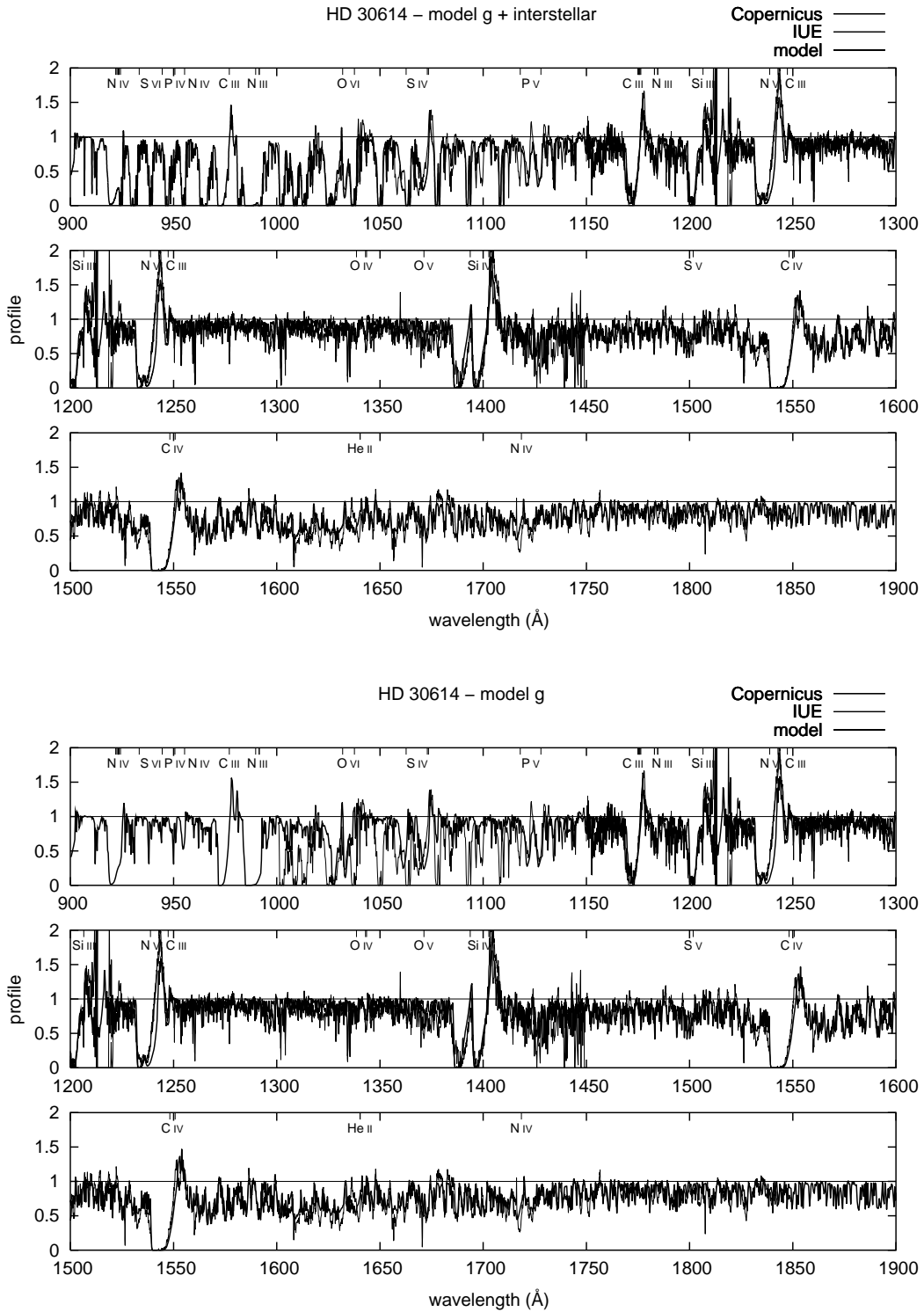


FIGURE 3-20. — Observed UV spectrum of α Cam compared to the synthetic spectrum of our best model (see section 4.1 and appendix D). In the upper panel absorption by the most important interstellar lines (cf. table 3-3) has been included in the synthetic spectrum; the lower panel shows the synthetic spectrum without an interstellar absorption line model.

4

UV spectral analysis as a constraint for the SEDs of massive stars

In this chapter, we will take a closer look at the synthetic UV spectra resulting from the model calculations, and compare them to the observed UV spectra of stars of similar stellar parameters. As already motivated in section 3.2 (see figure 3-2), such a comparison offers an indirect method to test the computed EUV spectral energy distributions (SEDs). Since the ionization balance in the atmosphere is determined mainly by EUV radiation field, and many of the affected ions in turn have lines in the observable UV range, the ionization balance and thus the shape of the EUV flux can be traced by the strength and structure of the UV spectral lines. (The EUV fluxes themselves are normally not directly observable due to absorption by interstellar hydrogen.)

A comparison has been performed for the Galactic O9.5 Ia supergiant α Cam (HD 30614) (as already published in Pauldrach, Hoffmann, and Lennon (2001), cf. appendix D) and the SMC O7 Iaf⁺ supergiant AV 232 (also known as Sk 80). The factors that make AV 232 — the SMC star — an interesting object for this type of comparison are an expected much lower metallicity (cf. Haser et al. 1998) — with a correspondingly different influence of the EUV line blocking — and a known radius. (Since the distance to the SMC is known, the radius of the star — derived from the observed (dereddened) visual flux, a corresponding model atmosphere flux, and the distance (as described, e.g., by Kudritzki et al. 1980) — is known with much greater accuracy than for Galactic stars, where the distance measurements are often affected by a large relative error.) Here we verify whether we can reach detailed agreement between observed and synthetic UV spectra by fine-tuning the wind parameters and abundances of this star, using the known radius as an important constraint for our models. We adopt radius and surface gravity from the study of Puls et al. (1996).

4.1. α Cam

Our detailed spectral analysis of the O9.5 supergiant α Cam has been published in Pauldrach, Hoffmann, and Lennon (2001) (cf. appendix D), and here we only summarize the main results. (Figure 3-20 (page 46) compares the spectrum of our best model to the observed UV spectrum.) From the analysis we conclude that our spectrum synthesis technique does, in principle, allow the determination of the effective temperature to within ± 1000 K and of the abundances to within about a factor of 2. Carbon and phosphorus show clear signs of an underabundance on the order of one tenth its solar value, as does oxygen with about 0.3 solar, whereas the abundance of iron must be at least solar to reproduce the spectrum of the numerous Fe IV and Fe V lines. To produce the ionization balance observed in the lighter elements C, N, O, and Si, the influence of shock radiation must start at larger radii where for shorter wavelengths the largest shock temperatures dominate. Thus, the way the X-ray spectral region selectively affects the ionization balance of different elements, observable through the lines in the EUV spectrum, provides constraints on the lower shock temperatures; we have determined maximum shock temperatures on the order of 2.0×10^6 K. Especially the Si III and C III lines have been found to be invaluable diagnostic instruments for this purpose. Our detailed analysis of the UV spectrum and the shocks needed to reproduce the observed lines has led to a significant difference in the ionizing flux compared to models without shocks. Thus we conclude that this type of analysis is a crucial test for the accuracy of the ionizing fluxes from models.

4.2. AV 232

Stellar and wind parameters. We begin with a model based on the parameters determined by Puls et al. (1996), (i.e., $T_{\text{eff}} = 37500$ K, $\log g = 3.30$, $R = 29.3 R_{\odot}$) and also choose the corresponding mass loss rate and terminal velocity of the wind ($\dot{M} = 5.5 \times 10^{-6} M_{\odot}/\text{yr}$, $v_{\infty} = 1400$ km/s). We choose a

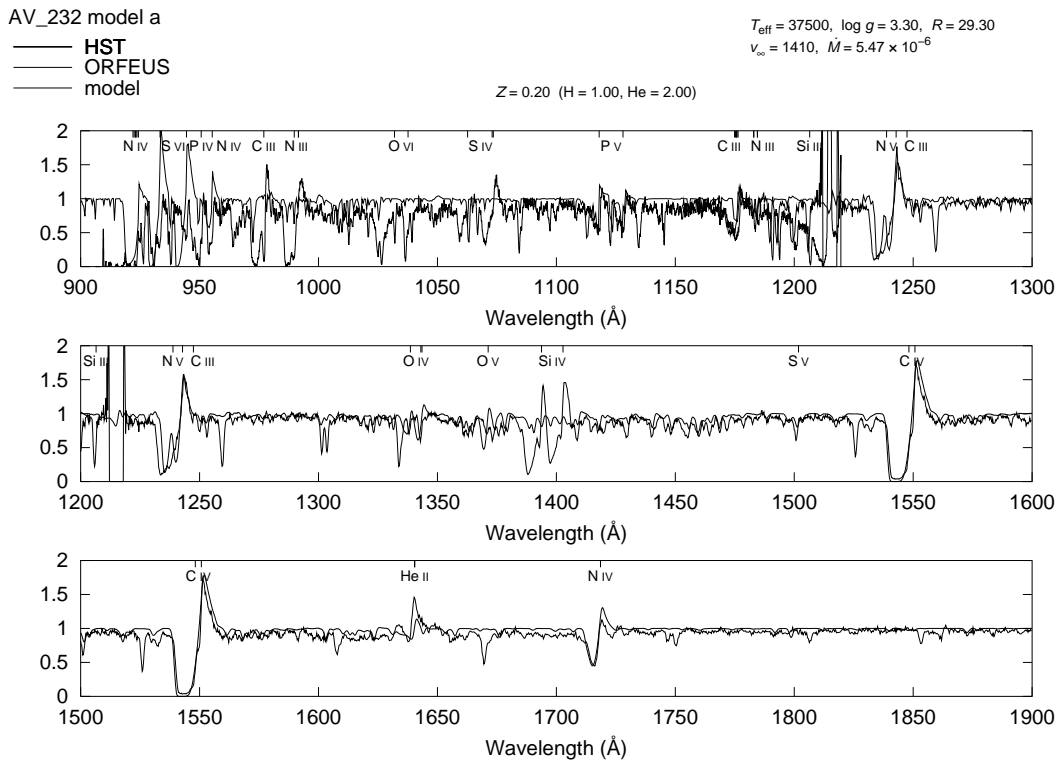


FIGURE 4-1. — Synthetic spectrum of our initial model for AV 232 compared to the observed spectrum. Too-weak lines of the lower ionization stages indicate that the effective temperature of the model is too high.

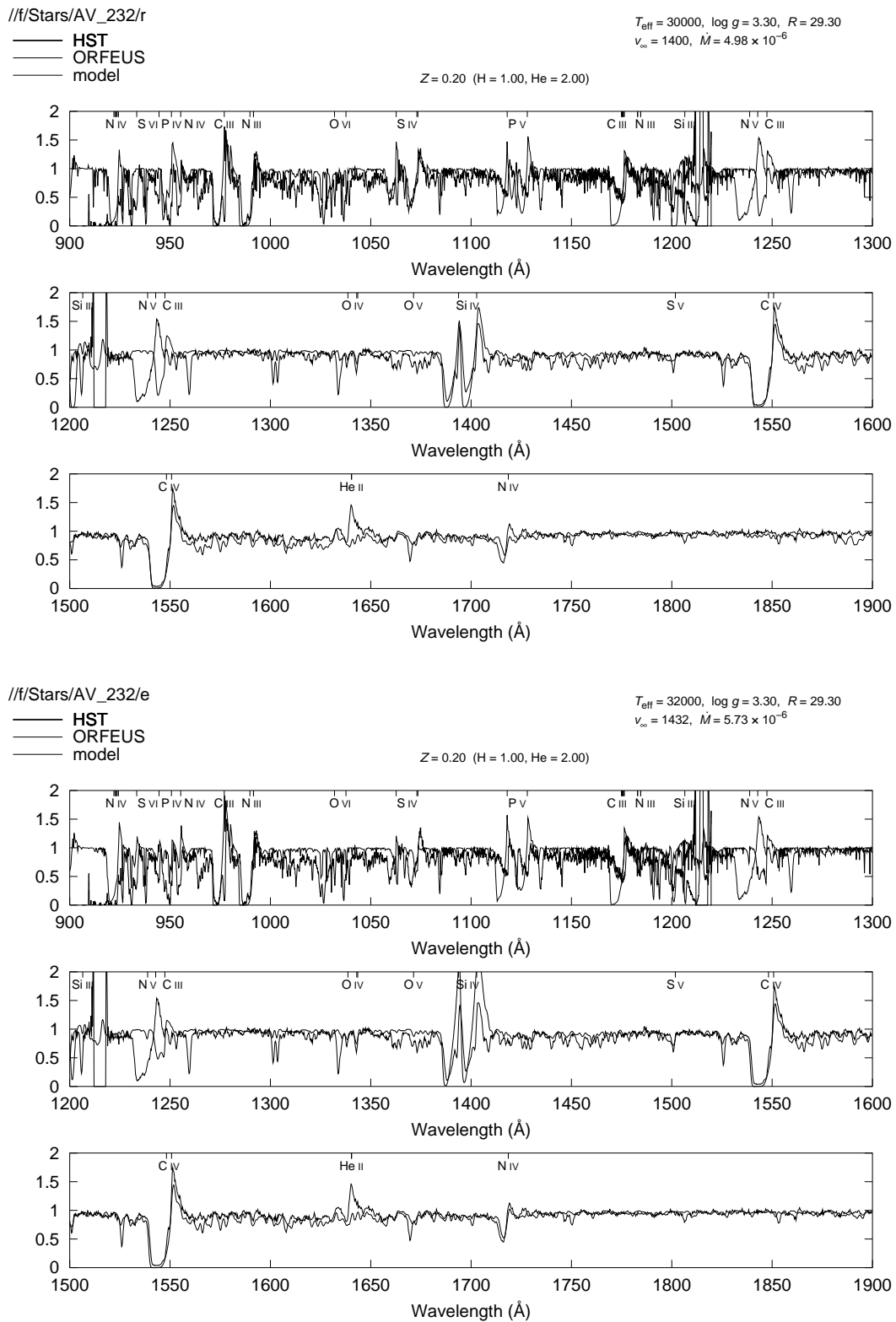


FIGURE 4-2. — Model sequence for AV 232 with varying effective temperature. Top: $T_{\text{eff}} = 30000$ K, bottom: $T_{\text{eff}} = 32000$ K.

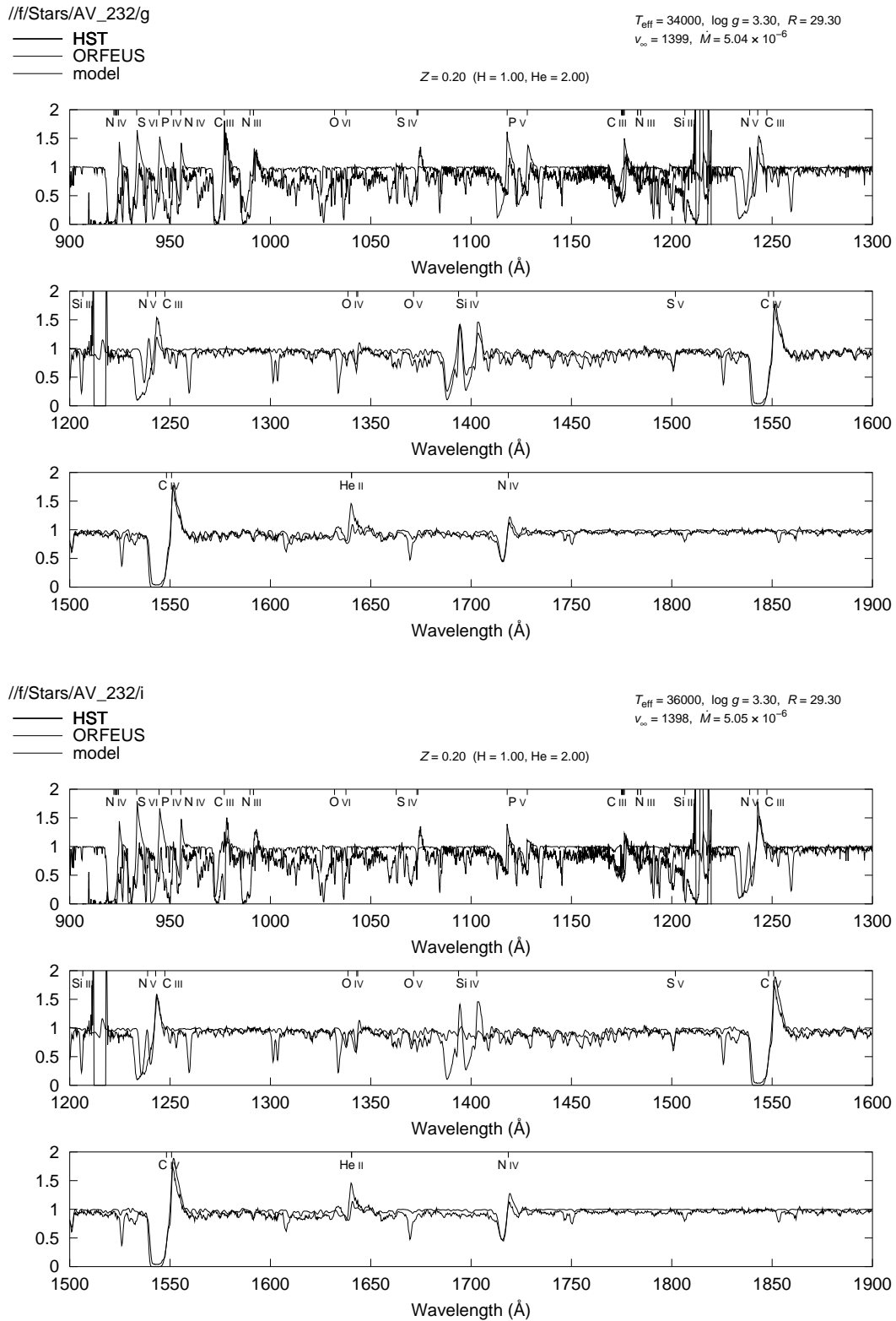


FIGURE 4-2. (continued) — Model sequence for AV 232 with varying effective temperature. Top: $T_{\text{eff}} = 34000$ K, bottom: $T_{\text{eff}} = 36000$ K.

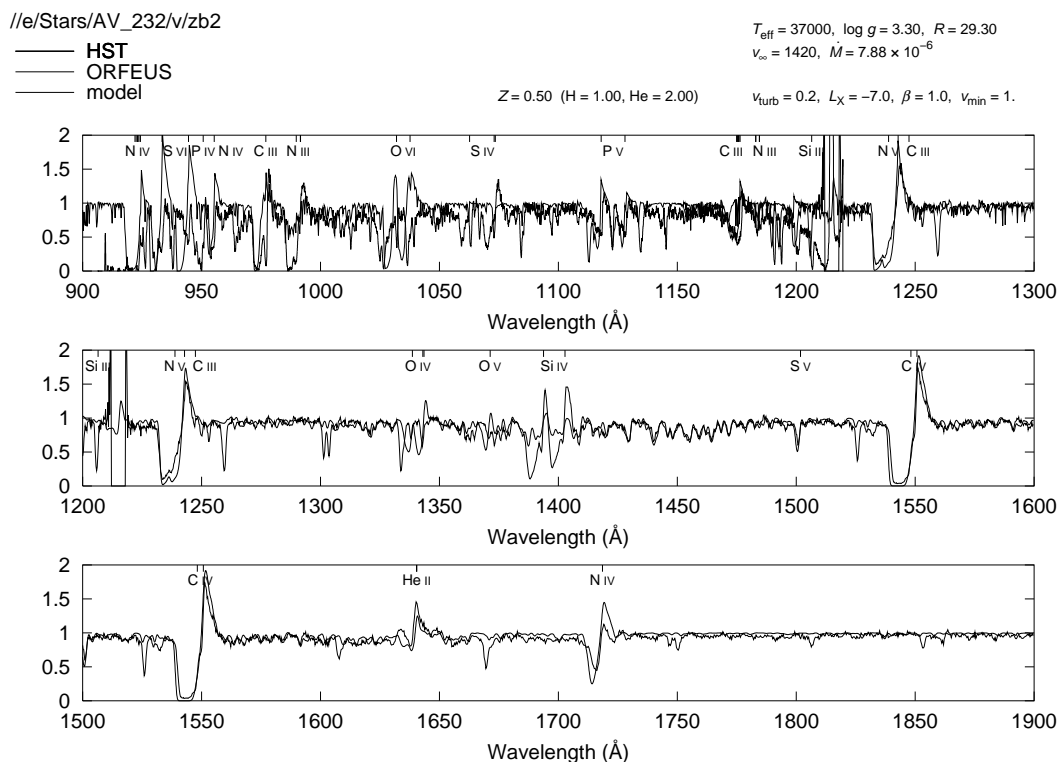


FIGURE 4-3. — The photospheric iron and nickel lines (1400 to 1500 Å) of AV 232 are best reproduced with a high effective temperature of $T_{\text{eff}} = 37000$ K and an increased metallicity of $Z = 0.5 Z_{\odot}$. However, at this temperature the low ionization stages (N III, C III, Si IV, S IV) in the wind cannot be reproduced. (Shocks have been included in this model, see below.)

metallicity of $Z = 0.2 Z_{\odot}$ (cf. Haser et al. 1998) and adopt the helium abundance found by Puls et al. (1996), $Y_{\text{He}} = 0.2$. Figure 4-3 shows the synthetic spectrum of this model compared to the rectified²² observed spectra from HST and ORFEUS. (The synthetic spectrum has been smoothed in the HST spectral range to correspond to the lower spectral resolution of the HST faint object spectrograph (FOS).)

In contrast to α Cam, where the Puls et al. (1996) parameters have already given a rather good fit, here we note a number of discrepancies. The lines of practically all lower ionization stages, in particular C III 977 Å, N III 991 Å, C III 1175 Å, Si IV 1394, 1403 Å, and S IV 1063, 1073 Å appear too weak, whereas O V 1372 comes out too strong. (The N V resonance line (1238, 1242 Å) is too weak due to the neglect of shocks in this model. The influence of shocks will be discussed later.)

Pauldrach et al. (1994) have encountered a discrepancy of similar quality in their analysis of ζ Pup, and diagnosed this to be the result of too little blocking in the EUV, leading to a too-strong radiation field and consequently too-high ionization rates for the low ionization stages. They have subsequently been able to nearly completely remove the discrepancies to the observed spectrum by simulating enhanced blocking by artificially decreasing the incident fluxes in the corresponding wavelength ranges. This option is not open to us here, since our approach is a selfconsistent description of line blocking, thus reducing the number of free parameters of the model.

However, we also note that the analysis of Puls et al. (1996) was performed using unblanketed models, and thus it is very likely that the effective temperature of this stars has been overestimated as a result. (Line-blocked and -blanketed models yield a higher photospheric temperature for a given T_{eff} , see section 3.2.) To verify whether a model with a reduced T_{eff} can provide a better fit to the observed spec-

²² An IDL program for the interactive rectification of observed spectra has been written by the author of this thesis and made available to the community.

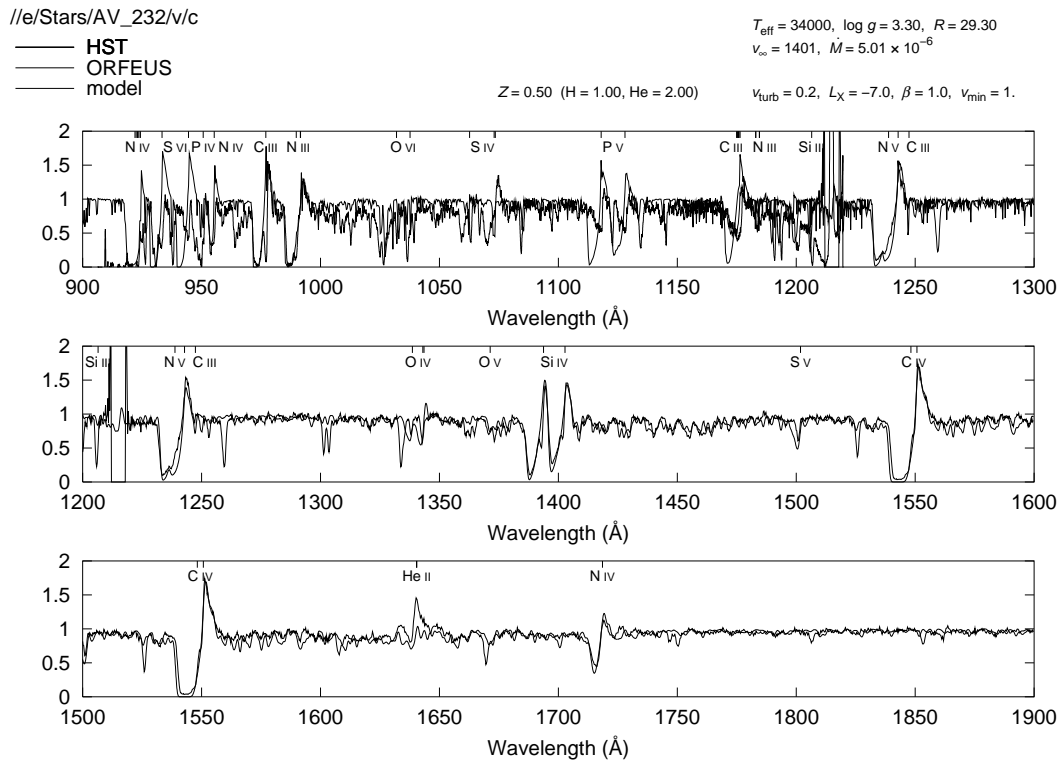


FIGURE 4-4. — The 34000 K model with an increased metallicity of $Z = 0.5Z_{\odot}$. Note that the photospheric lines from 1550 to 1650 Å become too strong with this metallicity at this temperature.

trum, we have computed a model sequence with effective temperature varying from 30000 K to 36000 K. The synthetic spectra of these models are shown in figure 4-2. Indeed we find that the fit of the P Cygni lines formed out in the wind improves at lower temperatures, whereas the (mostly photospheric) iron and nickel lines in the range from 1400 to 1500 Å are better reproduced with the higher temperatures (see figure 4-3), but we see that there is not a single temperature where the agreement is best for all lines.

Specifically, we note that S IV appears at its observed strength only at $T_{\text{eff}} = 30000$ K. The ORFEUS spectral range extends down to 920 Å, which, combined with the HST observation, gives us observed lines of three ionization stages of sulfur (S IV, S V, and S VI). This should in principle allow an accurate determination of the temperature as well as the sulfur abundance. Test calculations have confirmed that the discrepancy with regard to the S IV line cannot be removed with a change of the sulfur abundance, as the S VI line predicted by the model is already too strong at 34000 K, and any change in the sulfur abundance also leads to a markedly discrepant S V line. Of course we cannot exclude the possibility that this discrepancy might in part be due to inaccuracies in the atomic data, since the S IV atomic model has not yet reached the quality of those of other ionization stages (cf. table 3-1) and is still in a stage of rather incomplete description.

Two other factors which control the strength of the line blocking in the EUV, and can thus influence the observed strengths of the wind lines, are the mass loss rate and the metallicity. In figure 4-5 we show the influence of a change in the mass loss rate on the UV spectrum (using $T_{\text{eff}} = 34000$ K as a best compromise for the effective temperature). We see that the model with the lower mass loss rate of $\dot{M} = 2 \times 10^{-6} M_{\odot}/\text{yr}$ produces much too weak wind lines, whereas the model with the higher mass loss rate $\dot{M} = 8 \times 10^{-6} M_{\odot}/\text{yr}$ yields a significantly improved He II $\lambda 1640$ line, and a marginally improved fit of the photospheric iron lines. However, the situation with respect to the sulfur ionization balance has not improved. Phosphorus seems to be affected by a similar problem, giving a too strong P V line and a too weak P IV line.

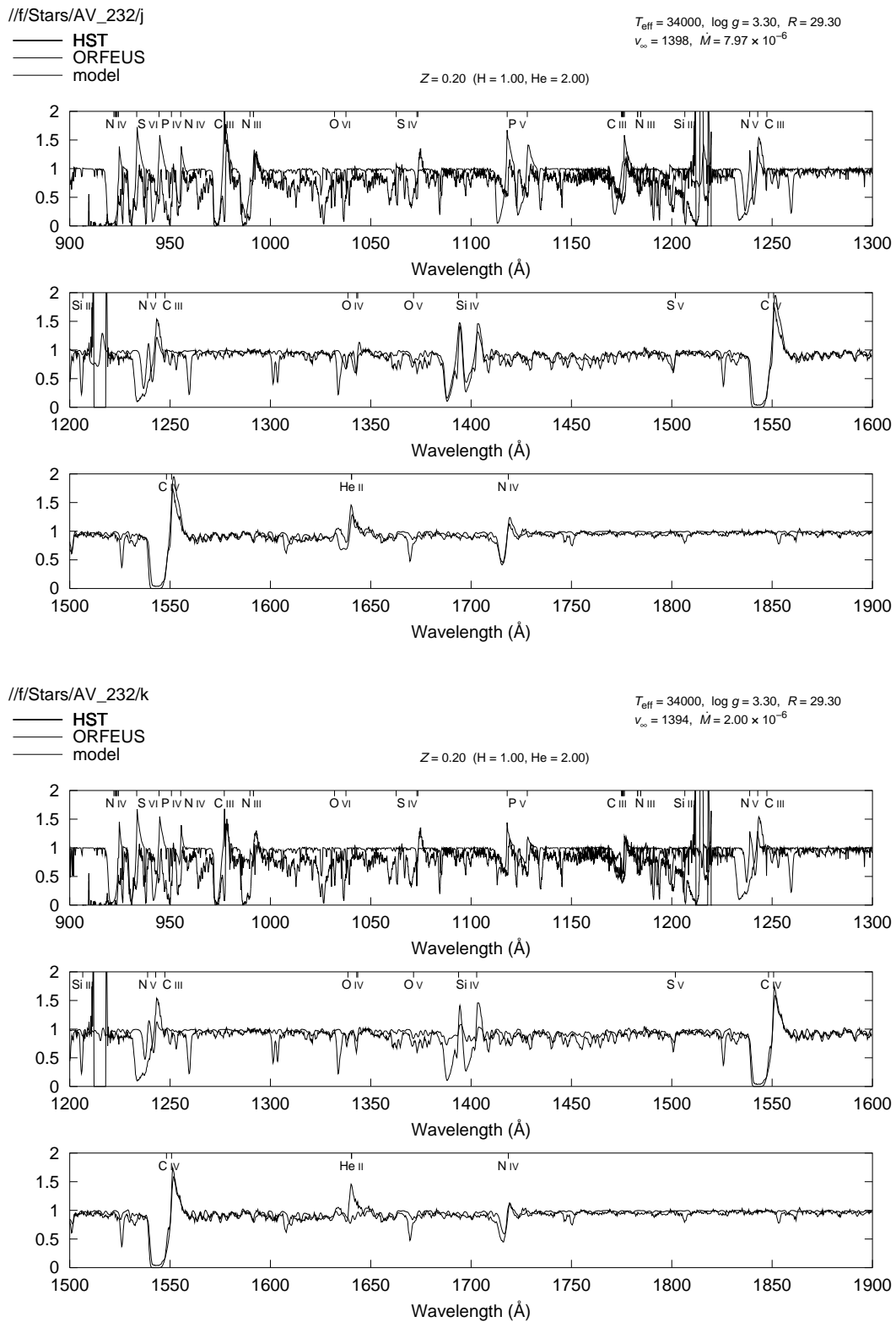


FIGURE 4-5. — Influence of the mass loss rate on the spectrum of AV 232. Top: $\dot{M} = 8 \times 10^{-6} M_{\odot}/\text{yr}$, bottom: $\dot{M} = 2 \times 10^{-6} M_{\odot}/\text{yr}$.

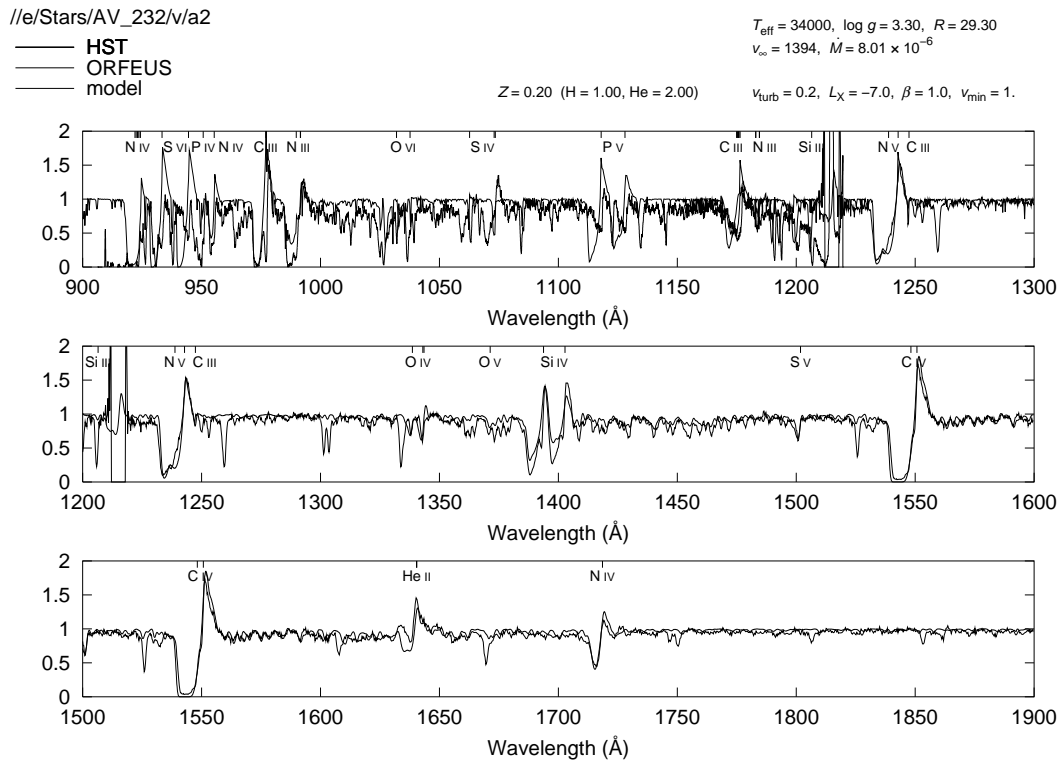


FIGURE 4-6. — The 34000 K model with the higher mass loss rate $\dot{M} = 8 \times 10^{-6} M_{\odot}/\text{yr}$ (see figure 4-5) with shocks included.

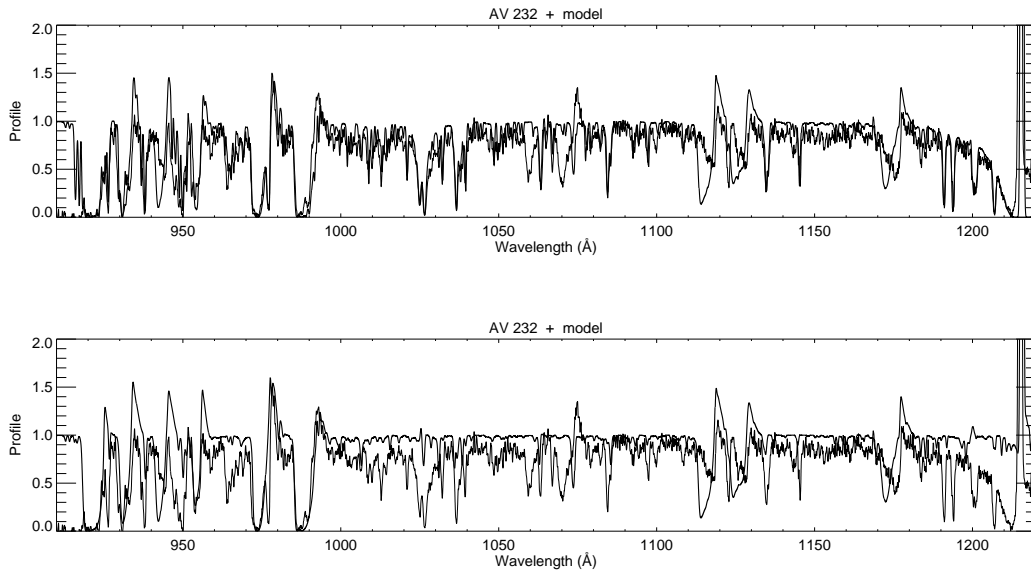


FIGURE 4-7. — Synthetic spectrum of AV 232 in the ORFEUS spectral range with (top) and without (bottom) a superposed interstellar absorption line model. The observed spectral features in the vicinity of the O VI resonance line near 1030 \AA are essentially purely interstellar.

Neither does a global increase of the metallicity have a significant influence on the sulfur ionization balance, as shown in figure 4-4, where we have increased the metallicity to $Z = 0.5 Z_{\odot}$. (The photospheric lines from 1550 to 1650 Å become too strong with this metallicity at this temperature.) However, we cannot at the moment rule out the possibility that some elements that do not have strong lines in the observable UV range (such as Ne or Mg), and whose abundances therefore cannot be determined directly from the UV spectrum, may show significant deviations from the solar abundance pattern with a non-negligible blocking influence on the EUV radiation field. Although no systematic investigation of the effects of abundance changes of these elements on the blocking behavior has been performed here, such an analysis might nonetheless prove useful in constraining the abundances of these elements.

From our analysis we can draw a number of possible conclusions. The first is that our treatment of line blocking is quantitatively not completely adequate, despite our efforts for a selfconsistent solution. However, since we were able to reach nearly perfect agreement with the observed spectrum in our analysis of α Cam, we regard it as rather unlikely that this is a principal problem of our models. The second is that the discrepancies encountered are the result of abundances deviating considerably from the usually-assumed solar pattern. This is the most probable explanation for our findings above, in particular because the analysis clearly shows that the iron and nickel lines are best reproduced with abundances corresponding to about 0.5 solar, whereas the lighter elements forming the wind lines can be adequately described with an abundance of about 0.2 solar. Finally, a third possibility is that we see some physical effect at work in the wind of this star which is not considered in the models. What this might be is not clear at the moment, but clumping in the wind (resulting in a lower ionization balance due to the higher densities) as a result of the intrinsic dynamic instabilities of the driving mechanism may be a reasonable working hypothesis. Future work must show whether this scenario can quantitatively explain the observed line strengths.

Shock parameters. With the higher effective temperature of AV 232 compared to α Cam, the Si III 1207 Å and C III 1247 Å lines that gave us a strong constraint on the shocks in α Cam are not available to us here. However, we note that with the chosen $T_{\text{eff}} = 34000$ K most of the unsaturated wind lines of the lower ionization stages are already on the weak side, and thus the additional influence of shock radiation cannot be large, since this would weaken these lines even further. This is additionally confirmed by the fact that practically no stellar O VI line is observable (see figure 4-7, which shows that the spectral features in the vicinity of the O VI resonance line near 1032, 1038 Å are essentially purely interstellar). We determine a maximum shock strength of $\log L_X = -7.0$ with a turbulence parameter $u_{\infty}/v_{\infty} = 0.2$ (and default values $\gamma = 1$, $m = 1$), which is sufficient to reproduce the observed strength of the N V resonance line, but which has no significant other effect on the remaining part of the UV spectrum (figure 4-6).

5

Investigation of stellar parameters as a constraint for the SEDs of massive stars

The models presented in the previous sections have been computed using pre-specified mass loss rates and terminal velocities — i.e., the line force parameters in the hydrodynamics have been adjusted so as to yield the desired mass loss rate and terminal velocity, without verifying whether these were actually compatible with the radiative force produced in the wind under these conditions. In this chapter we will extend the modelling procedure to also include this constraint of hydrodynamic consistency. As discussed in section 3.1, this requires an outer loop in which hydrodynamics and NLTE/line force calculation are iterated to consistency. With this constraint, the wind parameters become functions of the stellar parameters, and the number of free parameters of the model is reduced.

We will begin by demonstrating, using a small grid of models, how the wind parameters and the resulting UV spectra vary as function of the stellar parameters. Then we will verify the theoretically predicted metallicity dependence of the wind-momentum–luminosity relation with our consistent hydrodynamic models. Finally, we apply the modelling procedure to a large sample of Galactic O stars and compare the wind parameters we determine with our method to those derived in another study (Repolust et al. 2003) from an analysis of optical lines.

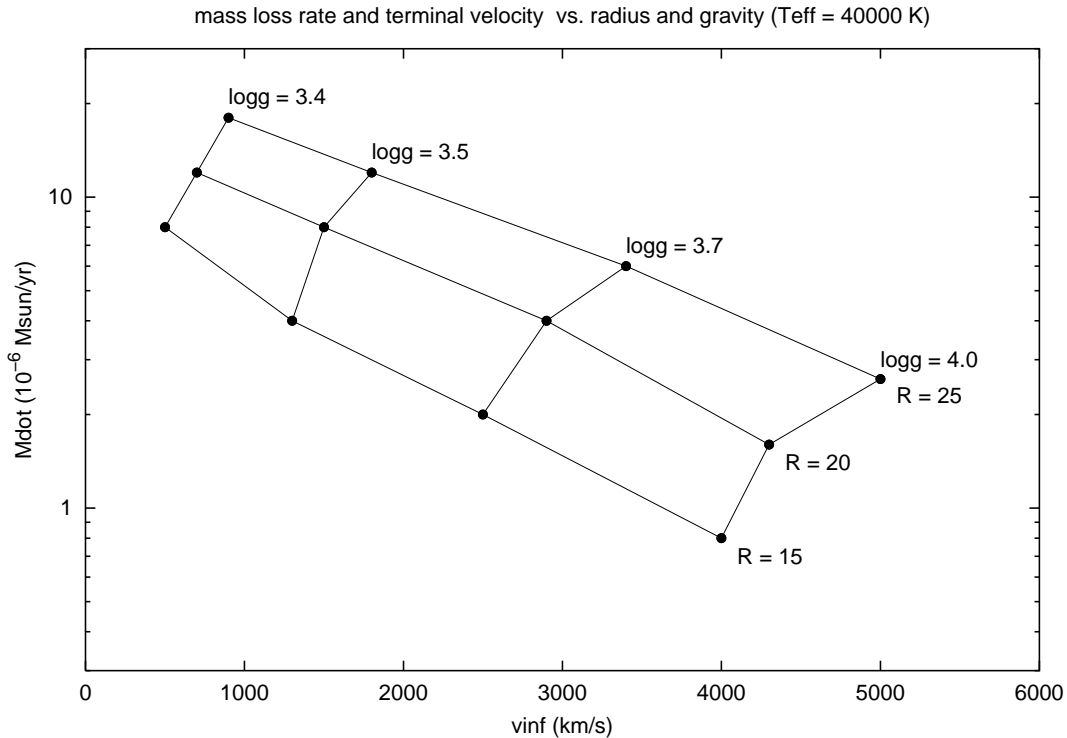


FIGURE 5-1. — Mass loss rate \dot{M} and terminal velocity v_∞ from dynamically consistent models in dependence of radius R and surface gravity $\log g$.

5.1. Dependence of \dot{M} and v_∞ on $\log g$ and R

Consistent hydrodynamics provides the link between the stellar parameters (T_{eff} , $\log g$, R) and the wind parameters (v_∞ , \dot{M}); it is the interplay of the NLTE model and the hydrodynamics that determines the appearance of the UV spectrum. Computing the wind dynamics consistently permits not only the determination of the wind parameters from given stellar parameters, but conversely makes it possible to obtain the stellar parameters from the observed UV spectrum alone. Although this idea is in principle not new (see Pauldrach et al. 1988, Kudritzki et al. 1992), only the new generation of models — in conjunction with the high-resolution synthetic UV spectra — has reached the degree of sophistication that makes such a procedure useful in practice (cf. Hoffmann and Pauldrach 2003; appendix B).

To illustrate the effect of a change in radius and gravity on the spectra and wind parameters, we have calculated a grid of models²³ with $T_{\text{eff}} = 40000 \text{ K}$ and consistent wind dynamics, using radii from 15 to $25 R_\odot$ and $\log g$ from 3.4 to 4.0. The resulting mass loss rates and terminal velocities are plotted in figure 5-1, the corresponding UV spectra are shown in figure 5-2. In principle, one can now immediately read off the stellar parameters simply by comparing an observed UV spectrum to such a grid at the appropriate effective temperature. Note in particular the sensitive dependence of the terminal velocity v_∞ on the surface gravity $\log g$ and thus on the mass M . Given that v_∞ is a quantity directly measurable from the UV spectrum, this dependence provides an extremely useful diagnostic tool (cf. appendix E).

²³ Note, however, that the parameter grid here was chosen strictly to demonstrate the behavior of the mass loss rate and the terminal velocity, and thus the appearance of the spectrum. Not all combinations will necessarily also occur in nature; in particular, the combination high- $\log g$, high- R gives unrealistically high stellar masses.

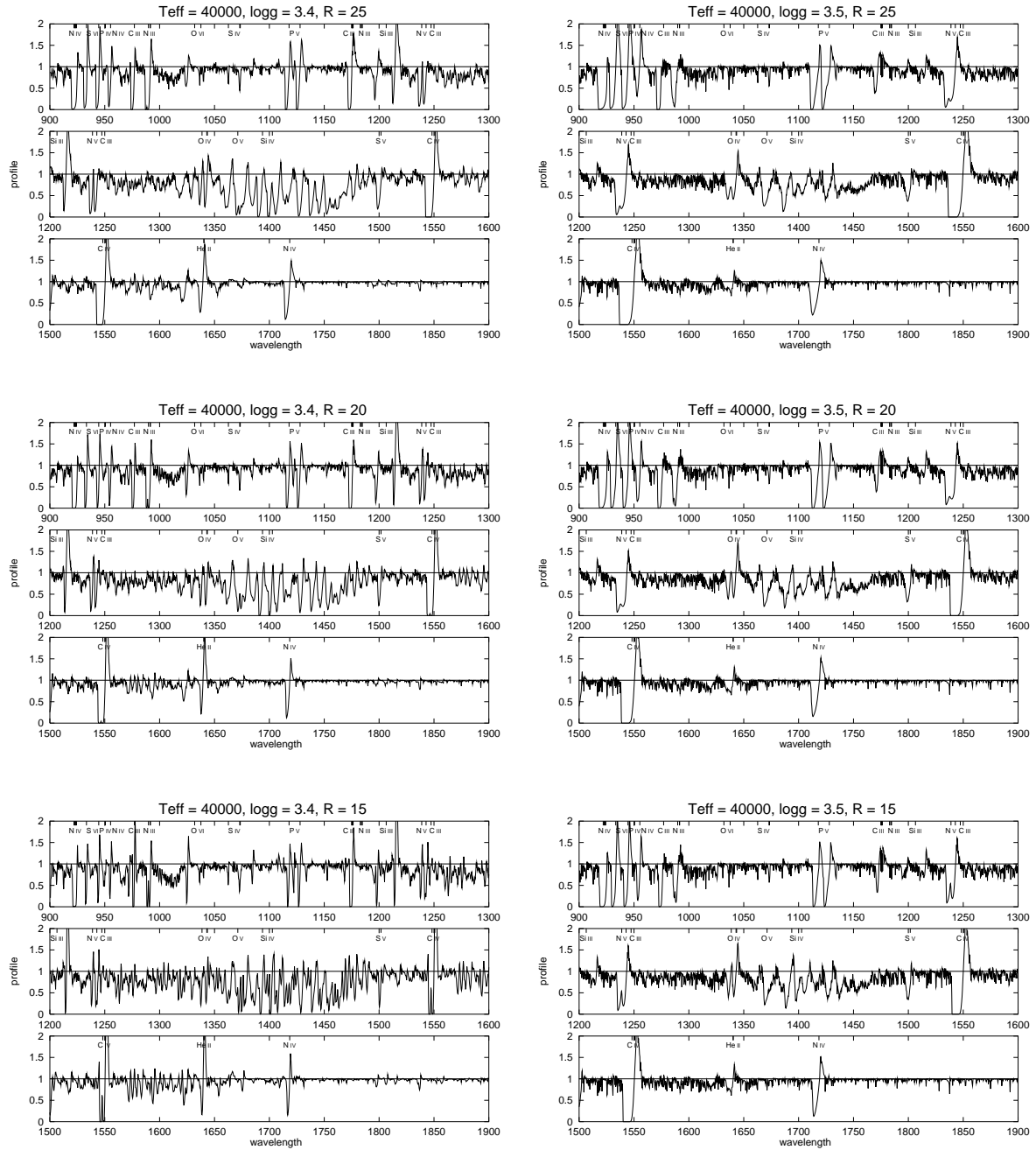


FIGURE 5-2. — Dependence of the UV spectrum on radius R and surface gravity $\log g$ for dynamically consistent models at a fixed temperature $T_{\text{eff}} = 40000$ K. R increases toward the top, $\log g$ increases to the right. The stellar parameters and the resulting wind parameters are given in table 5-1.

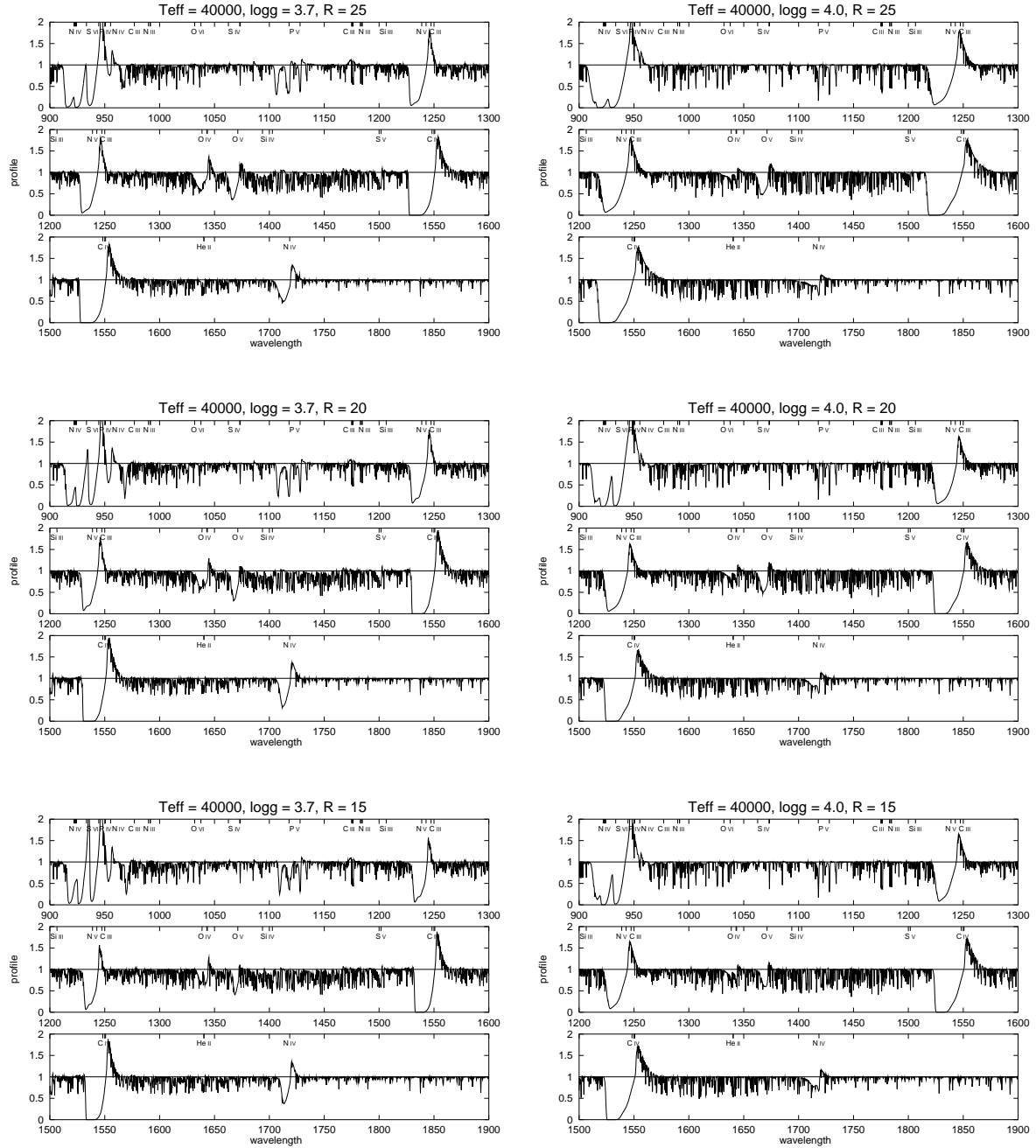


FIGURE 5-2. (continued) — Dependence of the UV spectrum on radius R and surface gravity $\log g$ for dynamically consistent models. (Stellar parameters and resulting wind parameters are given in table 5-1.)

TABLE 5-1. — Parameters of the model grid stars of figures 5-1 and 5-2.

T_{eff} (K)	$\log g$ (cm/s^2)	R (R_{\odot})	M (M_{\odot})	$\log \frac{L}{L_{\odot}}$	Γ	v_{esc} (km/s)	\dot{M} ($10^{-6} M_{\odot}/\text{yr}$)	v_{∞} (km/s)
40000.	3.40	15	21	5.72	0.66	420	8	500
40000.	3.50	15	26	5.72	0.51	570	4	1300
40000.	3.70	15	41	5.72	0.32	840	2	2500
40000.	4.00	15	82	5.72	0.16	1300	0.8	4000
40000.	3.40	20	37	5.97	0.65	500	12	700
40000.	3.50	20	46	5.97	0.51	660	8	1500
40000.	3.70	20	73	5.97	0.32	970	4	2900
40000.	4.00	20	146	5.97	0.16	1500	1.6	4300
40000.	3.40	25	57	6.16	0.65	560	18	900
40000.	3.50	25	72	6.16	0.51	730	12	1800
40000.	3.70	25	114	6.16	0.32	1100	6	3400
40000.	4.00	25	228	6.16	0.16	1700	2.6	5000

5.2. Dependence of wind momentum on metallicity

Due to the driving mechanism of the wind — transfer of momentum from the radiation field to the gas via photon absorption in metal lines — the mechanical momentum of the wind flow ($v_{\infty}\dot{M}$) is mostly a function of photon momentum (L/c) and is therefore related to the luminosity. Thus, the theory of radiation-driven winds predicts, for fixed abundances, a simple relation between the quantity $\dot{M}v_{\infty}$, which has the dimensions of a momentum loss rate, and the stellar luminosity (Lamers and Leitherer 1993; Puls et al. 1996):

$$\dot{M}v_{\infty} \sim R^{-1/2}L^{1/\alpha'}, \quad (5.1)$$

where α' , related to the power law exponent of the line strength distribution function, is ≈ 0.6 . It is practical to plot the log of $D = \dot{M}v_{\infty}R^{1/2}$ (known as the “modified wind momentum”) as a function of $\log L$. In this kind of plot the theory predicts, in first approximation, a linear relation, which is indeed followed by all kinds of massive hot stars (see, e.g., figure 5-4). The significance of this “wind-momentum–luminosity relation” lies in the fact that with observed wind-momentum rates of supergiant winds it allows for a determination of distances (Kudritzki et al. 1995) and thus has the potential to become an independent alternative to using Cepheids as distance indicators on the intermediate distance scale up to the Virgo and Fornax clusters.

However, since the winds are driven by metal lines, it is obvious that the wind strengths will also depend on metallicity. This plays a significant role, for example, in applying the wind-momentum–luminosity relation to distance measurements of extragalactic objects with a predominantly different metallicity. To avoid a systematic error in the derived distance the metallicity dependence of the wind momentum must be taken into account. Theory predicts (e.g., Kudritzki, Pauldrach, and Puls 1987; Puls et al. 2000) that the wind momentum should scale with metallicity Z as

$$D \sim Z^{(1-\alpha)/\alpha'} \quad (5.2)$$

where $\alpha - 2$ is the exponent of the line strength distribution function and α' is the reciprocal of the slope of the wind-momentum–luminosity relation.

To verify whether this dependence is reproduced by our detailed numerical simulations, we have computed the wind momenta for a small grid of models — a supergiant and a dwarf sequence with temperatures from 30 000 K to 50 000 K — at two different metallicities, namely solar and one-fifth solar metallicity. The stellar parameters were chosen so as to reproduce the observed parameters for these types of stars while at the same time covering a large range in luminosities.

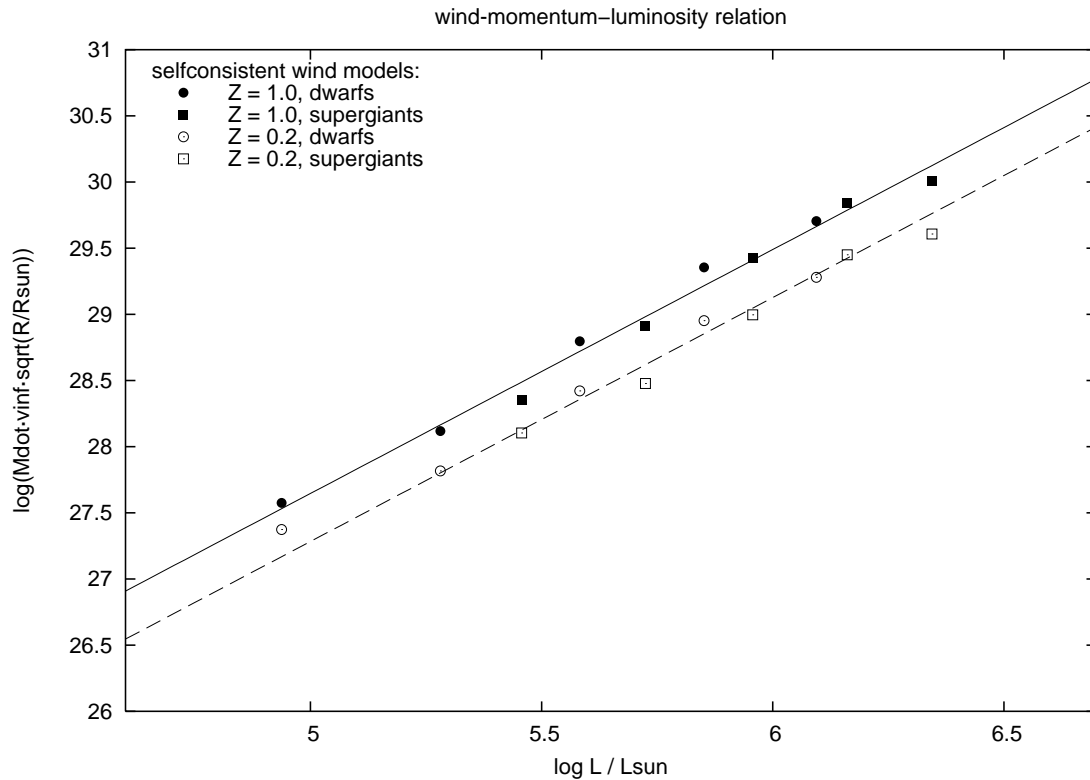


FIGURE 5-3. — The wind-momentum–luminosity relation for different metallicities.

Figure 5-3 shows the resulting wind-momentum–luminosity relation. Filled and open symbols represent the calculated wind momenta for solar metallicity and one-fifth solar metallicity stars, respectively. The solid line is a linear fit to the calculated wind momenta for solar metallicity, and the dashed line is this relation scaled using equation 5.2 with a value of $Z = 0.2$ (and using the representative value $\alpha = 2/3$, cf. Puls et al. 2000). As can be seen from the figure, there is excellent agreement between the calculated wind momenta of the models with $Z = 0.2 Z_{\odot}$ and this scaled relation (cf. Hoffmann, Pauldrach, and Puls 2003; appendix C).

5.3. Models for a sample of Galactic O stars

Before we can reliably use our method to determine stellar masses and radii we need to verify if the results given by the models are in agreement with the parameters derived from other observations. The large sample of galactic O stars from Puls et al (1996) has recently been reanalyzed with an improved version of the original code, now incorporating an approximate treatment of line blocking and blanketing (Repolust et al. 2003). We have computed hydrodynamically consistent models for the stellar parameters derived in this analysis.²⁴

²⁴ A major caveat with regard to our hydrodynamic computations, however, is that solar abundances (except for helium, for which the values from Repolust et al. (2003) have been taken) are used throughout. While this permits a strictly differential analysis with regard to the different stellar parameters of the sample, it might give wrong results for individual objects, as the mass loss rates depend on the metallicity, and, as we have seen from our analysis of α Cam in chapter 4, the assumption of solar abundances is not necessarily generally applicable even for galactic stars. Another point is that shocks have not been considered, which might influence the interpretation of the UV spectra, since it is not a priori clear which lines will be affected and to what extent.

TABLE 5-2. — Parameters of the sample stars. Radii are in solar radii, mass loss rates in $10^{-6} M_{\odot}/\text{yr}$, terminal velocities in km/s. The wind performance η is defined as $v_{\infty}\dot{M}/(L/c)$. $Y_{\text{He}} = n_{\text{He}}/n_{\text{H}}$ is the number density of helium relative to hydrogen.

Star	classification	T_{eff}	$\log g$	R	Y_{He}	Γ	observed	optical analysis		selfconsistent models		
							v_{∞}	\dot{M}	η	v_{∞}	\dot{M}	η
HD 93129A	O2 If*	42500	3.7	22.5	0.10	0.41	3200	26.30	2.78	2750	8.82	0.80
HD 93128	O3 V ((f))	46500	4.0	10.4	0.10	0.30	3100:	2.64	0.88	3300	1.71	0.61
HD 93250	O3 V ((f))	46000	3.95	15.9	0.10	0.32	3250	3.45	0.54	4050	4.04	0.79
HD 66811	O4 I(f)	39000	3.55	19.4	0.20	0.38	2250	8.80	1.25	2100	3.81	0.50
HD 303308	O4 V ((f ⁺))	41000	3.9	11.5	0.075	0.23	3100	1.63	0.74	2900	0.90	0.38
HD 14947	O5 If ⁺	37500	3.45	16.8	0.20	0.40	2350	8.52	1.93	1550	2.88	0.44
HD 15558	O5 III(f)	41000	3.8	18.2	0.10	0.28	2800	5.58	0.92	3200	2.82	0.53
HD 193682	O5 III(f)	40000	3.6	13.1	0.20	0.37	2800:	1.73	0.60	1700	2.11	0.45
HD 15629	O5 V ((f))	40500	3.7	12.8	0.08	0.35	3200	1.28	0.50	1850	1.89	0.43
HD 210839	O6 I(n) fp	36000	3.55	21.1	0.10	0.30	2250	6.85	1.12	2900	1.48	0.31
HD 190864	O6.5 III(f)	37000	3.55	12.3	0.15	0.32	2500	1.39	0.67	2050	0.79	0.31
HD 192639	O7 Ib (f)	35000	3.45	18.7	0.20	0.31	2150	6.32	1.42	2900	0.85	0.26
HD 193514	O7 Ib (f)	34500	3.3	19.3	0.10	0.45	2200	3.48	0.79	700	2.54	0.18
HD 24912	O7.5 III(n)((f))	35000	3.5	14.0	0.15	0.29	2450	1.08	0.50	2700	0.45	0.23
HD 203064	O7.5 III:n ((f))	34500	3.5	15.7	0.10	0.28	2550	1.41	0.56	2850	0.49	0.22
HD 217086	O7 V n	36000	3.5	8.6	0.15	0.32	2550	0.23	0.26	1500	0.31	0.21
HD 13268	ON8 V	33000	3.25	10.3	0.25	0.37	2150	0.26	0.24	850	0.45	0.17
HD 210809	O9 Iab	31500	3.1	21.2	0.14	0.47	2100	5.30	1.37	950	1.77	0.22
HD 207198	O9 Ib	33000	3.45	16.6	0.12	0.26	2150	1.79	0.64	2650	0.42	0.19
HD 30614	O9.5 Ia	29000	2.97	32.5	0.10	0.48	1550	6.04	0.69	900	2.60	0.17
HD 209975	O9.5 Ib	32000	3.2	22.9	0.10	0.42	2050	2.15	0.43	1200	1.45	0.17
HD 18409	O9.7 Ib	30000	2.95	16.3	0.14	0.55	1750:	1.02	0.45	350	1.94	0.17
HD 191423	O9 III:n*	32500	3.35	12.9	0.20	0.29	1150	0.41	0.14	1600	0.33	0.16
HD 149757	O9 V	32000	3.65	8.9	0.17	0.14	1550	0.18	0.18	2950	0.06	0.12

Table 5-2 list the stellar and wind parameters derived from the optical analysis as well as our wind parameters computed with the models. Note that the effective temperatures of the hotter objects have been considerably revised (to smaller values) by inclusion of line blocking and blanketing in the analysis compared to the earlier analysis by Puls et al. (1996). The radii have changed slightly because of new distance calibrations and slightly modified visual fluxes from the models due to blanketing effects. (The terminal velocities have been derived from UV spectra, except for HD 93128, HD 193682, and HD 18409, where no UV spectra are available; the terminal velocities of these three stars were estimated by Puls et al. (1996) on basis of the spectral type.)

The most conspicuous result given in table 5-2 is that the optical analysis suggests very high wind performance numbers for several of the objects. (The wind performance number $\eta = \dot{M}v_{\infty}/(L/c)$ is the ratio of mechanical momentum of the wind flow to photon momentum of the radiation field, and is a measure of the “efficiency” of the radiative driving force.) So far, no theoretical mechanism has been found to justify such high performance numbers, and our detailed numerical simulations also cannot confirm these high performances.²⁵ A similar investigation will now need to verify whether such a result is also obtained for a corresponding sample of stars in the Magellanic clouds, where the relative uncertainties in the distances are significantly smaller. If not, a systematic error in the radius determinations of the supergiants might be the reason for this discrepancy. The hypothesis of Puls et al. (1996) that the discrepancy is due to inadequate treatment of multi-line effects in the wind models is not confirmed, since multi-line effects are naturally considered as part of our procedure.

²⁵ We note that Vink et al. (2000) claim to achieve performances $\eta > 1$ in their models already for normal O stars with $\log L/L_{\odot} \geq 6$ and $T_{\text{eff}} \geq 40000$ K. However, their method is not completely consistent in that the mass loss rates are derived from global considerations, without requiring that the hydrodynamic equations are fulfilled at each point in the wind.

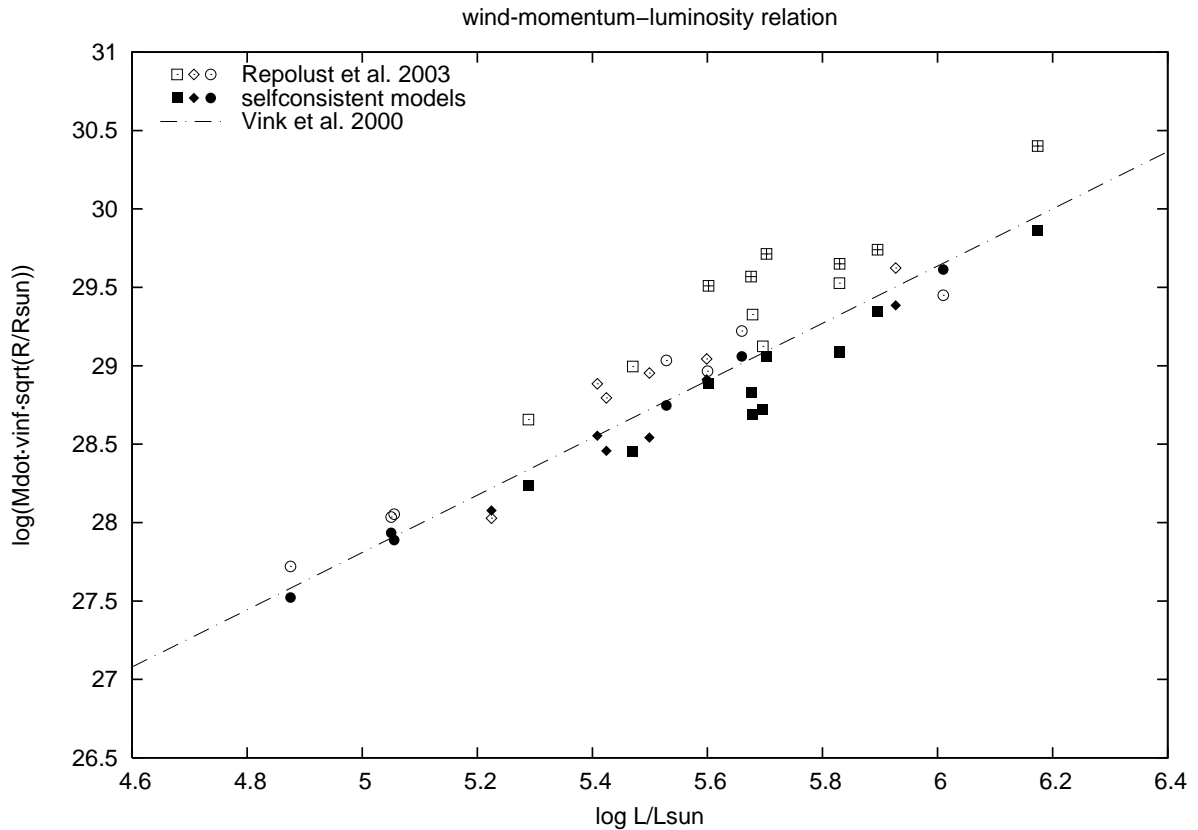


FIGURE 5-4. — Wind momenta based on the parameters given by Repolust et al. (2003) (open symbols) compared to those resulting from consistent wind dynamics based on the same stellar parameters (filled symbols). (Parameters given in table 5-2; luminosity classes are denoted as: I – squares; III – diamonds; V – circles.) The objects with anomalously high wind performances $\eta > 1$ are marked with a “+”. For comparison we have also shown the relation derived theoretically by Vink et al. (2000) using an entirely different approach.

One of the puzzling results in the study of the wind-momentum–luminosity relation (WLR) of O stars up to now has been the fact that supergiants seem to follow a distinct WLR different from that of giants and dwarfs (Puls et al. 1996), a finding which cannot be explained by theory under the usual assumptions (i.e., that the winds represent a smooth, stationary, spherically symmetric flow). Although the separation between the supergiants and the other luminosity classes seems to have decreased with the new parameters of Repolust et al. (2003) compared to the earlier values of Puls et al. (1996), a plot of the wind momenta (figure 5-4) still shows a number of distinct “outliers”, which are associated with very high wind performance numbers. In contrast, the wind momenta from the hydrodynamic models do not show a division between the luminosity classes. This is the same result as had already been found by Puls et al. (1996) using comparable hydrodynamic calculations; a similar theoretical result was found by Vink et al. (2000) using a completely different method to compute mass loss rates of a grid of models.

Based on the fact that a characteristic property of the outliers is a strong $H\alpha$ emission, Puls et al. (2003) (based in part on preliminary calculations of the models computed here) and again Repolust et al. (2003) have proposed that the winds of these objects may be clumped in the $H\alpha$ forming region, with subsequent stronger emission in $H\alpha$ than in the case of an unclumped wind.²⁶ Plotting the performance numbers (instead of the modified wind momenta) in a more physically motivated diagram, namely as

²⁶ Since $H\alpha$ is a recombination line in the wind, the emission is proportional to the square of the density.

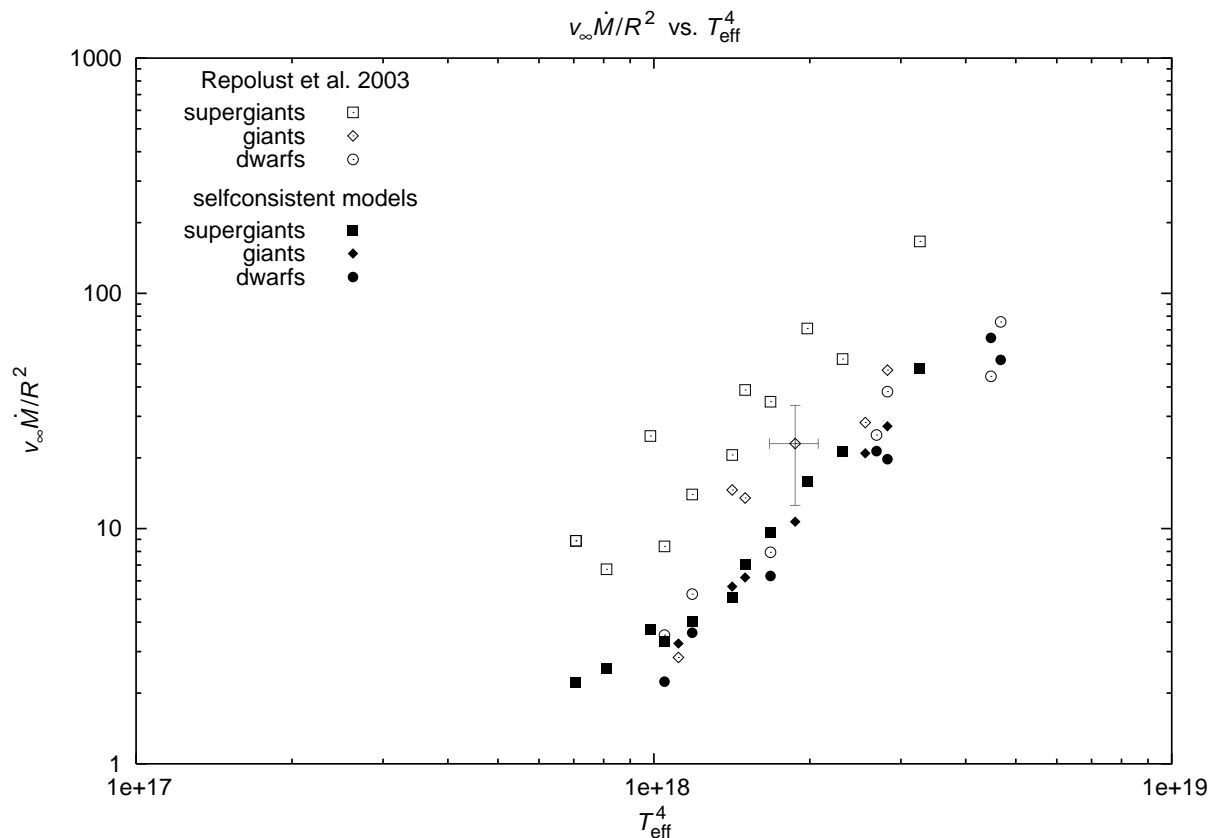


FIGURE 5-5. — Wind performances plotted as momentum loss rate per unit surface area vs. flux. The models (filled symbols) follow a unique relation for all luminosity classes, whereas the optical analysis (open symbols) would indicate higher performances for giants and supergiants. A typical error bar for the observed values (Repolust et al. 2003) is also shown.

$\dot{M}v_{\infty}/R^2$ vs. T_{eff}^4 , which is essentially the momentum loss rate per unit surface area vs. the flux,²⁷ however, reveals that the discrepancy is not limited to supergiants, but rather that there is a continuous trend towards higher performance numbers from dwarfs to supergiants (figure 5-5). This trend is not reproduced by the models, which instead follow the relation found for the dwarfs. (The scatter in the models represents the intrinsic uncertainty of the method with respect to parametrization of the force multiplier.)

To verify if there is further evidence supporting the clumping hypothesis we have computed two series of models and compared the resulting synthetic UV spectra to the observed UV spectra. (The spectra are given in appendix A.) For the first series, the line force parameters have been adjusted to yield approximately the observed terminal velocity and the mass loss rate suggested by the optical analysis of Repolust et al. (2003), regardless of whether these are dynamically consistent with the stellar parameters derived from this analysis. For the second series, the wind dynamics have been iterated to consistency with the stellar parameters.

We have at this stage not attempted to fit the terminal velocities of the consistent models to the observed ones, as this would require changes in the gravities and/or radii.²⁸ However, in those cases where we

²⁷ The astrophysical term *flux* is in common physical terms actually a *flux density*. The *luminosity* corresponds to the total flux.

²⁸ Note that the optical analysis cannot intrinsically determine the radii; they are based on distances given in the literature, observed visual magnitudes, and the optical fluxes from the models. In contrast, the principal strength of the dynamically consistent models is that radii and gravities can in principle be derived from the UV spectra alone, since both the mass loss rate and the terminal velocity depend on radius and surface gravity, which can therefore be

find a slightly different terminal velocity but an about equal wind performance number, we will not consider this a real discrepancy to the optical analysis, since we have seen from the grid in section 5.1 that a small change in $\log g$ — on the order of about 0.1, within the error bars of the optical analysis — can usually bring the terminal velocities in agreement without significantly changing the performance number (additional test calculations have confirmed this also at other temperatures).

From the comparison of the spectra (see appendix A) we draw the following conclusions. Considering the global ionization balance, in particular with regard to the photospheric iron and nickel line forest, we find no contradiction with the effective temperatures from the “new” optical analysis of Repolust et al. (2003). On the other hand, without inclusion of X-rays, C IV is almost always saturated, thus prohibiting any further conclusions from this line. N V in cooler stars (below 35000 K) is much too weak without X-rays, and (as is well known, cf. Pauldrach et al. 1990) Si IV reacts strongly to variations in \dot{M} . Considering in particular the subset of models where the selfconsistent terminal velocity agrees with the observed one, we find that for those objects where the observed and the theoretical mass-loss rates do not agree, Si IV seems to favor the “observed” one, whereas S V and the lines formed close to the photosphere (mainly Fe, Ni) seem to be consistent with a lower value. This is the behavior that would be expected from a clumped wind, but given the fact that all models have been computed using the assumption of solar abundances, it is not clear to what extent these findings can also be an abundance effect.

5.4. Summary

Using a grid of hydrodynamically consistent models we have briefly discussed the dependence of the UV spectrum on the stellar parameters, and we have verified the theoretically predicted metallicity dependence of the wind-momentum–luminosity relations with our models. For a large grid of Galactic O stars we have computed consistent hydrodynamic models based on the stellar parameters determined by Repolust et al. (2003) from an analysis of optical spectra. With the exception of a few extreme cases, the wind momenta computed with our hydrodynamic models agree with those from the optical analysis to within about a factor of two. In contrast to the findings of Repolust et al. (and similar earlier investigations), however, the hydrodynamic models do not show evidence of different wind-momentum–luminosity relations for supergiants and giants/dwarfs. Based on the fact that a characteristic property of the “outliers” is a strong H α emission, Puls et al. (2003) and Repolust et al. (2003) have proposed that the winds of these objects may be clumped in the H α forming region, with subsequent stronger emission in H α than in the case of an unclumped wind. This scenario is compatible with the appearance of the Si IV and S V/Fe/Ni lines in the synthetic UV spectra presented here.

constrained from a fit to the observed UV spectrum (cf. section 5.1). An example of this type of application is given in appendix E.

6

Spectral energy distributions (SEDs) for massive stars and evolving stellar clusters

One of the most important characteristics of hot stars is that they emit a large fraction of their total energy output as ionizing radiation in the EUV. This radiation ionizes and heats the surrounding interstellar material — generally the remains of the gas clouds from which the stars have formed (often in larger associations) — producing so-called H II regions (i.e., regions of ionized hydrogen) around these objects, and the *spectral distribution* of the ionizing radiation emitted from the stars determines the ionization ratios of the elements observed in the H II regions. Most of the EUV radiation absorbed by the ionized gas is reemitted in comparatively few emission lines — recombination lines of H and He, and collisionally excited lines of mostly O, Ne, N, C, S, and Ar — and due to the resulting high intensities in these emission lines the H II regions can be detected even at high redshifts. The analysis of the emission lines, via models which simulate the microphysical processes occurring in the ionized material, is an important tool to derive information about the stellar content of the ionizing sources.

A key input for these simulations are the spectral energy distributions of the ionizing radiation emitted by the stars. Because these ionizing fluxes are not directly observable due to absorption by interstellar hydrogen, they must be provided by stellar atmospheric models. In sections 6.1 and 6.2 we discuss the construction of a large grid of O star models of solar metallicity to be used for this purpose, and we compute the corresponding spectral energy distributions of these stars. Moreover, massive stars often form in clusters containing hundreds to thousands of individual massive stars; the SEDs of these clusters change with time as the stellar population ages. Such scenarios will be considered in section 6.3.

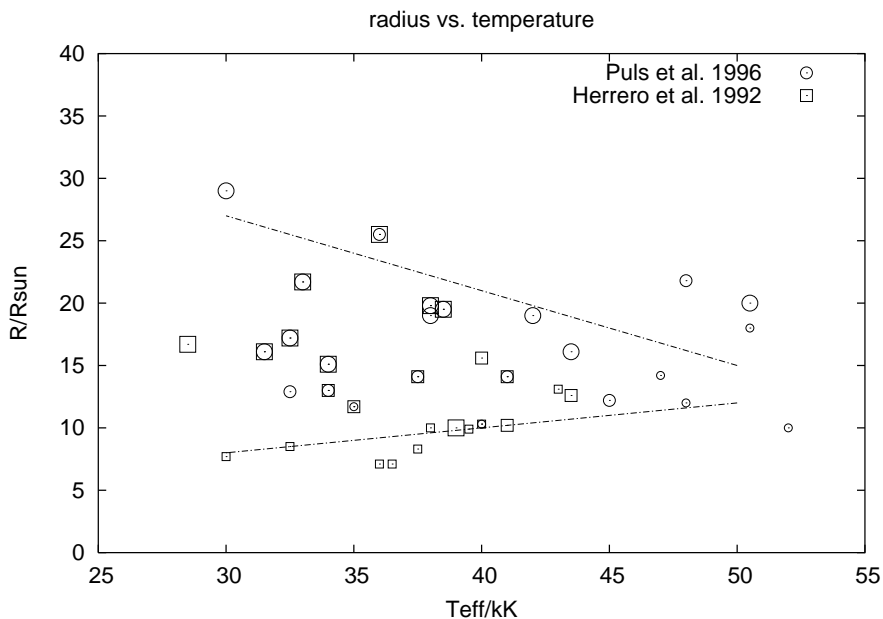


FIGURE 6-1. — Empirical stellar radii based on data derived by Herrero et al. (1992) (squares), and Puls et al. (1996) (circles). Small, medium, and large symbols represent dwarf, giant, and supergiant stars, respectively.

6.1. Basic parameters of the grid models

We have constructed a detailed grid of OB star model atmospheres for all luminosity classes, from main-sequence dwarfs to supergiants. We adopt solar metals abundances as compiled by Grevesse and Sauval (1998). The input parameters for each model are the effective temperature T_{eff} , surface gravity $\log g$, and stellar radius R , as well as the terminal wind velocity v_{∞} and mass-loss rate \dot{M} .

We choose parameter values based on observations. Herrero et al. (1992) and Puls et al. (1996) have determined the surface gravities, effective temperatures, and stellar radii for samples of OB stars, via the “spectral fitting” method. In these studies, $\log g$ and T_{eff} were determined for individual stars by matching spherical NLTE (but non-blanketed) atmosphere models to the observed hydrogen and helium absorption line profiles in the stellar spectra. Given the best fitting SEDs and predicted surface radiation flux densities, the radii were then inferred given the observed stellar (V-band) luminosities, following the technique introduced by Kudritzki (1980).

In figure 6-1 we display $\log g$ vs. T_{eff} and R vs. T_{eff} for the samples of O and B stars analyzed by Herrero et al. (1992) and Puls et al. (1996). It is evident that the OB stars of various types occupy well-defined regions in these diagrams. The empirical data allow us to define relations for “generic” dwarfs and supergiants (indicated by the dashed lines) which define the approximate boundaries, in these diagrams, within which OB stars of all luminosity classes are known to exist.

Our model atmosphere grid covers the full range of parameters within the “triangular wedge” that is defined by the dwarf and supergiant sequences in the $\log g$ vs. T_{eff} diagram (see figure 6-1 (a)). We computed atmospheres for T_{eff} ranging from 25 to 55 kK, in steps of 1 kK, and surface gravities $\log g$ (cm/s^2) ranging from (as low as) 3 to 4, in steps of 0.2 dex. For each T_{eff} and $\log g$ pair we set the stellar radius via linear interpolation, using $\log g$ as the independent parameter, between the dwarf and supergiant radii as specified by our dwarf and supergiant relations. The surface gravities, stellar radii, and effective temperatures of our models are displayed in figure 6-2 (a) and (b). The associated spectroscopic masses $M = gR^2/G$ and bolometric luminosities $L = 4\pi R^2 \sigma T_{\text{eff}}^4$ for our models are shown in figure 6-2 (c) and (d).

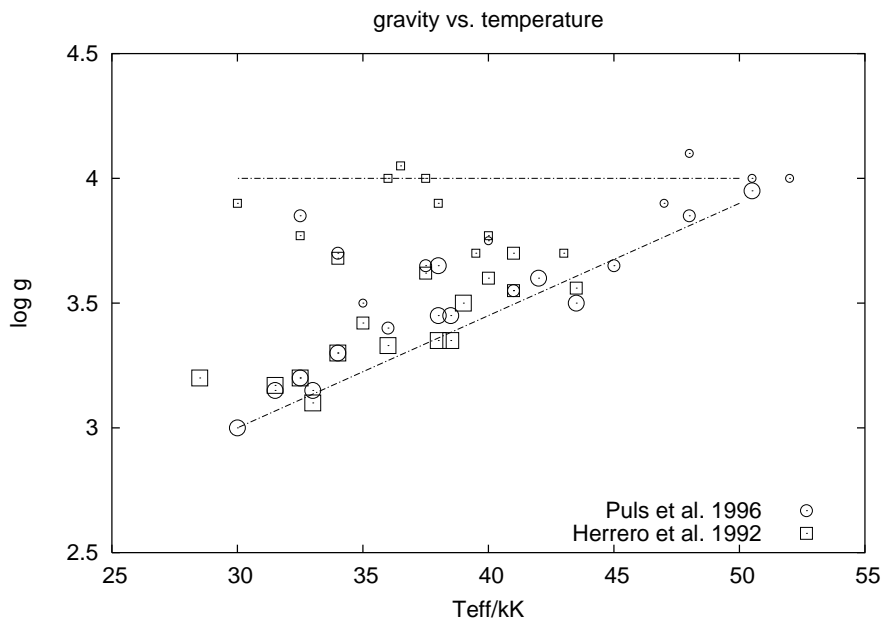


FIGURE 6-1. (continued) — Empirical stellar surface gravities based on data derived by Herrero et al. (1992) (squares), and Puls et al. (1996) (circles). Small, medium, and large symbols represent dwarf, giant, and supergiant stars, respectively.

In principle, the wind parameters v_∞ and \dot{M} are direct functions of the stellar parameters T_{eff} , R , and $\log g$, via the dependence of the radiative acceleration on the radiation field and the occupation numbers. Here we have, however, not attempted a selfconsistent solution of hydrodynamics and NLTE model, but instead adopt the wind parameters derived empirically from the observations (i.e., we adjust the line-force parameters k , α , and δ so that the solution of the hydrodynamic equation yields the observed v_∞ and \dot{M}).

The terminal velocities v_∞ of the winds of O and B stars are directly observable quantities (e.g., Lamers and Morton 1976), although the observed samples show a relatively large scatter as function of T_{eff} , even within the same luminosity class (Prinja, Barlow, and Howarth 1990; Kudritzki and Puls 2000). We adopt average relations based on these observations, which we show in figure 6-2 (e). With the stellar parameters and the terminal velocity specified, we can derive the mass loss rates \dot{M} from the empirical wind-momentum–luminosity relation (Kudritzki et al. 1995). This relation states that the “modified wind momentum” $D = \dot{M}v_\infty R^{1/2}$ is, to first approximation, a simple power-law function of the stellar luminosity,

$$\dot{M}v_\infty R^{1/2} \sim L^{1/\alpha'}, \quad (6.1)$$

with $\alpha' \approx 0.6$. Theory does predict this functional dependence of modified wind momentum on luminosity (cf. Puls et al. 1996), but the reason for the observed dependence of the wind-momentum–luminosity relation on luminosity class is not yet fully understood (see also section 5.3). We adopt the observed supergiant relation (as tabulated by Kudritzki and Puls 2000) for our models with $R > 14 R_\odot$ and the dwarf and giant relation for stars with $R < 14 R_\odot$. This choice leads to a discontinuity in the mass loss rates for the $\log g = 3.8$ sequence at the corresponding radius (see figure 6-2 (f)). Although it is physically unlikely that the transition between the wind-momentum–luminosity relations is as sudden as assumed here, we accept the approximation for now because it is of minor impact for our purposes, since it does not lead to significant discontinuities in the properties of the model atmospheres.

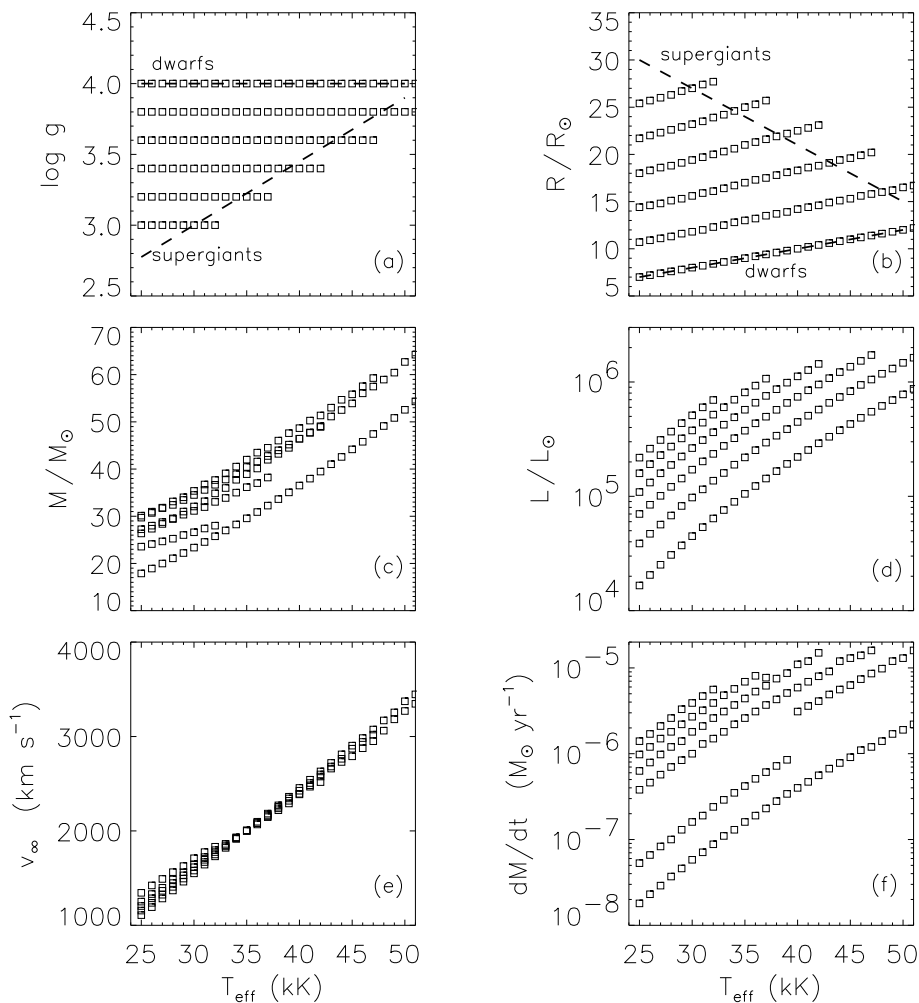


FIGURE 6-2. — Input stellar parameters for the model grid. (a) surface gravity $\log g$, (b) radius R , (c) mass M , (d) luminosity L , (e) terminal wind velocity v_∞ , and (f) wind mass-loss rate \dot{M} . The dashed lines in panels (a) and (b) represent the dwarf and supergiant sequences from figure 6-1.

6.2. SEDs and ionizing photon emission rates

In figure 6-4 we display a subset of our computed stellar atmosphere spectra as functions of T_{eff} and $\log g$, spanning the dwarf to supergiant parameter space. For each model we plot the surface flux density F_ν (erg/s/cm²/Hz) vs. the photon energy E , from 0 to 5 ryd. For comparison, for each model we also plot the blackbody flux densities, $\pi B_\nu(T_{\text{eff}})$, where B_ν is the Planck function.

The stellar SEDs consist of continua with numerous superposed absorption and emission features. Several noteworthy properties are apparent in the model atmosphere flux distributions. First, the enhanced ionizing continua that are expected in extended and expanding atmospheres (Gabler et al. 1989) are moderated and reduced by line-blocking effects (Pauldrach et al. 2001). Second, the prominent Lyman and He I ionization edges at 1 and 1.8 ryd disappear as the effective temperature increases, or as the surface gravity is reduced. Third, at high T_{eff} and low $\log g$, the SED continua near the ionization edges approach the blackbody curves.

This behavior may be understood as follows. Because the continuum on each side of an ionization edge is formed at a depth and temperature where the radiation becomes optically thick (i.e., where $\tau \approx 1$), and because of the generally larger opacity on the “blue” sides, prominent edges appear in systems with steep temperature gradients. The temperature gradients are, in turn, determined by the associated

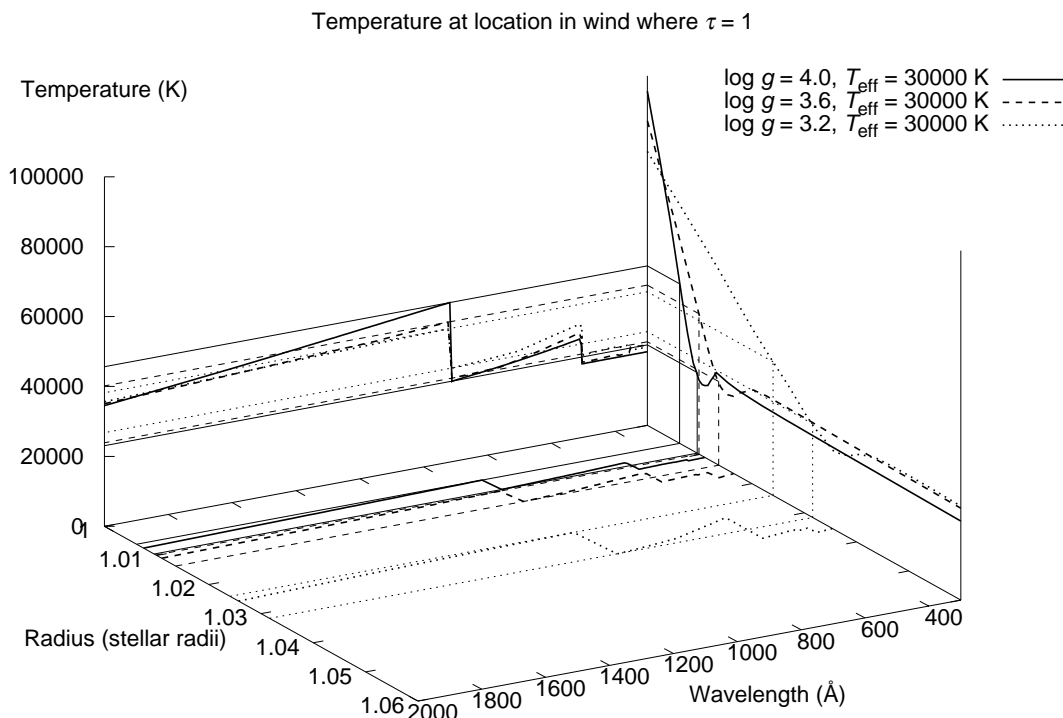


FIGURE 6-3. — Sketch illustrating how the geometrical depths of τ unity for the frequencies on both sides of an ionization threshold (in this example, the hydrogen Lyman edge) translate into the corresponding temperatures and thus the strength of the edge visible in the spectrum. With decreasing $\log g$, the temperature gradient flattens, and the differences in the temperature of the continuum-forming regions on both sides of the ionization edge shrink, resulting in a weaker visible edge in the spectrum.

hydrodynamical density gradients. Thus, when radiation pressure is most effective, as in high T_{eff} or low $\log g$ systems, the atmospheres are extended, the density gradients become smaller, and the ionization edges in the spectrum diminish. Figure 6-3 illustrates this relationship, indicating how the geometrical depths of optical depth unity on both sides of an ionization edge translate into the corresponding temperatures. With decreasing $\log g$, the temperature gradient flattens, and the differences in the temperature of the continuum-forming regions on both sides of the ionization edge shrink, resulting in a weaker visible edge in the spectrum. The overall continuum must then approach the blackbody form, given the definition of T_{eff} and flux conservation.

Figure 6-4 also shows that a He II continuum ($E > 4$ ryd) is absent in low T_{eff} and low $\log g$ systems (optically thick winds) but appears at high T_{eff} and high $\log g$ (optically thin winds). This illustrates the well-known fact that in stellar winds the He II continuum makes a sudden transition from optically thick to thin behavior at critical values of the mean wind density, depending on T_{eff} and the electron temperature at the base of the wind (Pauldrach et al. 1990). The transition from thick to thin winds is also triggered by an increase in the surface gravity. The transitions are sudden because near the critical points an increased He II opacity leads to diminished metals ionization and increased line blocking in the He II continuum, leading to a “run-away” increase in the He II opacity.

As one of the primary objectives of this study, we have computed the emission rates of photons (per second and cm^2 surface area) in the hydrogen and He I continua of the models,

$$q_X = \int_{\nu_X}^{\infty} \frac{F_\nu}{h\nu} d\nu, \quad (6.2)$$

where $h\nu_X$ is the ionization energy of hydrogen ($h\nu_{\text{H}} = 13.6 \text{ eV} = 1 \text{ ryd}$) resp. helium ($h\nu_{\text{HeI}} = 24.6 \text{ eV} = 1.8 \text{ ryd}$). These are plotted in figure 6-5 (panels (a) and (b)) as function of T_{eff} for the different $\log g$

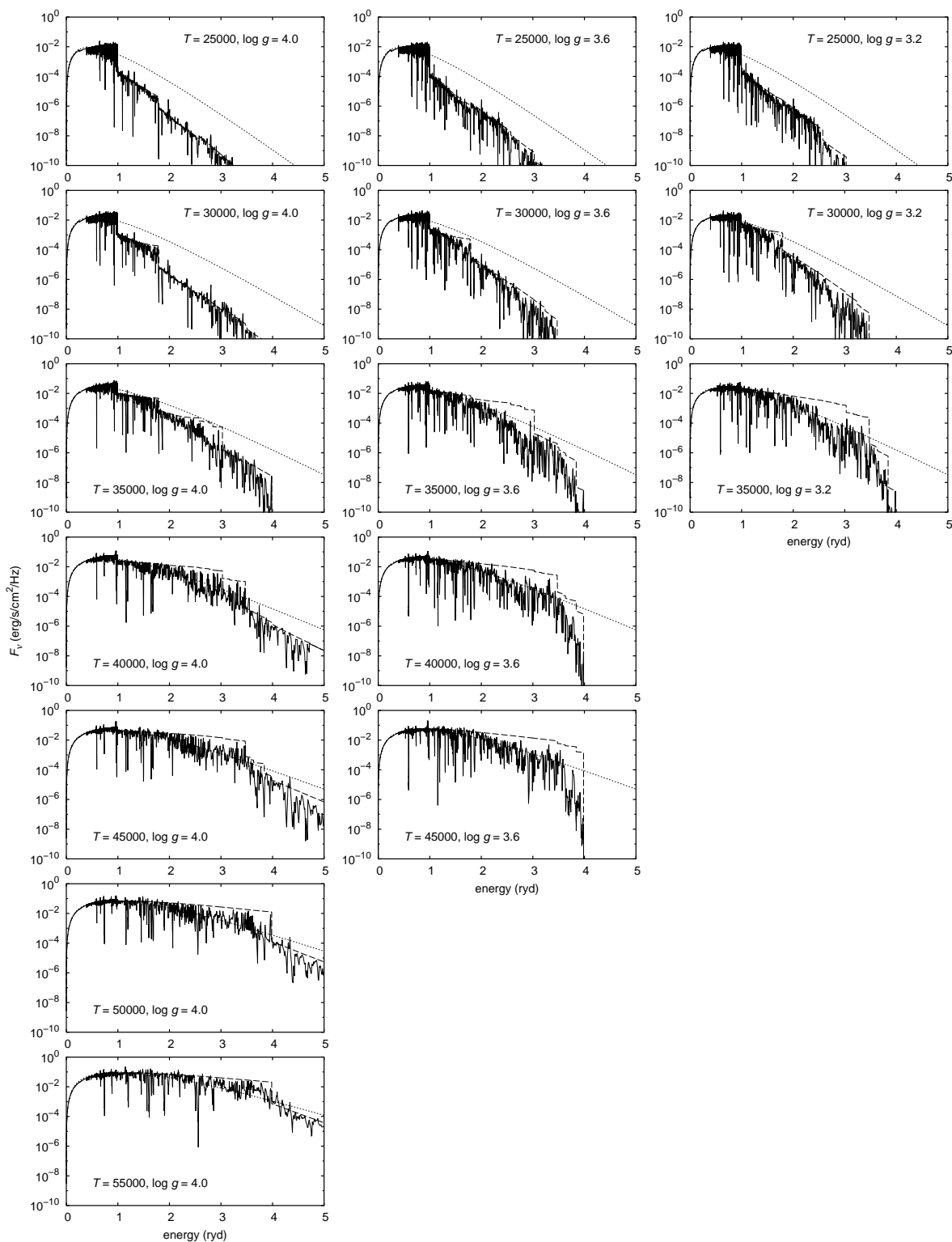


FIGURE 6-4. — EUV spectral energy distributions (solid curves) for a subsample of our model atmosphere grid, with T_{eff} ranging from 25 to 55 kK in steps of 5 kK (vertical), and $\log g$ (cm/s^2) ranging from 3.2 to 4 in steps of 0.4 dex (horizontal). For comparison, the continua of the models (long-dashed) as well as blackbody fluxes (short-dashed) at the corresponding temperatures are also shown. The difference between the continuum curves (long-dashed) and the actual flux (solid) is due to the blocking effect of spectral lines.

sequences. For comparison, blackbody fluxes at the corresponding temperatures are also shown. Due to the very large opacities in the hydrogen and helium ionization continua at the lower effective temperatures, the ionization continuum flux integrals of those model atmospheres lie below those of the corresponding blackbodies. With decreasing $\log g$ and increasing T_{eff} the integrals approach those of the blackbodies. This is of course a consequence of the behavior already noted in the discussion of the spectral energy distributions (figure 6-4).

The absolute photon emission rates per star, $Q_{\text{H}} = 4\pi R^2 q_{\text{H}}$ and $Q_{\text{HeI}} = 4\pi R^2 q_{\text{HeI}}$, are also plotted in figure 6-5 (panels (c) and (d)). In these plots, the separation between the curves representing the different $\log g$ sequences is greater than in plots (a) and (b) due to the correspondingly larger radii of the lower-gravity stars. Also indicated are the curves representing the dwarf and supergiant sequences as defined above.

6.3. Evolving cluster calculations

In the frame of a joint project (the collaboration involves A. Sternberg from the University of Tel Aviv) we have incorporated our stellar atmosphere models into the STARS population synthesis code (Sternberg 1998; Thornley et al. 2000) to compute time-dependent SEDs and ionizing photon emission rates for evolving stellar clusters. Background of these calculations is to develop tools for the analysis of galactic and extragalactic star-forming regions, deriving information about the star formation histories and star formation rates from the observed nebular emission line strengths and corresponding numerical simulations with nebular models (see below).

The principal modelling procedure here is as follows (see also Sternberg, Hoffmann, and Pauldrach 2003). Given the number of stars formed per mass interval as a function of time, we can follow the change in the stellar population by tracking the evolution of the individual member stars as determined by stellar evolutionary calculations. For this purpose we use the Geneva stellar evolutionary tracks for nonrotating stars with solar metallicity and enhanced mass-loss rates (Schaller et al. 1992). The luminosity of the cluster as function of wavelength or frequency at any time is obtained by summing up the contributions of the individual stellar fluxes according to the population distribution computed for that time.

In the calculations we assume that stars form with a Salpeter initial mass function (IMF), a power-law distribution with an exponent $-\alpha = -2.35$. The time-dependence is specified by a function $k(t)$, so that the number of stars per mass interval being formed per unit time is given by

$$n(m,t) = k(t) m^{-\alpha} \quad (6.3)$$

and the total mass per unit time (in M_{\odot}/yr) being formed into stars at time t is

$$r(t) = \int_{m_l}^{m_u} n(m,t) m \, dm = k(t) \int_{m_l}^{m_u} m^{1-\alpha} \, dm, \quad (6.4)$$

where m_l and m_u are the lower and upper mass cutoffs considered for the IMF.

The luminosity of the cluster at time t is then given by

$$L_v(t) = \int_{m_l}^{m_u} \int_0^t L_v(m,t') n(m,t-t') \, dt' \, dm. \quad (6.5)$$

Here, $L_v(m,t')$ refers to the frequential luminosity of a star of initial mass m at an age t' , the luminosity L and effective temperature T_{eff} of which are given by the evolutionary tracks in the H-R diagram. The number of stars of evolutionary age t' is determined by the star formation rate $n(m,t-t')$ at the retarded time $t-t'$. As our model grid is based on the (from the spectroscopist's view, more meaningful) "observable" variables T_{eff} and $\log g$, we determine the frequential luminosity via

$$L_v(m,t') = \frac{L}{\sigma T_{\text{eff}}^4} F_v(T_{\text{eff}}, \log g), \quad (6.6)$$

where $F_v(T_{\text{eff}}, \log g)$ is the flux of the model most closely corresponding to the T_{eff} and $\log g$ given by the

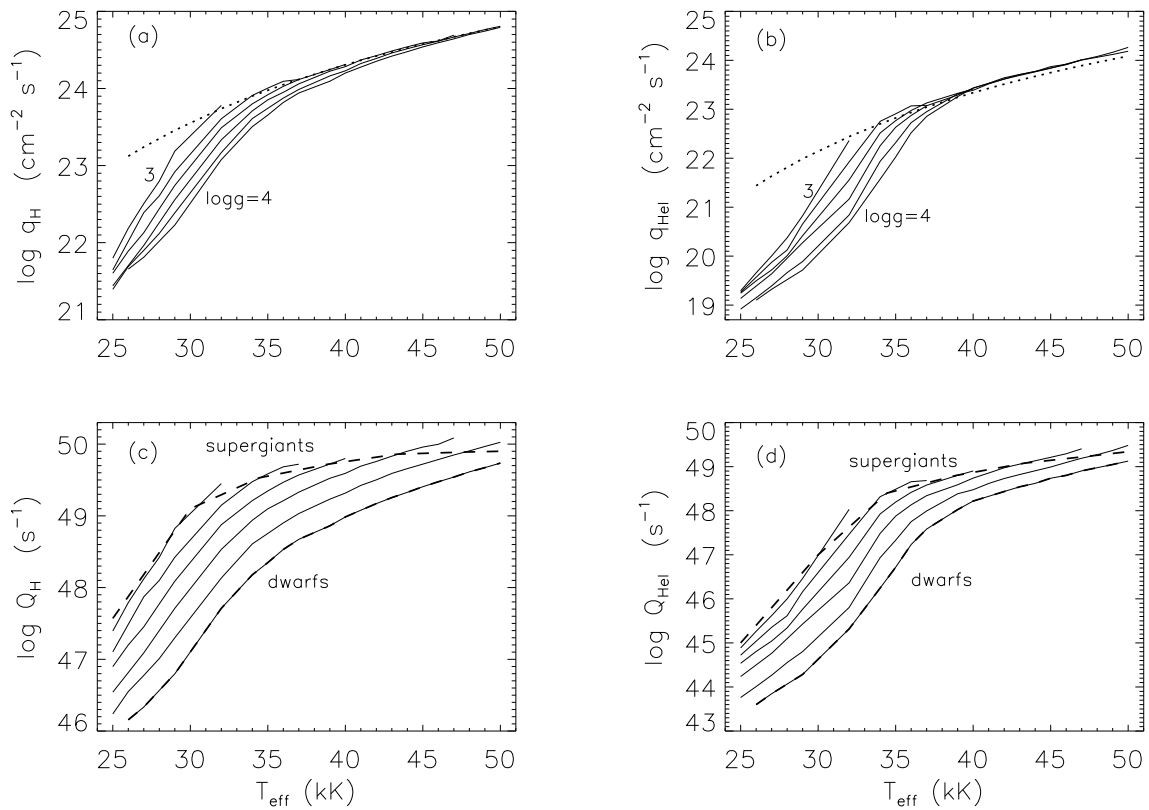


FIGURE 6-5. — (a) Hydrogen Lyman surface photon flux q_{H} , (b) He I photon flux q_{HeI} , (c) hydrogen Lyman photon emission rate Q_{H} , and (d) He I photon emission rate Q_{HeI} . The dotted lines in panels (a) and (b) are blackbody fluxes $\pi B_{\nu}(T_{\text{eff}})$. The solid curves are for stars with $\log g$ ranging from 3 to 4, in steps of $\Delta \log g = 0.2$. The dashed curves in panels (c) and (d) represent the dwarf and supergiant sequences.

evolutionary calculations for a star of initial mass m at age t' . This model atmosphere flux is rescaled with $L/\sigma T_{\text{eff}}^4$ to ensure consistency with the luminosity from the evolutionary calculations. The surface gravity $\log g$ in the above expression is the one given by the evolutionary calculations, and we note in this context that a principal “mass discrepancy” (Groenewegen et al. 1989; Herrero et al. 1992) of up to about 0.2 dex exists between the surface gravities $\log g$ derived from observations (as described in section 6.1) and those resulting from the stellar evolutionary calculations at the same point (T_{eff}, L) in the H-R diagram. We do not attempt to resolve this small inconsistency here.

For the time-dependence of the star formation we consider two different scenarios:

- ▷ *continuous star formation*: star formation is assumed to be constant in time, for time scales much longer than the lifetimes of massive stars. A star formation rate of $r = 1 M_{\odot}/\text{yr}$ is adopted.
- ▷ *impulsive star formation*: stars are formed “instantaneously”, i.e., in a “starburst” on a time scale much shorter than the lifetimes of massive stars, and it is assumed that no stars form after this burst. We assume a total cluster mass formed of $M_{\text{clus}} = 10^5 M_{\odot}$.

For both scenarios, the lower mass cutoff of the IMF is taken to be $m_l = 1 M_{\odot}$, and different values for the upper mass cutoff, from $m_u = 20 M_{\odot}$ to $m_u = 120 M_{\odot}$, are considered. (The contribution of cooler, lower-mass stars than those treated with our new models is considered using the Kurucz (1992) library of plane-parallel LTE atmospheres. These stars contribute negligibly to the ionizing flux, but do eventually dominate at longer wavelengths.)

The evolving spectral energy distributions for the two star formation scenarios, and upper mass cutoffs of $m_u = 30 M_{\odot}$ and $m_u = 120 M_{\odot}$, are shown in figure 6-6. For continuous star formation, the number of

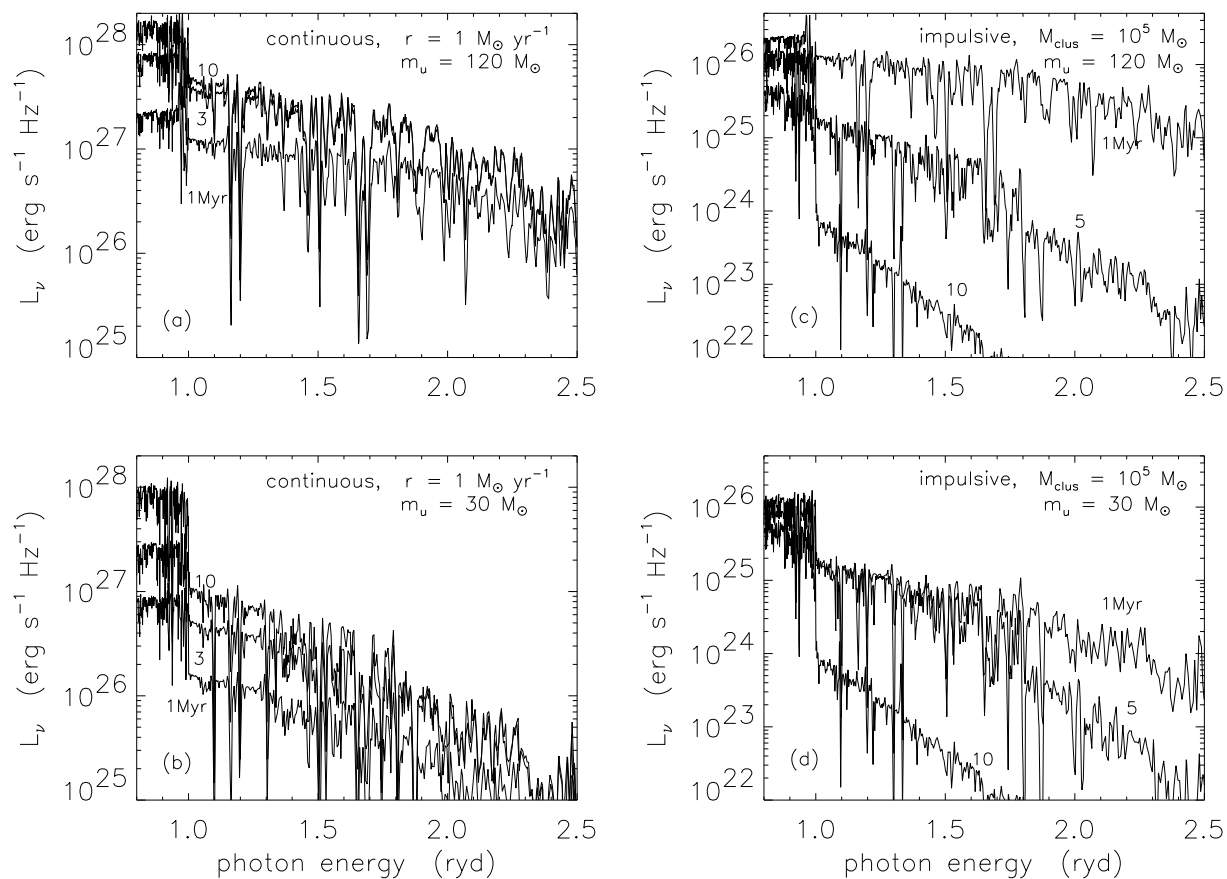


FIGURE 6-6. — Cluster spectral evolution. Left: continuous star-formation with $r = 1 M_{\odot}/\text{yr}$, and cluster ages equal to 1, 3 and 10 Myr; (a) $m_u = 120 M_{\odot}$, (b) $m_u = 30 M_{\odot}$. Right: impulsive star-formation with cluster mass $M_{\text{clus}} = 10^5 M_{\odot}$, and cluster ages equal to 1, 5 and 10 Myr; (c) $m_u = 120 M_{\odot}$, (d) $m_u = 30 M_{\odot}$.

ionizing photons emitted initially increases with time as the number of stars grows. The ionizing spectrum is at first dominated by the most massive stars, showing the flat spectral energy distribution of early-type O stars (particularly visible in the case of $m_u = 120 M_{\odot}$), but begins to steepen as the ratio of late-type to early-type O stars increases. After about 10 Myr the evolution of the ionizing SEDs reaches a stationary state, in which stellar aging and stellar birth come into equilibrium for massive stars. The emission of nonionizing photons, however, continues to grow with cluster age on these timescales, due to the accumulation of lower-mass stars with longer lifetimes, which become the principal contributors to the flux in this spectral range.

In the case of impulsive star formation, we essentially see the aging of the cluster, as the most massive stars with the shortest lifetimes disappear first. The total cluster luminosities decrease with time, and the characteristic of the ionizing SED changes from one dominated by early-type O stars to one dominated by late-type O stars, with a corresponding steepening of the SED and an increase of the strength of the Lyman edge with time. At later times the absolute ionizing luminosity of the cluster becomes larger in the case of $m_u = 30 M_{\odot}$ than in the case of $m_u = 120 M_{\odot}$ because both clusters started with the same total mass, but in the former case a greater fraction of this mass was formed into later-type stars (with longer lifetimes).

Figure 6-7 shows the evolution of the emission rates of photons above the hydrogen Lyman (Q_{H}) and the He I (Q_{HeI}) ionization thresholds as function of time for both scenarios and for different values of the IMF upper mass cutoff m_u . For continuous star formation, the emission rates initially increase linearly with cluster age and reach equilibrium after a time corresponding to the lifetimes of the most massive (and dominating) stars in the system (earlier in time in the case of a high upper mass limit and somewhat

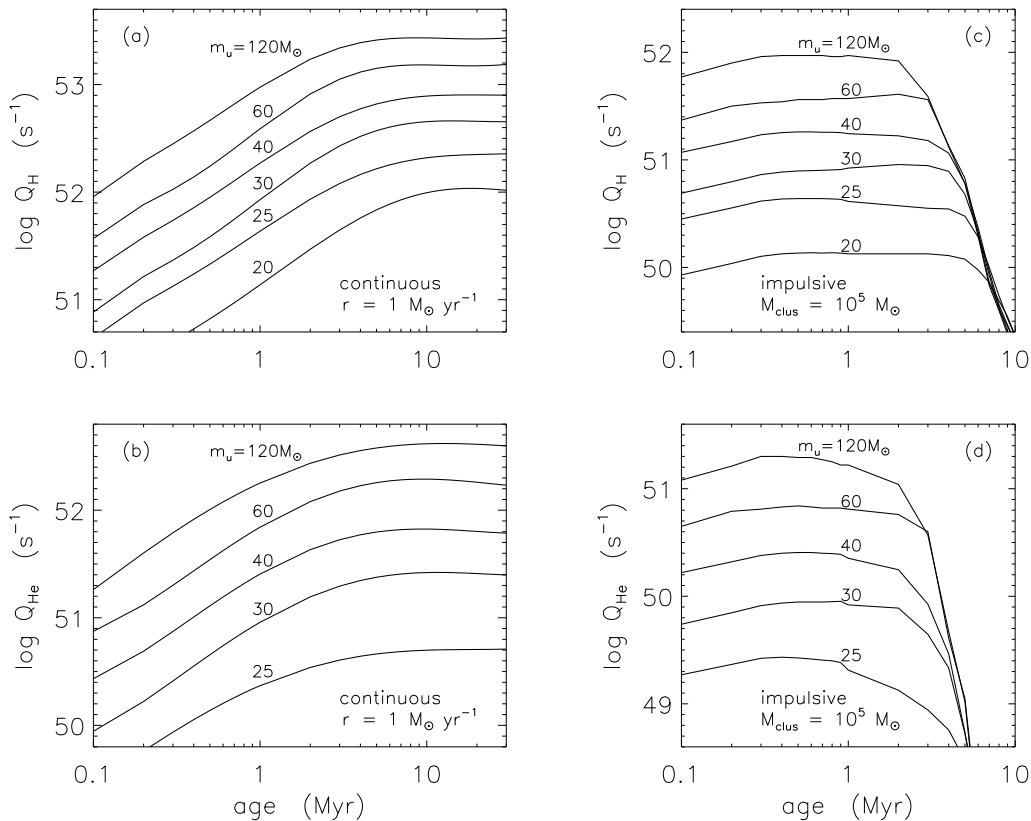


FIGURE 6-7. — (a) Cluster Lyman continuum photon emission rate Q_{H} , and (b) He I emission rate Q_{HeI} , for continuous star-formation with $r = 1 M_{\odot}/\text{yr}$. (c) Lyman emission rate Q_{H} , and (d) He I emission rate Q_{HeI} , for impulsive star-formation for a cluster mass $M_{\text{clus}} = 10^5 M_{\odot}$. A Salpeter IMF is assumed, with an upper mass cut-off m_u ranging from 25 to $120 M_{\odot}$.

later in the case of a smaller upper mass limit). The steady-state absolute emission rates, and the ratio of Q_{H} to Q_{HeI} , depend on the upper mass cutoff as a result of the different ensuing stellar mass distribution functions.

For impulsive star formation, the photon emission rates are approximately constant at early times (increasing slightly during the supergiant phases) and then decay rapidly as the hot stars age and disappear; the ionizing photons practically vanish at an age of about 10 Myr. As in the case of continuous star formation in equilibrium, here the absolute ionizing photon emission rates and the $Q_{\text{H}}/Q_{\text{HeI}}$ ratio in the early times depend on the upper mass limit m_u of the initial mass function.

As a result of the large differences in the shapes and magnitudes of the SEDs calculated for the different star formation histories, the characteristics of the emission line spectra of the corresponding H II regions will vary strongly, since these emission line spectra contain a number of lines whose strength depends sensitively on the nebular ionization balance and thus on the shape of the ionizing spectrum. As an example we mention the well-known [Ne III] problem in H II regions, which refers to the long-unexplained failure of nebular emission line calculations to reproduce the observed Ne line ratios. This is now understood (e.g., Sellmaier et al. 1996), to be a consequence of the use of SEDs from earlier, less sophisticated stellar atmosphere models in these calculations (see figure 6-9). A similar improvement regarding theoretical and observed infrared fine-structure lines has been found by Giveon et al. (2002), using the recent stellar atmosphere models of Pauldrach, Hoffmann, and Lennon (2001). Thus, using the SEDs calculated for the analysis of the H II regions surrounding starbursts even at cosmological distances with redshifts up to about 1 we will be able to determine the star formation histories, initial mass functions, and star formation rates. This will provide constraints on the chemical evolution of the host galaxies, which in turn will give us more insight into the evolution of the universe.

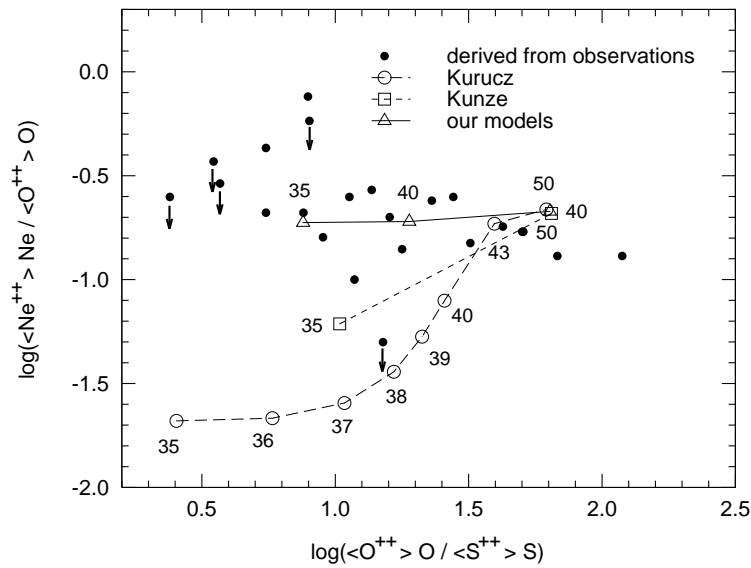


FIGURE 6-8. — Diagnostic diagram illustrating the so-called [Ne III] problem: nebular calculations using as input the SEDs of LTE (circles) or simple non-LTE (squares) stellar atmosphere models fail to reproduce the observed line ratios. Only the use of more sophisticated non-LTE models (triangles) with their significantly different SEDs can provide a convincing fit to the observations. (Figure from Sellmaier et al. 1996.)

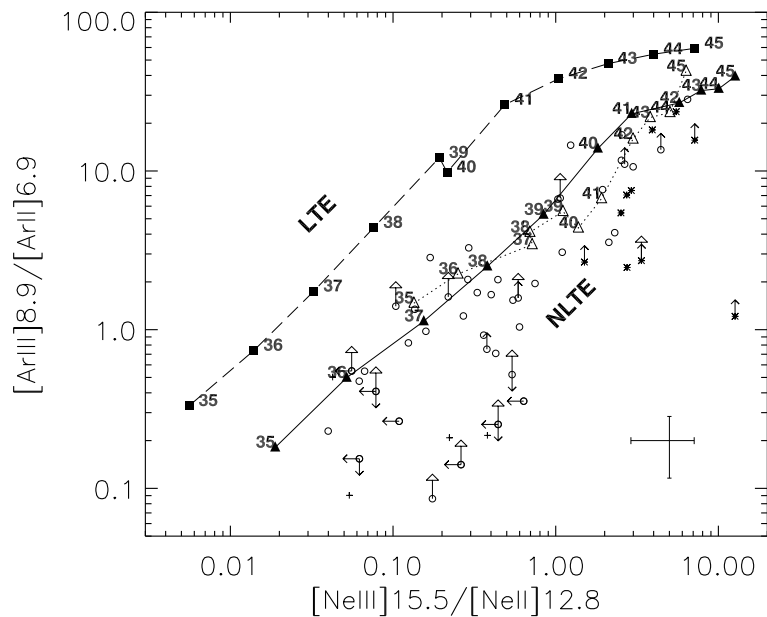


FIGURE 6-9. — Comparison of observed (circles) and computed infrared fine-structure line strength ratios obtained from nebular modelling using the recent hydrodynamic, non-LTE stellar atmosphere models of Pauldrach, Hoffmann, and Lennon (2001) (triangles) and hydrostatic, plane-parallel LTE models of Kurucz (1979, 1992) (squares). Note that the use of different SEDs can lead to order-of-magnitude differences in the calculated line strength ratios. (Figure from Giveon et al. 2002.)

7

Summary, conclusions, and future work

Using an improved model code, EUV spectral energy distributions (SEDs) have been computed for a large grid of stellar models spanning the parameter range observed for O and early B stars. These SEDs have been incorporated into an evolutionary population synthesis code to investigate the time-dependence of the integrated SEDs from evolving clusters of massive stars. Purpose of these calculations is to provide a crucial ingredient for the simulations of the photoionized gas in star-forming regions, which then yield information about the star-formation history of observed clusters.

The new method used for computing the SEDs renders the influence of spectral lines on the EUV radiation field in identical quality as the high-resolution synthetic spectra used for comparison with observed UV spectra.

By means of exemplary UV analyses of individual O stars it has been shown that the models reproduce most features of the observed UV spectra. As the appearance of the observable UV spectrum depends strongly on the spectral shape of the EUV radiation field, this result represents strong evidence that the computed SEDs are on a realistic level, an essential requirement for their application in photoionization calculations. Some minor discrepancies still remain, however, to be resolved in future work.

The mass loss rates and terminal velocities from models with consistently calculated hydrodynamics have been shown to reproduce the theoretically predicted wind-momentum–luminosity relation, as well as the predicted metallicity dependence thereof, showing no distinct differences for dwarfs and supergiants. Comparison of the observed UV spectra of a sample of galactic O stars with the synthetic spectra of two sets of models, one based on selfconsistent hydrodynamics, the other on wind parameters derived from an analysis of optical lines, shows discrepancies that are consistent with the scenario of a fragmented stellar wind, although an in-depth investigation of other possible explanations, such as non-solar abundance patterns, remains to be performed. (This will require a detailed spectral analysis and comparative

study of a sample of Galactic, LMC, and SMC stars.) The different relations previously obtained for dwarfs and supergiants from analyses of the H α line might therefore be the result of inadequate assumptions made in modelling the optical lines.

Future work

The overall good agreement of the synthetic spectra from the current generation of stellar models with the observations indicates that phenomena pertaining to deviations from symmetry and stationarity, such as the time-dependent phenomena (driving instabilities) and the influence of rotation, are obviously second-order effects. Our short to medium term research plans in the field of hot stars will therefore instead focus on applications such as the following:

1. A detailed comparison of the stellar and wind parameters derived from fits to the UV spectra via models with consistent dynamics and those determined from analyses of the optical lines that is unhampered by the current uncertainties in the distances to the individual stars. Most probably this will involve a sample of stars in the LMC or SMC, where the relative error in the distances is much smaller than for stars in our galaxy.
2. Using the population synthesis methods to calculate integrated spectra for a large range of stellar metallicities from synthetic UV spectra (using the same technique as described in chapter 6, but focusing on the observable UV range), for the determination of stellar abundances and the physical properties of the most UV-luminous stars in star-forming galaxies at high redshifts. A first tentative step in this direction has already been undertaken by Mehlert et al. (2001), comparing the observed spectrum of a high-redshift galaxy with the synthetic spectrum of a representative massive star of one-fifth solar metallicity.
3. Computing models for Population III stars, the very first generation of very massive, extremely low to zero metallicity stars, which are suspected to have played a significant role in the reionization of the universe. Questions to be addressed regard in particular the dynamics of stellar winds at such low metallicities.

Improvements and refinements planned in this regard for the atmosphere modelling comprise:

1. A more consistent treatment of shock emission.

Shocks have so far been mostly ignored in the computations of spectral energy distributions of stellar models used in photoionization calculations of H II regions or planetary nebulae, due to the lack of a consistent quantitative theory describing distribution and strength of the shock emission. As shocks, however, can increase the number of He⁺⁺-ionizing photons by several orders of magnitude, at least an approximate inclusion of shock emission in the models is necessary. We are currently implementing an improved semi-empirical description of shock emission, a preliminary version of which has already in the case of ζ Puppis been shown to simultaneously reproduce the observed ROSAT spectrum as well as the influence on the observed visible UV range (Pauldrach, Hoffmann, and Lennon 2001). It is suspected that a similar simultaneous fit of both X-ray and UV spectra for a series of stars with existing ROSAT observations should enable us to correlate the shock emission with the fundamental stellar parameters and/or give us the necessary expertise to obtain reasonable estimates of the shock emission on basis of the visible UV spectra alone. This knowledge can then be incorporated into an improved systematic computation of stellar SEDs.

2. A comoving-frame treatment of important hydrogen and helium lines.

To compute the NLTE line transition rates, we presently use the Sobolev-with-continuum method. This is an excellent approximation for most lines and allows a fast numerical treatment of (currently) over ten thousand line transitions in the computation of the occupation numbers. However, for a few tens of lines (among which are some H and He lines) it is known to be an imperfect approximation (e.g. Sellmaier et al. 1993). This has not been a major issue in the past, but for future planned analyses a more rigorous treatment of these particular lines will become necessary for two reasons:

- a. With decreasing metallicity, the hydrogen and helium lines gain in relative importance, and at very low metallicities it is essentially these comparatively few lines which drive the winds. Thus, to compute realistic mass loss rates at low metallicities, it is important that not only the occupation numbers of the connecting levels be accurate, but also the treatment of the transfer of momentum from the radiation field to the wind material via these lines (which in our models is at present treated in Sobolev-approximation).
 - b. For diagnostic purposes, i.e., to determine the parameters of individual observed stars and to verify the models via a comparison to observations, we have in the past relied primarily on UV spectra. The large number of resonance lines there is quite insensitive to minor approximations, and the presence of lines from several different ionization stages makes them suitable as tracers of the ionization balance throughout the wind. In the centers of galaxies, however, absorption by dust severely attenuates the UV spectral range, and we must turn to optical and infrared spectra for diagnostics. The lines in the optical and infrared ranges are weaker, subordinate lines, and although these lines are of minor importance in establishing the ionization balance, using them for diagnostic purposes requires a much more accurate treatment. In particular, for several of these lines broadening effects must be considered and the line source functions must be computed in the comoving frame.
3. A more consistent calculation and treatment of the line force.

Mass loss in hot stars has a profound influence on the spectral energy distributions and spectra of the stars, and one of the main effects of metallicity is its influence on the mass loss rate. Knowledge of the metallicity-dependence of the mass loss rate as function of the stellar parameters is essential to obtain realistic synthetic spectral energy distributions and integrated cluster spectra derived from individual synthetic stellar spectra. Although (as shown in this thesis) the current approach already seems to accurately reproduce the theoretically predicted dependence of the wind momenta on metallicity, a more correct determination of the line force (using, e.g., detailed observer's frame or comoving-frame calculations) must at least be investigated within the framework of our present models. In particular for very low metallicities (such as expected for high-redshift systems) where observational determinations of the mass loss rates do not (yet) exist and thus these parameters cannot be deduced from observations, this will be an important step in producing models with realistic spectral energy distributions.

References

- Abbott D. C., *ApJ* 242, 1183 (1980)
- Abbott D. C., *ApJ* 259, 282 (1982)
- Abbott D. C., Lucy L. B., *ApJ* 288, 679 (1985)
- Abbott D. C., Hummer D. G., *ApJ* 294, 286 (1985)
- Anderson L., in: Crivellari L., Hubeny I., Hummer D. G. (eds.), *Stellar Atmospheres: Beyond Classical Models*, NATO ASI Series C, Vol. 341, p. 29 (1991)
- Aufdenberg J. P., Hauschildt P. H., Shore S. N., Baron E., *ApJ* 498, 837 (1998)
- Bjorkman J. E., Cassinelli J. P., *ApJ* 409, 429 (1993)
- Blöcker T., *A&A* 299, 755 (1995)
- Briel U. G., Aschenbach B., Englhauser J., et al. (eds.), *ROSAT User's Handbook*, Max-Planck-Institut für extraterrestrische Physik (1997)
- Bromm V., Kudritzki R.-P., Loeb A., *ApJ* 552, 464 (2001)
- Cannon C. J., *ApJ* 185, 621 (1973)
- Cassinelli J. P., Swank J. H., *ApJ* 271, 681 (1983)
- Castor J. I., Abbott D. C., Klein R. K., *ApJ* 195, 157 (1975)
- Chlebowski T., Harnden F. R. Jr., Sciortione S., *ApJ* 341, 427 (1989)
- Conti P. S., Leep E. M., Lorre J. J., *ApJ* 214, 759 (1977)
- Cox D. P., Raymond J. C., *ApJ* 298, 651 (1985)
- Cunto W., Mendoza C., *Rev. Mex. Astron. Astrof.* 23, 107 (1992)
- Drew J. E., *ApJS* 71, 267 (1989)
- Drew J. E., *ApJ* 357, 573 (1990)
- Eissner W., Jones M., Nussbaumer H., *Computer Physics Comm.* 8, 270 (1974)
- Feldmeier A., Kudritzki R.-P., Palsa R., Pauldrach A. W. A., Puls J., *A&A* 320, 899 (1997a)
- Feldmeier A., Puls J., Pauldrach A. W. A., *A&A* 322, 878 (1997b)
- Gabler R., Gabler A., Kudritzki R.-P., Pauldrach A. W. A., Puls J., *A&A* 226, 162 (1989)
- Giveon U., Sternberg A., Lutz D., Feuchtgruber H., Pauldrach A. W. A., *ApJ* 566, 880 (2002)
- Grevesse N., Sauval A., in: *Space Science Reviews* 85, 161 (1998)
- Groenewegen M. A. T., Lamers H. J. G. L. M., Pauldrach A. W. A., *A&A* 221, 78 (1989)
- Hamann W.-R., Koesterke L., *A&A* 335, 1003 (1998)
- Harnden F. R., Branduardi G., Gorenstein P., Grindlay J., Rosner R., et al., *ApJ* 234, L51 (1979)
- Haser S. M., Pauldrach A. W. A., Lennon D. J., Kudritzki R.-P., Lennon M., Puls J., Voels S.A., *A&A* 330, 285 (1998)
- Haser S. M., PhD thesis, Ludwig-Maximilians-Universität München (1995)
- Henrichs H. F., *Proc. 4th Eur. IUE Conf.*, ESA-SP 218, p. 43 (1984)
- Herrero A., Kudritzki R.-P., Vilchez J. M., Kunze D., Butler K., Haser S., *A&A* 261, 209 (1992)
- Hillier D. J., Miller D. L., *ApJ* 496, 407 (1998)
- Hoffmann T. L., Diploma thesis, Ludwig-Maximilians-Universität München (1995)
- Hoffmann T. L., Pauldrach A. W. A., in: Kwok S., Dopita M., Sutherland R. (eds.), *Proc. IAU Symp.* 209, ASP, p. 189 (2003)
- Hoffmann T. L., Pauldrach A. W. A., Puls J., in: van der Hucht K. A., Herrero A., Esteban C. (eds.), *Proc. IAU Symp.* 212, ASP, p. 61 (2003)
- Hunsinger J., Diploma thesis, Ludwig-Maximilians-Universität München (1993)
- Hummer D. G., Seaton M. J., *MNRAS* 125, 437 (1963)
- Hummer D. G., Rybicki G. B., *ApJ* 293, 258 (1985)

- Hummer D. G., Berrington K. A., Eissner W., Pradhan Anil K., Saraph H. E., Tully J. A., *A&A* 279, 298 (1993)
- Kawaler S. D., ASP Conf. Series 226, p. 287 (2001)
- Kubát J., Puls J., Pauldrach A. W. A., *A&A* 341, 587 (1999)
- Kudritzki R.-P., Puls J., *ARA&A* 38, 613 (2000)
- Kudritzki R.-P., Hummer D. G., Pauldrach A. W. A., Puls J., Najarro F., Imhoff J., *A&A* 257, 655 (1992)
- Kudritzki R.-P., Lennon D. J., Puls J., in: Walsh J. R., Danziger I. J. (eds.), *Science with the Very Large Telescope*, ESO Astrophysics Symposia, Springer, Heidelberg, p. 246 (1995)
- Kudritzki R.-P., Méndez R. H., Puls J., McCarthy J. K., in: Habing H. J., Lamers H. J. G. L. M. (eds.), *Proc. IAU Symp.* 180, p. 64 (1997)
- Kudritzki R.-P., Puls J., Lennon D. J., et al., *A&A* 350, 970 (1999)
- Kurucz R. L., *ApJS* 40, 1 (1979)
- Kurucz R. L., *Rev. Mex. Astron. Astrof.* 23, 45 (1992)
- Labs D., *Z. Astrophys.* 29, 199 (1951)
- Lamers H. J. G. L. M., Leitherer C., *ApJ* 412, 771 (1993)
- Lamers H. J. G. L. M., Morton D. C., *ApJS* 32, 715 (1976)
- Leitherer C., Leão J., Heckman T. M., Lennon D. J., Pettini M., Robert C., *ApJ* 550, 724 (2001)
- Lucy L. B., Solomon P., *ApJ* 159, 879 (1970)
- Lucy L. B., White R. L., *ApJ* 241, 300 (1980)
- Lucy L. B., *ApJ* 255, 286 (1982)
- Lucy L. B., *ApJ* 274, 372 (1983)
- MacFarlane J. J., Cohen D. H., Wang P., *ApJ* 437, 351 (1994)
- Markova N., Puls J., Repolust T., Markov H., *A&A* in press (2003)
- Massa D., Fullerton A. W., Nichols J. S., Owocki S. P., Prinja R. K., et al., *ApJ* 452, L53 (1995)
- Mehlert D., Seitz S., Saglia R. P., Appenzeller I., Bender R., Fricke K. J., Hoffmann T. L., Hopp U., Kudritzki R.-P., Pauldrach A. W. A., *A&A* 379, 96 (2001)
- Méndez R. H., Groth H. G., Husfeld D., Kudritzki R.-P., Herrero A., *A&A* 197, L25 (1988a)
- Méndez R. H., Kudritzki R.-P., Herrero A., Husfeld D., Groth H. G., *A&A* 190, 113 (1988b)
- Méndez R. H., Kudritzki R.-P., Herrero A., *A&A* 260, 329 (1992)
- Meynet G., Maeder A., *A&A* 361, 101 (2000)
- Mihalas D., Hummer D. G., *ApJ* 179, 827 (1973)
- Mihalas D., *Stellar Atmospheres*, 2nd ed., W. H. Freeman and Comp., San Francisco (1978)
- Morrison R., McCammon D., *ApJ*. 270, 119 (1983)
- Morton D. C., *ApJS* 77, 119 (1991)
- Napiwotzki R., Green P. J., Saffer R. A., *ApJ* 517, 399 (1999)
- Nelan E., et. al., in prep. (2003)
- Nussbaumer H., Storey P. J., *A&A* 64, 139 (1978)
- Oey M. S., Massey P., *ApJ* 452, 210 (1995)
- Owocki S. P., Castor J. I., Rybicki G. B., *ApJ* 335, 914 (1988)
- Owocki S. P., Cranmer S. R., Blondin J. M., *ApJ* 424, 887 (1994)
- Pauldrach A. W. A., Puls J., Kudritzki R.-P., *A&A* 164, 86 (1986)
- Pauldrach A. W. A., *A&A* 183, 295 (1987)
- Pauldrach A., Herrero A., *A&A* 199, 262 (1988)
- Pauldrach A. W. A., Puls J., Kudritzki R.-P., Méndez R. H., Heap S. R., *A&A* 207, 123 (1988)
- Pauldrach A. W. A., Kudritzki R.-P., Puls J., Butler K., *A&A* 228, 125 (1990)
- Pauldrach A. W. A., Kudritzki R.-P., Puls J., Butler K., Hunsinger J., *A&A* 283 525 (1994)

- Pauldrach A. W. A., Feldmeier A., Puls J., Kudritzki R.-P., *Space Science Reviews* 66, 105 (1994a)
- Pauldrach A. W. A., Duschinger M., Mazzali P. A., Puls J., Lennon M., Miller D. L., *A&A* 312, 525 (1996)
- Pauldrach A. W. A., Lennon M., Hoffmann T. L., Sellmaier F., Kudritzki R.-P., Puls J., in: Howarth I. (ed.), *Proc. 2nd Boulder-Munich Workshop, PASPC 131*, p. 258 (1998)
- Pauldrach A. W. A., Hoffmann T. L., Lennon M., *A&A* 375, 161 (2001)
- Pauldrach A. W. A., Hoffmann T. L., Méndez R. H., in: Kwok S., Dopita M., Sutherland R. (eds.), *Proc. IAU Symp. 209, ASP*, p. 177 (2003)
- Pauldrach A. W. A., Hoffmann T. L., Méndez R. H., *A&A*, in press (2004)
- Petrenz P., Puls J., *A&A* 312, 195 (1996)
- Peytremann E., *A&A* 33, 203 (1974)
- Pistinner S. L., Hauschildt P. H., Eichler D., Baron E. A., *MNRAS* 302, 684 (1999)
- Prinja R. K., Barlow M. J., Howarth I. D., *ApJ* 361, 607 (1990)
- Prinja R. K., Howarth I. D., *ApJS* 61, 357 (1986)
- Puls J., *A&A* 184, 227 (1987)
- Puls J., Hummer D. G., *A&A* 191, 87 (1988)
- Puls J., Pauldrach A. W. A., in: Garmany C. (ed.), *Proc. Boulder-Munich Workshop, PASPC 7*, p. 203 (1990)
- Puls J., Kudritzki R.-P., Herrero A., et al., *A&A* 305, 171 (1996)
- Puls J., Springmann U., Lennon M., *A&AS* 141, 23 (2000)
- Raymond J. C., Smith B. W., *ApJ Suppl.* 35, 419 (1977)
- Raymond J. C., in: Pallavicini R. (ed.), *Hot Thin Plasmas in Astrophysics*, Kluwer, Dordrecht, p. 3 (1988)
- Repolust T., Puls J., Herrero A., *A&A* in press (2003)
- Rubin R. H., Simpson J. P., Haas M. R., Erickson E. F., *ApJ* 374, 564 (1991)
- Santolaya-Rey A. E., Puls J., Herrero A., *A&A* 323, 488 (1997)
- Schaerer D., de Koter A., *A&A* 322, 598 (1997)
- Seaton M. J., Yan Yu, Mihalas D., Pradhan Anil K., *MNRAS* 266, 805 (1994)
- Sellmaier F., Puls J., Kudritzki R.-P., Gabler A., Gabler R., Voels S. A., *A&A* 273, 533 (1993)
- Sellmaier F., Yamamoto T., Pauldrach A. W. A., Rubin R. H., *A&A* 305, L37 (1996)
- Sellmaier F., PhD thesis, Ludwig-Maximilians-Universität München (1996)
- Seward F. D., Forman W. R., Giacconi R., Griffiths R. E., Harnden F. R., et al., *ApJ* 234, L55 (1979)
- Silvestri N. M., Oswalt T. D., Wood M. A., et al., *ASP Conf. Series* 226, p. 246 (2001)
- Snedden C., Johnson H. R., Krupp B. M., *ApJ* 204, 281 (1976)
- Snow T. P., *ApJ*, 217, 760 (1977)
- Sobolev V. V., *Sov. Astron. Astrophys. J.* 1, 678 (1957)
- Springmann U., Pauldrach A. W. A., *A&A* 262, 515 (1992)
- Sternberg A., *ApJ*, 506, 721 (1998)
- Sternberg A., Hoffmann T., Pauldrach A. W. A., *ApJ*, in press (2003)
- Stock C., Diploma thesis, Ludwig-Maximilians-Universität München (1998)
- Taresch G., Kudritzki R.-P., Hurwitz M., et al., *A&A* 321, 531 (1997)
- Thornley M. D., Forster-Schreiber N. M., Lutz D., Genzel R., Spoon H. W. W., Kunze D., Sternberg A., *ApJ*, 539, 641 (2000)
- Tinkler C. M., Lamers H. J. G. L. M., *A&A* 384, 987 (2002)
- Vink J. S., de Koter A., Lamers H. J. G. L. M., *A&A* 362, 295 (2000)
- Werner K., Husfeld D., *A&A* 148, 417 (1985)
- van Regemorter H., *ApJ* 136, 906 (1962)

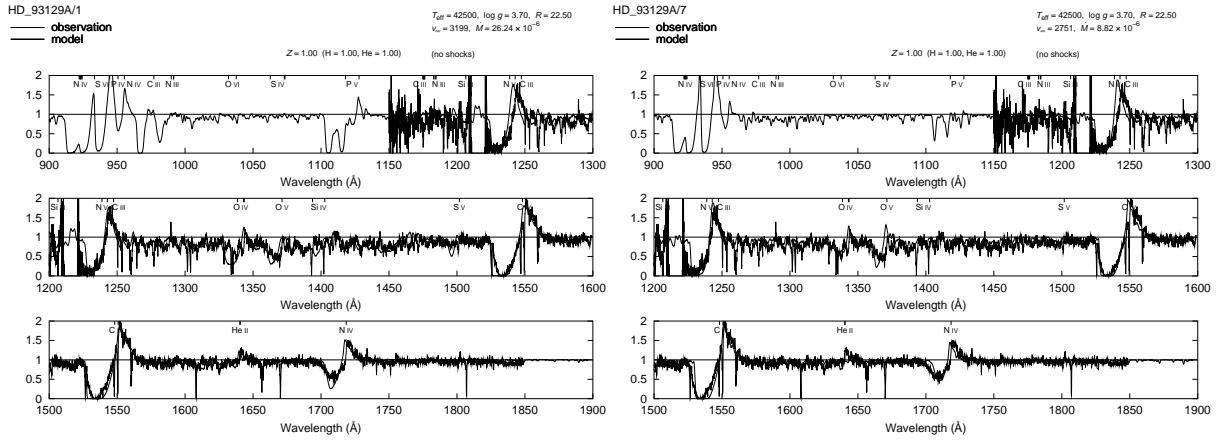
Appendix

A

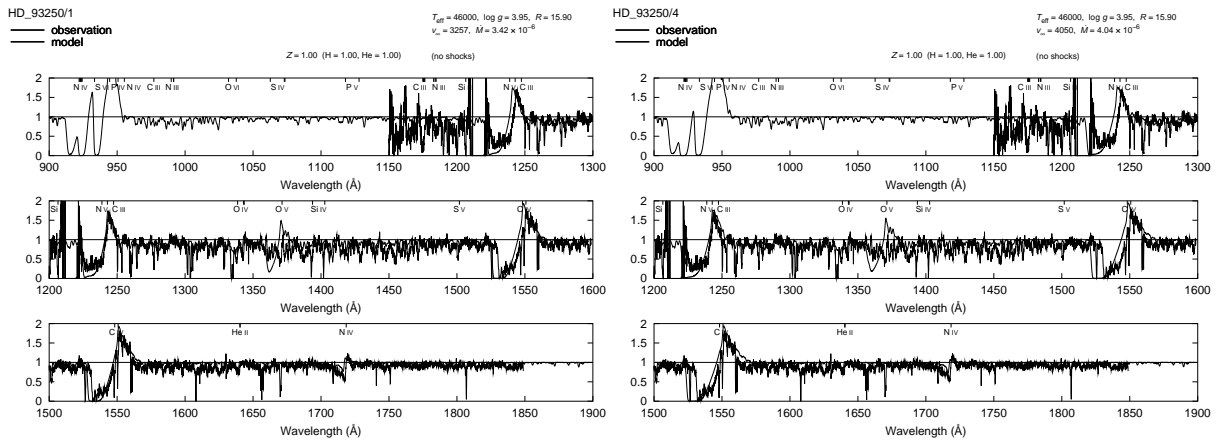
Synthetic UV spectra for the galactic O star sample

In the following, we present two series of models for the galactic O star sample from section 5.3, comparing the synthetic UV spectra of the models to the observed spectra (except for HD 93128, HD 193682, and HD 18409, where no observed UV spectra are available). For the models whose synthetic spectra are shown in the panels on the left, the line force parameters have been adjusted to yield approximately the observed terminal velocity and the mass loss rate suggested by the optical analysis, regardless of whether these are dynamically consistent with the stellar parameters derived from the optical analysis. For the models whose synthetic spectra are shown in the panels on the right, the wind dynamics have been iterated to consistency with the stellar parameters.

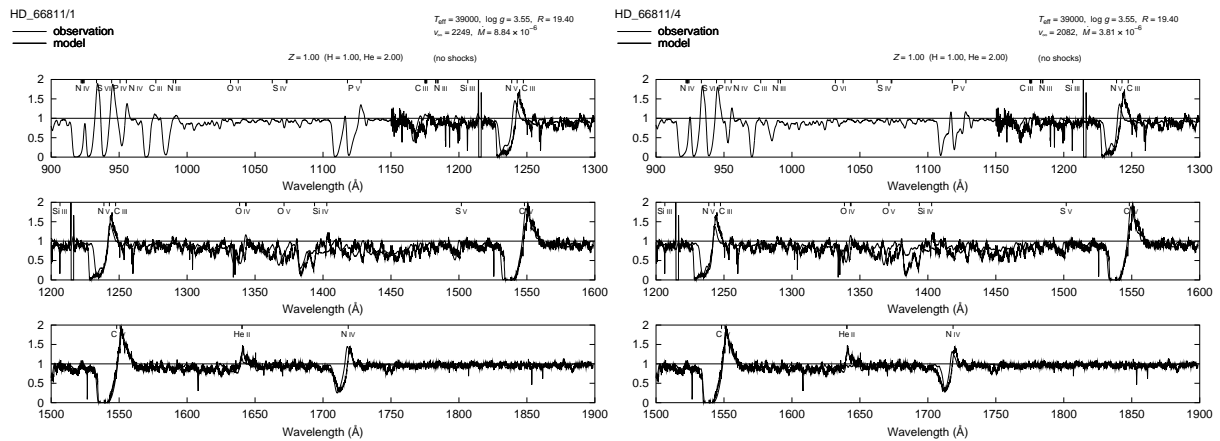
The synthetic spectra have been convolved with a rotational profile corresponding to the observed $v_{\text{rot}} \sin i$ as listed by Repolust et al. (2003). While this is necessary to properly assess the photospheric line spectrum with regard to the observed one, it is inappropriate for spectral features formed far out in the wind, and it incorrectly flattens the slopes of the blue edges of the P Cygni absorption troughs. As we will be interested in comparing terminal velocities to only within about ± 200 km/s, however, this latter point is of no concern here.



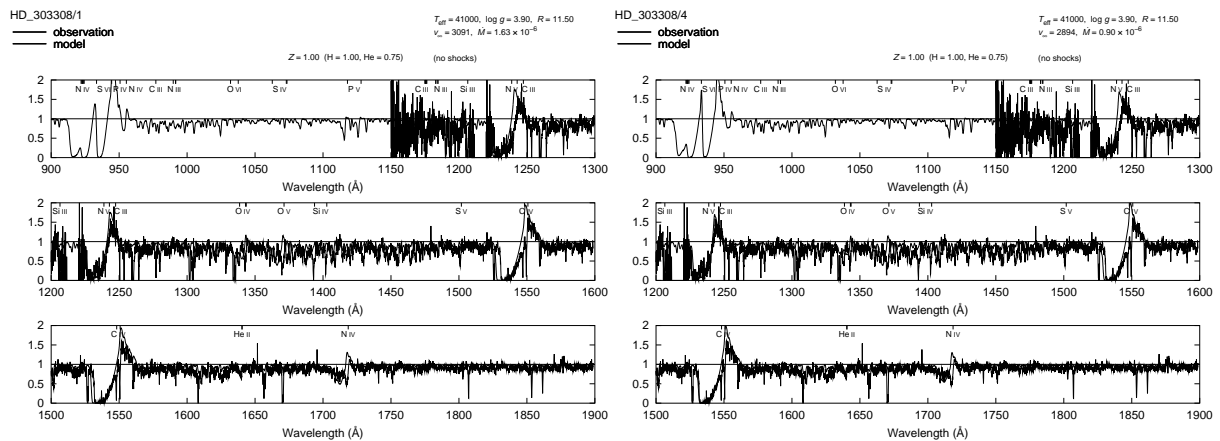
HD 93129A. The circumstance that HD 93129A is in fact a binary system (Nelan et al. 2003) may have influenced the optical analysis, since the mass loss rate appears to have been greatly overestimated, as can be seen by the strong depression in the flux in the region from 1300 to 1450 Å. This range is much better reproduced with the parameters from the hydrodynamic model, which, however, obtains a somewhat smaller terminal velocity. Since this can be solved with a slight correction of $\log g$ within the errors of the optical analysis, we do not consider this a real discrepancy. The He II line is better represented by the model with the higher mass loss rate, which, however, gives a too-strong S V line. Note also that both the O V as well as the O IV line are too strong, suggesting a reduced oxygen abundance.



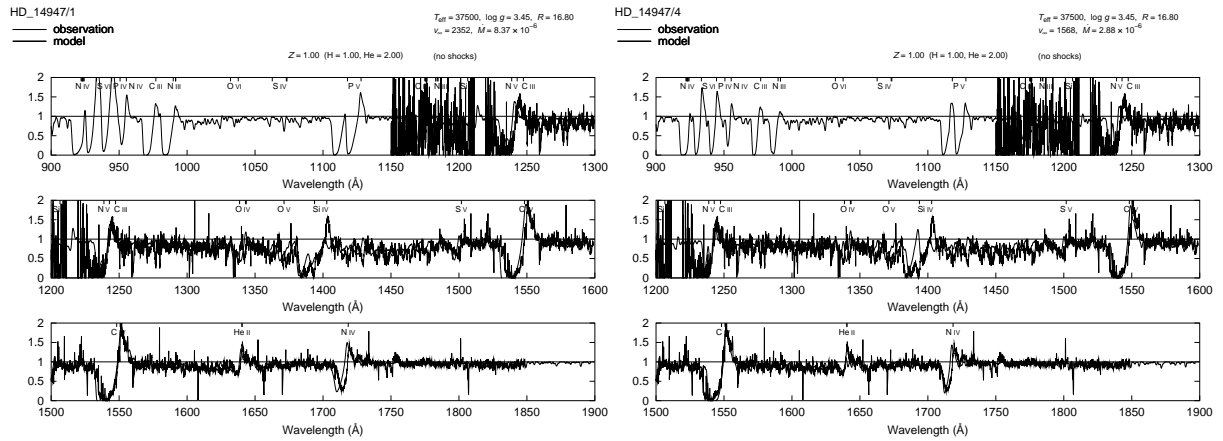
HD 93250. Both models have roughly the same mass loss rate, but the hydrodynamic solution yields a much too high terminal velocity. However, the similarity of the spectrum to that of HD 93129A, which is fitted much better at 42500 K, suggests a reduction in T_{eff} for this star also. This would influence the derived wind parameters, so the comparison for this object is not conclusive.



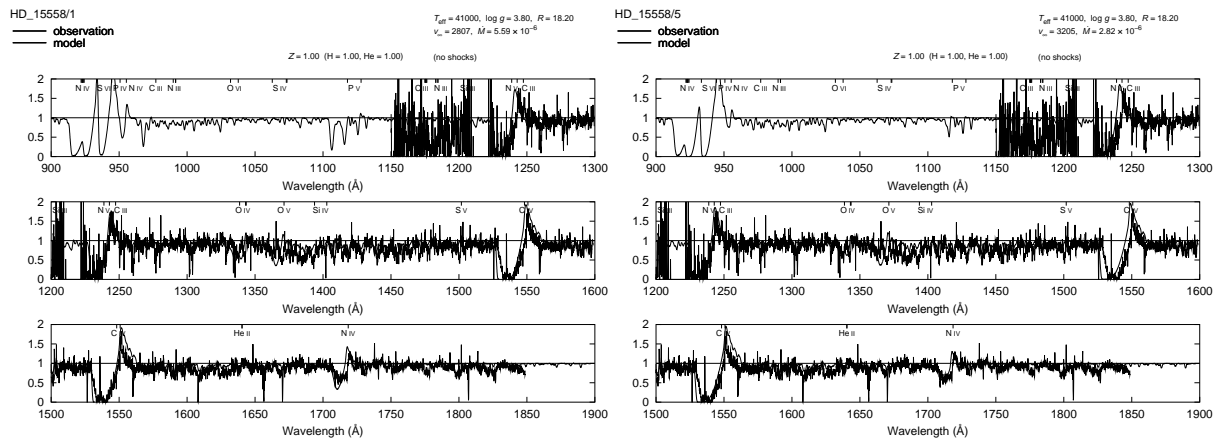
HD 66811. Both models have roughly the same terminal velocity. The mass loss rates differ by more than a factor of 2, but neither model correctly describes the photospheric line forest between 1400 and 1500 Å correctly. The He II line fits better with the mass loss rate from the optical analysis, but C III λ 1176 and S V seem somewhat too strong.



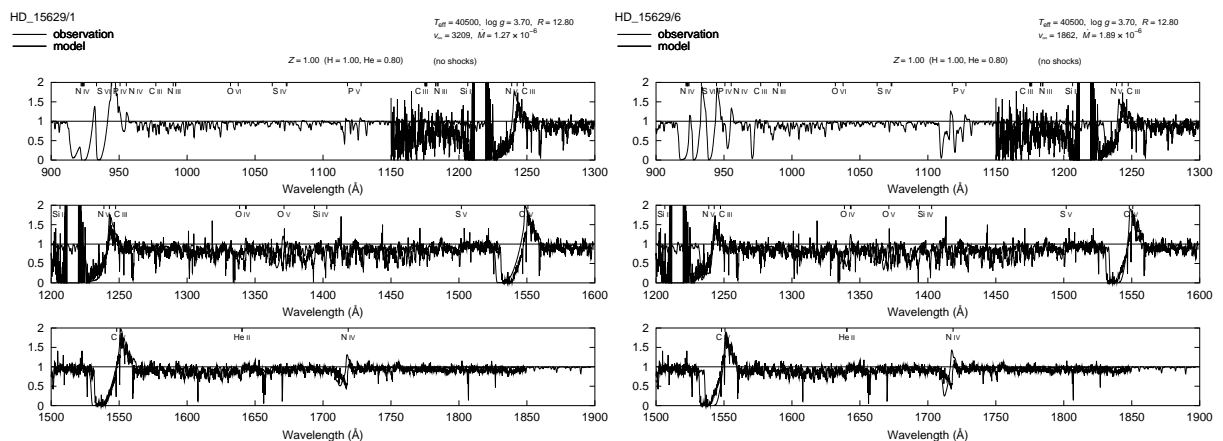
HD 303308. Here the comparison remains indecisive. The hydrodynamic model obtains almost the same terminal velocity, but with a considerably reduced mass loss rate. Since the mass loss rate is very small, however, most of the photospheric lines are hardly affected by the wind, and the strong resonance lines are saturated and show therefore no variation with the mass loss rate. Note that HD 303308 is has also recently been identified as a binary system (Nelán et al. 2003), with uncertain influence on the optical analysis.



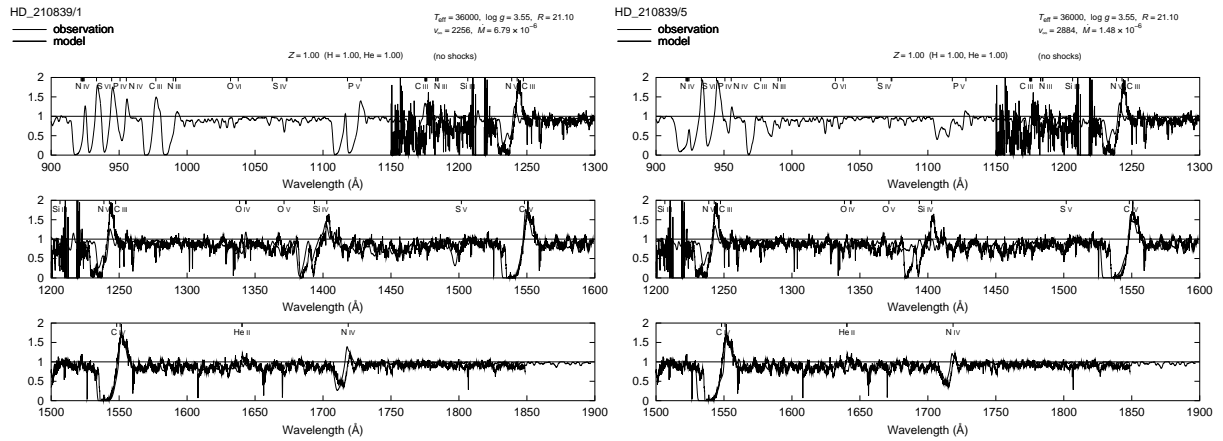
HD 14947. The parameters from the optical analysis represent the spectrum well, in particular the He II line. The terminal velocity from the hydrodynamic model is much too small at this value of $\log g$.



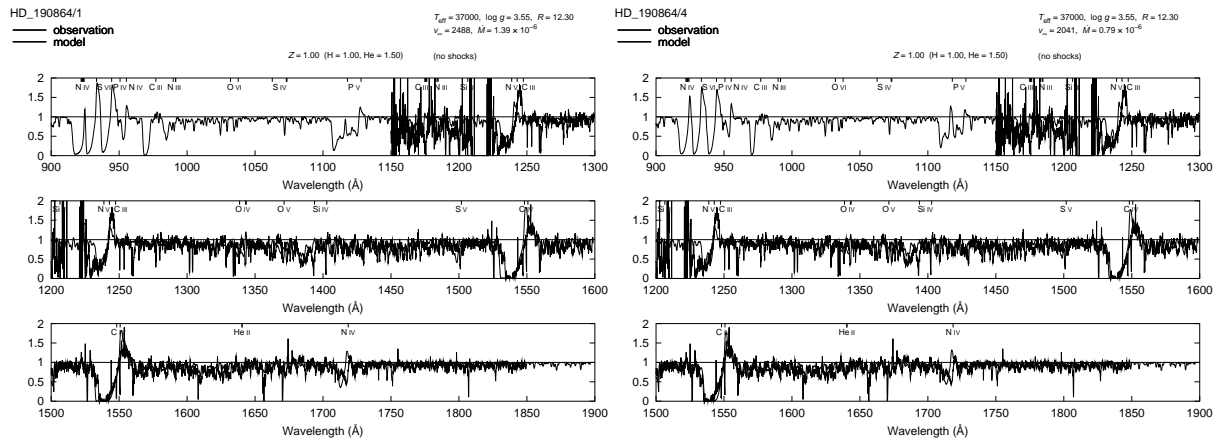
HD 15558. The terminal velocities differ not too much. The lower mass loss rate from the hydrodynamic model seems to fit the spectrum marginally better.



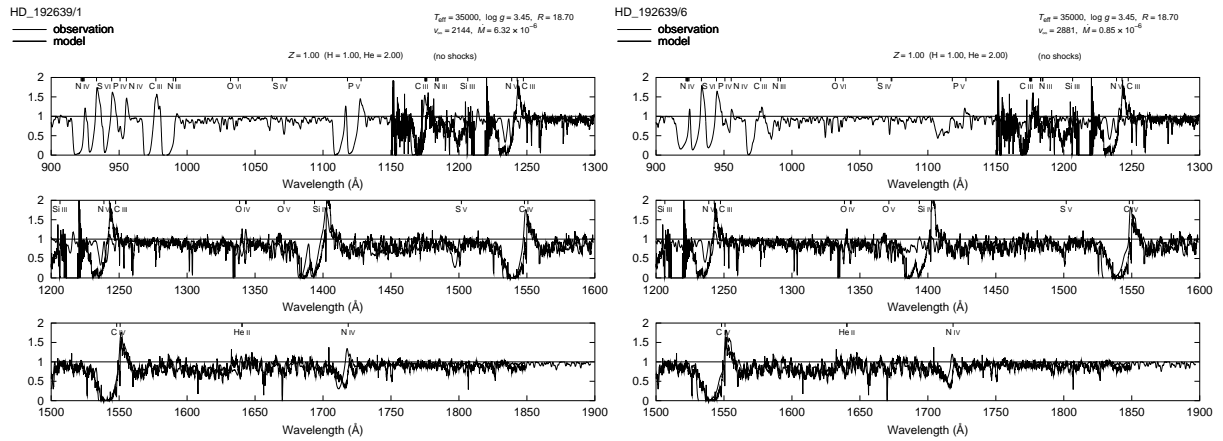
HD 15629. The hydrodynamic model obtains a too small terminal velocity but a somewhat higher mass loss rate. With a small change in $\log g$ both can be brought to good agreement, so we have no real discrepancy in this case.



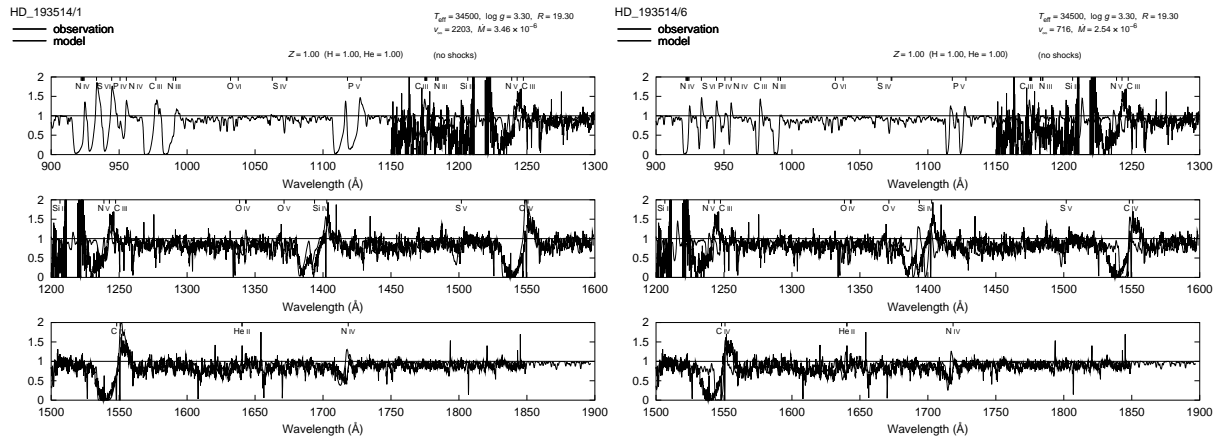
HD 210839. With regard to the Si IV and the He II line, the higher mass loss rate from the optical analysis yields a much better fit to the observed features. On the other hand, it gives a too strong S V line, which fits better with the mass loss rate from the hydrodynamic model. (This might be an abundance issue, which could be checked by comparison with the S IV line, if a corresponding observation were available.) With regard to the iron and nickel line spectrum around 1450 Å, this seems a bit too strong with the parameters from the optical analysis somewhat too weak with those from the hydrodynamic model. A better fit is likely with a slight reduction in log g , which would lower the terminal velocity and increase the mass loss rate of the hydrodynamic model.



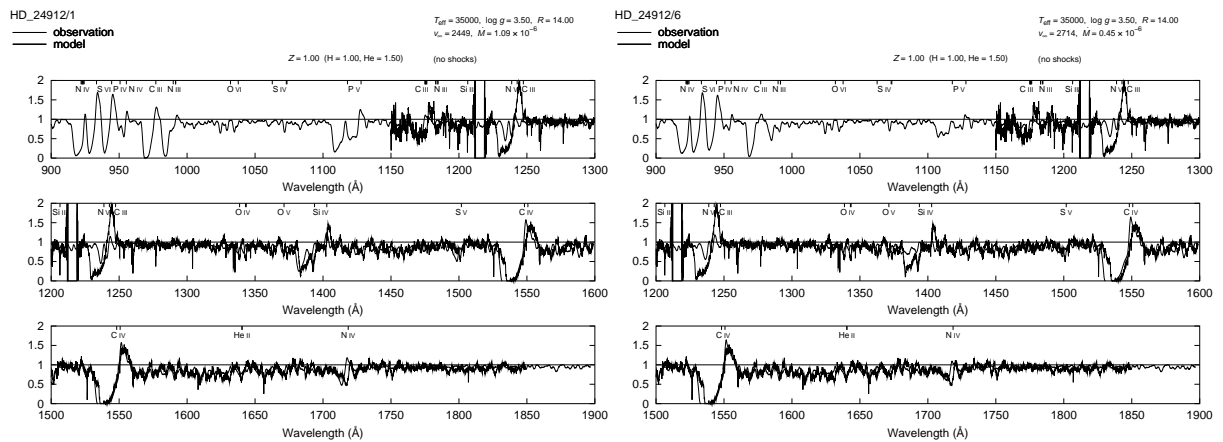
HD 190864. The terminal velocities are roughly similar, but the one from the hydrodynamic model fits the C IV resonance line better. With regard to the mass loss rates, Si IV fits better with the larger mass loss rate from the optical analysis, whereas S V is too strong in this case, and fits better with the smaller mass loss rate from the hydrodynamic model.



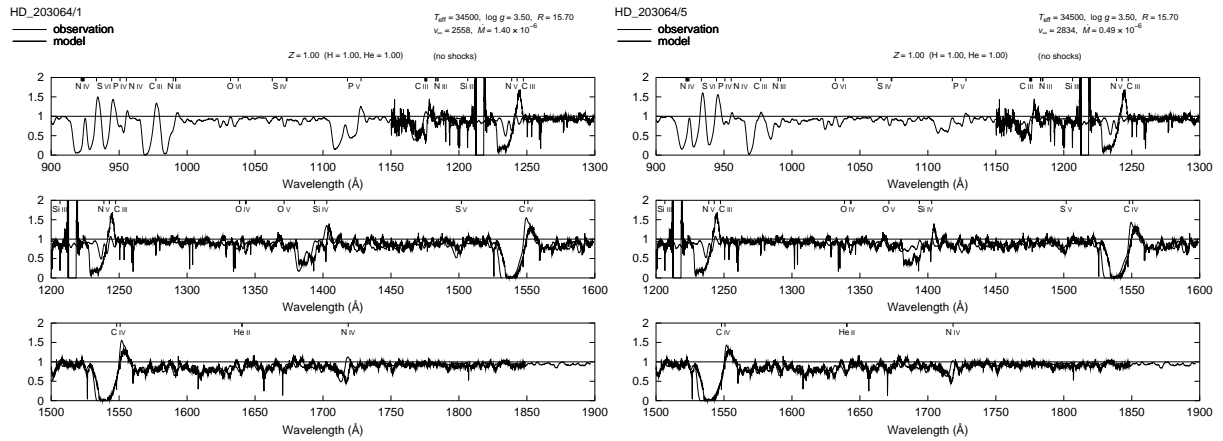
HD 192639. Analogous situation to that of HD 210839. Si iv and C iii fit better with the higher mass-loss rate of the optical analysis, whereas S v and the photospheric line forest are better represented with the lower mass loss rate of the hydrodynamic model.



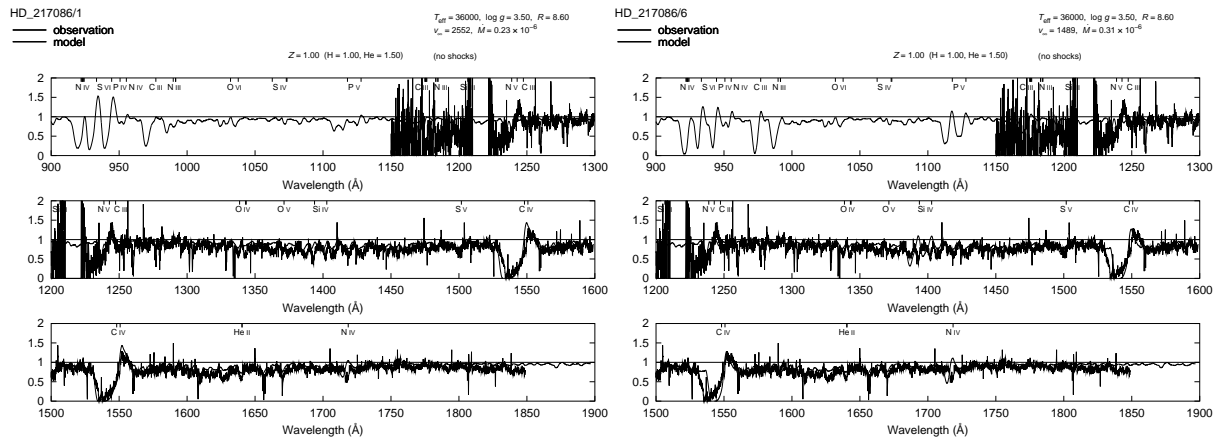
HD 193514. The hydrodynamic model yields a much too small terminal velocity, making a comparison difficult. With regard to the parameters from the optical analysis, we again have the situation of an essentially perfect fit of the Si iv line, while the S v line is somewhat too strong. Note also that despite the noise in the observed spectrum the C iii subordinate line at 1175 Å is clearly much too strong.



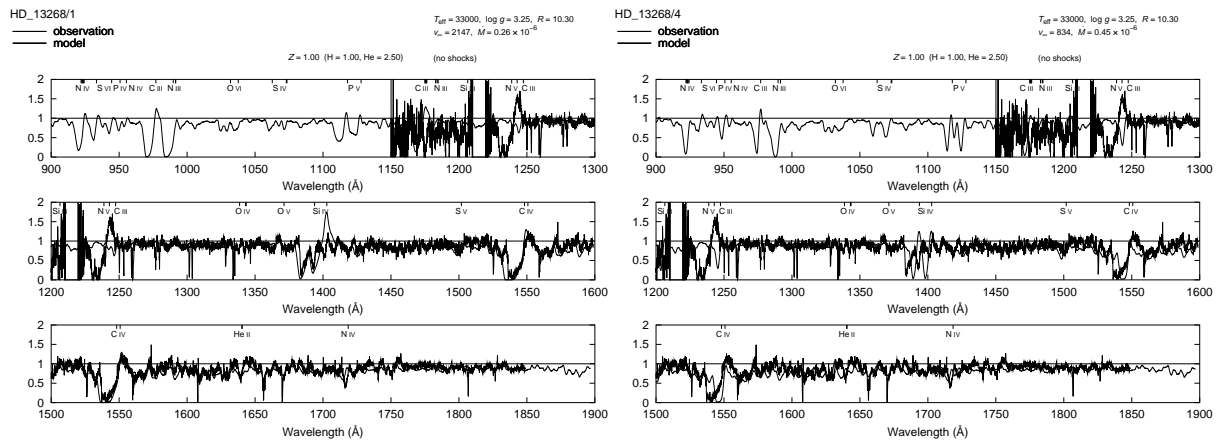
HD 24912. Almost perfect fit to the Si iv line with the parameters of the optical analysis, a better fit to the C iii line, but a somewhat too strong S v line. Otherwise, no significant differences.



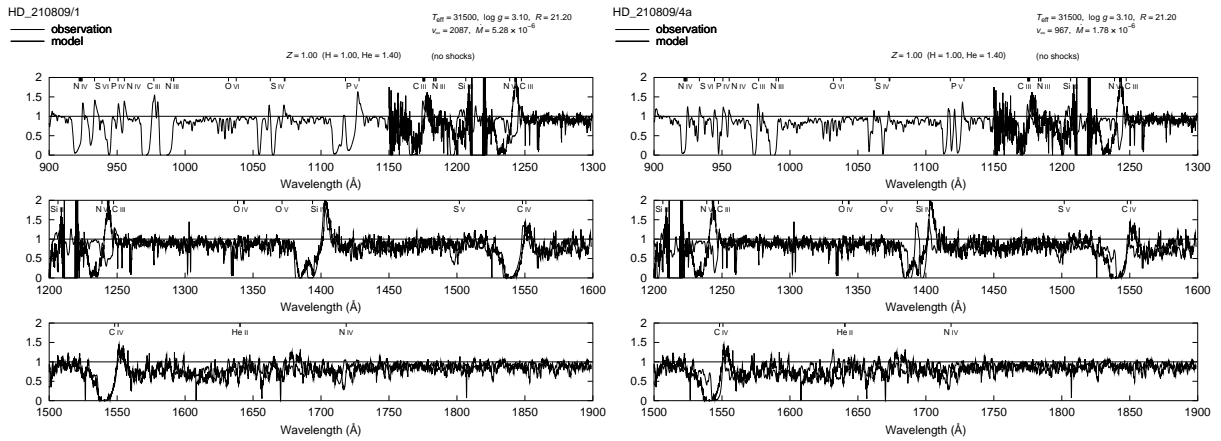
HD 203064. Same situation as with HD 24912.



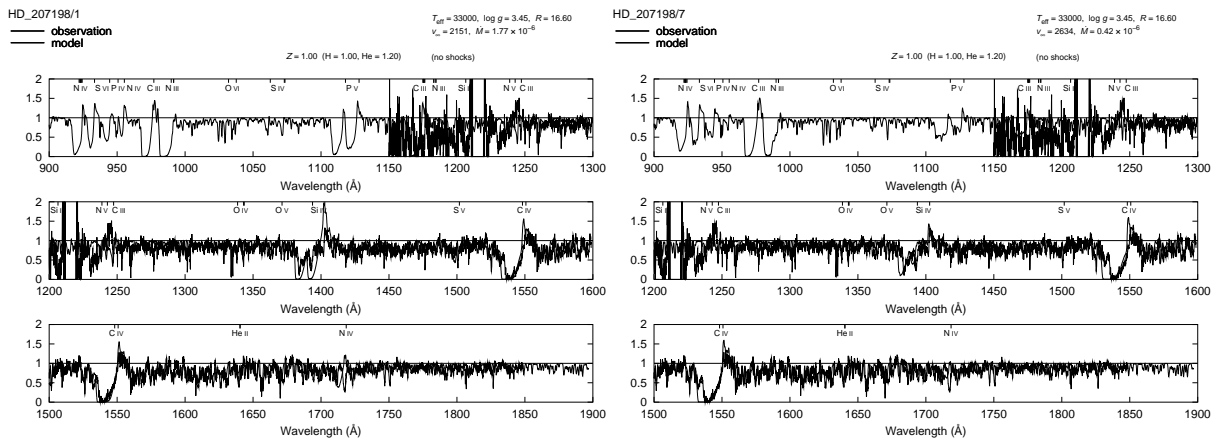
HD 217086. Essentially no discrepancy. The hydrodynamic model gives a higher mass loss rate but a lower terminal velocity. A slight correction of $\log g$ would bring these in agreement.



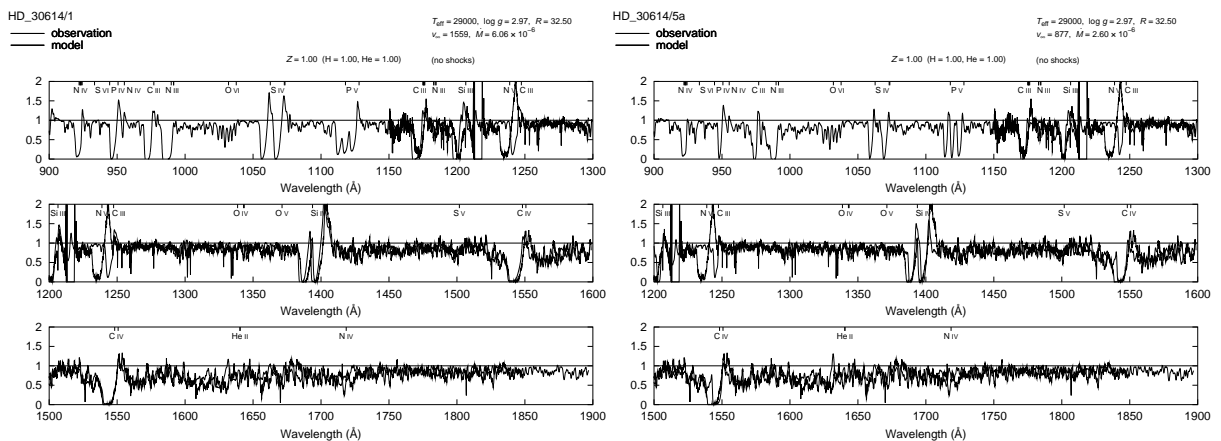
HD 13268. The parameters from the optical analysis yield a too strong Si iv line and a too strong C iii line. The hydrodynamic model gives a too small terminal velocity and a too strong mass loss rate, so a comparison is difficult. However, increasing $\log g$ to obtain the observed terminal velocity is likely to also lead to an improvement with regard to the mass loss rate.



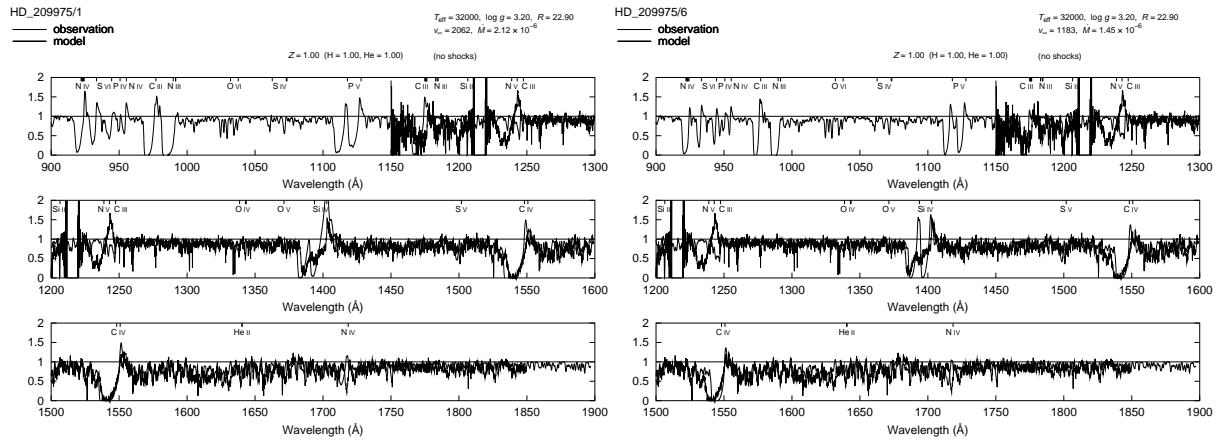
HD 210809. The parameters from the optical analysis yield a good overall fit; the S v is a bit too strong. The hydrodynamic model gives a too small terminal velocity, making this comparison difficult.



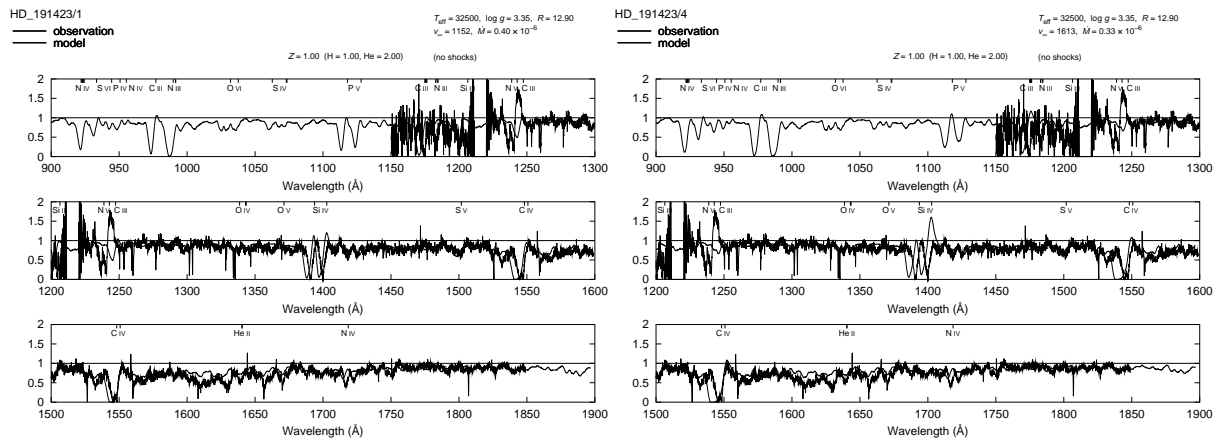
HD 207198. The parameters from the optical analysis lead to a much too strong Si iv line. The lower mass loss rate from the hydrodynamic model fits the observed spectrum much better, despite the too-high terminal velocity.



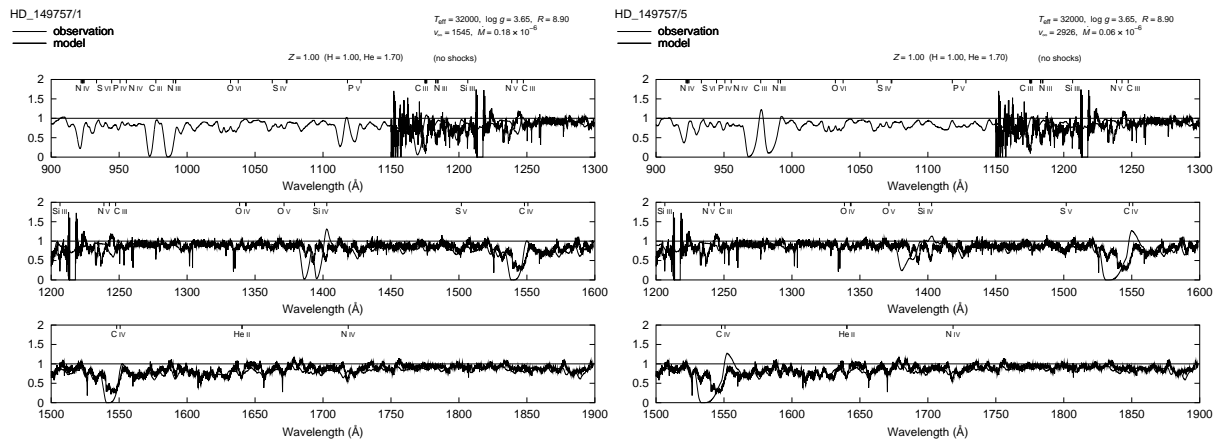
HD 30614. The parameters from the optical analysis yield an almost perfect fit to the spectrum. (Note that these are nearly the same parameters as derived by Pauldrach, Hoffmann, and Lennon (2001), appendix D.) The terminal velocity from the hydrodynamic model is much too small, suggesting a larger $\log g$ for this star.



HD 209975. The mass loss rate from the optical analysis leads to a somewhat too strong Si iv line. Again the terminal velocity from the hydrodynamic model is much too small.



HD 191423. The terminal velocity seems to have been overestimated by Puls et al. (1996), but otherwise the spectrum is reproduced well with the parameters from the optical analysis. The hydrodynamics yields a somewhat too large terminal velocity but a lower mass loss rate. No real discrepancy, since a slight change in $\log g$ can bring the models in good agreement. (Note that the correct slopes of the blue edges of the strong P Cygni profiles is only the result of the convolution with the rotational profile ($v_{\text{rot}} \sin i = 400 \text{ km/s}$); the intrinsic profiles are significantly steeper.)



HD 149757. Except for HD 93250, this is the only star in the sample with an unsaturated C IV resonance line. Both the optical analysis and the hydrodynamic model yield too-strong Si IV and C IV lines. The fit of the photospheric line forest is marginally better with the lower mass loss rate from the hydrodynamic model.

Appendix

B

Wind models for O-type stars

T. L. Hoffmann, A. W. A. Pauldrach

*Institut für Astronomie und Astrophysik der Universität München,
Scheinerstraße 1, 81679 München, Germany*

Abstract. We present fully consistent models for O-type stars that reproduce the observed UV spectra simultaneously with the observed terminal velocities and mass loss rates. We demonstrate how, as a consequence, the models can be used to determine the stellar parameters from the observed UV spectra alone.

1. Comparison with observations

For a detailed description of the treatment of non-LTE, radiation transfer, and line blocking and blanketing in our models we refer to Pauldrach et al. (2001). Here we focus on the aspect of consistent hydrodynamics which we have recently incorporated into our procedure (see Pauldrach and Hoffmann 2002), and show that these models can well reproduce all main features of the observed winds of individual massive O stars.

To test the quality of the models we have selected a sub-sample with well-known parameters and a wide temperature range from the sample of stars analyzed by Puls et al. (1996), for which we have computed models with hydrodynamics and NLTE iterated to consistency. (The hydrodynamics affects the NLTE model via density structure and velocity field (radiative transfer with Doppler-shifted spectral lines), but in turn is controlled by the line force determined by the occupation numbers and radiative transfer of the NLTE model.)

For the same stellar parameters (T_{eff} , $\log g$, R) our models give terminal velocities (v_{∞}) within 10% of the observed values and mass loss rates (\dot{M}) within a factor of 2 of those determined by Puls et al., as shown in Fig. 1. Since the analysis by Puls et al. did not yet include line blanketing, we expect the remaining small discrepancies to be further reduced by the currently ongoing reanalysis of the sample with an up-to-date method.

2. Determining stellar parameters from the UV spectrum

Consistent hydrodynamics provides the link between the stellar parameters (T_{eff} , $\log g$, R) and the wind parameters (v_{∞} , \dot{M}); it is the interplay of the NLTE model and the hydrodynamics that determines the appearance of the UV spectrum. Computing the wind dynamics consistently permits not only the determination of the wind parameters from given stellar parameters, but conversely makes it possible to obtain the stellar parameters from the observed UV spectrum alone.

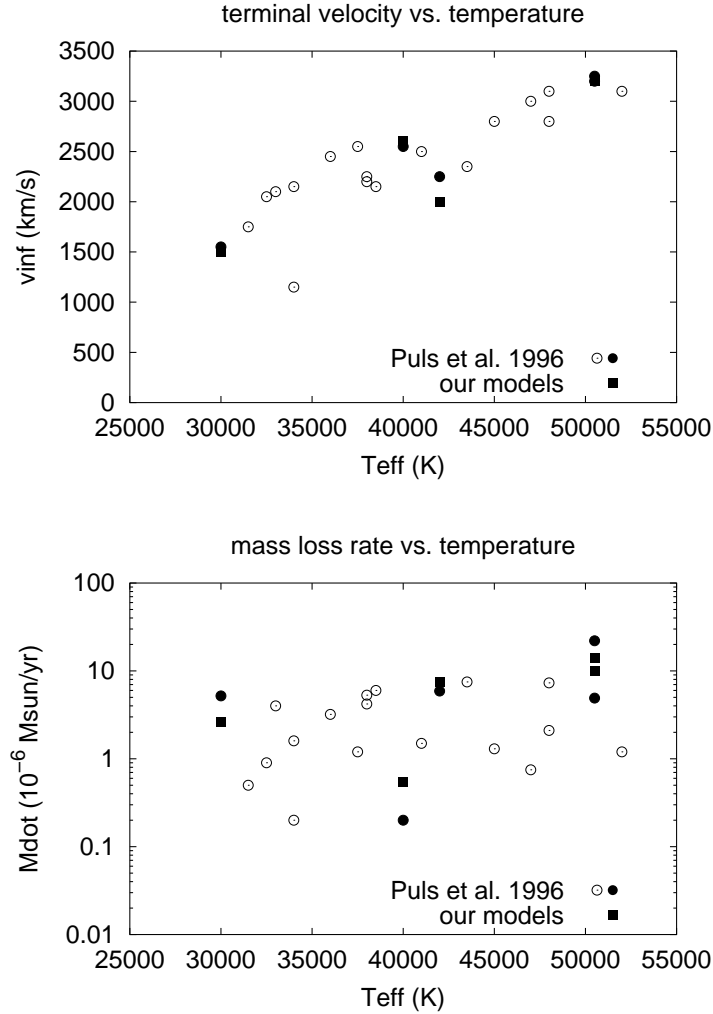


Figure 1. Terminal velocities (top) and mass loss rates (bottom) computed for a subsample (filled symbols) of the sample of Galactic O stars analyzed by Puls et al. (1996). Squares denote the values predicted by our model calculations, circles represent the corresponding observed values.

Although this idea is not new (see Pauldrach et al. 1988, Kudritzki et al. 1992), only the recent generation of models has reached the degree of sophistication that makes such a procedure practicable instead of purely academic. An application of this method to O-type central stars of planetary nebulae is given by Pauldrach et al. (these proceedings).

To briefly illustrate the effect of a change in radius and gravity on the spectra and wind parameters, we have calculated a grid of models with $T_{\text{eff}} = 40000$ K and consistent wind dynamics, using radii from 15 to $25 R_{\odot}$ and $\log g$ from 3.4

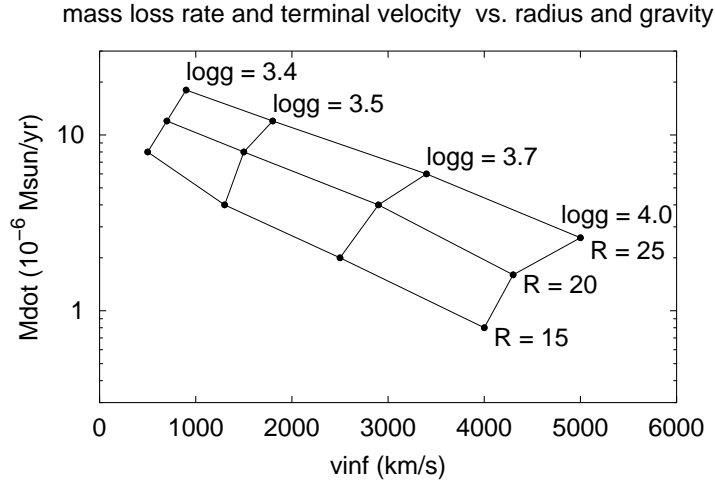


Figure 2. Mass loss rates and terminal velocities computed for a grid of models at $T_{\text{eff}} = 40000$ K.

to 4.0 The resulting mass loss rates and terminal velocities are plotted in Fig. 2, the corresponding UV spectra are shown in Fig. 3. In principle, one can now immediately read off the stellar parameters simply by comparing an observed UV spectrum to such a grid at the appropriate effective temperature.

Acknowledgments. This work was supported by the DLR under grant 50 OR 9909 2.

References

- Kudritzki R.-P., Hummer D. G., Pauldrach A. W. A., et al., A&A 257, 655 (1992)
- Pauldrach A. W. A., Puls J., Kudritzki R.-P., et al., A&A 207, 123 (1988)
- Pauldrach A. W. A., Hoffmann T. L., Méndez R. H., these proceedings
- Pauldrach A. W. A., Hoffmann T. L., Lennon M., A&A 375, 161 (2001)
- Pauldrach A. W. A., Hoffmann T. L., A&A in press (2002)
- Puls J., Kudritzki R.-P., Herrero A., et al., A&A 307, 171 (1996)

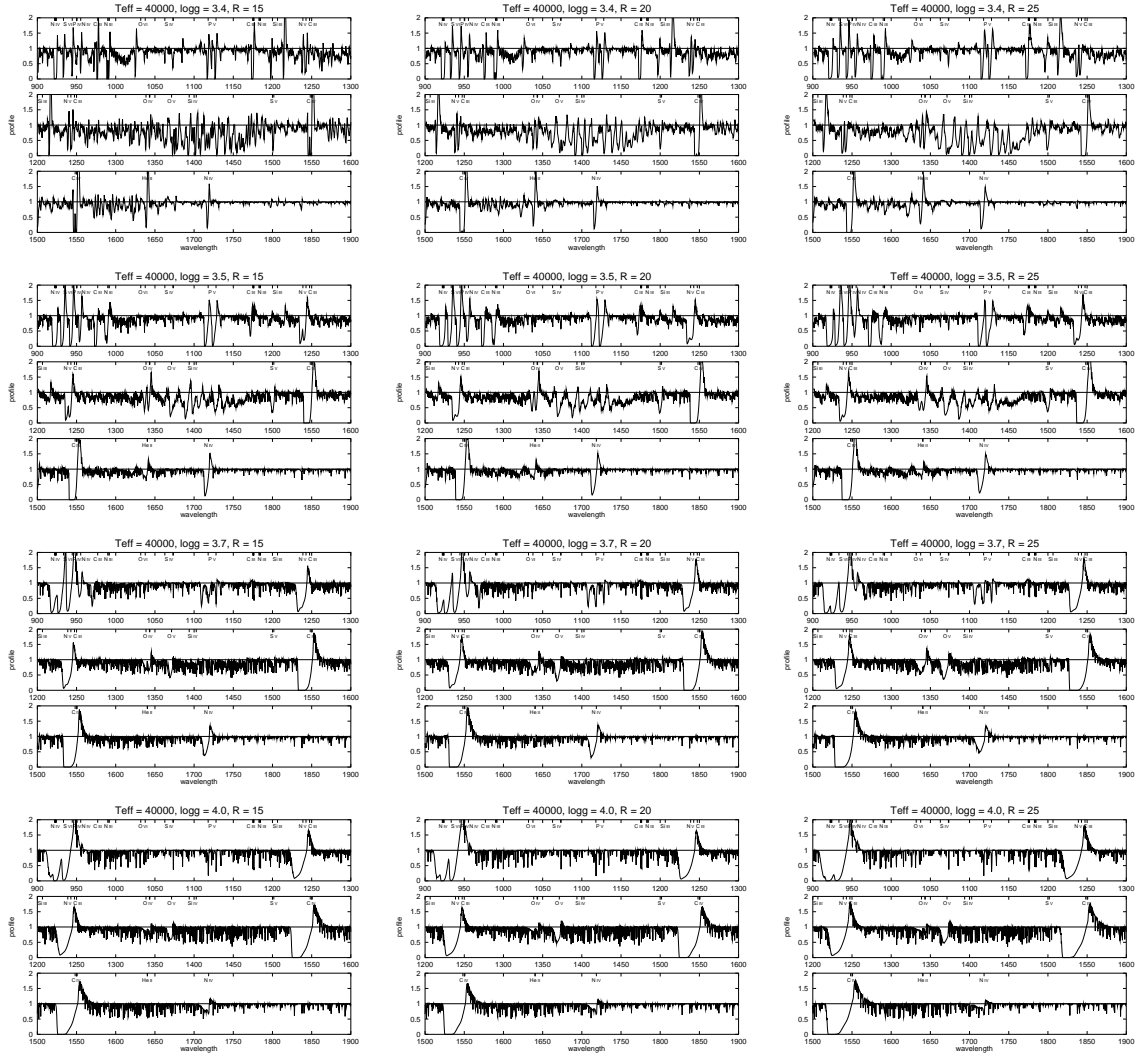


Figure 3. Synthetic UV spectra computed for the grid of models from Fig. 2. R increases from $15R_{\odot}$ (left) to $25R_{\odot}$ (right), $\log g$ from 3.4 (top) to 4.0 (bottom).

Appendix

C

Wind models and synthetic UV spectra for O-type stars

T. L. Hoffmann, A. W. A. Pauldrach, J. Puls

Universitätssternwarte München, Scheinerstraße 1, D-81679 München

Abstract. Spectral analysis of hot stars requires adequate model atmospheres which take into account the effects of non-LTE and radiation-driven winds properly. Here we present significant improvements of our approach in constructing detailed atmospheric models and synthetic spectra for O-type stars (model code *WM-basic*; see Pauldrach, Hoffmann, & Lennon 2001). The most important ingredients of these models with regard to a realistic description of stationary winds are: (1) a rigorous treatment of line blocking and blanketing; (2) a consistent determination of the radiative line acceleration; (3) a considerably improved and enhanced atomic data archive providing the basis for a detailed multilevel non-LTE treatment and an adequate representation of the radiative line driving; and (4) the inclusion of EUV and X-ray radiation produced by cooling zones originating from shock-heated matter. This new tool not only allows to constrain the properties of stellar winds, the stellar parameters, and the abundances via a comparison of observed and synthetic spectra, but also provides the astrophysically important information about the ionizing fluxes of these stars. We use this new method to compute selfconsistent wind parameters for a series of galactic stars analyzed in the optical and verify the theoretically predicted dependence of the wind momentum on metallicity.

1. Comparison with observed values

The large sample of Galactic O-stars from Puls et al. (1996) is currently being reanalyzed with an improved model code also including line blanketing effects (cf. Puls et al., these proceedings); we have computed the selfconsistent wind dynamics for the newly determined stellar parameters. The resulting wind momenta are shown in figure 1 (*LC* denotes luminosity class). In contrast to the optical analysis by means of unclumped models by Puls et al., the hydrodynamic models do not show evidence of different wind-momentum–luminosity relations for different luminosity classes.

We note, however, that for several of the stars the synthetic UV spectrum resulting from the models with the given stellar parameters is incompatible with the observed UV spectrum. While no attempt has been made at this point to reproduce the UV spectra (this would require changes of radii and/or gravities), such a procedure using our consistent hydrodynamic models would, in principle, allow the determination of stellar radii and gravities from the UV spectrum alone (cf. Kudritzki et al. 1992; Hoffmann & Pauldrach 2002), since both the mass loss rate and the terminal velocity depend on the stellar parameters (surface gravity, radius, and luminosity) through the interplay of radiative forces and gravitation.

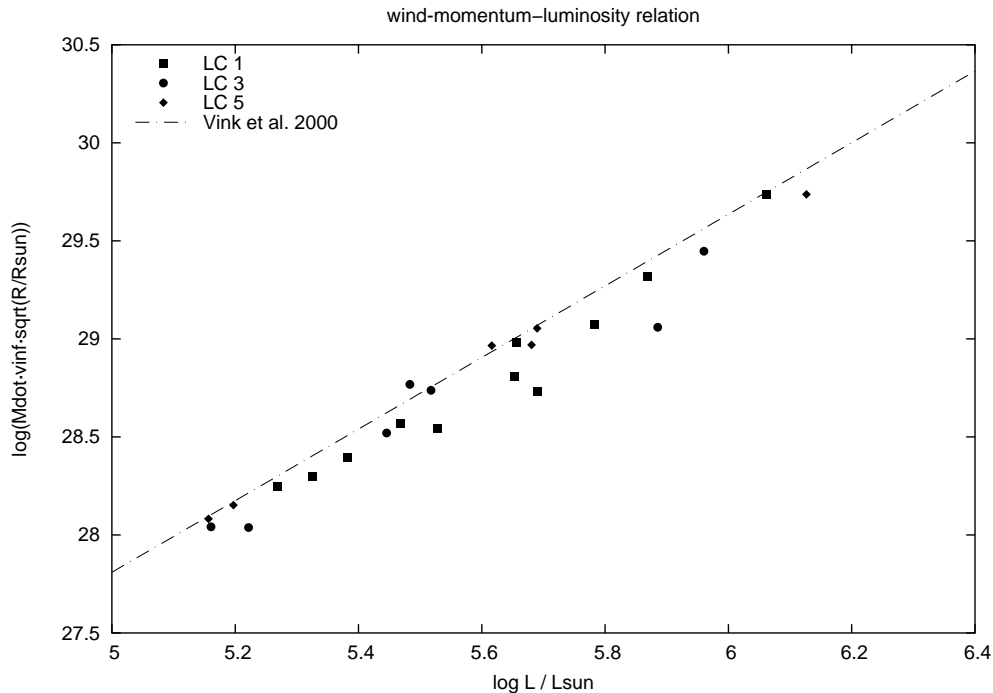


Figure 1. Wind momenta computed for the stellar parameters derived for a sample of Galactic O stars using the improved FASTWIND code (cf. Puls et al., these proceedings).

On the other hand, the method by Puls et al. cannot intrinsically determine the radii; they are based on the distances given in the literature and the optical fluxes from the models. Thus, some uncertainty remains in the derived stellar parameters, which we hope to resolve with an analysis of a sample of O-stars in M31, where the differential error in the distances is negligible.

2. Dependence of wind momentum on metallicity

To study the dependence of the wind strengths on metallicity we have calculated selfconsistent wind models for a grid of stellar models (consisting of a dwarf and a supergiant sequence) at solar and one-fifth solar metallicity. The stellar parameters were chosen so as to reproduce the observed parameters for these types of stars while at the same time covering a large range in luminosities. Theory predicts that the wind momentum should scale with the metallicity z as $z^{(1-\alpha)/\alpha'}$, where $\alpha - 2$ is the exponent of the line strength distribution function and α' is the reciprocal of the slope of the wind-momentum–luminosity relation. In the Figure on the right, it can be seen that our models quantitatively reproduce this predicted behavior. The filled and open symbols show the calculated wind momenta for solar metallicity and one-fifth solar metallicity stars, respectively. The solid line is a fit to the calculated wind momenta for solar metallicity; the dashed line is this relation scaled by the factor above using a

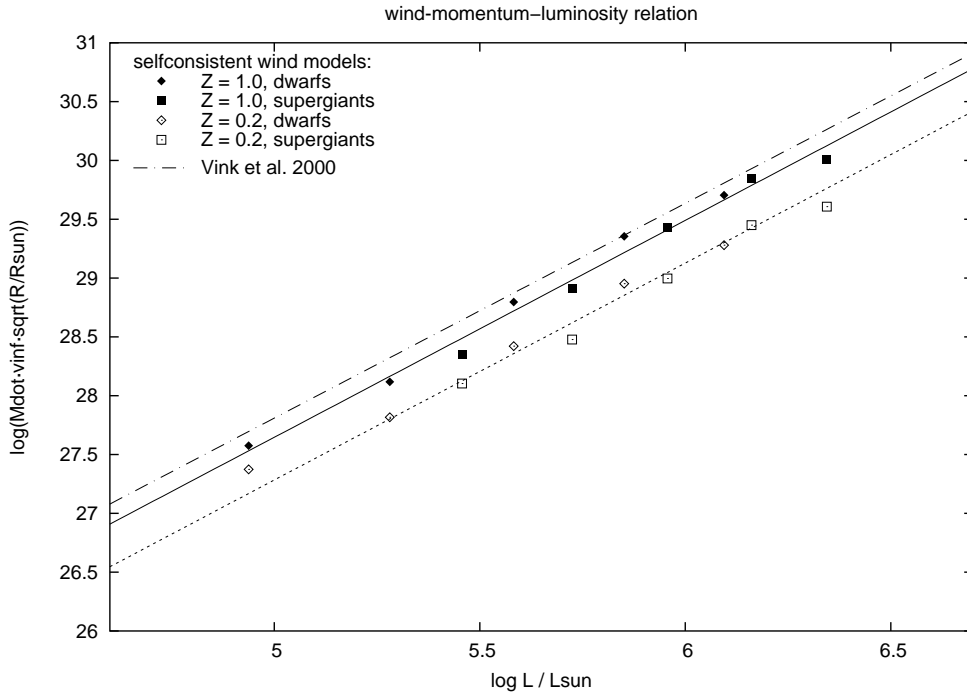


Figure 2. Wind momenta from detailed numerical simulations for a grid of stars at solar and one-fifth solar metallicity.

value of $z = 0.2$, yielding wind momenta in good agreement with the calculated ones for $z = 0.2z_{\odot}$. For comparison, we have also plotted the relation (for solar metallicity stars) as found by Vink et al. 2000 (dash-dotted).

Acknowledgments. This work has been supported by the DLR under grant RD-RX-50 OR 9909 2.

References

- Hoffmann T. L., Pauldrach A. W. A., proc. IAU Symp. 209 (2002)
 Kudritzki R.-P., Hummer D. G., Pauldrach A. W. A., et al., A&A 257, 655 (1992)
 Pauldrach A. W. A., Hoffmann T. L., Lennon M., A&A 375, 161 (2001)
 Puls J., Kudritzki R.-P., Herrero A., et al., A&A 307, 171 (1996)
 Puls J., Repolust T., Hoffmann T., Jokuthy A., Venero R., these proceedings
 Vink J. S., de Koter A., Lamers H. J. G. L. M., A&A 362, 295 (2000)

Appendix

D

Radiation-driven winds of hot luminous stars

XIII. A description of NLTE line blocking and blanketing towards realistic models for expanding atmospheres

A. W. A. Pauldrach, T. L. Hoffmann, and M. Lennon

Institut für Astronomie und Astrophysik der Universität München, Scheinerstraße 1, D-81679 München, Germany

Received (date) / Accepted (date)

Abstract. Spectral analysis of hot luminous stars requires adequate model atmospheres which take into account the effects of NLTE and radiation driven winds properly. Here we present significant improvements of our approach in constructing detailed atmospheric models and synthetic spectra for hot luminous stars. Moreover, as we regard our solution method in its present stage already as a standard procedure, we make our program package *WM-basic* available to the community (download is possible from the URL given below).

The most important model improvements towards a realistic description of stationary wind models concern:

- (i) A sophisticated and consistent description of line blocking and blanketing. Our solution concept to this problem renders the *line blocking influence on the ionizing fluxes* emerging from the atmospheres of hot stars – mainly the spectral ranges of the EUV and the UV are affected – in identical quality as the *synthetic high resolution spectra* representing the observable region. In addition, the line blanketing effect is properly accounted for in the energy balance.
- (ii) The atomic data archive which has been improved and enhanced considerably, providing the basis for a detailed multilevel NLTE treatment of the metal ions (from C to Zn) and an adequate representation of line blocking and the radiative line acceleration.
- (iii) A revised inclusion of EUV and X-ray radiation produced by cooling zones which originate from the simulation of shock heated matter.

This new tool not only provides an easy to use method for O-star diagnostics, whereby physical constraints on the properties of stellar winds, stellar parameters, and abundances can be obtained via a comparison of observed and synthetic spectra, but also allows the astrophysically important information about the ionizing fluxes of hot stars to be determined automatically. Results illustrating this are discussed by means of a basic model grid calculated for O-stars with solar metallicity. To further demonstrate the astrophysical potential of our new method we provide a first detailed spectral diagnostic determination of the stellar parameters, the wind parameters, and the abundances by an exemplary application to one of our grid-stars, the O9.5Ia O-supergiant α Cam. Our abundance determinations of the light elements indicate that these deviate considerably from the solar values.

Key words. Line: formation – Stars: atmospheres – Stars: early type – Stars: mass-loss – Stars: individual: α Cam – X-rays: stars

1. Introduction

Spectral analyses of hot luminous stars are of growing astrophysical interest as they provide a unique tool for the determination of the properties of young populations in galaxies. This objective, however, requires spectral observation of individual objects in distant galaxies. That this is feasible has already been shown by Steidel et al. (1996) who detected galaxies at high redshifts ($z \sim 3.5$) and

found that the corresponding optical spectra show the typical features usually found in the UV spectra of hot stars. In order to determine stellar abundances and physical properties of the most UV-luminous stars in at least the Local Group galaxies via quantitative UV spectroscopy another principal difficulty needs to be overcome: the diagnostic tools and techniques must be provided. This requires the construction of detailed atmospheric models and synthetic spectra for hot luminous stars. It is a continuing effort of several groups to develop a standard code for solving this problem. Recent basic papers of the differ-

Send offprint requests to: A. W. A. Pauldrach
(<http://www.usm.uni-muenchen.de/people/adi/adi.html>)

ent groups concerning O-stars are Pistinner et al. 1999, Aufdenberg et al. 1998, Schaerer and de Koter 1997, Pauldrach et al. 1994, 1994a, 1998, Drew 1989, 1990, and Abbott and Hummer 1985; and concerning WR-stars, Hamann and Koesterke 1998 and Hillier and Miller 1998.

The most important output of this kind of model calculation are the ionizing fluxes and synthetic spectra emitted by the atmospheres of hot stars. As these spectra consist of hundreds of not only strong, but also weak wind-contaminated spectral lines which form the basis of a quantitative analysis, and as the energy distribution from hot stars is also used as input for the analysis of emission line spectra (e. g., of gaseous nebulae) which depend sensitively on the structure of the emergent stellar flux, a sophisticated and well tested method is required to produce these data sets accurately.

However, developing such a method is not straightforward, since modelling hot star atmospheres involves replicating a tightly interwoven mesh of physical processes: the equations of radiation hydrodynamics including the energy equation, the rate equations for all important ions (from H to Zn) including the atomic physics, and the radiative transfer equation at all transition frequencies have to be solved simultaneously.

The most complicating effect in this system is the overlap of thousands of spectral lines of different ions. Especially concerning this latter point we have made significant progress in developing a fast numerical method which accounts for the blocking and blanketing influence of all metal lines in the entire sub- and supersonically *expanding atmosphere*.

As we have found from previous model calculations that the behavior of most of the UV spectral lines depends critically on a detailed and consistent description of *line blocking and line blanketing* (cf. Pauldrach 1987, Pauldrach et al. 1990, Pauldrach et al. 1994, Sellmaier et al. 1996, Taresch et al. 1997, Haser et al. 1998; this has also been pointed out by Schaerer and Schmutz 1994, Schaerer and de Koter 1997, and Hillier and Miller 1998), special emphasis has been given to the correct treatment of the Doppler-shifted line radiation transport, the corresponding coupling with the radiative rates in the rate equations, and the energy conservation.

In Section 3 we will demonstrate that the realistic and consistent description of line blocking and blanketing and the involved modifications to the models lead to changes in the energy distributions, ionizing continua, and line spectra with much better agreement with the observed spectra when compared to previous, not completely consistent models. This will obviously have important repercussions for the quantitative analysis of hot star spectra.

In the next two sections we will first summarize the general concept of our procedure and then discuss the current status of our treatment of hydrodynamical expanding atmospheres.

2. The general method

The basis of our approach in constructing detailed atmospheric models for hot luminous stars is the concept of *homogeneous, stationary, and spherically symmetric radiation driven winds*, where the expansion of the atmosphere is due to scattering and absorption of Doppler-shifted metal lines (Lucy and Solomon 1970). In contrast to previous papers of this series, the above approximations are now the most significant ones for the present approach. These approximations are, however, quite restrictive, since only the time-averaged mean of the observed spectral features can be described correctly by our method. Nevertheless we believe that it is reasonable to continue with the stationary, spherically symmetric approach and to improve its inherent physics, since the detailed comparison with the observations, which is the only way to demonstrate the reliability of this concept, leads to promising results (cf. Section 4).

Before we describe the latest improvements in detail we first summarize the principal features of our procedure of simulating the atmospheres of hot stars. (For particular points, a comprehensive discussion is also found in the papers cited above.)

Figure 1 gives an overview of the physics to be treated in various iteration cycles. A complete model atmosphere calculation consists of three main blocks,

- (i) *the solution of the hydrodynamics*
- (ii) *the solution of the NLTE-model (calculation of the radiation field and the occupation numbers)*
- (iii) *the computation of the synthetic spectrum*

which interact with each other.

In the first step the **hydrodynamics** is solved in dependence of the stellar parameters (effective temperature T_{eff} , surface gravity $\log g$, stellar radius R_* (defined at a Rosseland optical depth of $2/3$), and abundances Z (in units of the corresponding solar values)) and of pre-specified force multiplier parameters (k_0 , α_0 , δ_0), which are used for describing the radiative line acceleration. In addition, the continuum force is approximated by the Thomson force, and a constant temperature structure ($T(r) = T_{\text{eff}}$) is assumed in this step. In a second step the hydrodynamics is solved by iterating the complete continuum force $g_C(r)$ (which includes the opacities of all important ions) and the temperature structure (both are calculated using a spherical grey model), and the density $\rho(r)$ and the velocity structure $v(r)$. In a final outer iteration cycle these structures are iterated again together with the line force $g_L(r)$ obtained from the spherical NLTE model. (New force multiplier parameters (k , α , δ), which are depth dependent if required, are deduced from this calculation.)¹

The main part of the code consists of the solution of the **NLTE-model**. In this step the radiation field (rep-

¹ This latter step is currently not available for the download version of the code; it will be made available for version 2.0.

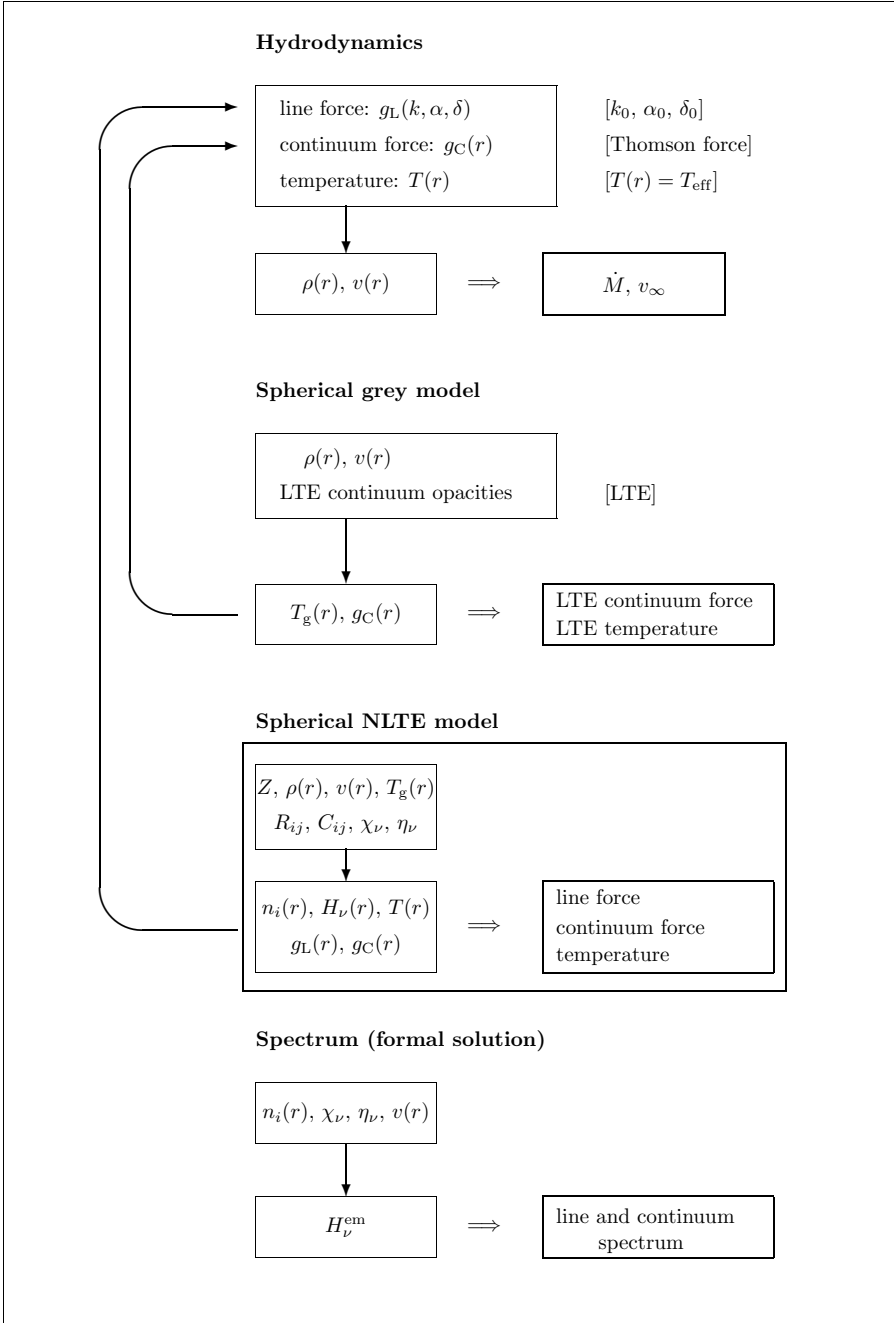


Fig. 1. Sketch of a complete model atmosphere calculation. Starting procedures are presented in brackets. For a discussion see the text.

represented by the Eddington-flux $H_\nu(r)$ and the mean intensity $J_\nu(r)$, the final temperature structure $T(r)$, occupation numbers $n_i(r)$, and opacities χ_ν and emissivities η_ν are computed using detailed atomic models for all important ions. For the solution of the radiative transfer equation the influence of the spectral lines (i. e., the UV and EUV *line blocking*) is properly taken into account in addition to the usual consideration of continuum opacities and source functions consisting of Thomson-scattering and free-free and bound-free contributions of all important ions. Moreover, the *shock source functions* produced by radiative cooling zones which originate from a revised simulation of shock heated matter are also included. For the calculation of the *final NLTE temperature structure*

the *line blanketing* effect, which is a direct consequence of line blocking, is considered by demanding luminosity conservation and the balance of microscopic heating and cooling rates. The *rate equations* which yield the occupation numbers contain collisional (C_{ij}) and radiative (R_{ij}) transition rates, as well as low-temperature dielectronic recombination and Auger-ionization due to K-shell absorption (considered for C, N, O, Ne, Mg, Si, and S) of soft X-ray radiation arising from shock-heated matter. (Further details concerning the solution method of the NLTE-model are described in Section 3.)

The last step consists of the computation of the **synthetic spectrum** for the purpose of comparison with observations. In dependence of the occupation numbers, the

opacities and the emissivities, a formal integral solution of the transfer equation in the observer's frame is performed (cf. Puls and Pauldrach 1990).

As results of the iterative solution of this system of equations we obtain not only the *synthetic spectra and ionizing fluxes* which can be used in order to determine stellar parameters and abundances, but also the hydrodynamical structure of the wind (thus, constraints for the *mass-loss rate* \dot{M} and the *velocity structure* $v(r)$ can be derived).

3. The consistent NLTE model

The construction of realistic models for expanding atmospheres requires a correct and *completely consistent* description of the main part of the simulation, the *NLTE model*. In this regard, the most crucial point in our present improved treatment is an exact description of line blocking and blanketing.

The effect of line blocking – mainly acting in between the He II and the H I edge – is that it influences the ionization and excitation and the momentum transfer of the radiation field significantly. This of course has important consequences for both the spectral line formation and the dynamics of the expanding atmosphere. Nevertheless, it is still not a common procedure to treat the line opacities and emissivities in the radiative transfer equation and their back-reaction on the occupation numbers via the radiative rates *correctly*. We will therefore first discuss the effects of line blocking and blanketing for *expanding atmospheres of hot stars* in more detail.

The huge number of metal lines present in hot stars in the EUV and UV attenuate the radiation in these frequency ranges drastically by radiative absorption and scattering processes (an effect known as *line blocking*). Only a small fraction of the radiation is re-emitted and scattered in the outward direction; most of the energy is radiated back to the surface of the star producing there a *backwarming*. Due to the increase of the Rosseland optical depth (τ_{Ross}) resulting from the opacities enhanced by the line blocking, and, in consequence, of the temperature, the radiation is redistributed to lower energies (this refers to *line blanketing*). In principle these effects influence the NLTE model with respect to:

- (i) the radiative photoionization rates R_{ik} ,
- (ii) the radiative bound-bound rates R_{ij} ,
- (iii) the radiation pressure g_{rad} ,
- (iv) the energy balance.

The terms of the first two items are directly connected to the radiation field, and line blocking in general reduces them considerably. Concerning the third item, the blocked incident radiation reduces the radiative acceleration term in the inner part, whereas it can be enhanced in the outer part due to multiple scattering processes (cf. Puls 1987 and references therein). In contrast to this, the energy equation – last item – is mostly influenced by the impact of the line opacities, and this *blanketing effect* results in

an increased temperature (steeper gradient) in the deeper layers of the photosphere.

Although the method for treating blanketing effects is well established for cold stars, where the atmospheres are hydrostatic and where the assumption of LTE is justified (cf. Kurucz 1979 and 1992), the work to develop an adequate method for hot stars, where not only NLTE effects are prominent, but where the atmospheres are also rapidly expanding, is still under way. (For the various approaches taken to this end, see the references listed in Section 1.) In this case – hot stars with expanding atmospheres – in addition to the four items given above, the solution of the radiative transfer also has to account for the *lineshift* caused by the Doppler effect due to the velocity field. The important effect of this point is that the velocity field increases the frequential range which can be blocked by a single line (see below). In the presence of a velocity field the blocking effect is therefore more pronounced.

Concerning the basic requirements for calculating adequate line opacities and source functions for expanding atmospheres of hot stars we have to concentrate on the following points:

- (1) *consistent* NLTE occupation numbers,
- (2) a complete and accurate line list in connection with detailed atomic models,
- (3) a proper concept for treating the line blocking with due regard to the lineshifts in the wind, in the course of which the method for solving the complete radiative transfer including the spectral lines has to be efficient with regard to computational time,
- (4) a correct treatment of the influence of the blanketing effect on the temperature structure,
- (5) an adequate approximation of the EUV and X-ray radiation produced by cooling zones of shock-heated matter.

3.1. The concept of the solution of ionization and excitation

It is obvious that ionization and excitation plays the major role in calculating the emergent flux and spectrum of a hot star. Therefore, a consistent and accurate description of the occupation numbers is extremely important for a realistic solution of the NLTE model.

Figure 2 presents a sketch of our iteration scheme for the calculation of the occupation numbers. To save more than a factor of 20 in computation time, the iteration is performed in two major steps, which differ mainly in the accuracy achieved by the methods employed: in a *pre-iteration*, a modified opacity sampling technique (method I) is used to take into account in the solution of the radiation transfer the hundreds of thousands of spectral lines in the UV and EUV. The main requirements for this step are that it is sufficiently accurate for the iteration to converge near the final solution, but fast enough to make the model calculation feasible with today's computers. In the *final iterations*, the radiation transfer (taking

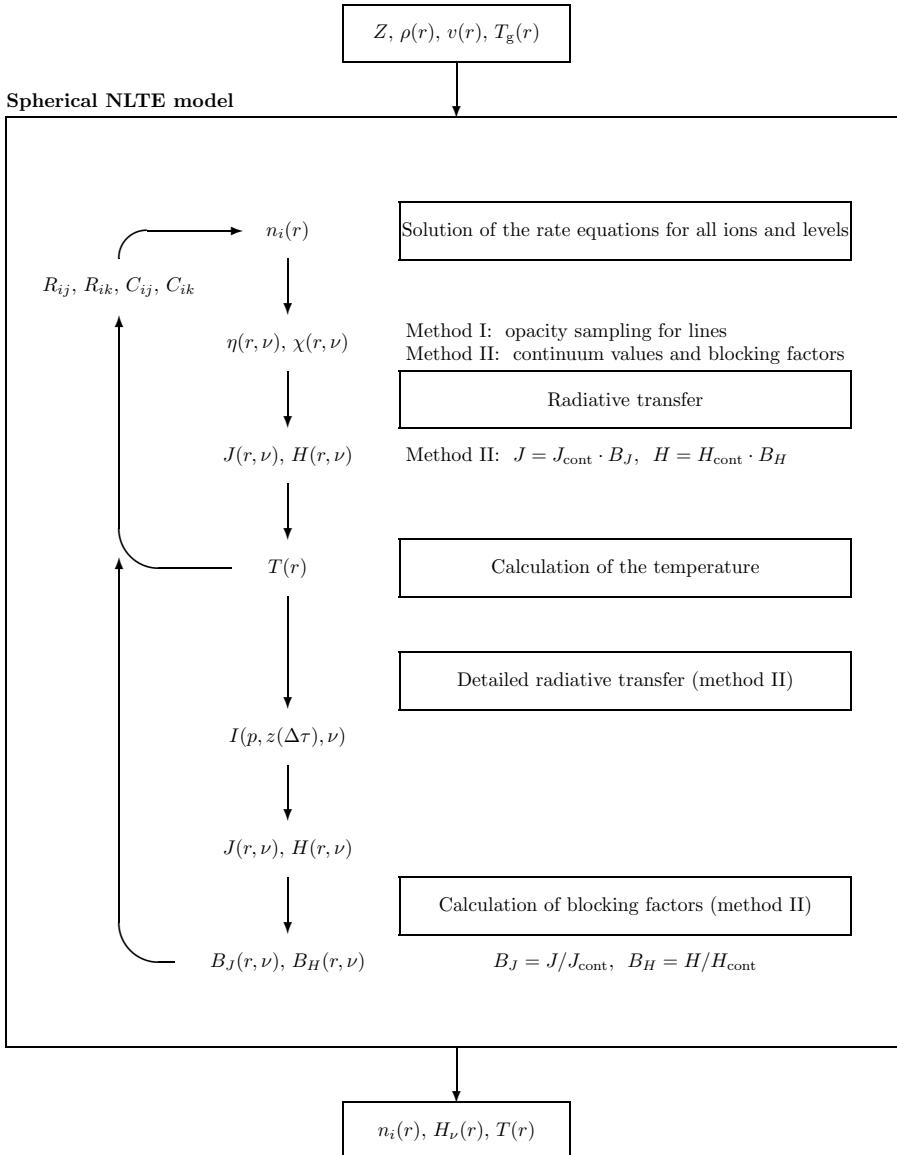


Fig. 2. Iteration scheme for the calculation of the NLTE occupation numbers. An *Accelerated Lambda Iteration* procedure is involved in the blocking and blanketing cycles. Note that two successive iteration cycles of different quality (method I is used for at least 500–600 iterations, and then method II for at least another 30–150 iterations) are applied for the blocking and blanketing part of the model calculation (see text).

into account the same lines as in method I) is calculated with an exact solution of the transfer equation in the observer’s frame (method II). The advantage of this method is that it is free from all major approximations; its disadvantage is its comparatively high computational cost. As the pre-iteration has already converged near the final solution, however, only very few of these final iteration steps are needed. Details are discussed in the following paragraphs.

Note that both methods are used successively – method I for at least 500–600 iterations, and then method II for at least another 30–150 iterations – and the same quantities are iterated (see Fig. 2). Both methods are of course based on the same radius and frequency grids and take into account the same lines. The whole purpose of method I is to give good starting values for the final (real) iteration cycle using method II. In fact, as will be shown below, the starting values produced by method I turned out to be rather excellent.

In dependence of the abundances (Z), the density ($\rho(r)$) and velocity ($v(r)$), and a pre-specified temperature structure ($T_g(r)$) (see Section 2), the occupation numbers are determined by the rate equations containing collisional (C_{ij}) and radiative (R_{ij}) transition rates. The most crucial dependency of the rates is not the density, which is nevertheless important for the collisional rates and the equation of particle conservation, but the velocity field which enters not only directly into the radiative rates via the Doppler shift, but also indirectly through the radiation field determined by the equation of transfer, which in turn is again dependent on the Doppler shifted line opacities and emissivities.

For the calculation of the radiative bound-bound transition probabilities R_{ij} we make use of the Sobolev-plus-continuum method (Hummer and Rybicki 1985; Puls and Hummer 1998). Only for some weak second-order lines in the subsonic region of the atmospheric layers where the continuum is formed might this be just a poor approxima-

tion (cf. Sellmaier et al. 1993). A more important point of our procedure concerns the problem of *self-shadowing* (cf. Pauldrach et al. 1998). This problem occurs because the rate equations are not really solved simultaneously with the radiative transfer, but instead in the framework of the accelerated lambda iteration (*ALI*), in which the radiation field and the occupation numbers are alternately computed (cf. Pauldrach and Herrero 1988). Hence, the radiation field which enters into a bound-bound transition probability is already affected by the line itself, since the line has also been considered for the blocking opacities. This procedure will lead to a systematic error if a line transition dominates within a frequency interval (see Section 3.3.1). The solution for correctly calculating the bound-bound rates even in these circumstances is quite simple and has been described by Pauldrach et al. (1998, Section 3.2).

The spherical transfer equation yields the radiation field at 2,500 frequency points (see below) and at every depth point, including the layers where the radiation is thermalized and hence the diffusion approximation is a proper boundary condition. The solution includes all relevant opacities. In particular, the effects of wind and photo-spheric EUV line blocking on the ionization and excitation of levels are treated on the basis of 4 million lines, with proper consideration of the influence of the velocity field on the line opacities and emissivities and on the radiative rates.

Regarding the latter point, the inclusion of line opacities and emissivities in the transfer equation, two different concepts are employed for iterating the occupation numbers and the temperature structure until a converged radiation field ($J_\nu(r)$ and $H_\nu(r)$) is obtained. In a first step, a pre-iteration cycle with an opacity sampling method is used (method I). This procedure has the advantage of only moderate computing time requirements, allowing us to perform the major part of the necessary iterations with this method. Its disadvantage, however, is that it involves a few substantial approximations (cf. Section 3.3). In a second step, the final iteration cycle is therefore solved with the detailed radiative line transfer (method II). Although this procedure is extremely time-consuming, it has the advantage that it is not affected by any significant approximations. With this second method, blocking factors $B_J(r, \nu)$ and $B_H(r, \nu)$ are calculated, defined as the ratio of the radiative quantities obtained by considering the total opacities and emissivities to those which include only the corresponding continuum values (cf. Pauldrach et al. 1996). $B_J(r, \nu)$ and $B_H(r, \nu)$ are then used as multiplying factors to the continuum quantities calculated in the next NLTE-ALI-cycle with the current continuum opacities, in order to iterate the radiative rates R_{ij} (both continuum and lines) and the resulting occupation numbers until convergence (details are described in Section 3.3).

In total, almost 1000 ALI iterations are required by the complete NLTE procedure, divided into blocks of 30 iterations each. (One iteration comprises calculation of the occupation numbers and the radiation field.) Up to 31

of these iteration blocks are performed using the opacity sampling method (method I), updating the temperature structure and the Rosseland optical depth after each third ALI-iteration, and the total opacities and emissivities after each iteration block. All following iterations are then performed using method II, updating temperature, optical depth, and opacities and emissivities as before, and additionally calculating the blocking factors with the detailed radiative transfer after each iteration block. (Several iteration blocks using method II can be executed, but 1 is usually sufficient – see below.) In this phase the radiative transfer solved in the ALI-iterations within one iteration block is just based on continuum opacities and emissivities, and the blocking factors are applied to get the correct radiative quantities used for calculating the radiative rates.

As a final result of the complete iteration cycle, the converged occupation numbers, the emergent flux, and the final NLTE temperature structure are obtained.

3.2. The atomic models

It is obvious that the quality of the calculated occupation numbers and of the synthetic spectrum is directly dependent on the quality of the input data. We have therefore extensively revised and improved the basis of our model calculations, the atomic models.

Up to now the atomic models of all of the important ions of the 149 ionization stages of the 26 elements considered (H to Zn, apart from Li, Be, B, and Sc) have been replaced in order to improve the quality. This has been done using the *Superstructure* program (Eissner et al. 1974; Nussbaumer and Storey 1978), which employs the configuration-interaction approximation to determine wave functions and radiative data. The improvements include more energy levels (comprising a total of about 5,000 observed levels, where the fine structure levels have been “packed” together²) and transitions (comprising more than 30,000 bound-bound transitions for the NLTE calculations and more than 4,000,000 lines for the line-force and blocking calculations^{3,4}, and 20,000 individual transi-

² Note that artificial emission lines may occur in the blocking calculations if the lower levels of a fine structure multiplet are left unpacked but the upper levels of the considered lines are packed – the fine structure levels of an ionization stage should either be all packed or all unpacked.

³ Note further that the consistency of the model calculation requires that the wavelength of the bound-bound transition connecting packed levels in the NLTE calculations to be identical to the wavelength of the strongest component of the multiplet considered in the blocking calculations in order to solve the line radiative transfer and especially the problem of *self-shadowing* properly.

⁴ The Superstructure calculations involve many more excited levels than actually used in the NLTE calculation. Our line list does, however, include transitions to such highly excited levels above our limit of considering the level structure; occupation numbers of these upper levels are estimated using the two-level

Table 1. Summary of revised atomic data calculated with *Superstructure*. In columns 2 and 3 the number of levels used in the NLTE calculations are given in packed and unpacked form. Columns 4 and 5 list the number of lines used in the rate equations and for the line-force and blocking calculations.

Ion	levels		lines		Ion	levels		lines	
	packed	unpacked	rate eq.	blocking		packed	unpacked	rate eq.	blocking
C II	36	73	284	11005	S VI	18	32	59	142
C III	50	90	520	4406	S VII	14	26	39	1031
C IV	27	48	103	229	Ar V	40	86	328	3007
C V	5	7	6	57	Ar VI	42	93	400	1335
N III	40	82	356	16458	Ar VII	47	87	483	2198
N IV	50	90	520	4401	Ar VIII	15	27	41	111
N V	27	48	104	229	Mn III	50	141	364	175593
N VI	5	7	6	57	Mn IV	50	124	467	131821
O II	50	117	595	39207	Mn V	50	124	508	61790
O III	50	102	554	24506	Mn VI	13	25	35	87
O IV	44	90	435	17933	Fe II	50	148	405	227548
O V	50	88	524	4336	Fe III	50	126	246	199484
O VI	27	48	102	231	Fe IV	45	126	253	172902
Ne IV	50	113	577	4470	Fe V	50	124	451	124157
Ne V	50	110	534	2664	Fe VI	50	138	452	60458
Ne VI	50	112	343	1912	Fe VII	22	62	91	10123
Mg III	50	96	529	2457	Fe VIII	42	96	300	4777
Mg IV	50	117	589	3669	Co III	50	141	469	200637
Mg V	50	100	547	3439	Co IV	41	97	70	146252
Mg VI	21	44	54	305	Co V	45	126	253	182780
Al IV	50	96	529	2523	Co VI	43	113	317	124053
Al V	50	117	588	18317	Co VII	34	80	246	50270
Al VI	19	37	41	153	Ni III	40	102	281	131508
Si III	50	90	480	4044	Ni IV	50	146	528	183267
Si IV	25	45	90	245	Ni V	41	97	70	179921
Si V	50	98	531	3096	Ni VI	45	126	253	186055
Si VI	50	116	596	3889	Ni VII	43	113	317	123386
P V	25	45	90	245	Ni VIII	34	80	246	43778
P VI	14	26	41	1096	Cu IV	50	124	477	17466
S V	44	78	404	903	Cu V	50	146	527	30457
					Cu VI	50	126	246	10849

tion probabilities of low-temperature dielectronic recombination and autoionization).

Additional line data were taken from the Kurucz (1992) line list: approximately 20,000 lines have been added to the *Superstructure* data for ions of Mn, Fe, Co, and Ni. These concern transitions to even higher levels than those having been calculated with *Superstructure*, but which might nonetheless be of significance in the blocking calculations. From the Opacity Project (cf. Seaton et al. 1994; Cunto and Mendoza 1992) another 4,466 lines have been included, as well as photoionization cross-sections (almost 2,000 data sets have been incorporated). Collisional data have become available through the IRON project (see Hummer et al. 1993) – almost 1,300 data sets have been included.

approximation on the basis of the (known) occupation number of the lower level.

Table 1 gives an overview of the ions affected by the improvements. (Users of the program package *WM-basic* should note that the model calculations will become inconsistent if the atomic data sets are changed haphazardly by those who are not familiar with the source code.)

3.3. The treatment of line blocking

As the thermal width of a UV metal line covers just a few mÅ, a simple straightforward method would require considering approximately 10^7 frequency points in order to resolve the lines in the spectral range affected by line blocking. Such a procedure would lead to a severe problem concerning the computational time. The alternatives are either to calculate the complete radiative transfer in the comoving frame – again a time-consuming procedure – or to use a tricky method which saves a lot of computation time through the application of some minor approxima-

tions (method I), dropping these approximations in the final iteration steps (method II) in order to come to a realistic solution. Our treatment described here uses the second approach.

Although frequently applied, a method using *opacity distribution functions* (ODFs) (cf. Labs 1951; Kurucz 1979), where the opacities are rearranged within a rough set of frequency intervals in such a way that a smoothly varying function is obtained which conserves the statistical distribution of the opacities, is not applicable in our case, since there is no appropriate way to treat the lineshift in the wind, and due to the rearrangement of the opacities the frequential position of the lines is changed. This, however, prevents a correct computation of the bound-bound transitions used for the solution of the statistical equilibrium equations.

The approach best suited for our purpose in the first step (method I) is the *opacity sampling* technique (cf. Peytremann 1974; Sneden et al. 1976; Anderson 1991) which compared to the ODF-method is computationally a bit more costly, but does not suffer from the limitations mentioned above. This method allows us to account for the *lineshift* in the wind and the correct influence of line blocking on the bound-bound transitions (cf. Section 3, item (ii)), since it preserves the exact frequential position of the lines.

3.3.1. The opacity sampling method (method I)

Following the idea of the *opacity sampling*, a representative set of frequency points is distributed in a logarithmic wavelength scale over the relevant spectral range, and the radiative transfer equation is solved for each point. (For O-stars the actual range depends on T_{eff} ; for hot objects the lower value is at $\approx 90 \text{ \AA}$ and for cooler objects the upper value is at 2000 \AA ; note that accurate ionization calculations require extending the line blocking calculations to the range shortward of the He II edge – cf. Pauldrach et al. 1994.)

In this way the exact solution is reached by increasing the number of frequency points. A smooth transition is obtained when the number of frequency points is increased up to the number $\sim 10^7$ – which is required to resolve the thermal width of the UV lines. It is obvious however that convergence can be achieved already with significantly less points (see below). Furthermore, special blocking effects on selected bound-bound transitions can be investigated more thoroughly by spreading additional frequency points around the line transition of interest.

In the following subsection we will investigate how many sampling points are required in order to represent the physical situation in a correct way.

The influence of line blocking on the photoionization integrals. The most important effect of line blocking on the

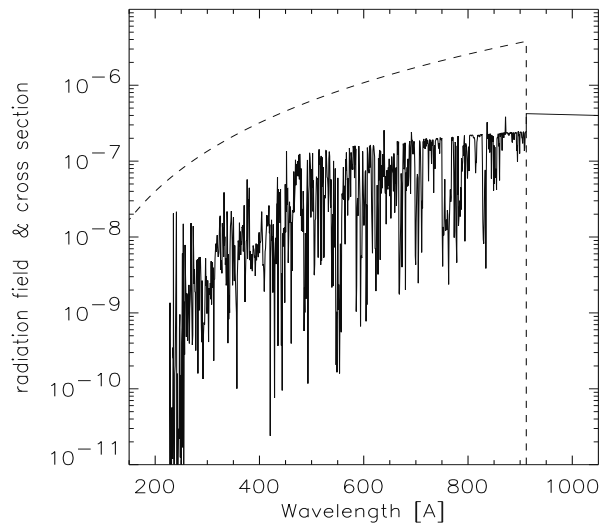


Fig. 3. Mean radiation field J_ν together with the photoionization cross section σ_{ik} of the ground state of H (in arbitrary units).

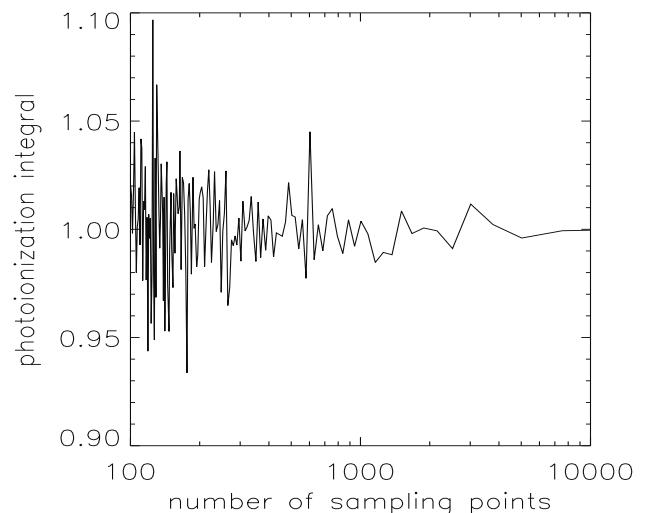


Fig. 4. Accuracy of the normalized photoionization integral R_{ik} of the groundstate of H in dependence of an increasing number of sampling points within the Lyman continuum.

emergent spectrum is the influence on the ionization structure via the photoionization integrals

$$R_{ik} = 4\pi \int \frac{J_\nu}{h\nu} \sigma_{ik}(\nu) d\nu. \quad (1)$$

This can be verified from Fig. 3 where it is shown that the mean radiation field J_ν changes rapidly over the frequency interval covered by a typical smooth bound-free cross section σ_{ik} – several 100 \AA are affected. (Note that dielectronic resonances which may occur in addition are not shown here.)

It is obvious from Fig. 3 that the photoionization rates are sensitive functions of the blocking influence on J_ν , and hence, on the number of sampling points in the relevant frequency range.

In order to determine the number of sampling points required for an accurate description of the bound-free (photoionization) and bound-bound (line) radiative rates we performed empirical tests by calculating models with an increasing number of sampling points. Representative for the behavior of the radiative rates, and thus the occupation numbers, Fig. 4 shows the dependence of the normalized photoionization integral of the ground state of hydrogen on the number of frequency points. For small numbers of sampling points there is no systematic trend, and the rates converge for higher numbers of sampling points. We conclude that 1,000 sampling points within the Lyman continuum on a logarithmic wavelength scale guarantee a sufficient accuracy of about 1 to 2 percent. By means of a separate investigation Sellmaier (1996) showed the given number of sampling points to be reasonable, since it reproduces the actual line-strength distribution function quite well.

The treatment of the lineshift. The total opacity at a certain sampling frequency ν is given by adding the line opacity χ_{lb} to the continuum opacity χ_c

$$\chi_\nu = \chi_{\text{lb}}(\nu) + \chi_c(\nu), \quad (2)$$

where χ_{lb} is the sum over all (integrated) single line opacities $\bar{\chi}_1$ multiplied by the line profile function $\varphi_1(\nu)$

$$\chi_{\text{lb}}(\nu) = \sum_{\text{lines}} \bar{\chi}_1 \varphi_1(\nu). \quad (3)$$

Here $\bar{\chi}_1$ is

$$\bar{\chi}_1 = \frac{h\nu_0}{4\pi} (n_i B_{ij} - n_j B_{ji}), \quad (4)$$

and the analogous expression for the emissivity is

$$\bar{\eta}_1 = \frac{h\nu_0}{4\pi} n_j A_{ji}. \quad (5)$$

(B_{ij} , B_{ji} , and A_{ji} are the Einstein coefficients of the line transition at the frequency ν_0 , and h is Planck's constant.)

In the static part of the atmosphere a line's opacity covers with its (thermal and microturbulent) Doppler profile φ_D only a very small interval around the transition frequency ν_0 (illustrated in Fig. 5 on the right hand side of both figures; note that with regard to our sampling grid about 40 percent of the available lines are treated in this part). The effect of these lines on the radiation field is nevertheless considerable (cf. Fig. 3), if the lines are strong enough to become saturated.

In the expanding atmospheres of hot stars the effect of line blocking is enhanced considerably in the supersonic region due to the nonlinear character of the radiative transfer. A velocity field $v(r)$ enables the line to block the radiation also at other frequencies $\nu = \nu_0(1+v(r)/c)$, i. e., the Doppler shift increases the frequency interval which can be blocked by a single line to a factor of ≈ 100 . On the other hand, the velocity field reduces the spatial area

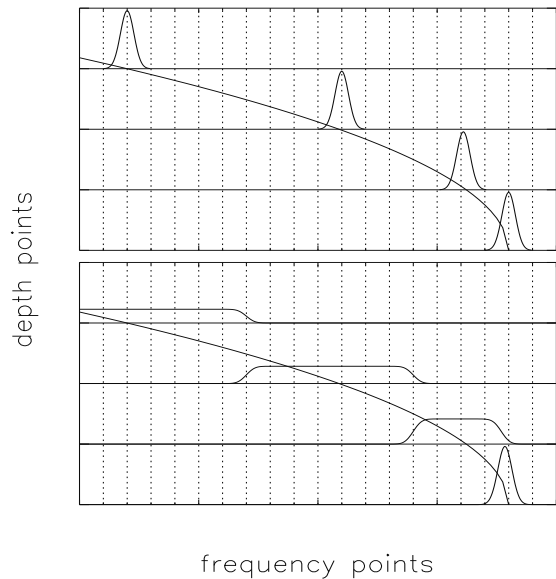


Fig. 5. upper panel: simply shifting the line profile along ν_{CMF} (represented by the curve) at each radius grid point (standard opacity sampling) causes the line to be missed at most frequency points; **lower panel:** this problem is solved by assuming a boxcar profile for each depth point with a width corresponding to the difference in Doppler shift between two successive radius points (“Doppler-spread opacity sampling”).

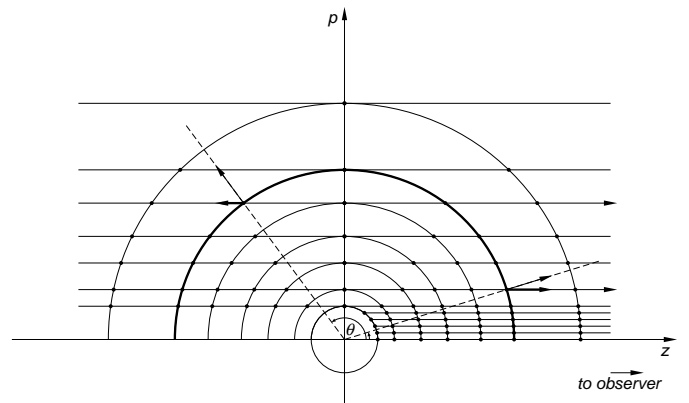


Fig. 6. (p, z)-geometry for the spherically symmetric radiative transfer. For any given depth point, a different Doppler shift must in principle be considered for every p -ray, since the projected velocity varies with $\cos \theta$. However, as no analogy to the boxcar method exists in this case, in our opacity sampling method we take the Doppler shift of the central ray as being representative for all other rays (see text).

where a photon can be absorbed by a line. If a line is optically thick, however, the effect of blocking will ultimately be increased compared to a static photosphere.

The lineshift due to the velocity field is applied to the individual line opacities before the summation in Eq. 3 is carried out at each sampling and depth point (otherwise the effect of the lineshift would be underestimated with respect to the ratio of line width to sampling distance – see below). However, in our approach this is done by applying

the Doppler shift of the radial ray to all p -rays (see Fig. 6), ignoring the angular dependence of the Doppler shift (see below). Apart from the intrinsic character of the sampling method this is the most restrictive approximation in our first iteration cycle. Nevertheless, the main effect of the frequency shift due to the expanding wind – increase of the frequential range of line absorption – is included, and that is what has to be iterated in this first cycle.

From the upper panel of Fig. 5 it is obvious that if the line opacity is simply shifted along the comoving frame frequency (ν_{CMF}) to every radius point successively, many frequency points will miss the line, since the radius grid is too coarse to treat large lineshifts in the observer’s frame. This behaviour is corrected by convolving the intrinsic Doppler profile of the line with a boxcar profile $\varphi_{\Delta v}$ representing the velocity range around each radius point (Fig. 5, lower panel).

The boxcar profile is the mean profile obtained by considering the velocity shifts Δv of the two corresponding intermesh points (ν_1, ν_2) on both sides of the regarded radius grid point in the way that the gaps in the frequency grid are closed. This can be expressed in terms of the Heaviside function θ :

$$\varphi_{\Delta v}(\nu) = \frac{\theta(\nu_2 - \nu) - \theta(\nu_1 - \nu)}{2(\nu_2 - \nu_1)} \quad (6)$$

ν_1 and ν_2 are the observer’s frame frequencies belonging to the velocities of two successive radius points (r_1 and r_2), i. e., $\nu_{1,2} = \nu_0(1 + v(r_{1,2})/c)$. Assuming thermal Doppler broadening for the intrinsic line profile,

$$\varphi_{\text{D}}(\nu) = \frac{e^{-x^2}}{\sqrt{\pi}\Delta\nu_{\text{D}}} \quad \text{with} \quad x = \frac{\nu - \nu_0}{\Delta\nu_{\text{D}}}, \quad (7)$$

where $\Delta\nu_{\text{D}}$ is the thermal Doppler width, the convolution ($\varphi_{\text{D}} \otimes \varphi_{\Delta v}$)(ν) results in the final profile function

$$\phi(\nu) = (\varphi_{\text{D}} \otimes \varphi_{\Delta v})(\nu) = \frac{\text{erf}(x_2 - x) - \text{erf}(x_1 - x)}{2(x_2 - x_1)\Delta\nu_{\text{D}}}. \quad (8)$$

This profile can be used for the entire sub- and supersonic region. For $\Delta v < v_{\text{therm}}$ it gives, as a lower limit, the *ordinary opacity sampling*, and for sufficiently high velocity gradients ($\Delta v > v_{\text{therm}}$) the integration over a radius interval represents the *Sobolev optical depth* ($\tau_{\text{Sob}}(r)$) of a local resonance zone for a radial ray

$$\begin{aligned} \Delta\tau &= \int_{r_1}^{r_2} \bar{\chi}_1 \cdot \phi(\nu) \, dr \\ &\approx \bar{\chi}_1 \cdot \frac{1 - (-1)}{2(x_2 - x_1) \cdot \Delta\nu_{\text{D}}} \cdot (r_2 - r_1) \\ &= \bar{\chi}_1 \cdot \frac{r_2 - r_1}{v_2 - v_1} \cdot \frac{c}{\nu_0} \\ &\approx \bar{\chi}_1 \cdot \frac{c}{\nu_0} \cdot \left(\frac{dv}{dr}\right)^{-1} \\ &= \tau_{\text{Sob}}(r). \end{aligned} \quad (9)$$

At sufficiently high velocity gradients all lines are included in the radiative transfer if the sampling grid is fine enough

(see also Sellmaier 1996). In this case our *Doppler-spread opacity sampling method* therefore becomes an *exact solution*.

In summary, our Doppler-spread sampling technique makes opacity sampling usable even at large velocity gradients where the standard sampling would miss a line at many frequency points. Broadening of the line with the boxcar profile does not overestimate the line blocking effect, since the convolution (Eq. 8) preserves the frequency-integrated line strength. Rather, the Sobolev optical depth (Eq. 9) is the upper limit for the optical thickness of a blocking line as treated with the boxcar profile. The statistical character inherent in opacity sampling is greatly diminished, since at high velocity gradients all available lines are considered.

Furthermore, broadening the lines leads neither to an increased nor a decreased line overlap, since the broadening only spreads a line over the frequencies corresponding to the Doppler shifts between one depth point and the next one. If lines overlap through this broadening at a certain radius grid point, they must also overlap in reality (see Fig. 10) in the interval between that radius point and the adjacent one, because the basic relationship between frequency shift and radius (via the velocity field) is independent of the resolution of the radius grid.

Essentially, the broadening projects the sharply peaked line opacities and emissivities inside a radial interval, which would otherwise be overlooked in the radiation transfer in the discretized scheme, onto a point at the edge of that interval so that the radiation transfer on the discretized radius grid can be performed correctly. For any particular radius interval and spectral line, this affects all frequencies in the interval determined by the Doppler shifts corresponding to the velocities at the edges of the radial interval in question, irrespective of the number of frequency points that actually lie in that frequency interval. Increasing this number of frequency points does not influence this geometric configuration⁵, whereas increasing the radial resolution improves the quality of this procedure, finally converging to the exact solution (cf. method II).

In principle, one would have to account for the angular variation (see Fig. 6) of the Doppler shift in a similar manner, but as no analogy to the boxcar profile method exists in this case, as mentioned above we simply apply the (correctly calculated, radially dependent) opacities ($\chi_{\text{lb}}(\nu, r)$) of the central p -ray to the other p -rays, regarding these opacities as being representative. A welcome result of this simplification is the fastness of the method, a very important consideration in this iteration cycle.

⁵ Note that the minimum resolution required for the frequency grid *per se* is determined by the Doppler spread between the radius grid points, in order to intercept a line at several radius points in succession. As stated above, at sufficiently high velocity gradients all lines are included in the radiative transfer for approximately 1000 frequency points in the Lyman continuum. Moreover, as illustrated in Fig. 4, the chaotic behavior for less than about 1000 frequency points vanishes in this case.

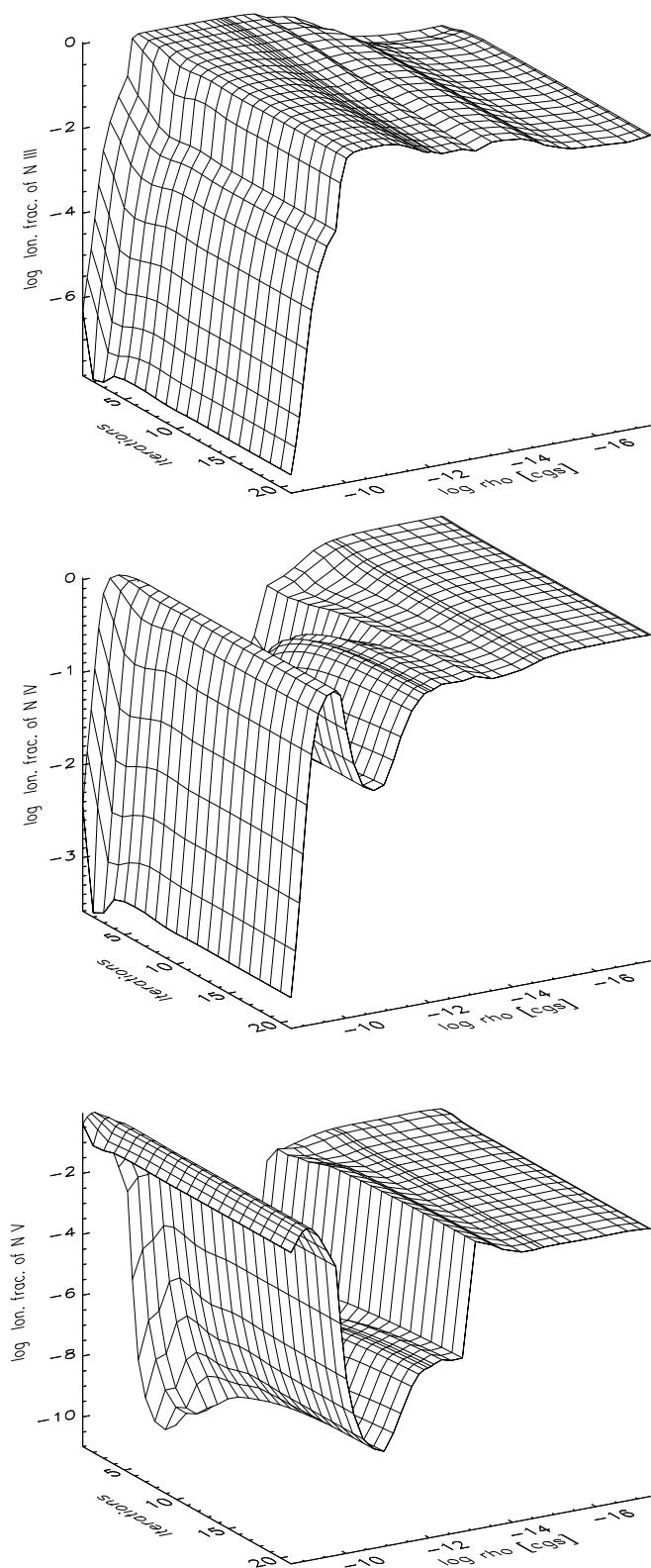


Fig. 7. Logarithm of the ionization fractions of N III (*upper panel*), N IV (*middle panel*), and N V (*lower panel*) versus density and iteration block number for an O supergiant model ($T_{\text{eff}} = 29\,000\text{ K}$, $\log g = 3.0$, $R_*/R_{\odot} = 27.0$). The region between two successive contour lines (one iteration block) corresponds to 30 iterations.

Concerning our *WM-basic* program package running on a normal scalar processor, however, the method is still not fast enough (a model calculation would require an amount of computing time of about 20 hours). The reason is that the Rybicki-method which is used in this step for the solution of the second-order form of the equation of transfer (cf. Mihalas 1978) requires more than 80% of the computing time of a model calculation. (Note that the Rybicki-method is applied in each iteration just once per frequency point; in order to improve the accuracy, the radiative quantities are then further iterated internally by using the moments equation of transfer (cf. Mihalas 1978). Because of strong changes in the opacities and emissivities within the NLTE iteration cycle it is necessary to start with the Rybicki-method nevertheless.) We have therefore rethought the solution concept of the Rybicki-scheme and developed a method which is 10 times faster on a vector processor and 3 to 5 times faster on a scalar processor – the actual factor depends on the quality of the level-2 BLAS functions available with professional compiler programs and which do most of the work in our method (see Appendix A).

In order to illustrate the behaviour of convergence of our method I, the ionization fractions of N III, IV, and V are shown versus density and the iteration block number in Fig. 7 for the first 600 iterations as an example. As displayed, the model converges within 400 iterations – the remaining iterations are required to warrant the luminosity conservation (see Section 3.4). The steep increase of N V in the wind part results from the EUV and X-ray radiation produced by shock-heated matter (see Section 3.5).

We finally note that first results obtained with a version of this procedure as described here so far have already been published. Sellmaier et al. (1996) showed that their NLTE line-blocked O-star wind models solve the long-standing Ne III problem of H II-regions for the first time, and Hummel et al. (1997) carried out NLTE line-blocked models for classical novae.

Special problems. From first test calculations performed in the manner described we recognized and solved two additional nontrivial problems:

The first problem concerns the artificial effect of *self-shadowing* (see above) which occurs because the incident intensity used for the calculation of a bound-bound transition that enters into the rate equations is already affected by the line transition itself, since the opacity of the line has been used for the computation of the radiative quantities in the previous iteration step. If the lines contained in a frequency interval are of almost similar strength, this is no problem, since the used intensity $I_{\nu_n}(r)$ calculated at the sampling point represents a fair mean value for the *true incident radiation* of the individual lines in the interval. If however, a line has a strong opacity with a dominating influence in the interval, the intensity taken at the sampling point for the same bound-bound transition in the radiative rates is much smaller than the *true incident radiation*

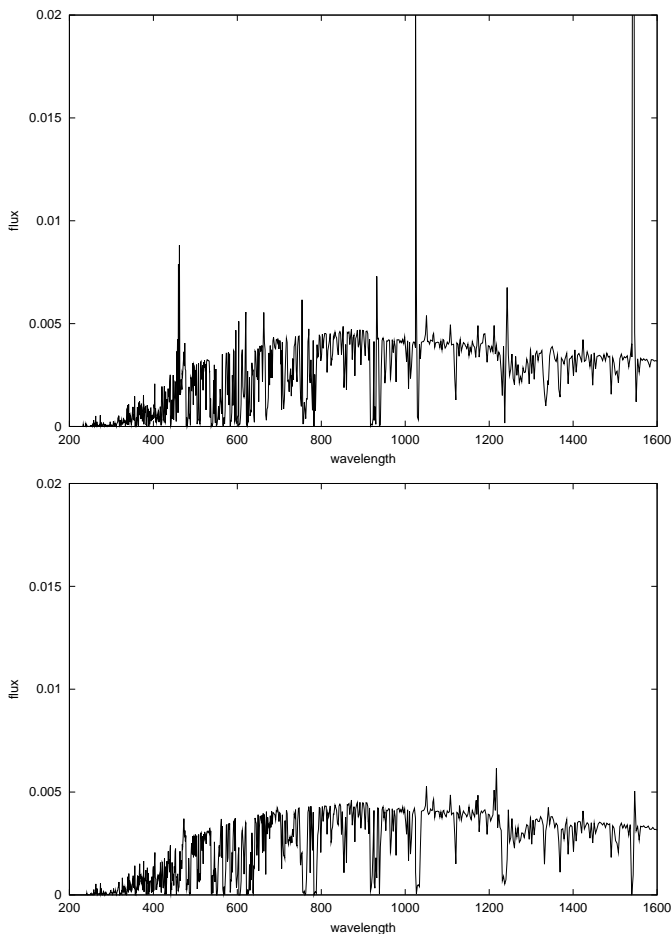


Fig. 8. Part of the synthetic EUV spectrum (200–1600 Å) of the S-45 supergiant model ($T_{\text{eff}} = 45000$ K, $\log g = 3.6$, $R_*/R_\odot = 18.0$) calculated with the opacity sampling method and the differential form of the transfer equation. The upper panel shows the spectrum obtained with the standard Feautrier coefficients, which produces several strong artificial emission lines. The lower panel shows the correct spectrum resulting with our modified Feautrier coefficients.

for this line, because the line has already influenced this value considerably. In consequence the source function of this line is underestimated and the radiative processes – the scattering part is mostly affected – are not correctly described in the way that the line appears systematically too weak.

The solution to this problem is rather simple: in calculating the bound-bound rates of the dominating lines, we use an incident intensity which is independent of the lines in the considered interval (cf. Pauldrach et al. 1998).

The second problem involves the discretization of the transfer equation in its differential form, for computing the radiative quantities (Feautrier method). In the standard approach (see, for example, Mihalas 1978) the equation of transfer is written as a second-order differential equation with the optical depth τ as the independent variable:

$$\frac{d^2u}{d\tau^2} = u - S, \quad (10)$$

where S is the source function and $u = \frac{1}{2}(I^+ + I^-)$, with I^+ and I^- being the intensities in positive and negative τ direction along the ray considered.

This differential equation is then converted to a set of difference equations, one for each radius point i on the ray,

$$\frac{d^2u}{d\tau^2}\Big|_{\tau_i} \approx \frac{\frac{du}{d\tau}\Big|_{\tau_{i+\frac{1}{2}}} - \frac{du}{d\tau}\Big|_{\tau_{i-\frac{1}{2}}}}{\tau_{i+\frac{1}{2}} - \tau_{i-\frac{1}{2}}} \quad (11)$$

$$\approx \frac{\frac{u_{i+1} - u_i}{\tau_{i+1} - \tau_i} - \frac{u_i - u_{i-1}}{\tau_i - \tau_{i-1}}}{\frac{1}{2}(\tau_{i+1} + \tau_i) - \frac{1}{2}(\tau_i + \tau_{i-1})}, \quad (12)$$

resulting in a linear equation system

$$a_i u_{i-1} + b_i u_i + c_i u_{i+1} = S_i \quad (13)$$

with coefficients

$$\begin{aligned} a_i &= -\left(\frac{1}{2}(\tau_{i+1} - \tau_{i-1})(\tau_i - \tau_{i-1})\right)^{-1} \\ c_i &= -\left(\frac{1}{2}(\tau_{i+1} - \tau_{i-1})(\tau_{i+1} - \tau_i)\right)^{-1} \\ b_i &= 1 - a_i - c_i, \end{aligned} \quad (14)$$

(and appropriate boundary conditions). This linear equation system has a tridiagonal structure and can be solved economically by standard linear-algebra means.⁶ Note that the equations contain only *differences* in τ , which can easily be calculated from the opacities and the underlying z -grid (cf. Fig. 6) as

$$\tau_{i+1} - \tau_i = \frac{1}{2}(\chi_{i+1} + \chi_i)(z_{i+1} - z_i), \quad (15)$$

with χ_i being the opacity at depth point i .

The equation systems are well-behaved if the opacities and source functions vary only slowly with z . Caution must be taken if this cannot be guaranteed, for example, whenever a velocity field is involved at strong ionization edges or with the opacity sampling method at strong lines, since the velocity field shifts the lines in frequency, causing large variations of the opacity from depth point to depth point for a given frequency. In particular, a problematic condition occurs if a point with a larger-than-average source function S_i and low opacity χ_i borders a point with a high opacity χ_{i+1} (and low or average source function S_{i+1}). In reality, this large source function should have little impact, since it occurs in a region of low opacity, and thus the emissivity is small. However, the structure of the equations is such that the emission is computed to be on the order of

$$\begin{aligned} \Delta I &\approx \bar{S} \cdot \Delta\tau \\ &\approx \frac{1}{2}(S_{i+1} + S_i) \cdot \frac{1}{2}(\chi_{i+1} + \chi_i)(z_{i+1} - z_i), \end{aligned} \quad (16)$$

where, if the other quantities are comparatively small (in accordance with our assumptions), the term $S_i \chi_{i+1}$

⁶ In practice, a Rybicki-type scheme (cf. Mihalas 1978; and Appendix A, this paper) is used for solving the equation systems for all p -rays simultaneously, since the source function contains a scattering term (see Eq. A.4) which redistributes the intensity at each radius shell over all rays intersecting that shell.

dominates,⁷ leading to artificially enhanced emission. In Figure 8 (upper panel) we show the exaggerated emission of the strongest spectral lines in the emergent flux of a stellar model computed using this standard discretization, leading to false results. Even a simple example can serve to illustrate this effect, as demonstrated in Appendix B.

However, with a subtle modification of the equation system coefficients the method can nevertheless be salvaged. The subtle point involves writing the transfer equation as an equation not in τ , but in z for derivation of the coefficients, since only this formulation treats correctly the z -dependence of χ :

$$\frac{1}{\chi} \frac{d}{dz} \left(\frac{1}{\chi} \frac{du}{dz} \right) = u - S. \quad (17)$$

(Note that the grid should still be spaced so as to cover τ more-or-less uniformly.) Again approximating the differential equation with a system of differences we obtain

$$\begin{aligned} \frac{1}{\chi_i} \left(\frac{d}{dz} \left(\frac{1}{\chi} \frac{du}{dz} \right) \right) \Big|_i &\approx \\ &\approx \frac{1}{\chi_i} \frac{\left(\frac{1}{\chi} \frac{du}{dz} \right) \Big|_{i+\frac{1}{2}} - \left(\frac{1}{\chi} \frac{du}{dz} \right) \Big|_{i-\frac{1}{2}}}{z_{i+\frac{1}{2}} - z_{i-\frac{1}{2}}} \end{aligned} \quad (18)$$

$$\approx \frac{1}{\chi_i} \frac{\frac{1}{\chi_{i+1,i}} \frac{u_{i+1} - u_i}{z_{i+1} - z_i} - \frac{1}{\chi_{i,i-1}} \frac{u_i - u_{i-1}}{z_i - z_{i-1}}}{\frac{1}{2}(z_{i+1} + z_i) - \frac{1}{2}(z_i + z_{i-1})}, \quad (19)$$

so that

$$\begin{aligned} a_i &= -\left(\frac{1}{2} \chi_i (z_{i+1} - z_{i-1}) \cdot \bar{\chi}_{i,i-1} (z_i - z_{i-1}) \right)^{-1} \\ c_i &= -\left(\frac{1}{2} \chi_i (z_{i+1} - z_{i-1}) \cdot \bar{\chi}_{i+1,i} (z_{i+1} - z_i) \right)^{-1} \\ b_i &= 1 - a_i - c_i. \end{aligned} \quad (20)$$

Even though these coefficients seem not too different from those of the standard method, their impact on the computed radiation field is significant, as witnessed by the drastic improvement in the emergent flux shown in the lower panel of Figure 8. The crucial difference in the coefficients is that the first factor in a and c now contains only the *local* opacity. (We naturally make the corresponding changes in the coefficients of the moments equation as well.)

Test calculations have shown that for the second factor in the coefficients the geometric mean (an arithmetic mean on a logarithmic scale)

$$\bar{\chi}_{i+1,i} = \sqrt{\chi_{i+1} \cdot \chi_i} \quad (21)$$

gives good results, as demonstrated in Figure 9, where the spectrum of a model computed with the opacity sampling method is compared to that of our detailed radiative line transfer, described in the next section. Considering the relative coarseness of the opacity sampling method, and

⁷ The physical reason for the failure of the system is that the source function only has meaning relative to its corresponding opacity. Multiplying the source function from one point with the opacity at another point is complete nonsense.

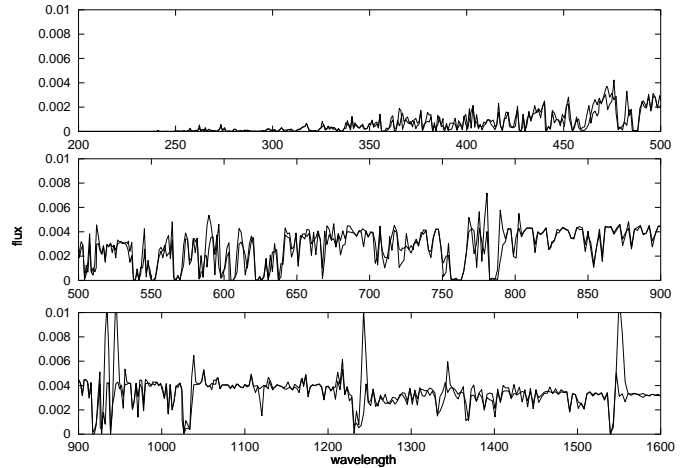


Fig. 9. Comparison of the synthetic EUV spectrum (200–1600 Å) of the S-45 supergiant model ($T_{\text{eff}} = 45000$ K, $\log g = 3.6$, $R_*/R_\odot = 18.0$) calculated with the *Doppler-spread opacity sampling method* (thick line) and the detailed method (thin line) on the same frequency grid. Due to simplifications in our implementation the sampling method cannot produce P Cygni emission; nevertheless it provides an extremely good basis for the final iterations using the detailed method.

the fact that the detailed line transfer suffers none of the approximations of the sampling method, the agreement is indeed remarkable. Note again that through our *single-p-ray approximation* for the sampling opacities (see above), our method I (opacity sampling) *cannot* produce P Cygni profiles, since the P Cygni emission is a direct result of the different Doppler shifts of a particular spectral line along different rays.

3.3.2. The detailed radiative line transfer (method II)

The detailed radiative line transfer (method II), used for the final iterations, is an exact solution of the transfer equation in the observer’s frame, and is completely equivalent to a comoving frame solution. It removes the two most significant simplifications of our opacity sampling method (method I), i. e., it accounts for:

- (1) Correct treatment of the angular variation of the opacities,
- (2) Spatially resolved line profiles⁸ (implying correct treatment of multi-line effects).

Whereas in method I the former is completely ignored, the lack of spatial resolution was already compensated for to a large extent through the use of our Doppler-spread sampling. (Multi-line interaction is partly included in our method I, but without regard for the sign of the Doppler shift (using just that of the central ray), and without re-

⁸ Note that this will not by itself solve the problem of self-shadowing, since that is an intrinsic property of any method using an “incident radiation” in solving for the bound-bound radiative rates with a continuum already affected by the transition being considered. In the iteration cycle using method II we therefore also have to apply our correction for self-shadowing.

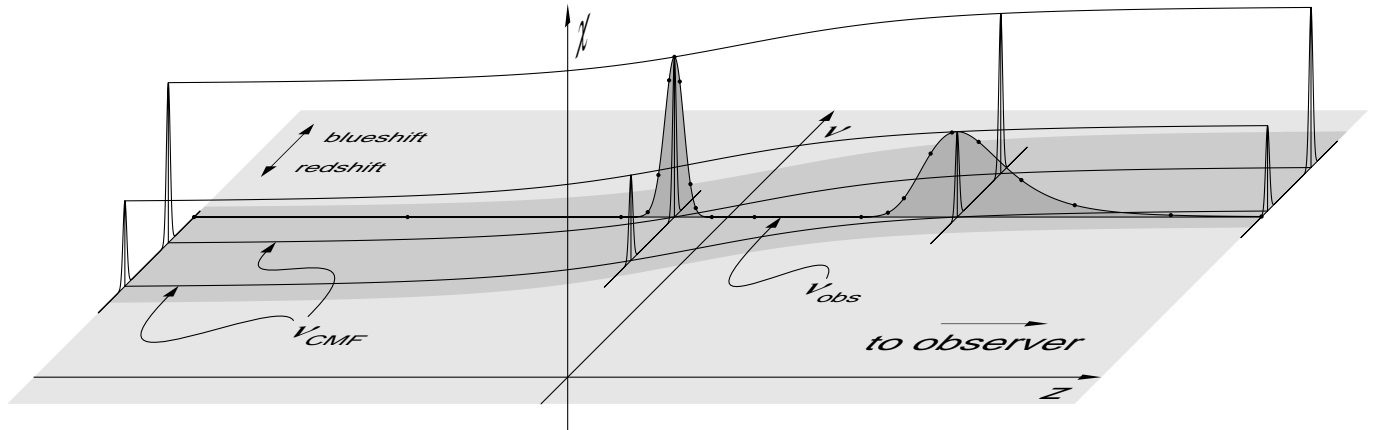


Fig. 10. Diagram (not to scale) illustrating the basic relationship of the rest-frame frequencies of spectral lines (ν_{CMF}) to observer's frame frequency (ν_{obs}) for one particular (non-core) p -ray in the spherically symmetric geometry (cf. Figure 6). Shown are two spectral lines which get shifted across the observer's frame frequency by the velocity field in the wind. The dots represent the stepping points of the adaptive microgrid used in solving the transfer equation in the detailed radiative line transfer.

gard for the order of the lines along the ray within a radius interval, as the Doppler-spread sampling effectively “maps” the lines to the nearest radius point.)

With all major approximations removed, the biggest shortcoming that remains in method II is that only Doppler broadening is considered for the lines, as Stark broadening has not yet been implemented. However, this is of no relevance for the UV spectra, as it concerns only a few lines of Hydrogen and Helium in the optical frequency range. It will, however, be important for our future planned analysis of the optical H and He lines. (Stark broadening is not considered in the sampling method either, but here this is of minor significance, as all other approximations are much more serious.)

In contrast to our method I, where the symmetry and our assumption of only radially (not angular) dependent Doppler shifts allowed solving the transfer equation for only one quadrant,⁹ a correct treatment of the both red and blue Doppler-shifted line opacities (see Figure 6) requires a solution in two quadrants¹⁰ (corresponding to, from the observer's viewpoint, the front and back hemispheres; the rotational symmetry along the line-of-sight is taken care of through the angular integration weights).

The method employed is an adaptation of the one described by Puls and Pauldrach (1990), using an integral formulation of the transfer equation and an adaptive stepping technique which ensures that the optical depth in each step (“microgrid”) does not exceed $\Delta\tau = 0.3$, so that the radiation transfer in each micro-interval can be

⁹ The 2nd-order differential representation of the transfer equation accounts for both the left- and right-propagating radiation simultaneously, the unknowns being the symmetric averages of the two.

¹⁰ A one-quadrant solution is also possible, but requires both a red- and a blue-shifted opacity for each (p, z) -point and separate treatment of the left- and right-directed radiation, thus being equivalent in computational effort to the two-quadrant solution that solves for radiation going in only one direction.

approximated to high accuracy by an analytical formula assuming a linear run of opacity and emissivity between the micro-interval endpoints:

$$I(\tau_0) = \int_{\tau_0}^{\tau_n} S(\tau) e^{-(\tau-\tau_0)} d\tau + I(\tau_n) e^{-(\tau_n-\tau_0)}, \quad (22)$$

where the integral is performed as a weighted sum on the microgrid

$$\begin{aligned} \int_{\tau_0}^{\tau_n} S(\tau) e^{-(\tau-\tau_0)} d\tau &= \\ &= \sum_{i=0}^{n-1} \left(e^{-(\tau_i-\tau_0)} \int_{\tau_i}^{\tau_{i+1}} S(\tau) e^{-(\tau-\tau_i)} d\tau \right), \end{aligned} \quad (23)$$

each “microintegral” being evaluated as

$$\int_{\tau_i}^{\tau_{i+1}} S(\tau) e^{-(\tau-\tau_i)} d\tau = w_i^{(a)} S(\tau_i) + w_i^{(b)} S(\tau_{i+1}) \quad (24)$$

with weights

$$w_i^{(a)} = 1 - \frac{1 - e^{-\Delta\tau_i}}{\Delta\tau_i}, \quad w_i^{(b)} = \frac{1 - e^{-\Delta\tau_i}}{\Delta\tau_i} - e^{-\Delta\tau_i} \quad (25)$$

where $\Delta\tau_i = \tau_{i+1} - \tau_i$. To accurately account for the variation of the line opacities and emissivities due to the Doppler shift, all line profile functions φ_l (cf. Eq. 3) are evaluated correctly for the current microgrid- (z, p) -coordinate on the ray, thus effectively resolving individual line profiles. Only the slowly-varying occupation numbers (or equivalently, the integrated, frequency-independent line opacities $\bar{\chi}_l$ and emissivities $\bar{\eta}_l$) and the velocity field are interpolated between the regular radius grid points.

Figure 10 depicts schematically the relationship between the Doppler-shifted frequencies of spectral lines (which are constant in the comoving frame) and the observer's frame frequency for which the radiative transfer is being calculated. The figure also illustrates the *line overlap* in accelerating, expanding atmospheres: lines clearly

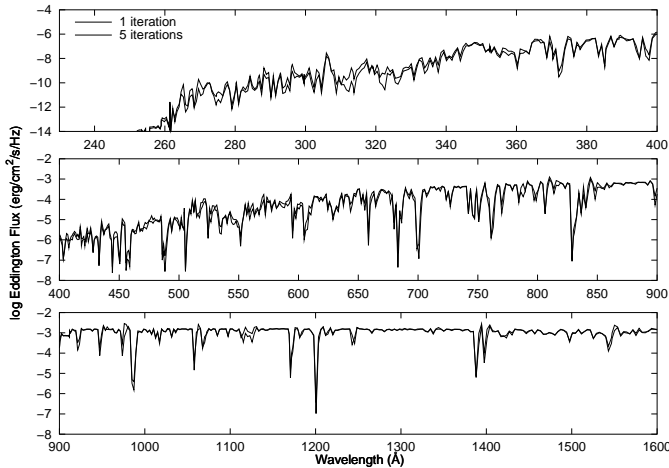


Fig. 11. Flux of our S-29 supergiant model ($T_{\text{eff}} = 29\,000\text{ K}$, $\log g = 3.0$, $R_*/R_{\odot} = 27.0$) after 1 and 5 iteration blocks of method II.

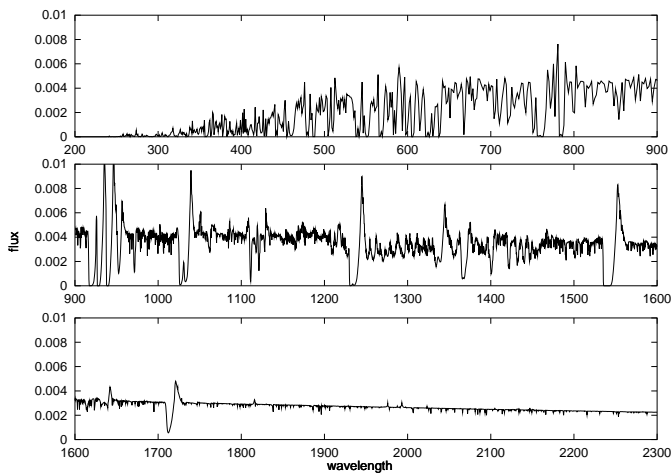


Fig. 12. The final – completely converged – spectrum from 200 to 2300 Å of the S-45 supergiant model. The observable UV region redward of the Lyman edge has been computed with a high resolution (for comparison with observed spectra).

separated in the comoving frame (slices parallel to the (ν, χ) -plane) overlap in the observer’s frame (slice parallel to the (z, χ) -plane at ν_{obs}) due to large Doppler shifts many times the intrinsic (thermal and microturbulent) linewidth. The areas shaded in dark gray correspond to the spatially resolved Sobolev resonance zones of the two lines for this particular observer’s frame frequency and p -ray. Note that the dimensions are not to scale, i. e., the intrinsic width of the lines, and consequently the thickness in z of the resonance zones, has been greatly exaggerated in relation to the total velocity shift.

All lines whose maximum Doppler shift $\Delta\nu = \pm\nu_0 v_{\infty}/c$ puts them in range of the observer’s frame frequency for which the radiative transfer is being calculated are considered for that frequency point. In Figure 10, these correspond to those lines whose rest frequencies lie in the gray band in the (ν, z) -plane at $z = 0$.

Broadening of the lines includes thermal and microturbulent contributions. For every atomic species and depth point, the correct thermal Doppler broadening based on atomic weight and local temperature is used. The microturbulence we have used here is about 10 km/s in the photosphere and grows with the outflow velocity to a maximum value of $0.1 v_{\infty}$ in the outer regions of the wind. This is generally in good agreement with the observations.

After the occupation numbers have converged in the iteration cycle using method I, one iteration block with method II is usually sufficient for full convergence of the model, as demonstrated by Figure 11, where the emergent spectrum of our S-30 model after 1 iteration block of method II is compared to the spectrum resulting from 5 iteration blocks.

A high-resolution spectrum is computed for the purpose of comparison with observations (wavelength range usually from 900 to 1600 Å) after full convergence of the model. This spectrum is generated with the same procedure as used for the detailed line blocking calculations. The high-resolution spectrum is then merged with the (usually) lower-resolution blocking flux for the final flux output (Figure 12).

3.4. Line blanketing

Line absorption and emission also has an important effect on the atmospheric *temperature structure*. The corresponding influence on the radiation balance is usually referred to as *line blanketing*. The objective now is to calculate an atmospheric temperature stratification which conserves the radiative flux and which treats the impact of the line opacities and emissivities properly. In principle there are three methods for calculating electron temperatures in model atmospheres. The commonly used one is based on the condition of radiative equilibrium. The second one uses a flux correction procedure, and the third one is based on the thermal balance of heating and cooling rates. As the first method has some disadvantages (see below), we use the second and the third method (cf. Pauldrach et al. 1998; for discussions on calculating temperature structures in other models for expanding atmospheres, see the references listed in Section 1; especially Drew (1989, 1990) presented a comprehensive discussion of her method). In deeper layers ($\tau_{\text{Ross}} > 0.1$) where true absorptive processes dominate we use the flux correction procedure, and the thermal balance is used in the outer part of the expanding atmosphere ($\tau_{\text{Ross}} < 0.1$), where scattering processes start to dominate.

The flux correction procedure. The idea of this method is straightforward: the local temperature has to be adjusted in such a way that the radiative flux is conserved. This requires, however, that the temperature is the dominant parameter on which the flux depends, and that the effect of a change in temperature on the flux is known. The first condition is certainly the case for $\tau_{\text{Ross}} > 0.1$. With regard to

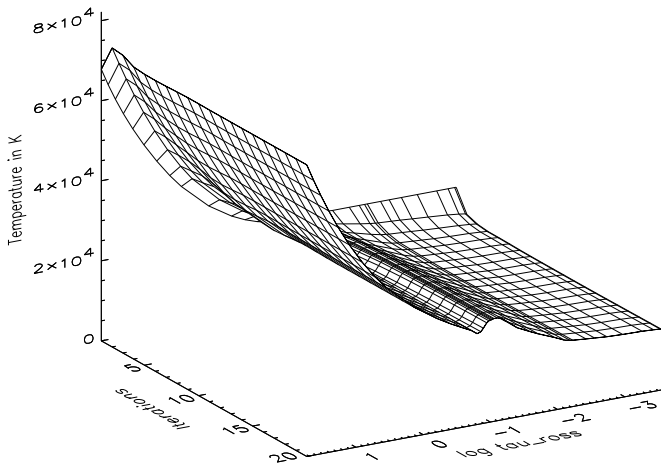


Fig. 13. The temperature structure versus the Rosseland optical depth and the iteration block number for the same O supergiant model as in Fig. 7 ($T_{\text{eff}} = 29\,000\text{ K}$, $\log g = 3.0$, $R_*/R_\odot = 27.0$).

the second condition, a law for the temperature structure is required which is controlled by some global parameters that can be adjusted in a proper way in order to conserve the flux. The “Hopf function”, usually applied for the grey case, has an appropriate functional dependence which has been adapted to the spherical NLTE case by Santolaya-Rey et al. (1997) recently in a general way. The main characteristic of the Hopf method is that the Rosseland optical depth is the decisive parameter on which the temperature stratification depends. Thus, in deeper layers the temperature structure can be calculated efficiently by using this new concept of the *NLTE Hopf function*:

$$T^4(r) = T_{\text{eff}}^4 \frac{3}{4} \frac{\tilde{\tau}_{\text{Ross}}}{\tau_{\text{Ross}}} (q_N(\tilde{\tau}_{\text{Ross}}) + \tau_{\text{Ross}}) \quad (26)$$

where $\tilde{\tau}_{\text{Ross}}$ is the radial optical depth in the spherical case,

$$d\tilde{\tau}_{\text{Ross}} = \chi_{\text{Ross}}(r) \left(\frac{R_*}{r} \right)^2 dr, \quad (27)$$

and

$$q_N(\tilde{\tau}_{\text{Ross}}) \simeq q_\infty + (q_0 - q_\infty) \exp(-\gamma \tilde{\tau}_{\text{Ross}}) \quad (28)$$

is the spherical NLTE Hopf function, where the parameters q_0 , q_∞ , and γ are fitted to a predefined run of the $q_N(\tau_{\text{Ross}})$ stratification (cf. Santolaya-Rey et al. 1997). Test calculations performed with fixed parameters (q_0 , q_∞ , and γ) and without metal lines lead to almost identical results for the temperature structures obtained by our code and the completely independently developed code of Santolaya-Rey et al. (cf. Pauldrach et al. 1998). The reliability of the method has been further proven by the resulting flux conservation which turns out to be on the 1% level.

In the next step, *line blocking* has to be *treated consistently*. Although the line processes involved are complex,

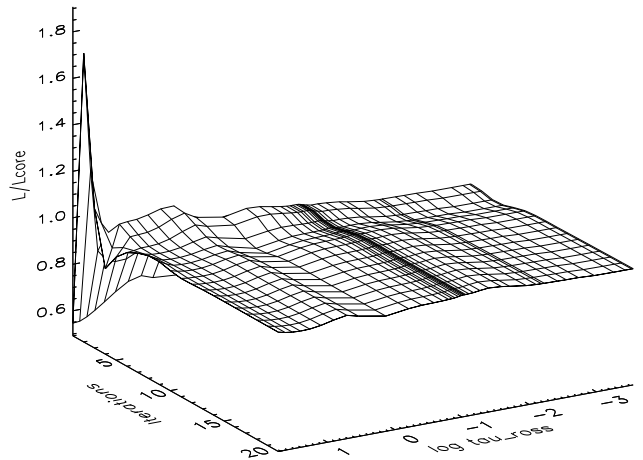


Fig. 14. The flux conservation versus the Rosseland optical depth and the iteration block number for the same O supergiant model as in Fig. 7 ($T_{\text{eff}} = 29\,000\text{ K}$, $\log g = 3.0$, $R_*/R_\odot = 27.0$). The accuracy of the flux conservation is on the 1% level for the final iteration blocks.

they always increase the Rosseland optical depth (τ_{Ross}). In the deeper layers ($\tau_{\text{Ross}} > 0.1$) this leads directly to an enhancement of the temperature law (backwarming). Using the method of the *NLTE Hopf functions* we thus have to increase the parameter q_0 first by using the flux deviation at $\tau_{\text{Ross}} \approx 3$. This parameter is updated in the corresponding iteration cycle until the flux is conserved at this depth on the 0.5% level. Afterwards the same is done with the parameter q_∞ at an optical depth of $\tau_{\text{Ross}} \approx 0.1$. In case the flux deviation at $\tau_{\text{Ross}} \approx 3$ becomes larger than 0.5% the parameter q_0 is iterated again with a higher priority. As a last step in this procedure the parameter γ is adjusted in order to conserve the flux at an optical depth of $\tau_{\text{Ross}} \approx 1$.

The resulting temperature structure and the corresponding flux deviation for an O supergiant model ($T_{\text{eff}} = 29\,000\text{ K}$, $\log g = 3.0$, $R_*/R_\odot = 27.0$) are shown in Fig. 13 and Fig. 14, respectively. As can be inferred from the figure, the flux is conserved for this model with an accuracy of a few percent. (We note that from test calculations where line blocking was treated, but parameters of the NLTE Hopf function were held fixed, thus effectively ignoring blanketing effects, we found a flux deviation which already starts in the inner part ($\tau_{\text{Ross}} < 50$) and reaches a value of up to 50% at $\tau_{\text{Ross}} \approx 0.1$.) This clearly shows the importance of blanketing and backwarming effects and the need to include them. As these test calculations have also shown that absorptive line opacities dominate the total opacity down to an optical depth of $\tau_{\text{Ross}} > 0.1$, the temperature structure is influenced by backwarming effects in the entire atmosphere – cf. Eq. 26.

The thermal balance. In the outer part of the expanding atmosphere ($\tau_{\text{Ross}} < 0.1$), where scattering processes start

to dominate, the effects of the line influence on the temperature structure are more difficult to treat. Of the two possible treatments, calculating for radiative equilibrium or for thermal balance, we have chosen the latter one, as the convergence of the radiative equilibrium method turned out to be problematic since the τ_{Ross} -values are small in this part, and, hence, most frequency ranges are optically thin. (This has recently also been proven by Kubat et al. (1999), where the corresponding equations of the method are also presented.) In calculating the heating and cooling rates (Hummer and Seaton 1963), all processes that affect the electron temperature have to be included – bound-free transitions (ionization and recombination), free-free transitions, and inelastic collisions with ions. For the required iterative procedure we make use of a linearized Newton-Raphson method to extrapolate a temperature that balances the heating and cooling rates.

Fig. 13 displays for the model above the resulting temperature structure vs. the number of iterations and shows a pronounced bump and a successive decrease of the temperature in the outer atmospheric part. (For an explanation of this effect, see Mihalas 1978 and references therein.) That the mismatch of the heating and cooling rates immediately goes to 0% in the outer part ($\tau_{\text{Ross}} < 0.07$) where they are applied for correcting the temperature structure has already been presented by Pauldrach et al. (1998).

We note at this place that the direct influence of X-rays (see next section) on the temperature structure via thermalization is negligible, since the energy contained is very small ($L_X/L_{\text{bol}} \approx 10^{-7}$). However, X-rays can indirectly influence the temperature by changing the ionization balance – the corresponding change of opacities in the EUV and UV can then affect the temperature via normal radiative processes. This, however, is properly considered in our procedure.

3.5. Revised inclusion of EUV and X-ray radiation

The *EUV and X-ray radiation* produced by cooling zones which originate from the simulation of *shock heated matter* arising from the non-stationary, unstable behavior of radiation driven winds (see Lucy and Solomon 1970, who found that radiation driven winds are inherently unstable, and Lucy and White 1980 and Lucy 1982, who explained the X-rays by radiative losses of post-shock regions where the shocks are pushed by the non-stationary features) is, together with K-shell absorption, included in our radiative transfer. The primary effect of the EUV and X-ray radiation is its influence on the ionization equilibrium with regard to high ionization stages like NV and OVI (cf. the problem of “superionization”, the detection of the resonance lines of OVI, NV, S VI in stellar wind spectra (cf. Snow and Morton 1976); in a first step this problem was investigated theoretically by Cassinelli and Olson 1979) where the contribution of enhanced direct photoionization due to the EUV shock radiation is as important as the effects of Auger-ionization caused by the

soft X-ray radiation (cf. Pauldrach 1987; Pauldrach et al. 1994 and 1994a). In order to treat this mechanism accurately it is obviously important to describe the radiation from the shock instabilities in the stellar wind flow properly. Note that in most cases a small fraction of this radiation leaves the stellar wind to be observed as soft X-rays with $L_x/L_{\text{bol}} \approx 10^{-7}$ (cf. Chlebowski et al. 1989). Thus, the reliability of the shock description can be further demonstrated by a comparison to X-ray observations, by ROSAT for instance.

In principle, a correct calculation of the creation and development of the shocks is required for the solution of the problem. This means that a detailed theoretical investigation of time-dependent radiation hydrodynamics has to be performed (for exemplary calculations see Owocki, Castor, and Rybicki 1988 and Feldmeier 1995). However, these calculations favor the picture of a stationary “cool wind” with embedded randomly distributed shocks where the shock distance is much larger than the shock cooling length in the accelerating part of the wind. They also indicate that only a small amount of high velocity material appears with a filling factor not much larger than $f \approx 10^{-2}$, and jump velocities of about $u_s = 300 \dots 700$ km/s which give immediate post-shock temperatures of approximately $T_s = 1 \times 10^6$ to 8×10^6 K. We also note that the reliability of these results was already demonstrated by a comparison to ROSAT-observations (cf. Feldmeier et al. 1997).

On the basis of these results we had developed an empirical approximative description of the EUV and X-ray radiation, where the shock emission coefficient

$$\epsilon_\nu^s(r) = \frac{f}{4\pi} n_p n_e \Lambda_\nu(T_s(r) n_e) \quad (29)$$

was incorporated in dependence of the volume emission coefficient Λ_ν calculated by using the Raymond and Smith (1977) code for the X-ray plasma, the velocity-dependent post shock temperatures T_s , and the filling factor f which enter as fit parameters – these values are determined from a comparison of the calculated and observed ROSAT “spectrum”. With this description the effects on the high ionization stages (NV, OVI) lead to synthetic spectral lines which reproduce the observations almost perfectly (cf. Pauldrach et al. 1994 and 1994a). However, with this method we were not able to reproduce the ROSAT-observations with the same model parameters simultaneously (see below). We therefore had to determine the filling factor and the post-shock temperatures by a separate and hence in view of our concept not consistent procedure (cf. Hillier et al. 1993). In order to overcome this problem refinements to our method are obviously required.

In the present treatment the outlined approximative description of the EUV and X-ray radiation has been revised. The major improvement consists of the consideration of *cooling zones* of the randomly distributed shocks embedded in the stationary cool component of the wind. Up to now we had assumed, for reasons of simplicity, that the shock emission is mostly characterized by the imme-

diate post-shock temperature, i.e., we considered *non-stratified, isothermal* shocks. This, however, neglects the fact that shocks have a cooling structure with a certain range of temperatures that contribute to the EUV and X-ray spectrum. Our revision comprises two modifications to the shock structure. The first one concerns the inner region of the wind, where the cooling time can be regarded to be shorter than the flow time. Here the approximation of *radiative* shocks can be applied for the cooling process (cf. Chevalier and Imamura 1982). The second one concerns the outer region, where the stationary terminal velocity is reached, the radiative acceleration is negligible, and the flow time is therefore large. Here radiative cooling of the shocks is of minor importance and the cooling process can be approximated by *adiabatic expansion* (cf. Simon and Axford 1966, who investigated a pair of reverse and forward shocks that propagate through an ambient medium under these circumstances). For our purpose we followed directly the modified concept of isothermal wind shocks presented recently by Feldmeier et al. (1997).

Compared to Eq. 29 we account for the density and temperature stratification in the shock cooling layer by replacing the values of the volume emission coefficient ($\Lambda_\nu(T_s(r) n_e)$) through adequate integrals over the cooling zones denoted by $\hat{\Lambda}_\nu(T_s(r))$. Thus, $\epsilon_\nu^s(r)$ is replaced by

$$\hat{\epsilon}_\nu^s(r) = \frac{f}{4\pi} n_p n_e \hat{\Lambda}_\nu(T_s(r)), \quad (30)$$

where

$$\hat{\Lambda}_\nu(T_s(r)) = \pm \frac{1}{x_s} \int_r^{r \pm x_s} \hat{f}^2(r') \Lambda_\nu(T_s(r') \cdot \hat{g}(r')) dr', \quad (31)$$

and r is the location of the shock front, r' is the cooling length coordinate with a maximum value of x_s , the plus sign corresponds to forward and the minus sign to reverse shocks, and $\hat{f}(r')$ and $\hat{g}(r')$ denote the normalized density and temperature structures with respect to the shock front. The improvement of our treatment is now obviously directly connected to the description of the latter functions. In the present step we used the analytical approximations presented by Feldmeier et al. (1997), which are based on the two limiting cases of radiative and adiabatic cooling layers behind shock fronts (see above).

3.5.1. Test calculations and first results

In the following we present results of test calculations showing the influence of our modified treatment of shock emission. For this purpose we selected the O4f-star ζ Puppis as a test object and ignored for the corresponding model calculations the improved blocking and blanketing treatment discussed above. This restriction makes our results directly comparable to those of Pauldrach et al. (1994a), who used the old, simplified treatment for the shock emission. The stellar parameters of ζ Puppis, used as basic input for our models, have been adopted

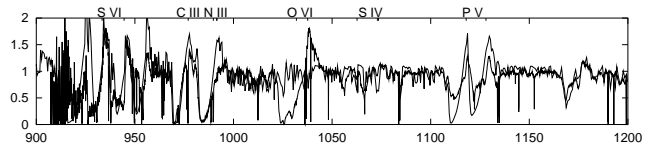


Fig. 15. Calculated and observed UV spectrum for the O4f-star ζ Puppis. The calculated spectrum belongs to a model where the influence of shock emission has been neglected. The high resolution observations have been obtained with the IUE and Copernicus satellites. (Note that the improved blocking and blanketing treatment has not been considered for the model calculations of this object – see text.)

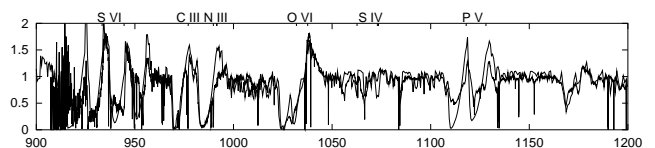


Fig. 16. Calculated and observed UV spectrum for the O4f-star ζ Puppis. The calculated spectrum belongs to a model where the influence of shock emission has been included (model 1).

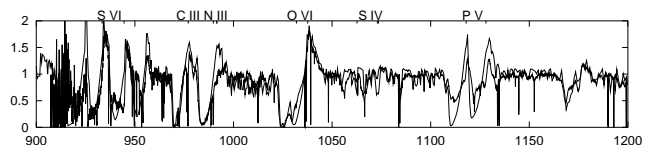


Fig. 17. Calculated and observed UV spectrum for the O4f-star ζ Puppis. The calculated spectrum belongs to a model where the influence of shock emission has been included in accordance with our improved method (model 2).

$\log(\frac{L}{L_\odot})$	$\frac{T_{\text{eff}}}{10^3\text{K}}$	$\log g$	$\frac{R_*}{R_\odot}$	$\frac{v_\infty}{\text{km/s}}$	$\frac{\dot{M}}{10^{-6} M_\odot/\text{yr}}$
6.006	42	3.625	19	2250	5.9

Table 2. The stellar parameters of the O4f-star ζ Puppis.

$Y_{\text{He}} = 1.20 Y_{\text{He},\odot}$	$Y_{\text{C}} = 0.35 Y_{\text{C},\odot}$
$Y_{\text{N}} = 8.00 Y_{\text{N},\odot}$	$Y_{\text{O}} = 0.75 Y_{\text{O},\odot}$

Table 3. Abundances used for the ζ Puppis model. $Y_X := n_X/n_{\text{H}}$, where $Y_{X,\odot}$ denotes the solar abundance. For all other abundances solar values were used.

$\log(\frac{T_s}{\text{K}})$	$\frac{f}{10^{-3}}$	$\log(\frac{N_{\text{H}}}{\text{cm}^{-2}})$
6.75	4.3	20.00

Table 4. Parameters required for describing the cooling zones of the shocked gas.

from Pauldrach et al. 1994 (see Table 2), together with the abundances listed in Table 3. (These abundances have recently been confirmed by Kahn et al. (2000) from high resolution X-ray spectroscopy of ζ Puppis with the XMM Newton reflection grating spectrometer.)

Although the final objective of our treatment is the determination of the maximum post-shock temperature (T_s) and the filling factor (f) from a comparison of the calculated and observed ROSAT spectrum, we have also adopted these values for the present test calculations from the similar fits performed by Feldmeier et al. (1997). The values are given in Table 4 together with the interstellar column density of hydrogen ($\log(N_H)$, cf. Shull and van Steenberg 1985).

We start with a spectrum synthesis calculation where EUV and X-ray radiation by shock heated matter *is neglected*. The comparison between the observed and the synthetic spectrum (Fig. 15) shows clearly that the strong observed resonance lines of O VI are not reproduced by the model. This striking discrepancy illustrates what is meant by the problem of “*superionization*”. In Fig. 16 we demonstrate, however, that this problem has already been solved by making use of the EUV and X-ray radiation resulting from the treatment of isothermal shocks (model 1). The observed resonance lines of O VI are reproduced quite well, apart from minor differences. Thus it seems that the wind physics are correctly described. That this is not completely the case can be inferred from Fig. 18 where the ROSAT PSPC spectrum (error bars) is shown together with the result of model 1 (thin line). The deficiency of the non-stratified isothermal shocks is obvious – the model yields too little radiation in the soft X-ray part (shortward of 0.7 keV the spectrum is more likely characterized by a cooler shock component of $\log T_s \approx 6.30$) and too much in the harder energy band.

Following the strategy outlined above we now investigate how far the structured cooling zones behind the shocks can influence this negative result. Fig. 18, which shows in addition the calculated X-ray spectrum of our improved model (model 2, thick line), illustrates the improvement. Strikingly, the new calculations can quite well reproduce the ROSAT PSPC spectrum and the comparison shown is at least of the same quality as that obtained by Feldmeier et al. (1997) with their best fit (see also Stock 1998) – note that the total X-ray luminosity of this model is given by

$$L_x = \int_{0.1 \text{ keV}}^{2.5 \text{ keV}} L_\nu d\nu = 10^{-7.1} L_{\text{bol}}. \quad (32)$$

Actually, it is the fact that, compared to the non-stratified isothermal shocks, the post-shock cooling zones with their temperature stratifications radiate much more efficiently in the soft spectral band which leads to the improved fit. This is portrayed in Fig. 19.

Fig. 20 shows the location of the optical depth unity in the relevant energy band of ROSAT. Apart from displaying the influence of the K-shell opacities, it becomes evident from this figure that the wind is optically thick up

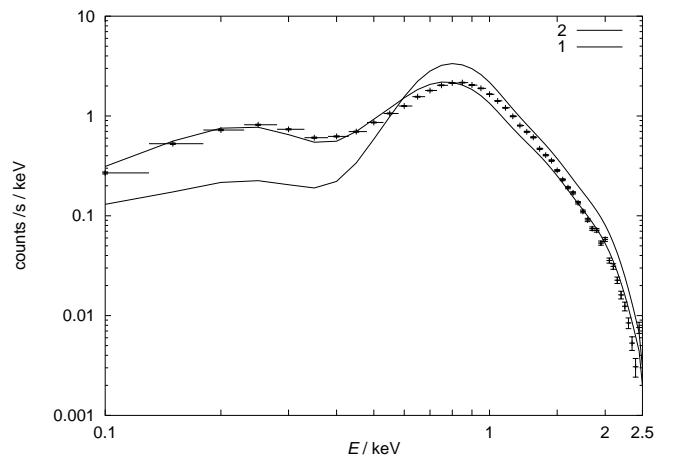


Fig. 18. Comparison of the ROSAT-observations (error bars) with the results of model 2 (thick line) and model 1 (thin line) for ζ Puppis.

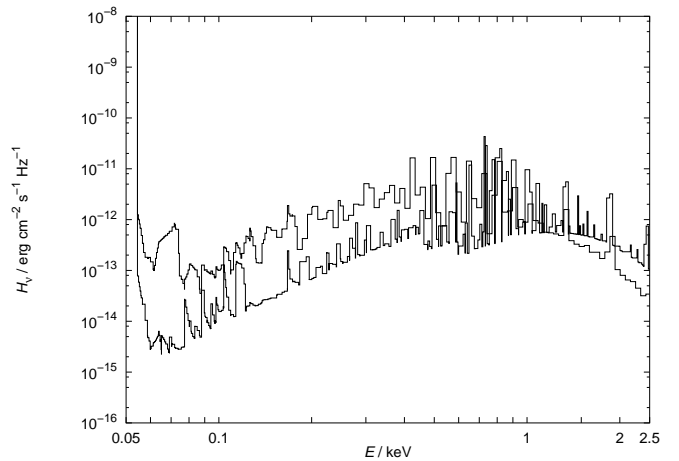


Fig. 19. The Eddington flux in the EUV and X-ray band resulting from model 2 (thick line) and model 1 (thin line) for ζ Puppis. Note that the maximum shock temperatures are identical for both models.

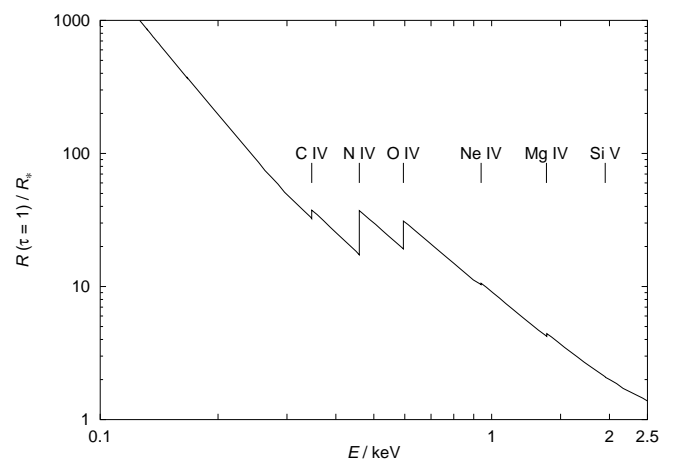


Fig. 20. Spatial location of the optical depth unity in the relevant energy band of ROSAT, displaying the origin of the observed flux. Also shown is the influence of the K-shell opacities for model 2 of ζ Puppis.

Table 5. The parameters of our basic model grid stars. The Zanstra integrals given here are defined as $Q_X = \int_{\nu_X}^{\infty} \frac{H_\nu}{h\nu} d\nu$, where $h\nu_X$ is the ionization energy of ion X .

Model	T_{eff} (K)	$\log g$ (cgs)	R (R_\odot)	v_∞ (km/s)	\dot{M} ($10^{-6} M_\odot/\text{yr}$)	$\log Q_{\text{H}}$	$\log Q_{\text{He}^+}$	$H_\nu(5480 \text{ \AA})$ ($10^{-3} \text{ erg/s/cm}^2/\text{Hz}$)
Dwarfs								
D-30	30000	3.85	12	1800	0.008	21.42	8.42	0.3702
D-35	35000	3.80	11	2100	0.05	22.65	11.41	0.4771
D-40	40000	3.75	10	2400	0.24	23.15	17.63	0.5859
D-45	45000	3.90	12	3000	1.3	23.45	18.99	0.6817
D-50	50000	4.00	12	3200	5.6	23.69	20.28	0.7743
D-55	55000	4.10	15	3300	20	23.89	20.17	0.8881
Supergiants								
S-30	30000	3.00	27	1500	5.0	22.32	6.39	0.4229
S-35	35000	3.30	21	1900	8.0	22.88	9.70	0.4935
S-40	40000	3.60	19	2200	10	23.19	11.24	0.5998
S-45	45000	3.80	20	2500	15	23.48	11.84	0.7160
S-50	50000	3.90	20	3200	24	23.71	18.34	0.8204

to large radii, especially in the soft X-ray band. This fact reduces the significance of the fit of the ROSAT spectrum, because most of the observed X-ray radiation is obviously emitted in the outermost part of the wind and thus only the properties of the radiation produced in this outer region can be analyzed from the observed spectrum. This, however, is not the case for the EUV and X-ray radiation which populates the occupation numbers connected with the resonance lines of N V and O VI, since due to their P-Cygni structure these lines provide information about the complete wind region, and the properties of the influencing radiation produced in the the whole wind region can therefore be analyzed by means of spectral line diagnostics.

Hence, for the significance of our modified method it is therefore extremely convincing that the synthetic UV-spectrum resulting from model 2 also reproduces the observed resonance lines of N V and O VI (the latter is shown in Fig. 17). That both model 1 and model 2 yield a good fit of the P-Cygni lines shows, on the other hand, that distinguishing between two different models from the profiles alone is not always possible. The fact that our improved treatment accounting for the structured cooling zones behind the shocks solves not only the problem of “*superionization*”, but reproduces for the first time consistently the ROSAT PSPC spectrum *as well as* the resonance lines of N V and O VI gives us confidence in our present approach.

From Figs. 16 and 18 we deduce that the method corresponding to model 1, which we will use in the calculations in Section 4, nevertheless turned out to be a good description of the shock radiation (considering the greater importance, as discussed in the previous paragraph, of a fit of the UV resonance lines of the highly ionized species compared to a fit of the Rosat spectrum), as it reproduces the UV spectral lines of the highly ionized species as well as the improved method and also leads to a rather good description of the X-ray spectrum, which can be used as

long as the Rosat observations are not required to be fitted perfectly. (Note that the improved treatment of the X-ray radiation is not yet available in the download version of the code; it will be implemented in an upcoming version (2.x).)

4. Results

In the following we apply our improved code for expanding atmospheres to a basic model grid of O-stars. The objectives of these calculations are to present ionizing fluxes which can be used for the quantitative analysis of emission line spectra of H II-regions and Planetary Nebulae, and to prove our method and demonstrate its reliability by means of synthetic UV spectra which are qualitatively compared to corresponding observations. (Note that for the standard model calculations the EUV and X-ray shock radiation is not included – using our *WM-basic* program package this should always be the first step. For succeeding models in an advanced stage we have used solely our previous method based on isothermal shocks (cf. Section 3.5), since this is the method which is presently available for WM-basic and thus the models presented in the following can be reproduced by this offered tool.)

Finally, one of the grid models is chosen for a detailed comparison between observed and calculated synthetic spectra, where the primary objective has been to develop diagnostic tools for the verification of stellar parameters, and the determination of abundances and stellar wind properties entirely from the UV spectra. This has been carried out for a cooler O9.5 Ia supergiant, α Cam – a cooler object has been chosen since several aspects tend to make these generally more problematic, such as the ionization balance (more stages are affected) and the optical thickness of the continuum in the wind part.

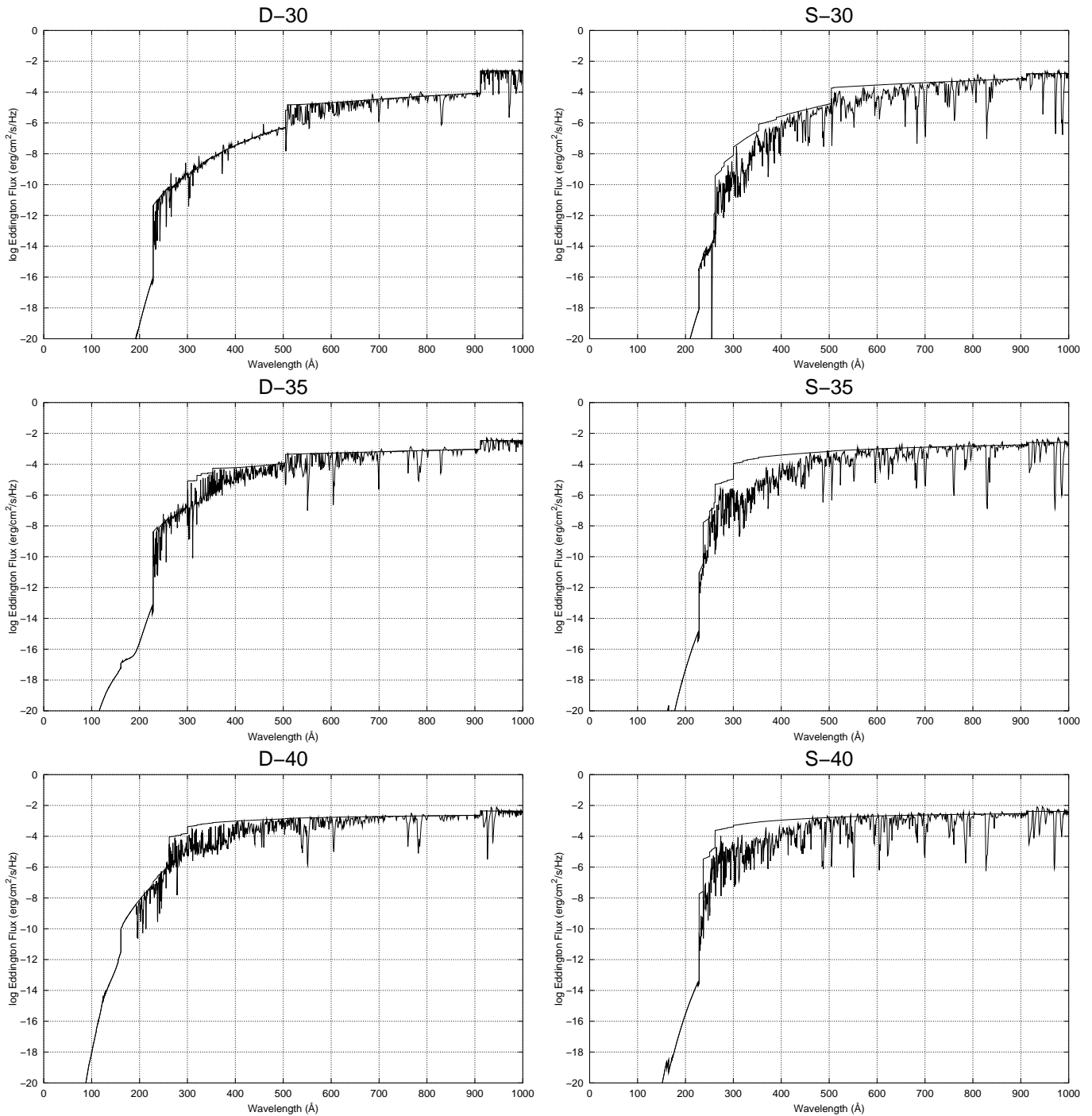


Fig. 21. Calculated ionizing fluxes (Eddington flux in cgs units) versus wavelength of the model grid stars; dwarfs on the left, supergiants on the right.

4.1. The basic model grid

In this section we present the ionizing fluxes and synthetic spectra of a basic model grid of O-stars of solar metallicity, comprising dwarfs and supergiants with effective temperatures ranging from 30,000 to 50,000 K. The model parameters, summarized in Table 5, were chosen in accordance with the range of values deduced from observations as tabulated by Puls et al. 1996.

In Fig. 21 we show for each model the primary result, the ionizing emergent flux together with the corresponding continuum. It can be verified from the figure that the influence of the line opacities, i.e., the difference between the continuum and the total flux, increases from dwarfs to supergiants and from cooler to hotter effective temperatures. Both points are not surprising, because they are directly coupled to the mass loss rate (\dot{M}) which increases exactly in the same manner (cf. Table 5). Due to the increasing \dot{M} the optical depth of the lines also increases in the wind

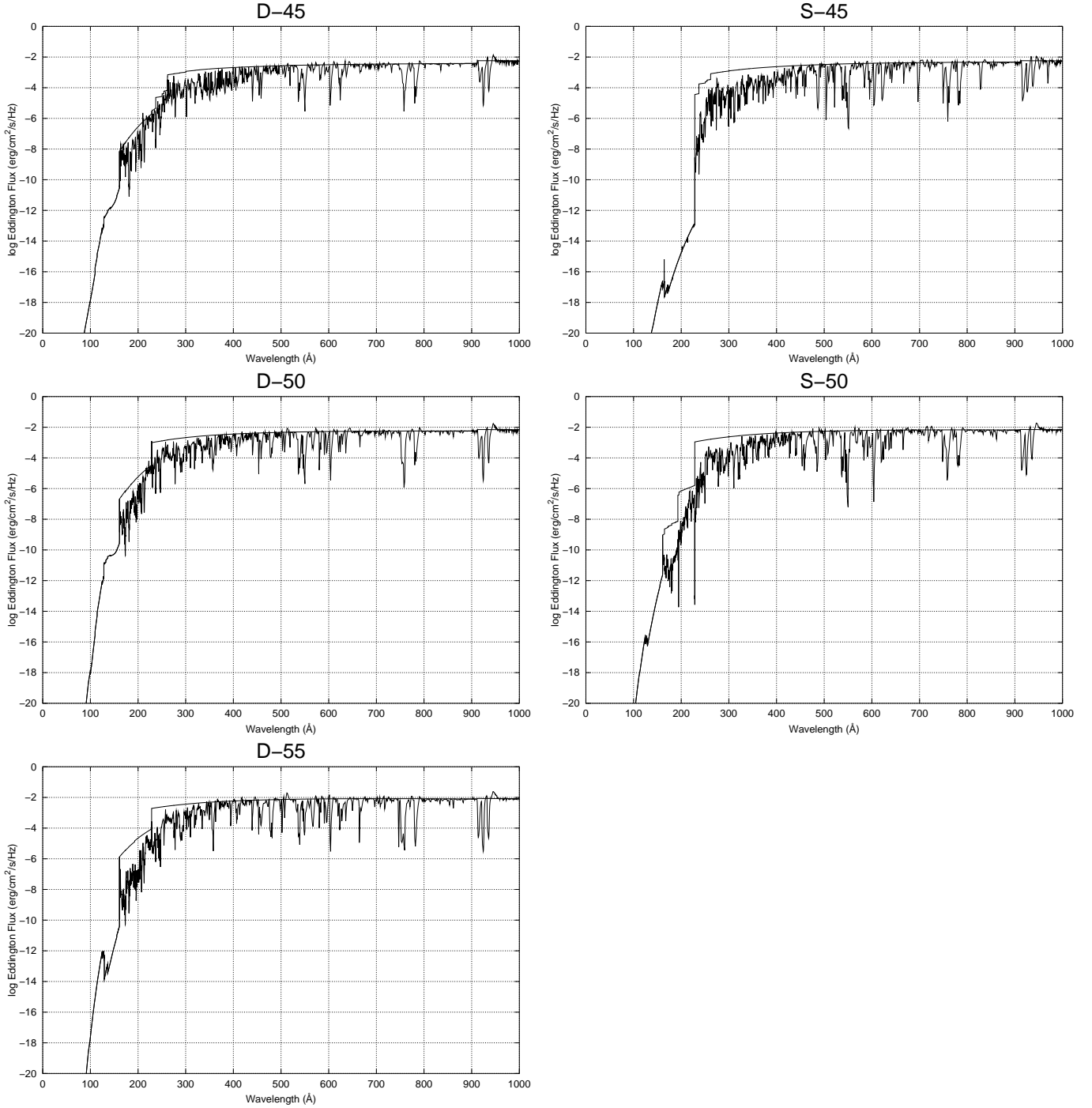


Fig. 21. (continued) Calculated ionizing fluxes (Eddington flux in cgs units) versus wavelength of the model grid stars; dwarfs on the left, supergiants on the right.

part and in consequence the line blocking effect is more pronounced. This behavior, however, saturates for objects with effective temperatures larger than $T_{\text{eff}} = 45\,000$ K, since in this case higher main ionization stages are encountered (e. g., Fe V and Fe VI) which are known to have less bound-bound transitions (cf. Pauldrach 1987). Thus, as can be verified from Fig. 21 the effect of line blocking is strongest for supergiants of intermediate T_{eff} . In Table 5 we also present the numerical values of the integrals of ionizing photons emitted per second for H ($\log Q_{\text{H}}$) and

He II ($\log Q_{\text{He}^+}$), as well as the flux at the reference wavelength $\lambda = 5480$ Å, which can be used directly to calculate Zanstra ratios and Strömgen radii.

The next step is to demonstrate the reliability of the calculated emergent fluxes. As the wavelength region shortward of the Lyman edge usually cannot be observed and thus a direct comparison of the fluxes with observations is not possible, an indirect method to test their accuracy is needed. In principle, two such methods exist. The first one is to test the ionizing fluxes by means of

Table 6. Model grid stars and real-world examples with similar spectral types. The parameters of the observed example stars are from Puls et al. 1996.

Model / Example	classi- fication	T_{eff} (K)	$\log g$ (cgs)	R (R_{\odot})	M (M_{\odot})	$\log \frac{L}{L_{\odot}}$	v_{∞} (km/s)	\dot{M} ($10^{-6} M_{\odot}/\text{yr}$)
Dwarfs								
D-30		30000	3.85	12	37	5.02	1800	0.008
HD 149757 (ζ Oph)	O9 III	32500	3.85	12.9	43	5.22	1550	≤ 0.03
D-40		40000	3.75	10	21	5.36	2400	0.24
HD 217068	O7 V n	40000	3.75	10.3	22	5.39	2550	≤ 0.2
D-50		50000	4.00	12	53	5.91	3200	5.6
HD 93250	O3 V ((f))	50500	4.00	18	118	6.28	3250	4.9
Supergiants								
S-30		30000	3.00	27	27	5.73	1500	5.0
HD 30614 (α Cam)	O9.5 Ia	30000	3.00	29	31	5.79	1550	5.2
S-40		40000	3.60	19	53	5.92	2200	10
HD 66811 (ζ Pup)	O4 I (f)	42000	3.60	19	53	6.00	2250	5.9
S-50		50000	3.90	20	116	6.35	3200	24
HD 93129A	O3 I f*	50500	3.95	20	130	6.37	3200	22

their influence on the emission lines of gaseous nebulae, i. e., using the ionizing fluxes as input for nebular models and comparing the calculated emission line strengths to observed ones. However, as a first step this procedure is questionable, since the diagnostics of gaseous nebulae is still not free from uncertainties – dust clumps, complex geometric structure, etc. – and therefore, if discrepancies are encountered, it is difficult to decide which of the assumptions is responsible for the disagreement. (As an example we mention the Ne III problem discussed comprehensively by Rubin et al. 1991 and Sellmaier et al. 1996.) Rather, nebular modelling and diagnostics should be able to build upon the reliability of the ionizing fluxes, and thus the quantitative accuracy of the fluxes needs to be tested independently of their use in nebular emission line analysis.

The second – and in the light of the difficulties discussed above, the only trustworthy – method is quite analogous, but instead of an external nebula involves *the atmosphere of the star itself*. The rationale is that the emergent flux is but the outer value of a radiation field *calculated selfconsistently throughout the entire wind*, which influences the ionization balance at *all depths*. This ionization balance can be traced reliably through the strength and structure of the wind lines formed everywhere in the atmosphere. Hence it is a natural and important step to test the quality of the ionizing fluxes by virtue of their direct product: *the UV spectra of O stars*.

4.2. Qualitative comparison with observations

The test is performed by means of synthetic UV spectra which are *qualitatively* compared to observed IUE spectra and as such cannot be expected to conform in all details. (Minor discrepancies can only be discussed at hand of detailed comparisons. How such discrepancies might be

removed by an adjustment of the stellar parameters is shown, as an example, by means of a detailed comparison for α Cam in Section 4.3. In several spectral regions with numerous absorption lines (Fe IV, Fe V, Ni IV) discrepancies might also be due to difficulties in placing the continuum of the observations.) For this qualitative comparison we have chosen, for each model of a subset of our grid, a real object from the list of Puls et al. 1996 whose supposed stellar and wind parameters come very close to those of the model. The parameters of the model stars and the selected real objects are summarized in Table 6. (The influence of shock radiation on the models has been neglected at this qualitative step.)

First we investigate the spectra of the dwarf models. As can be inspected from Fig. 22 the comparison of the models D-30 and D-40 with their counterparts HD 149757 and HD 217068 show in principle an overall agreement, whereas the D-50 model, compared with its counterpart HD 93250, shows a severe discrepancy concerning the O V subordinate line at 1371 Å (the calculated line is much too strong) and a less pronounced discrepancy of the N IV subordinate line at 1718 Å (the calculated line is somewhat too weak). Hence we have to realize that either the wind physics is not completely described, or the stellar or the wind parameters of this model are too different from those of HD 93250.

Regarding the first point one might speculate that the inclusion of shock radiation leads to an improvement for the O V line, although this effect would weaken the N IV line further. As is shown below, shock radiation cannot solve the problem, as it does not affect the strength of the O V line at all (cf. the discussion of the S-50 model below). Regarding the second point there are three parameters which could lead to an improvement for both lines. The first one is the effective temperature which, however, would have to be decreased by at least 5000 K. This is on

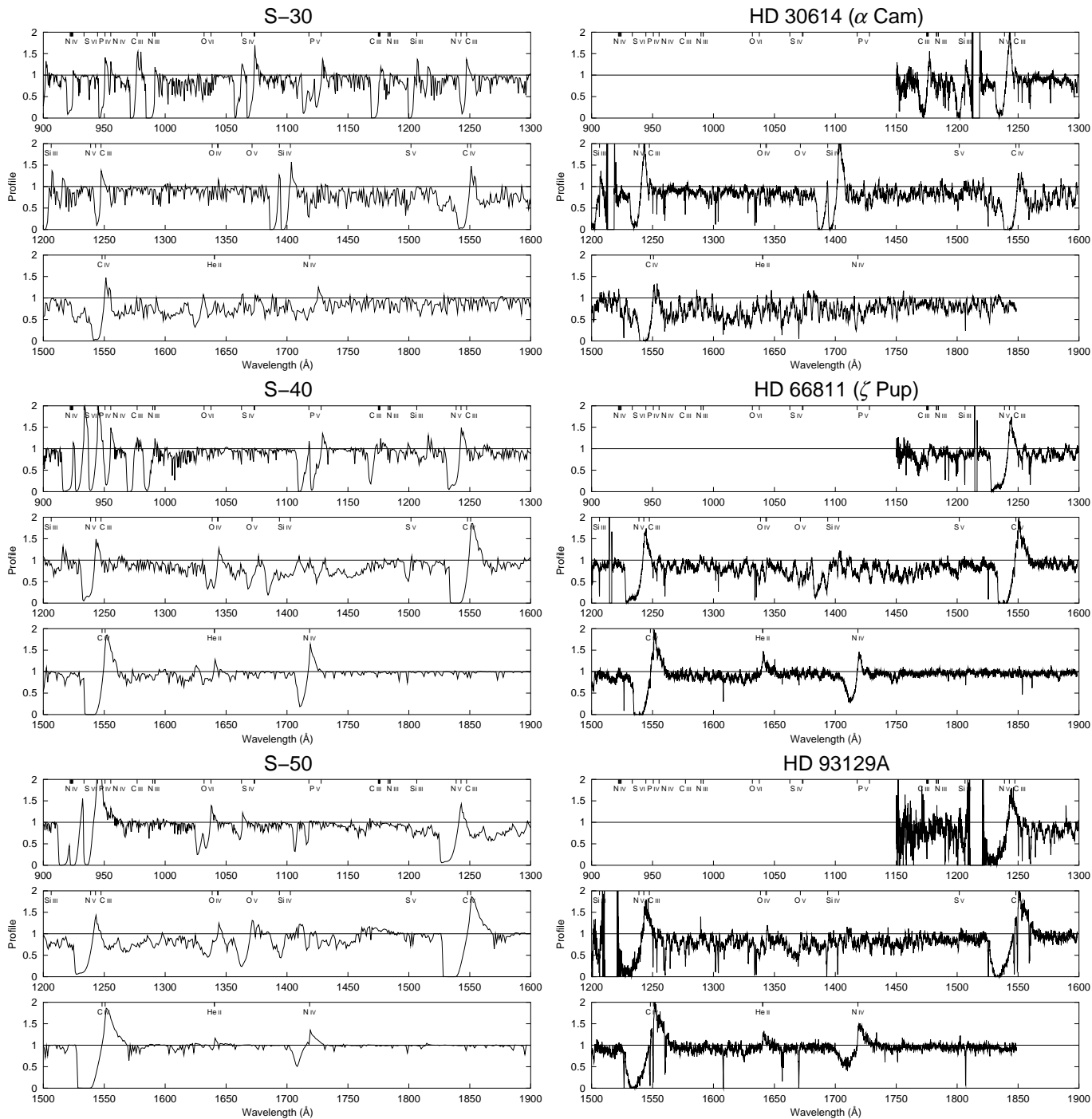


Fig. 23. Calculated UV spectra of the model grid supergiants (left) compared to observed IUE spectra (right) of stars of similar spectral type.

one with a higher mass loss rate. Hence we conclude that the mass loss rate has to be larger by a factor of ≈ 2 – note that this is also indicated by the stellar parameters of HD 93250 which are very close to those of HD 93129A, which means that the wind parameters have to be similar too; note further the strong similarity of the observed spectra of HD 93129A and HD 93250, which points in the same direction (cf. Fig. 25, upper panel); in addition, the abundances of the CNO elements have to be reduced strongly compared to the solar values (for oxygen a reduced value

of approximately a factor of 50 is required to weaken the strength of both the O IV and the O V line, as has been inferred from additional test calculations). This, however, should not be the case for the heavier elements (Fe, Ni) since a solar-like abundance of these elements is required to account for the radiative acceleration necessary to produce the higher mass loss rate (cf. Pauldrach 1987).

Now we inspect the comparison of the supergiant models (Fig. 23). As is shown, the observed spectra are reproduced in principle quite well apart from minor differ-

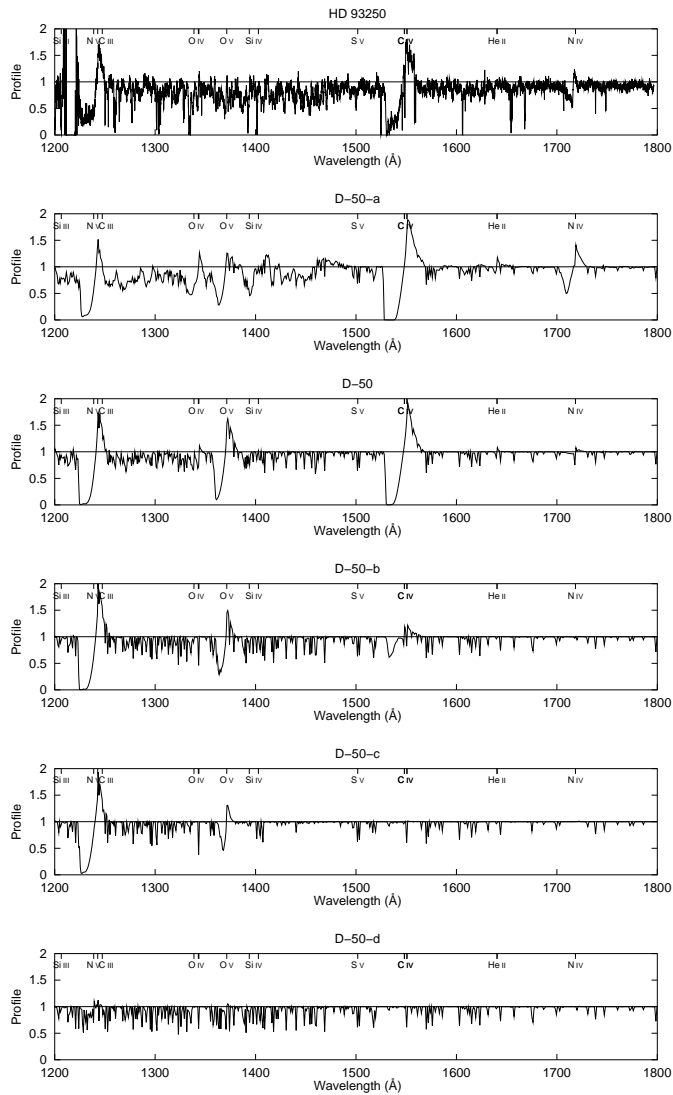


Fig. 24. Spectra obtained for a mass loss rate sequence for the D-50 dwarf model. For comparison, the IUE spectrum of HD 93250 is also shown. The mass loss rates of the models are given in Table 7. Lowering the mass loss rate cannot solve the problem of the too-strong O V line, as this is one of the last lines to disappear with diminishing mass loss rate.

ences which can be attributed to a change of abundances (note that the discrepancy of the N V resonance line is due to the omitted shock radiation – see below). Again, the most conspicuous difference regards the O IV and O V subordinate lines which are both too strong, especially for the S-40 and the S-50 models. From the investigation above it is already quite clear that the abundance(s) of the (CN)O element(s) has (have) to be reduced in order to overcome this discrepancy. Nevertheless, we investigate now whether the inclusion of shock radiation leads to an improvement. We have therefore computed an additional model for the S-50 supergiant, model S-50-a, where the influence of shocks on the spectrum has been accounted for; the shock parameters are given in Table 8.

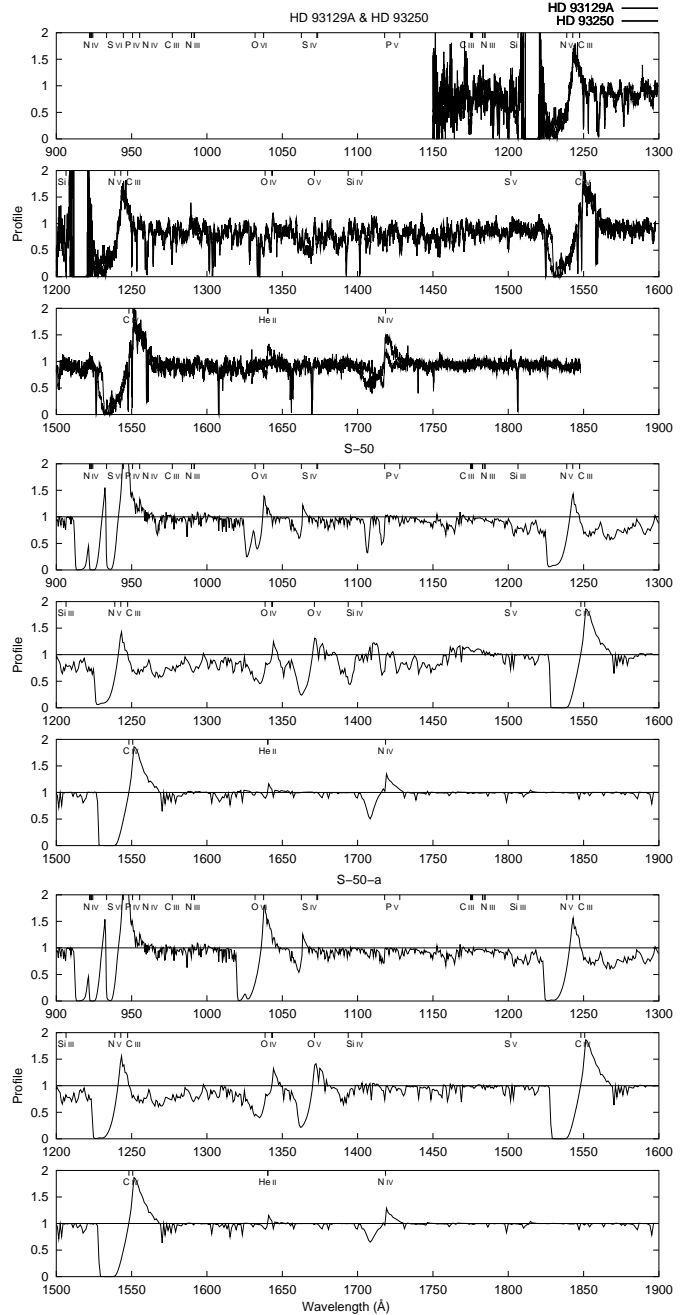


Fig. 25. Upper panel: Comparison of the IUE spectra of HD 93129A (O3If) and HD 93250 (O3V(f)). Apart from the strength of a few lines of light elements (e.g., the N IV line at 1718 Å) the spectra are almost identical. Other panels: Influence of shocks on the spectrum of the S-50 supergiant model. Middle panel: without shocks, lower panel: with shocks. The influence of the shocks on the strength of the O IV and O V lines is negligible.

Figure 25 shows that the influence of the shocks on the strength of the O IV and O V lines, and hence the ionization balance, is negligible – just O VI is enhanced selectively, which can be seen by the strength of the O VI resonance line. Another line which is considerably affected by shock emission is the Si IV resonance line. This is because the soft X-ray radiation field of the shocks enhances

Model	D-50-a	D-50	D-50-b	D-50-c	D-50-d
\dot{M} ($10^{-6} M_{\odot}/\text{yr}$)	11.0	5.6	0.56	0.12	0.01

Table 7. Mass loss rates for the models shown in Figure 24. All other parameters are identical to those of the D-50 model shown in Table 5.

$\log(L_X/L_{\text{bol}})$	v_t/v_{∞}	γ	m
-7.0	0.1	1	1

Table 8. Shock parameters for the S-50-a model shown in Figure 25. For an explanation of the parameters see Section 4.3.

the ionization of Si v, and thus the recombination to Si iv is decreased (cf. Pauldrach et al. 1994). As can be inferred from Fig. 25 this improves the fit of the Si iv line significantly. Concerning oxygen we come to the same conclusion as for the dwarf models, namely that the abundance has to be reduced strongly compared to the solar value.

4.3. Detailed analysis of α Cam

In this section we provide, using our S-30 grid model as a starting point, a detailed determination of the abundances and stellar wind properties, and verification of the stellar parameters of α Cam. Special emphasis is given to the shock radiation needed for a fit of the N v and O vi resonance lines. Although preliminary results from our new shock description look very promising (see Section 3.5), this new method is not yet fully implemented in WM-basic. For this investigation we therefore use the method based on isothermal shocks. See Pauldrach et al. 1994 and 1994a for a detailed explanation of the shock parameters and the rationale behind the parameterization.

We wish to point out here that we have not attempted an exact determination of $\log g$ and stellar radius, but have rather kept the values of our S-30 grid model. The reason is that in contrast to the hydrodynamics the UV spectrum depends only marginally on these parameters, the main influence being due to T_{eff} and \dot{M} (i. e., density). The radius and the surface gravity ($\log g$) can in principle be determined from a selfconsistent calculation of the hydrodynamics and the NLTE model, in which both values would be adapted in such a way that the hydrodynamics, with consistent force multiplier parameters from the NLTE occupation numbers (in turn again dependent on the hydrodynamic solution), would yield the mass loss rate and the terminal velocity deduced from H_{α} and the observed UV spectrum (cf. Pauldrach et al. 1994, 1994a). This latter procedure has however not yet been implemented in WM-basic.

In Fig. 26 we compare the spectrum of our basic S-30 grid model with the spectra of α Cam observed with IUE and Copernicus. With the exception of a few strong lines, notably the N v resonance doublet at 1238, 1242 Å and the subordinate C iii line at 1247 Å, the agreement is

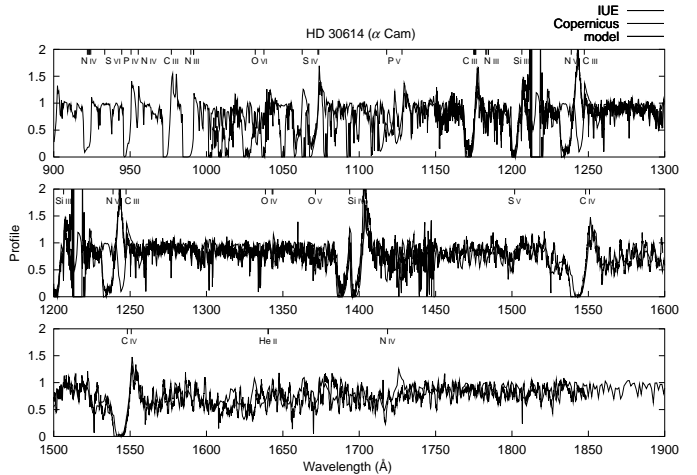


Fig. 26. Comparison of the basic S-30 grid model with spectra of α Cam observed by IUE and Copernicus.

very good for a first step, especially with respect to the iron and nickel “forest” between 1400 and 1600 Å. As the two lines mentioned above are mainly affected by shock radiation, and as it is not clear *a priori* how shocks affect the lines used to determine, e. g., the temperature, we will first attempt to fit the shock parameters before verifying the stellar parameters. We note in passing that the strong lines from 1000 to 1100 Å (with the recurring pattern), that complicate an exact fit of the O vi resonance line, are absorption by interstellar molecular hydrogen.

A model with reasonable “first guess” values for the shock parameters (model a, Table 9) already gives a very good fit to the N v resonance line, as shown in Fig. 27, the emission, however, completely decimated by the much too strong C iii λ 1247 line. Increasing the X-ray luminosity ($\log(L_X/L_{\text{bol}})$) to reduce the C iii occupation unfortunately also tends to ionize Si iii to Si iv, thus reducing the strength of the Si iii line. Modifying v_t/v_{∞} (the ratio of the maximum jump velocity to the terminal velocity, where v_t characterizes the immediate post-shock temperature; see Pauldrach et al. 1994) does not change this fact, as we have confirmed by calculating a grid of models with values of $\log(L_X/L_{\text{bol}})$ ranging from -8 to -6.5 and v_t/v_{∞} ranging from 0.1 to 0.2. For example, a model sequence (models b1–b3) is shown in Fig. 28, in which we vary $\log(L_X/L_{\text{bol}})$ from -7.5 to -6.5, keeping all other parameters constant (cf. Table 9). As can be seen, the Si iii line already begins to weaken, while C iii still remains too strong. Adjusting the parameter γ (which controls the strength of the shocks relative to the local velocity – cf. Pauldrach et al. 1994) does not help either, as both the C iii and the Si iii line are formed in the inner part of the wind, thus both being subject to the same radiation field.

From this we conclude that solar abundances cannot reproduce the observed spectrum. A model, however, with a reduced carbon abundance of one tenth solar (model c) can indeed give a good fit of the line, as shown in Fig. 29. We will use this abundance for the following calculations,

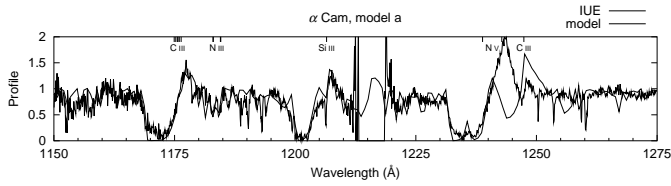


Fig. 27. Model a, using our “first guess” values for the shock parameters. C III λ 1247 is much too strong.

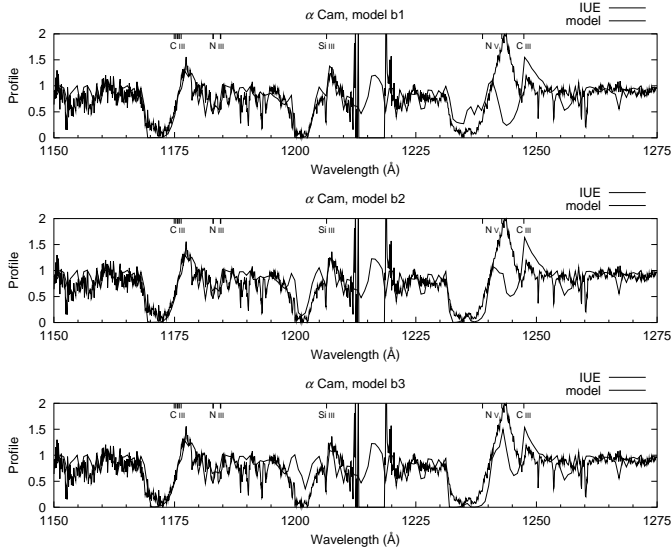


Fig. 28. Models b1–b3, a sequence showing the influence of increasing $\log(L_X/L_{bol})$. Note that Si III disappears before C III has decreased to its observed strength.

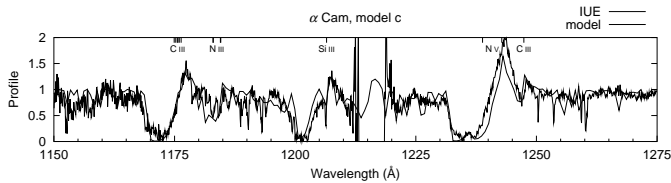


Fig. 29. Model c. Here we have adapted the shock parameters and abundances (see Table 9) to provide for a reasonable fit of Si III and C III.

unless stated otherwise. As carbon thus shows indications of the CNO-process, we have for reasons of consistency also increased the nitrogen abundance by a factor of 10, but such a large factor is not compatible with the fit of the nitrogen lines; from the final models we determined the nitrogen abundance to be approximately solar.

Despite the good fit, this model is still not satisfactory, as it shows no signs of O VI. Since the C III/Si III-balance strongly constrains the shock strength in the inner regions, this cannot be achieved simply by increasing the X-ray luminosity. However, the onset of shocks can be adapted with the parameter m , which gives the ratio of outflow to sound velocity where shocks start to form, and as the jump velocity is correlated to the outflow velocity, the corresponding radius (cf. Pauldrach et al. 1994). Increasing this parameter allows shocks in the outer regions (O VI appears close to v_∞), while leaving the inner regions (where

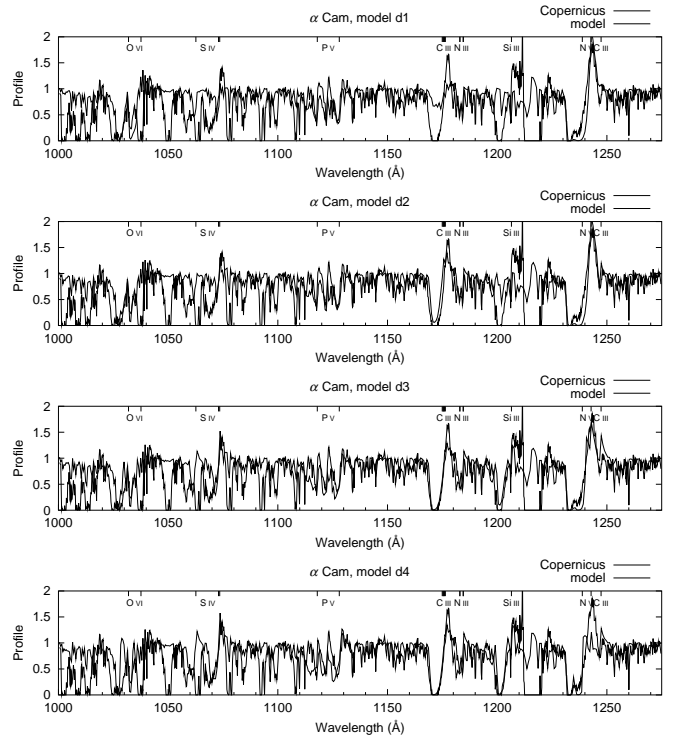


Fig. 30. Models d1–d4, a sequence in which the radius at which shocks start to form has been successively moved outwards, keeping all other parameters equal. In model d4, where Si III remains fairly unaffected by shocks, the P Cygni emission of O VI and N V has completely disappeared.

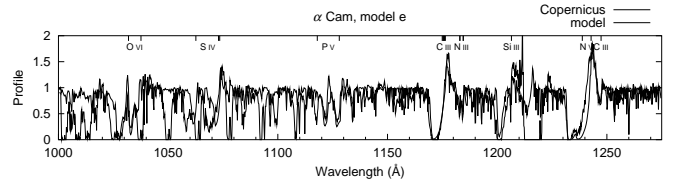


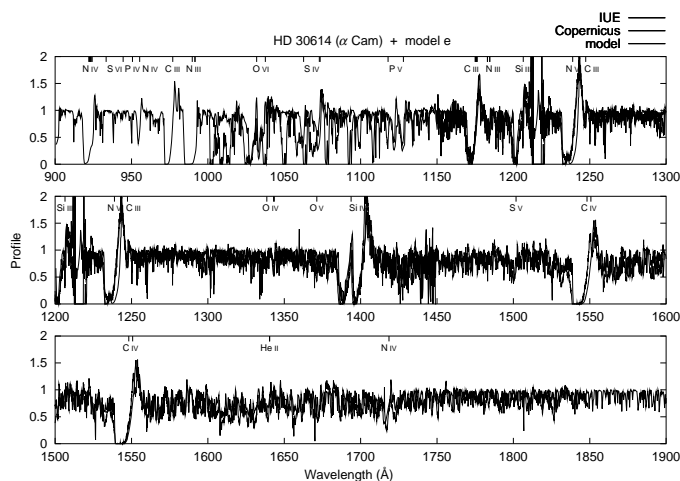
Fig. 31. Model e. Increasing the shock jump velocity provides for harder shock radiation that has a stronger influence on O VI and N V than on Si III. The abundances of C, N, O, and P have also been adapted.

Si III is present) largely undisturbed. This behaviour of the shocks is already an important result from our analysis.

Fig. 30 shows a model sequence in which m is increased from 1 to 60; $\log(L_X/L_{bol})$ has been increased compared to model c to provide for sufficient O VI. It can be seen that in model d4 ($m = 60$), where Si III retains its correct strength and the absorption of O VI and N V is of the correct magnitude, the emission of both latter lines has disappeared completely. This is because the emission of P Cygni lines due to resonance scattering arises to a large part from the inner regions of the wind, where the stellar radiation field is still strong; in this model however, N V and O VI hardly exist in these regions, since the shock radiation responsible for the presence of these ions is only produced far out in the wind and the ionization continuum is still optically thick at the corresponding photoionization thresholds. We conclude that the onset of shocks

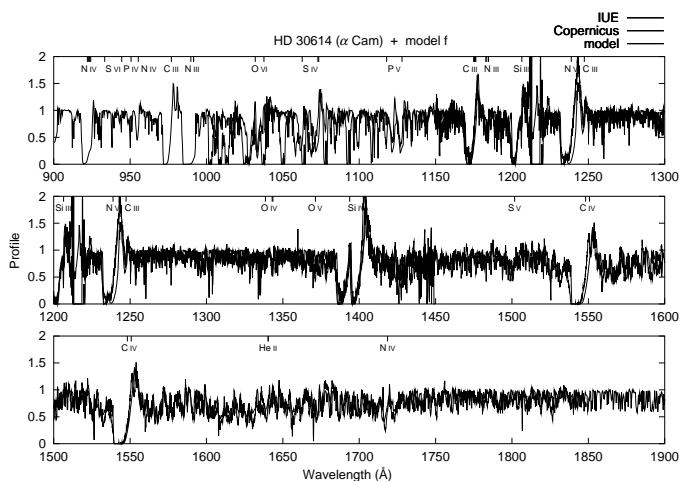
Table 9. Model parameters for α Cam. Abundances not explicitly mentioned are solar; if given, the number is the factor relative to the solar value. T_{eff} is in K, \dot{M} in $10^{-6} M_{\odot}/\text{yr}$.

Model	T_{eff}	\dot{M}	v_t/v_{∞}	$\log(L_X/L_{\text{bol}})$	γ	m	abundances
a	30000	5	0.125	-7.5	1	1	solar
b1	30000	5	0.14	-7.5	1	1	solar
b2	30000	5	0.14	-6.0	1	1	solar
b3	30000	5	0.14	-6.5	1	1	solar
c	30000	5	0.20	-7.5	0.5	1	C = 0.1, N = 10., O = 1.0, P = 0.1, S = 2.0
d1	30000	5	0.14	-7.0	0.5	1	— " —
d2	30000	5	0.14	-7.0	0.5	30	— " —
d3	30000	5	0.14	-7.0	0.5	40	— " —
d4	30000	5	0.14	-7.0	0.5	60	— " —
e	30000	5	0.25	-6.5	0.5	30	C = 0.1, N = 2.0, O = 0.3, P = 0.05, S = 1.0
f	29000	5	0.25	-6.5	0.5	30	— " —
best fit → g	29000	5	0.25	-6.5	0.5	30	C = 0.05, N = 1.0, O = 0.3, P = 0.05, S = 1.0
h	28000	5	0.25	-6.5	0.5	30	— " —
i	28000	2.5	0.25	-6.5	0.5	30	— " —
j	28000	10	0.25	-6.5	0.5	30	— " —

**Fig. 32.** The complete EUV spectrum of model e ($T_{\text{eff}} = 30000$ K).

must lie further in, and, correspondingly, the shock radiation must be harder (maximum at smaller wavelengths) than attainable with a v_t/v_{∞} value of 0.14, so as to have a comparatively larger influence on N V and O VI via Auger-ionization than on Si III via photoionization.

This reasoning is confirmed by model e (Fig. 31), in which we have reduced m to 30 and increased v_t/v_{∞} to 0.25 (corresponding to a maximum shock temperature of 2.0×10^6 K). The shock parameters of this model yield the best overall agreement of the most important UV spectral lines. Note that for this model we have in addition reduced the phosphorus abundance to 0.05 times solar, to obtain a fit of the P V line. As it concerns only a single element and since evidence for an underabundance of phosphorus has already been encountered from an analysis of another hot star, namely the O4f-star ζ Puppis (cf. Pauldrach et al. 1994; and Section 3.5, this paper), it is most likely that the discrepancy between the observed and calculated P V resonance line is caused by the proposed abundance effect.

**Fig. 33.** Model f. Like model e, but with a T_{eff} of 29000 K. Note the better fit of Si III and O IV.

We further note that the imbalance of S IV and S V is most likely due to a combination of abundances and imperfect atomic data, as our S IV atomic model has not yet reached the quality of those of other ionization stages and is still in a stage of rather incomplete description (cf. Table 1). Note that we have also reduced the oxygen abundance, thereby improving the fit of both O IV and O VI.

Having thus constrained the strength and distribution of the shocks, we still need to check to what extent the effective temperature and the mass loss rate can be constrained further through our analysis of the UV spectrum. For this purpose, we have computed a model with T_{eff} of 29000 K but otherwise same parameters (model f), whose spectrum is shown in Figure 33. Comparing this to the spectrum of model e (30000 K) (Fig. 32) we note a marginally better fit of the spectral region from 1450 to 1650 Å, and a slight improvement in Si IV and O IV. More significant is the extreme sensitivity of the Si III and the C III line to this small change in temperature, which

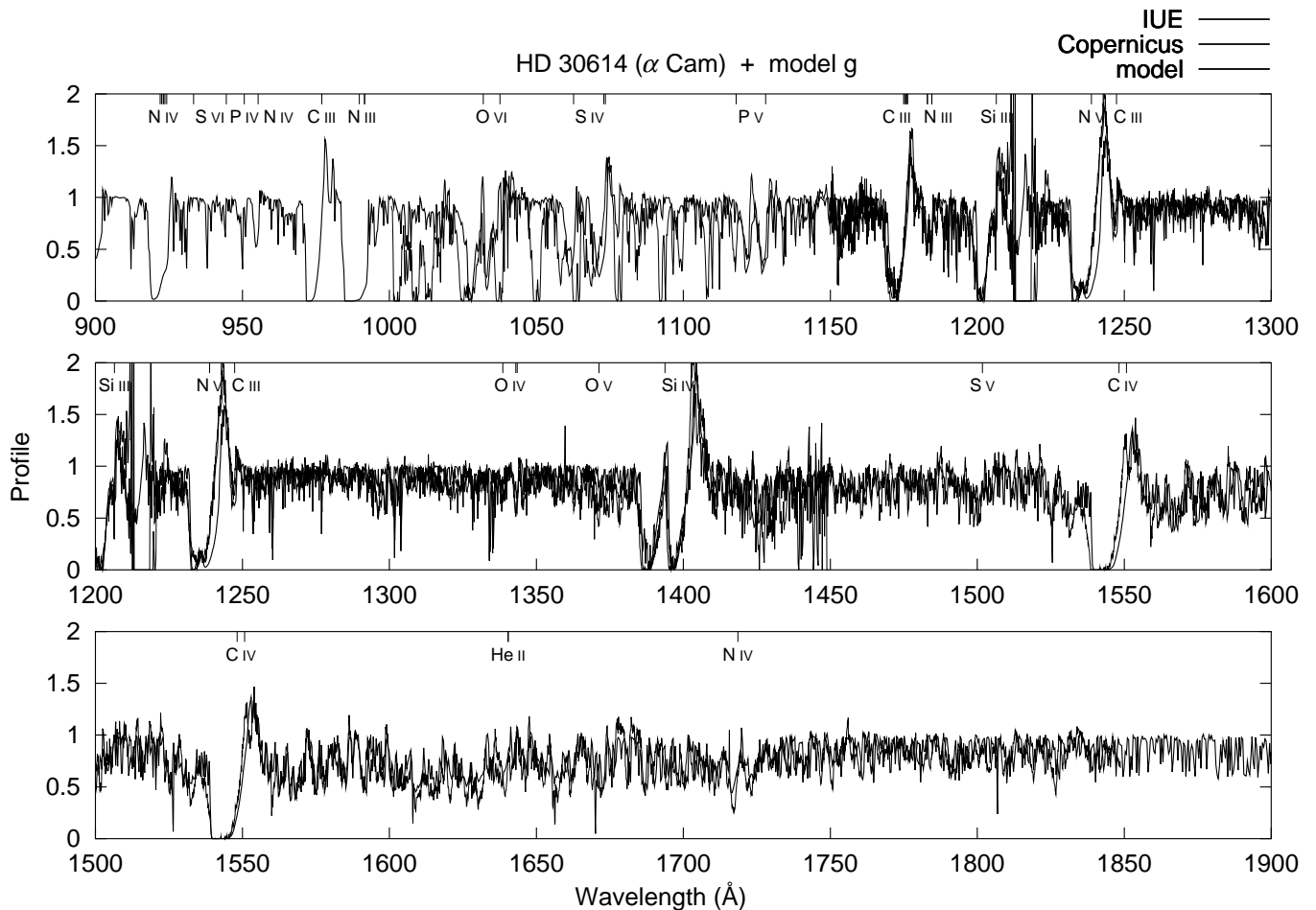


Fig. 34. Model g. Like model f, but with adapted abundances (see Table 9). This is our best fit.

reveals that these lines can be utilized as temperature indicators in this spectral range. We concede that the fit of N V is still somewhat imperfect, but point out that the shock model used is not in a final stage (see above); we expect this to improve with our new method. In a next step we have reduced the carbon abundance further (to 0.05 solar) and nitrogen to solar abundance, as this improved not only the N V/C III fit, but also the N III line at 1183,1185 Å (model g, Fig. 34). Note also that the saturated C IV resonance line is not affected by this change of the carbon abundance.

If one assumes the conservation of CNO abundances and believes that the abundances produced in the innermost part of the star appear in the same ratio at the surface of the star, then the results obtained above for the CNO abundances indicate that the ZAMS abundances of the light elements in α Cam deviate from the solar values. (Latest evolutionary calculations by Meynet and Maeder (2000) incorporating the effects of rotational mixing show that processed material is more efficiently transported to the surface than previously thought.) Our analysis shows a nitrogen overabundance relative to carbon and oxygen; whether this will have implications concerning the metal dependence of the formation of massive stars is not clear at this time.

Lowering the effective temperature further to 28 000 K worsens the fit, as the iron and nickel lines around 1500 Å become too strong (Fig. 35). As the strength of these lines depends also on the mass loss rate, it is conceivable that an adaptation of this parameter can again improve the fit. However, \dot{M} is strongly constrained by the strength of the He II line, as demonstrated in figures 36 ($\dot{M} = 2.5$) and 37 ($\dot{M} = 10$). We have confirmed in test calculations that the iron abundance must be solar ($Z = 1.0$) to reproduce the observed spectrum and to account for the radiative acceleration needed to produce the observed mass loss rate (cf. Pauldrach 1987), a finding compatible with our earlier statement concerning the relative abundances of iron to the light CNO elements.

Finally, we wish to illustrate the influence of the shocks on the ionizing flux of α Cam. In Figure 38 we compare the ionizing flux of our S-30 supergiant grid model, where shocks have been neglected, to that of our model e for α Cam. (We have used model e for this comparison, and not our final model g, since model e and the grid star S-30 both have the same effective temperature of 30 000 K. The other models (a–j) of course have similar X-ray and EUV fluxes to that of model e.) Due to the lower optical depth redward of the He II edge, the shock radiation enhances the flux as far as redward as 400 Å; this might

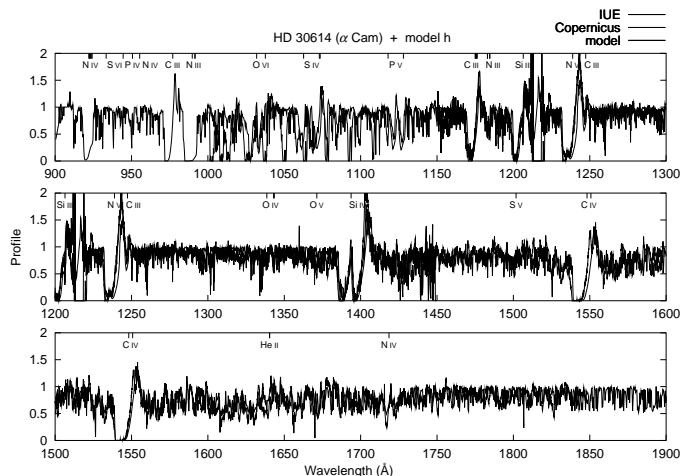


Fig. 35. Model h. Same as model g, but with $T_{\text{eff}} = 28000$ K.

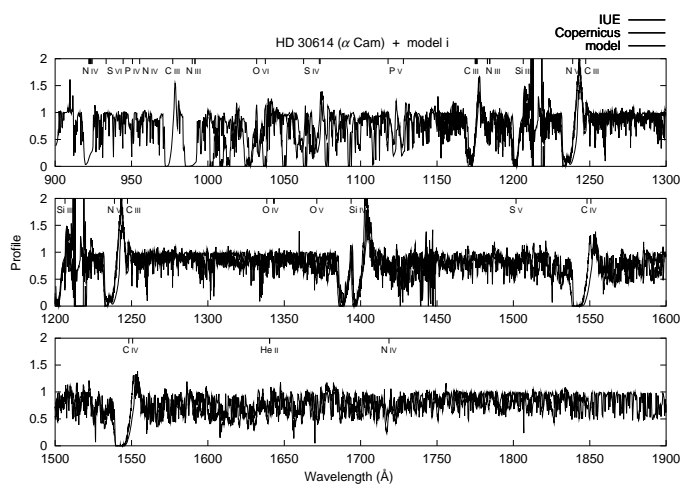


Fig. 36. Model i. As model h, but with a lower mass loss rate ($\dot{M} = 2.5 \times 10^{-6} M_{\odot}/\text{yr}$ compared to $\dot{M} = 5 \times 10^{-6} M_{\odot}/\text{yr}$ for model h).

have important implications concerning the solution of the Ne III problem (cf. Sellmaier et al. 1996), pending further investigation. Note: the Zanstra integral for He II is increased from $\log Q_{\text{He}^+} = 6.39$ for the S-30 model to 15.07 for model e!

(The influence of the shocks on the EUV spectrum is larger in α Cam than in ζ Puppis, due to the lower effective temperature and thus overall lower EUV fluxes – this is in agreement with MacFarlane et al. (1994), who show how the importance of X-rays decreased from B type stars and late O types to earlier types. The influence of the shocks on the whole spectral regime from EUV to radio has been shown by Pauldrach et al. (1994a, their Fig. 11) and especially for EUV and UV by Sellmaier et al. (1993); the expected influence on the ionizing fluxes has also been discussed by Schaerer and de Koter (1997).)

5. Conclusions

After a long period of work in the areas of non-LTE radiative transfer, hydrodynamics, and atomic physics we have

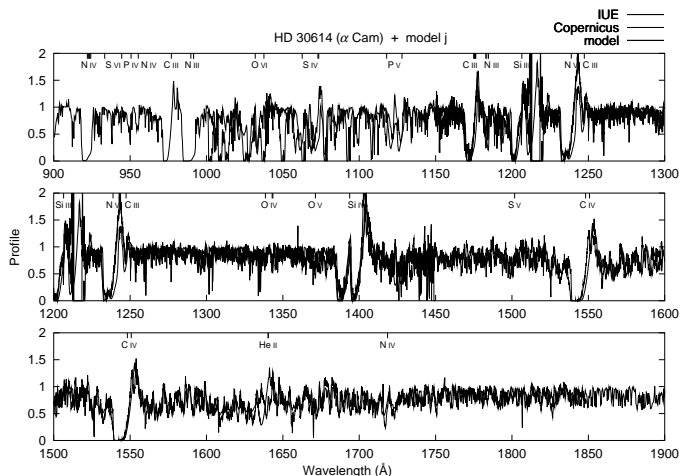


Fig. 37. Model j. As before, but with a higher mass loss rate ($\dot{M} = 10 \times 10^{-6} M_{\odot}/\text{yr}$). Note the change in the strength of the He II line.

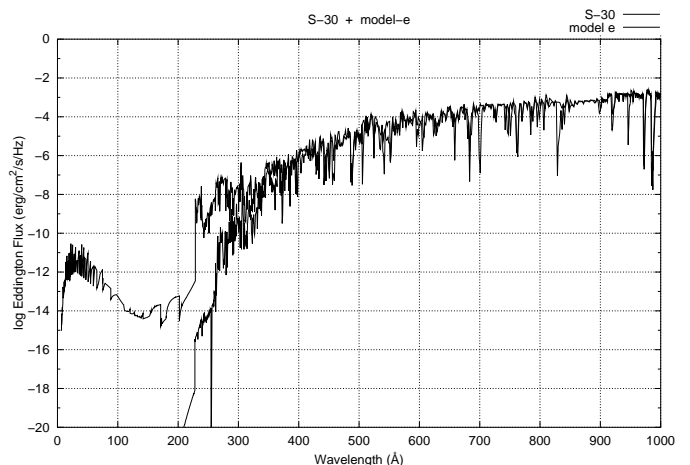


Fig. 38. Comparison of the ionizing flux of our S-30 grid star, where shocks have been neglected, to that of model e, showing the non-negligible influence of shocks on the ionizing fluxes.

now developed a fast numerical model code for expanding atmospheres which incorporates for the first time the required physics without restrictive approximations – rate equations for individual levels of all ions using detailed up-to-date atomic models, the equations of stationary radiation hydrodynamics, the energy equation, the radiative transfer equation including the effects of overlap of numerous spectral lines of different ions, and a realistic description of shock emission from instabilities in the stellar wind flow – thus making a quantitative analysis of observed high-resolution UV spectra via comparison with synthetic spectra reasonable. One of the most complicating effects in this complex physical system is the overlap of thousands of spectral lines of different ions. Especially concerning this latter point we have made significant progress with regard to our model code; the decisive factor has been to relax some rather severe approximations concerning the correct treatment of Doppler-shifted line radiation transport and the corresponding coupling with the radiative rates in the

rate equations. We have demonstrated that these modifications to the models concerning the energy distributions, ionizing continua, and line spectra lead to much better agreement with the observed UV spectra. This has important repercussions for the quantitative analysis of hot star spectra.

With this new method in hand we have already presented a new basic model grid of stars of solar metallicity that can be used as input for the analysis of spectra of emission line nebulae. The qualitative diagnostic investigation performed on basis of the model grid revealed that for the most massive stars of our sample (HD 93129 A and HD 93250) the oxygen abundance is considerably reduced compared to the solar value. In fact, it is conceivable that these stars are extremely massive precisely because the cooling behavior of the protostellar clouds from which they formed is correlated with a lower oxygen abundance. This would mean, however, that a lower oxygen abundance should be observed in all massive stars younger than O5. This conclusion is in addition supported by the fact that no very strong O V lines are observed for this kind of objects.

From the first detailed analysis of the O9.5 supergiant α Cam we conclude that our spectrum synthesis technique does, in principle, allow the determination of effective temperature and abundances – in fact, a determination of the effective temperature to within ± 1000 K and of the abundances to within a factor of 2 seems not unreasonable. Carbon and phosphorus show clear signs of an underabundance on the order of one tenth its solar value, as does oxygen with about 0.3 solar, whereas the abundance of iron must be roughly solar to reproduce the spectrum of the numerous Fe IV and Fe V lines. To produce the ionization balance observed in the lighter elements C, N, O, and Si, the influence of shock radiation must start at larger radii where for shorter wavelengths the largest shock temperatures dominate. Thus, the way the X-ray spectral region selectively affects the ionization balance of different elements, observable through the lines in the EUV spectrum, provides constraints on the lower shock temperatures; we have determined maximum shock temperatures on the order of 2.0×10^6 K. Especially the Si III and C III lines have been found to be invaluable diagnostic instruments for this purpose. Our detailed analysis of the UV spectrum and the shocks needed to reproduce the observed lines has led to a significant difference in the ionizing flux compared to models without shocks. Thus we conclude that this type of analysis is indispensable and must be regarded as the ultimate test for the accuracy of ionizing fluxes from models.

Our research plan for the future has three major objectives. First, we will have to implement further improvements to the model atmosphere code, especially concerning the planned analysis of optical lines. For this purpose Stark broadening has to be included for the affected spectral lines (e. g., H and He I lines) and concerning the rate equations instead of using the Sobolev-plus-continuum method some of these lines should be treated

in the comoving frame, if they are used for diagnostic purposes (cf. Sellmaier et al. 1993, who found that compared to the comoving frame treatment the Sobolev-plus-continuum approximation leads to a non-negligible change of the strength of some H and He lines). In connection with this some minor approximations will also have to be checked in detail.

Second, we plan to apply the model atmosphere code to a comprehensive sample of stars of different metallicities for modelling ionizing fluxes and line spectra, the qualitative review of the model grid presented in this paper being just a first step for a detailed quantitative analysis of ionizing fluxes and quantitative verification of the accuracy and reliability of the models. Furthermore, spectral analysis in the UV and the optical range of individual stellar objects in Local Group galaxies and in galaxies as distant as the Virgo Cluster will be performed.

Third, we plan on using the technique of population synthesis to calculate integrated spectra for a large range of stellar metallicities from synthetic UV spectra of our new models, for the determination of stellar abundances and the physical properties of the most UV-luminous stars in star-forming galaxies even at high redshifts. With our new diagnostic tool of detailed models for expanding atmospheres, and the observations of the HST space observatory and the ESO VLT ground-based telescope which are already available, the concept of using luminous hot stars for quantitative UV spectral analyses for determining the properties of young populations in galaxies is not only reasonable, but first tentative steps in this direction have already been taken (see, for instance, Mehlert et al. (2000, 2001), whose first diagnostic investigations have shown that, considering proper reddening, the spectra of galaxies they had observed at high redshifts ($z \sim 3$) can in principle be fitted with synthetic spectra from our hot star models).

Acknowledgements. We wish to thank our colleagues Dr. J. Puls, Dr. R.-P. Kudritzki and Dr. K. Butler for helpful discussions and Dr. S. Becker for help in improving the atomic data. It is a special pleasure to thank Dr. J. Puls additionally for providing us with a basic solver routine for the formal integral. We also thank the anonymous referee for convincing us of the necessity of making the complexities of our method understandable for everyone. This research was supported by the Deutsche Forschungsgemeinschaft in the ‘‘Gerhard Hess Programm’’ under grant Pa 477/2-3, by the DLR under grant 50 QV 9704 1, and by the German-Israeli Foundation under grant I-551-186.07/97.

Appendix A: A new concept for a fast solution of the Rybicki-method

Here we present for the solution of the Rybicki-scheme a concept which is compared to the standard procedure 10 times faster on a vector processor and 3 to 5 times faster on a scalar processor (see Section 3.3).

We start from the final system for the solution of the mean intensity – the vector \mathbf{J} describes its depth variation (the number of depth points is N):

$$\mathbf{J} = W^{-1}\mathbf{Q} \quad (\text{A.1})$$

with (N' is the number of p -rays)

$$W = \tilde{W} - \mathbf{1} = -\mathbf{1} - \sum_{j=1}^{N'} T_j^{-1} U_j, \quad \mathbf{Q} = - \sum_{j=1}^{N'} T_j^{-1} \mathbf{K}_j \quad (\text{A.2})$$

where

$$T_j = T'_j w_j^{-1}, \quad w_j = \begin{pmatrix} w_{1,j} & & \\ & \ddots & \\ & & w_{N_j,j} \end{pmatrix}, \quad (\text{A.3})$$

and N_j is the number of radius points for the j th p -ray (cf. Fig. 6). w_j is the diagonal matrix of the integration weights, and T'_j is a tri-diagonal matrix defined by the coefficients of the difference equation of transfer

$$a_{i,j} u_{i-1,j} + b_{i,j} u_{i,j} + c_{i,j} u_{i+1,j} - \beta_i J_i = (1 - \beta_i) S_i \quad (\text{A.4})$$

where $a_{i,j}$, $b_{i,j}$, and $c_{i,j}$ are the coefficients as in Eq. 20 (Section 3.3.1) for the j th p -ray,

$$T'_j = \begin{pmatrix} b_{1,j} & c_{1,j} & & \\ \cdot & \cdot & \cdot & \\ & a_{N_j,j} & b_{N_j,j} & \end{pmatrix}. \quad (\text{A.5})$$

The variables $u_{i,j}$ are the symmetric averages of the intensities, the coefficients β_i are the ratios of Thomson-opacities to total opacities, and the diagonal matrix U_j and the vector \mathbf{K}_j are defined as

$$U_j = \begin{pmatrix} -\beta_1 & & \\ & \ddots & \\ & & -\beta_{N_j} \end{pmatrix} \quad \mathbf{K}_j = \begin{pmatrix} (1 - \beta_1) S_1 \\ \vdots \\ (1 - \beta_{N_j}) S_{N_j} \end{pmatrix}. \quad (\text{A.6})$$

The usual, but time-consuming solution method is to calculate the inverse matrices T_j^{-1} – by a forward-elimination and back-substitution procedure – and from these, obtaining \mathbf{Q} and W , and, finally, \mathbf{J} .

Due to the diagonal character of the matrix U_j this is, however, not necessary, because from the solution of the first column of \tilde{W} obtained by using just the first column of U_j in Eq. A.2 the solutions of the remaining columns of \tilde{W} can be generated. Hence, the elimination procedure only has to be applied to the following two sets of equations (N'_i is the maximum number of p -rays for the i th radius point):

$$\mathbf{Q}_i = - \sum_{j=1}^{N'_i} \tilde{K}_{j,i} \mathbf{1} \quad (\text{A.7})$$

$$\tilde{W}_{i,1} = - \sum_{j=1}^{N'_i} \tilde{U}_{j,i} = - \sum_{j=1}^{N'_i} \tilde{B}_{j,i} V_{j,1} \quad (\text{A.8})$$

with

$$\tilde{\mathbf{K}}_j = T_j^{-1} \mathbf{K}_j, \quad \tilde{\mathbf{B}}_j = T_j^{-1} \mathbf{B}_j \quad (\text{A.9})$$

where

$$V_{j,1} = \begin{pmatrix} -\beta_1 \\ \vdots \\ -\beta_1 \end{pmatrix} \quad \mathbf{B}_j = \begin{pmatrix} 1 \\ 0 \\ \vdots \\ 0 \end{pmatrix}. \quad (\text{A.10})$$

Note that since the solution procedure is not recursive with respect to the index j the elimination can be performed simultaneously for all p -rays. Note further that the structure of the sums in Eqs. A.7 and A.8 are equivalent to the operations $x = A \cdot y$ where A is a triangular matrix. Thus, BLAS level-2 routines can be applied.

For the construction of the remaining columns of W we now make use of the already calculated matrix $\tilde{B}_{j,i}$ and two auxiliary matrices obtained as a byproduct during the forward-elimination procedure by solving Eq. A.8.

The first one is:

$$F'_{j,i} = F'_{j,i-1} f_{j,i}, \quad i = 1, \dots, N-1 \quad (\text{A.11})$$

with

$$F'_{j,0} = 1, \quad f_{j,i} = -a_{j,i+1} / \tilde{b}_{j,i}. \quad (\text{A.12})$$

Here $\tilde{b}_{j,i}$ is the updated value of $b_{j,i}$ obtained after the forward-elimination step by solving Eq. A.8 ($\tilde{b}_{j,i+1} = b_{j,i+1} + f_{j,i} c_{j,i}$).

The second one is:

$$F''_{j,i} = F''_{j,i+1} g_{j,i}, \quad i = N-1, \dots, 1 \quad (\text{A.13})$$

with

$$F''_{j,N} = 1, \quad F''_{N'_i,i} = 1, \quad g_{j,i} = -c_{j,i} / \tilde{b}_{j,i}. \quad (\text{A.14})$$

The final step – construction of the columns $l = 2, \dots, N$ of W (where l denotes the position of the unity value for the vector \mathbf{B}_j in Eq. A.10) – consists of two parts, where the first part replaces the forward-elimination and the second part the back-substitution procedure:

In the first part the components $i = l, \dots, N$ of the l th column of \tilde{W} are determined by

$$\tilde{W}_{i,l} = - \sum_{j=1}^{N'_i} \tilde{B}_{j,i} V'_{j,l} \quad (\text{A.15})$$

where

$$V'_{j,l} = V_{j,l} / F'_{j,l-1}. \quad (\text{A.16})$$

Again, a triangular matrix has simply to be multiplied by a vector using a BLAS level-2 routine.

In the second part the components $i = l-1, \dots, 1$ of the l th column of \tilde{W} are determined by

$$\tilde{W}_{i,l} = - \sum_{j=1}^{N'_i} F''_{j,i} V''_{j,l} \quad (\text{A.17})$$

where

$$V''_{j,l} = V'_{j,l} \tilde{B}_{j,l} / F''_{j,l}. \quad (\text{A.18})$$

Now, a rectangular matrix has simply to be multiplied by a vector again using a BLAS level-2 routine. Hence, instead of a number of operations $\sim N^3$ a number of operations only $\sim N^2$ must be performed, and as extremely fast routines are used to solve the non-recursive system, the solution of the Rybicki-scheme is now almost as fast as the solution of the moments equation.

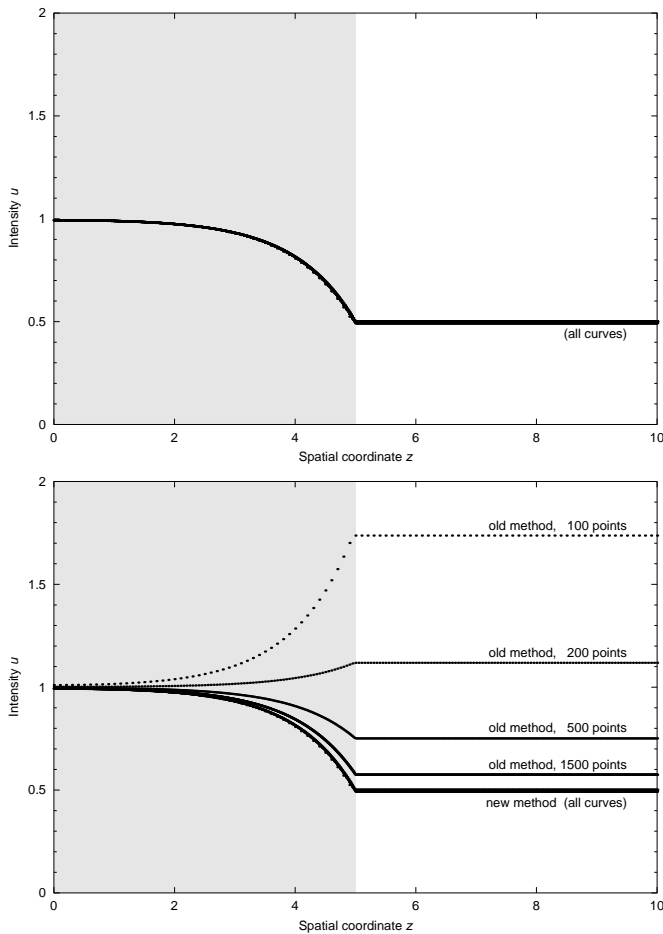


Fig. B.1. Upper panel: Mean intensity in a one-dimensional nebula; constant source function, high opacity on the left (shaded in gray), low opacity on the right. Both discretization methods give the same results. **Lower panel:** If the first grid point with low opacity is given a high source function, the old method produces artificial emission. The new method does not show this behavior.

Appendix B: A simple demonstration of the failure of the standard τ discretization of the equation of transfer

Let us assume a one-dimensional, sharply bounded cloud of material of moderate opacity,

$$\chi = \begin{cases} 1, & |z| < 5 \\ 10^{-10}, & |z| \geq 5 \end{cases} \quad (\text{B.1})$$

with a symmetric boundary condition at $z = 0$ (the middle of the cloud) and no influx from the outside (i. e., $I^- = 0$ at $z = 10$).

With a constant source function $S = 1$ everywhere, both the old and the new discretization of the transfer equation yield essentially the same radiation field (upper panel of Figure B.1), a solution which is immediately obvious: The center of the cloud ($z = 0$) is optically thick, the intensity there thus equal to the source function. Towards the edge of the cloud, more and more radiation escapes, and the intensity decreases. On the outside of the cloud, essentially no emission is produced

(nothing is absorbed, either); only the radiation emitted by the cloud contributes to the local intensity (since we have no influx from the right), therefore $u = \frac{1}{2}S$.

The results change considerably if we adopt a high source function of $S = 100$ for the *single grid point* at $z = 5$, the first grid point *outside* of the cloud. As illustrated in the lower panel of Figure B.1, the old method produces extra emission on a scale of

$$\Delta I = \frac{1}{2}S \cdot \Delta\tau \approx \frac{1}{2}100 \cdot \frac{1}{2}(1 + 10^{-10})\Delta z \quad (\text{B.2})$$

$$\approx \frac{1}{4}100\Delta z. \quad (\text{B.3})$$

For the grid with 100 points, $\Delta z = 0.1$, giving us an intensity

$$u \approx 0.5 + \frac{1}{2} \cdot \frac{1}{4}100 \cdot 0.1 = 1.75 \quad (\text{B.4})$$

outside the cloud. (0.5 is from the normal emission of the cloud as before, and the factor 1/2 in the second term is again due to the fact that $u = \frac{1}{2}(I^+ + I^-)$, with $I^- = 0$ on the outside of the cloud, so that $u = \frac{1}{2}I^+$.) The extra emission is proportionally reduced in the finer grids as Δz gets smaller.

The new method, on the other hand, is essentially indifferent to the grid spacing in this particular configuration, since the emission is only computed on the basis of the *local* opacity, which is low for the point in question. If we were to choose a point inside the cloud to have a high source function, then both methods again produce similar results, also dependent on grid spacing, since in this case the point in question *does* have a high opacity, and therefore produces substantial emission proportional to the interval length.

Concluding, it can be said that the discretization methods differ in the assumptions that are made about the emissivity (in the old method, based on average values of opacity and source function assuming linear run between the grid points; in the new method, extrapolating the local value) – information not available given just the values at the grid points, and which *must* therefore be supplied separately through the choice of discretization coefficients. It just so happens that the new method produces results which are more compatible with our detailed formal integral.

References

- Abbott D. C., Hummer D. G., 1985, ApJ 294, 286
- Anderson L., 1991, in: Stellar Atmospheres: Beyond Classical Models, NATO ASI Series C, Vol. 341, p. 29, eds. L. Crivellari, I. Hubeny, D. G. Hummer
- Aufdenberg J. P., Hauschildt P. H., Shore S. N., Baron E., 1998, ApJ 498, 837
- Cassinelli J. P., Olson G. L., 1979, ApJ 229, 304
- Chlebowski T., Harnden F. R. Jr., Sciortione S., 1989, ApJ 341, 427
- Chevalier R. A., Imamura J. N., 1982, ApJ 261, 543
- Cunto W., Mendoza C., 1992, Rev. Mex. Astron. Astrof. 23, 107
- Drew J. E., 1989, ApJS 71, 267
- Drew J. E., 1990, ApJ 357, 573
- Eissner W., Jones M., Nussbaumer H., 1974, Computer Physics Comm. 8, 270
- Feldmeier A., 1995, A&A 299, 523
- Feldmeier A., Kudritzki R.-P., Palsa R., Pauldrach A. W. A., Puls J., 1997, A&A 320, 899

- Hamann W.-R., Koesterke L., 1998, *A&A* 335, 1003
- Haser S.M., Pauldrach A.W.A., Lennon D.J., Kudritzki R.-P., Lennon M., Puls J., Voels S., 1998, *A&A* 330, 285
- Hillier D.J., Kudritzki R.-P., Pauldrach A.W.A., et al., 1993, *A&A* 276, 117
- Hillier D.J., Miller D.L., 1998, *ApJ* 496, 407
- Hummel W., Pauldrach A.W.A., Williams R., Lennon M., Kudritzki R.-P., 1997, in: 13th North American Workshop on Cataclysmic Variables, PASPC, eds. S. Howell, E. Kuulkers, C. Woodward
- Hummer D.G., Seaton M.J., 1963, *MNRAS* 125, 437
- Hummer D.G., Berrington K.A., Eissner W., Pradhan Anil K., Saraph H.E., Tully J.A., 1993, *A&A* 279, 298
- Hummer D.G., Rybicki G.B., 1985, *ApJ* 293, 258
- Kahn S.M., Leutenegger M.A., Cottam J., Rauw G., Vreux J.-M., den Boggende A.J.F., Mewe R., Güdel M., 2000, *A&A* in press
- Kubat J., Puls J., Pauldrach A.W.A., 1999, *A&A* 341, 587
- Kurucz R.L., 1979, *ApJ Suppl.* 40, 1
- Kurucz R.L., 1992, *Rev. Mex. Astron. Astrof.* 23, 45
- Labs D., 1951, *Z. Astrophys.* 29, 199
- Lucy L.B., Solomon P., 1970, *ApJ* 159, 879
- Lucy L.B., White R., 1980, *ApJ* 241, 300
- Lucy L.B., 1982, *ApJ* 255, 286
- Meynet G., Maeder A., 2000, *A&A* 361, 101
- MacFarlane J.J., Cohen D.H., Wang P., 1994, *ApJ* 437, 351
- Mehlert D., Seitz S., Saglia R.P., et al., 2000, in: Proc. of the Ringberg workshop on High Redshift Galaxies
- Mehlert D., Seitz S., Saglia R.P., et al., 2001, *A&A* in press
- Mihalas D., 1978, *Stellar Atmospheres*, 2nd ed., W.H. Freeman and Comp., San Francisco
- Nussbaumer H., Storey P.J., 1978, *A&A* 64, 139
- Owocki S.P., Castor J.I., Rybicki G.B., 1988, *ApJ* 335, 914
- Pauldrach A.W.A., 1987, *A&A* 183, 295
- Pauldrach A.W.A., Herrero A., 1988, *A&A* 199, 262
- Pauldrach A.W.A., Kudritzki R.P., Puls J., Butler K., 1990, *A&A* 228, 125
- Pauldrach A.W.A., Kudritzki R.-P., Puls J., Butler K., Hunsinger J., 1994, *A&A* 283, 525
- Pauldrach A.W.A., Feldmeier A., Puls J., Kudritzki R.-P., 1994a, *Space Science Reviews* 66, 105
- Pauldrach A.W.A., Duschinger M., Mazzali P.A., Puls J., Lennon M., Miller D.L., 1996, *A&A* 312, 525
- Pauldrach A.W.A., Lennon M., Hoffmann T.L., Sellmaier F., Kudritzki R.-P., Puls J., 1998, in: Proc. 2nd Boulder-Munich Workshop, PASPC 131, 258
- Peytremann E., 1974, *A&A* 33, 203
- Pistinner S.L., Hauschildt P.H., Eichler D., Baron E.A., 1999, *MNRAS* 302, 684
- Puls J., 1987, *A&A* 184, 227
- Puls J., Hummer D.G., 1988, *A&A* 191, 87
- Puls J., Pauldrach A.W.A., 1990, in: Proc. Boulder-Munich Workshop, PASPC 7, ed. C. Garmany, p. 203
- Puls J., Kudritzki R.-P., Herrero A., et al., 1996, *A&A* 305, 171
- Raymond J.C., Smith B.W., 1977, *ApJ Suppl.* 35, 419
- Rubin R.H., Simpson J.P., Haas M.R., Erickson E.F., 1991, *ApJ* 374, 564
- Santolaya-Rey A.E., Puls J., Herrero A., 1997, *A&A* 323, 488
- Schaerer D., de Koter A., 1997, *A&A* 322, 598
- Schaerer D., Schmutz W., 1994 *A&A* 288, 231
- Seaton M.J., Yan Yu, Mihalas D., Pradhan Anil K., 1994, *MNRAS* 266, 805
- Sellmaier F., 1996, doctoral thesis at the Universitätssternwarte München, Munich
- Sellmaier F., Yamamoto T., Pauldrach A.W.A., Rubin R.H., 1996, *A&A* 305, L37
- Sellmaier F., Puls J., Kudritzki R.-P., et al., 1993, *A&A* 273, 533
- Shull J.M., van Steenberg M.E., 1985, *ApJ* 294, 599
- Simon M., Axford W.I., 1966, *Planetary Space Science* 14, 901
- Snedden C., Johnson H.R., Krupp B.M., 1976, *ApJ* 204, 281
- Snow T.P., Morton D.C., 1976, *ApJ Suppl.* 32, 429
- Steidel C.C., Gialalisco M., Pettini M., Dickinson M., Adelberger K.L., 1996, *ApJ* 462, L17
- Stock C., 1998, Diplomarbeit at the Universitätssternwarte München, Munich
- Taresch G., Kudritzki R.-P., Hurwitz M., et al., 1997, *A&A* 321, 531

Appendix

E

Radiation-driven winds of hot luminous stars

XV. Constraints on the mass–luminosity relation of central stars of planetary nebulae

A. W. A. Pauldrach¹, T. L. Hoffmann¹, and R. H. Méndez²

¹ Institut für Astronomie und Astrophysik der Universität München, Scheinerstraße 1, 81679 München, Germany

² Institute for Astronomy, University of Hawaii, 2680 Woodlawn Drive, Honolulu, HI 96822, U.S.A.

Received date / Accepted date

Abstract. We present a new model atmosphere analysis of nine central stars of planetary nebulae. This study is based on a new generation of realistic stellar model atmospheres for hot stars; state-of-the-art, hydrodynamically consistent, spherically symmetric model atmospheres that have been shown to correctly reproduce the observed UV spectra of massive Population I O-type stars. The information provided by the wind features (terminal velocity, mass loss rate) permits to derive the physical size of each central star, from which we can derive the stellar luminosity, mass, and distance, without having to assume a relation between stellar mass and luminosity taken from the theory of stellar structure and AGB and post-AGB evolution. The results of our analysis are quite surprising: we find severe departures from the generally accepted relation between post-AGB central star mass and luminosity.

Key words. stars: central stars of planetary nebulae – atmospheres – winds, outflows – evolution – fundamental parameters – early-type

1. Introduction

In recent years there has been substantial progress in the modelling of expanding atmospheres of hot stars. It is now possible to produce synthetic UV spectra of O stars that resemble the real, observed ones nearly perfectly. The state-of-the-art wind models deal with radiatively driven, homogeneous, stationary, extended, outflowing, spherically symmetric atmospheres. A complete model atmosphere calculation involves solving the hydrodynamics and the NLTE problem (rate equations for all important elements, radiative transfer, and energy equation). The solution of the total interdependent system of equations has thereby to be based on a non-restrictive treatment. This permits the calculation of the predicted or synthetic spectrum, which is then compared to the observed UV spectrum (cf. Pauldrach et al. 2001). The process is repeated using different stellar parameters until a satisfactory fit is obtained. In this kind of work it is not necessary to adopt an arbitrary velocity law for the wind; the solution is hydrodynamically consistent and gives us the velocity law as well as the mass-loss rate. (The details and technical background of the latter procedure are described in Pauldrach 1987 and Pauldrach et al. 1994. Moreover, we note that recent modifications of our method are described in detail in Pauldrach and Hoffmann 2004, and

that a description of the complete method and first results with regard to massive O-stars have already been published in Pauldrach 2003.)

A very important consequence of these recent developments is that the fits to the UV spectral features provide information about all the basic stellar parameters: effective temperature (T_{eff}), radius (R) – or equivalently, luminosity (L) –, mass of the star (M), terminal wind velocity (v_{∞}), and mass loss rate (\dot{M}). Therefore we have a purely spectroscopic method to obtain separately L and M .

Using this new generation of realistic stellar model atmospheres, Pauldrach et al. (2001), Pauldrach (2003), and Pauldrach and Hoffmann (2004) present analyses of the massive O supergiants HD 30614 (α Cam) and HD 66811 (ζ Pup) which provide excellent matches to the observable UV spectra, thus determining the basic stellar parameter sets of these objects. Further examples of this kind of work are given by Hoffmann and Pauldrach (2001), who confirm in their analysis of a subsample of galactic massive O stars the parameters derived by Puls et al. (1996) from an optical investigation.

Since this method produces reasonable results when applied to massive Population I stars, we now want to apply it to another kind of hot stars: the central stars of planetary nebulae (CSPNs in what follows). This permits, for the first time, to test the predictions from post-AGB evolutionary calculations. (The idea is described together with a first application by

Send offprint requests to: A. W. A. Pauldrach,
<http://www.usm.uni-muenchen.de/people/adi/adi.html>

Pauldrach et al. 1988; preliminary results of the present investigation have been published by Pauldrach et al. 2001a.) The earlier work on CSPNs, based on plane-parallel non-LTE model atmospheres (e.g., Méndez et al. 1988a, 1988b) could not provide a completely independent test, in the following sense: since the plane-parallel model fits to H and He photospheric absorption lines can only produce information about surface temperature, He abundance and surface gravity ($\log g$), we cannot derive stellar masses or luminosities, but only L/M ratios. This is exactly the same problem we face when dealing with low-gravity early-type “supergiant” stars at high Galactic latitudes: are they luminous and massive, or are they evolving away from the AGB? We need some independent evidence to settle the issue – for example, the distance to the star. Unfortunately, we lack reliable distances to almost all CSPNs.

What could be done was to plot the positions of CSPNs in the $\log g$ – $\log T_{\text{eff}}$ diagram, and compare them with plots of post-AGB tracks, translated from the $\log L$ – $\log T_{\text{eff}}$ diagram. After doing this translation it is possible to read the stellar mass in the $\log g$ – $\log T_{\text{eff}}$ diagram. From this, we can derive L and, if we know the visual dereddened apparent magnitude, a so-called “spectroscopic distance”. All this work, however, is based on *assuming* that the evolutionary models give us the correct relation between stellar mass and luminosity. It is not a real test of the evolutionary models, but only a consistency check.

The new models allow us to overcome this limitation and produce for the first time information on L and M which is completely independent from the theory of stellar structure and evolution. In this paper we present the initial outcome of the project. For our investigation we have chosen the same sample of stars as Kudritzki et al. (1997), but here we will consider only the UV spectra of the stars; a discussion of the optical Balmer lines is beyond the scope of this paper. Our future plans include using the optical lines for diagnostic purposes as well, but this requires a particular numerical treatment for some of these lines (cf. Sellmaier et al. 1993), and in this context we note that the optical analysis of CSPNs is also non-trivial, with some still unsolved problems. For instance the optical analyses fit $H\alpha$ in order to obtain the mass-loss rate, and they fit $H\gamma$ in order to obtain $\log g$. However, $H\beta$, which is formed at an atmospheric depth in between these two lines, can in most cases not be reproduced with the same accuracy. (This has been published, for example, by Kudritzki et al. (1997), their figure 2.)

In Section 2 we describe the available spectrograms. In Section 3 we present the necessary information about the new wind models and we outline the fitting procedure. Section 4 introduces the relation between wind momentum loss rate and stellar luminosity, predicted by the theory of radiatively driven winds, and briefly describes earlier efforts to verify if the CSPNs follow this relation. Then in Sections 5 and 6 we present the UV spectral fits using the new wind models, explaining what discrepancies there are with respect to the earlier modelling and producing a table with the stellar parameters determined. Section 7 gives the interpretation of the CSPN winds and a discussion of the results concerning stellar luminosities and masses. In Section 8 we estimate the spectroscopic distances and compare them with other distance determinations,

with inconclusive results. Section 9 deals with other estimates of pre-white dwarf masses. In Section 10 we summarize the conclusions.

2. The UV spectrograms

The sample of CSPNs we have analyzed is defined by the availability of adequate high-resolution UV spectra (except IC 4637, for which only a low-resolution spectrum is available), covering the spectral region between 1000 and 2000 Å.

With the exception of that of He 2-108, all UV spectra of our sample were obtained from the INES Archive Data Server on the Web at <http://ines.laef.esa.es/>, providing access to IUE Final Archive data. Apart from rectification “by eye” (aided by our experience with UV spectra from massive O stars), no further processing was done on the spectra.

The spectrum of He 2-108 is an HST/FOS spectrum (Proposal ID 5339, PI RHM) rectified by Haser (1995). Here, interstellar Lyman- α absorption has been taken into account in the rectification process, leading to an empty band around 1216 Å with noisy edges.

3. The modelling procedure

The UV spectrum between 1000 and 2000 Å carries a lot of information: P-Cygni-type profiles of resonance lines of several ions of C, N, O, Si, S, P, as well as hundreds of strongly wind-contaminated lines of Fe IV, Fe V, Fe VI, Cr V, Ni IV, Ar V, Ar VI. But the information about the stellar parameters can be extracted only after careful analysis. A very important recent improvement of our method concerns the development of a substantially consistent treatment of the blocking and blanketing influence of all metal lines in the entire sub- and supersonically expanding atmosphere. All the results we will present are based on this new generation of models.

The analysis method is based on modelling a homogeneous, stationary, extended, outflowing, spherically symmetric radiation-driven atmosphere. A detailed description is given by Pauldrach et al. (2001), Pauldrach (2003), and Pauldrach and Hoffmann (2004).

The procedure is as follows. A preliminary inspection of the visual and/or UV spectrum of the star to be analyzed gives an estimate of T_{eff} . (The effective temperature is determined from the ionization balance in the wind, reflected in the strengths of the lines of successive ionization stages of several elements. In particular we have found the Fe IV/Fe V ionization balance well suited for this purpose. The wavelength range from 1400 to 1550 Å is dominated by lines from Fe V, whereas Fe IV lines dominate in the range from 1550 to 1650 Å, and a comparison of the relative strengths of the lines in these wavelength ranges in the observed and the synthetic UV spectrum usually allows the effective temperature to be constrained to within about ± 1000 K. (See also Pauldrach et al. 2001, where this is demonstrated using observed and synthetic UV spectra of the O supergiant α Cam.)) The terminal wind velocity v_{∞} can be measured directly from the UV spectrum. Now, initial values for the stellar radius R (defined at a Rosseland optical depth of 2/3) and for the stellar mass M are assumed.

With the current values of R , T_{eff} , M , and assuming a set of abundances, we can solve the model atmosphere and calculate the velocity field, the mass loss rate \dot{M} , and the synthetic spectrum. If the calculated terminal wind velocity v_{∞} of the model differs from the observed one, we modify M until agreement is reached (since v_{∞} scales with $(M/R)^{1/2}$ according to the theory of radiation-driven winds). Now the predicted spectrum is compared to the observed one. If the fit is not satisfactory, we need to modify \dot{M} via a change of R (since $\log \dot{M} \sim \log L$, according to radiation-driven wind theory). The change in R forces us to change the mass, too, in order to keep v_{∞} consistent with the observed value. The new model is calculated and the process is repeated until we obtain a good fit to all features in the observed spectrum. (Additionally, T_{eff} might need to be corrected slightly during this iteration, if the initial guess was not satisfactory. This is also done iteratively, by computing models for a series of temperatures and choosing the one that fits best.)

With this procedure our current models produce satisfactory results for massive Population I stars. What happens if we apply the same procedure to CSPNs?

4. The wind properties of hot stars

As a first point of our investigation we examine the dynamical parameters v_{∞} and \dot{M} of radiation-driven CSPN winds.

The significance of these parameters is obvious, since it is the consistent hydrodynamics which provides the link between the stellar parameters (T_{eff} , M , R) and the appearance of the UV spectra, because the latter are determined by the interplay of the NLTE model and the hydrodynamics. The link is the line force which controls the hydrodynamics, and which is controlled by the occupation numbers, and the radiative transfer of the NLTE model. The hydrodynamics in turn affects the NLTE model and thus the spectra via the density and velocity structure.

4.1. The relation between wind-momentum loss rate and luminosity

A tool for illustrating the behavior of the dynamical parameters is offered by the so called *wind-momentum–luminosity relation*.

The significance of this relation is based on the fact that, due to the driving mechanism of hot stars, the mechanical momentum of the wind flow ($v_{\infty}\dot{M}$) is mostly a function of photon momentum (L/c) and is therefore related to the luminosity. Thus, the radiatively driven wind theory predicts, for fixed abundances, a simple relation between the quantity $\dot{M}v_{\infty}$, which has the dimensions of a momentum loss rate, and the stellar luminosity:

$$\dot{M}v_{\infty} \sim R^{-1/2}L^{1/\alpha}$$

where α , related to the power law exponent of the line strength distribution function, is $\simeq 2/3$ (slightly dependent on temperature and metallicity; see, for example, Puls et al. 1996). As the expression $v_{\infty}\dot{M}R^{1/2}$ is an almost directly observable quantity (see below), it is practical to plot the log of $\dot{M}v_{\infty}R^{1/2}$ as a function of $\log L$. In this kind of plot the theory predicts, in first approximation, a linear relation, which is indeed followed by all kinds of massive hot stars, as shown in Figure 1.

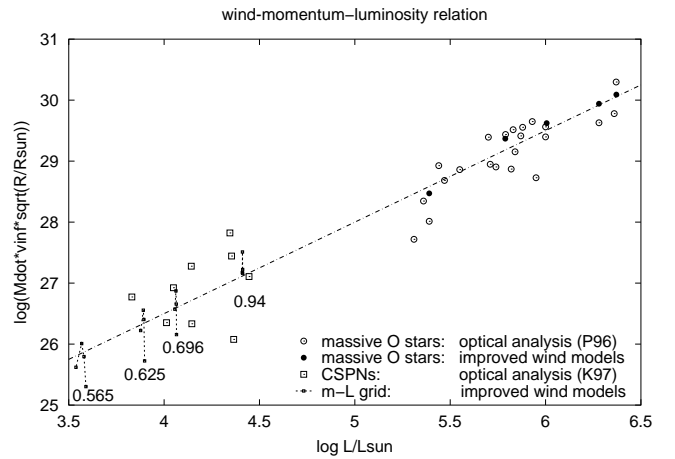


Fig. 1. The wind-momentum–luminosity relation for massive O stars and CSPNs. P96 designates the analysis based on $H\alpha$ profiles by Puls et al. 1996, K97 that of CSPNs by Kudritzki et al. 1997. Also plotted are the calculated wind momenta for a sample of massive O stars and for a grid of stars following post-AGB evolutionary tracks (masses given in M_{\odot}).

An initial attempt to verify if CSPNs follow the wind-momentum–luminosity relation was partly successful (see Figure 3 in Kudritzki et al. 1997 and also our Figure 1). In that paper, terminal wind velocities v_{∞} were taken from observed UV spectra and Q -values (a quantity relating mass loss rate and stellar radius, $Q \sim \dot{M}(Rv_{\infty})^{-3/2}$) were derived from observed $H\alpha$ profiles¹. Stellar masses were derived from T_{eff} and $\log g$, using post-AGB tracks plotted in the $\log g$ – $\log T_{\text{eff}}$ diagram. The stellar radii (and thus, mass loss rates) and luminosities were then obtained from the masses and the post-AGB mass–luminosity relation. The CSPNs were found to be at the expected position along the wind-momentum–luminosity relation, indicating a qualitatively successful prediction by the theory of radiatively driven winds. However, the situation was not satisfactory because there appeared to be a large dispersion in wind strengths at a given luminosity (strong-winded and weak-winded CSPNs) and some of the CSPN masses and luminosities were very high ($M > 0.8 M_{\odot}$), in contradiction with theoretical post-AGB evolutionary speeds.

Thus, at that point we had a qualitatively positive result, namely that in principle the CSPN winds appear to obey the same physics as the massive O star winds; but we also had some unsolved problems.

This situation has been recently discussed by Tinkler and Lamers (2002), who try to improve the central star parameters by imposing consistency between the evolutionary age of the central star and the dynamical age of its PN. As result of scaling the distances and stellar parameters according to their method they obtain a scatter diagram with no clear dependence of wind momentum on luminosity. So in this way we find a conflict between the predictions of post-AGB evolution theory

¹ We refer to this as “optical analysis”, since although v_{∞} was taken from UV spectra, this is a quantity that can be derived easily and does not require much analysis. The real analysis determining Q and $\log g$ using model atmospheres was performed using optical spectra.

and the theory of radiatively driven stellar winds! Are the post-AGB evolutionary tracks not complete? Or is the behavior of the photon-momentum transfer different in the atmospheres of O-type CSPNs and massive O-stars?

We now want to rediscuss this situation using our improved model atmospheres.

As a preparatory step we have used our models to calculate the terminal velocities and mass loss rates for a grid of stars following the current theoretical post-AGB evolutionary tracks with surface temperatures from 30000 to 90000 K (see, for instance, Blöcker 1995); the resulting wind momenta are also plotted in Figure 1 (labelled “m–L grid”). The numerical models do nicely follow, as expected, the theoretical wind momentum–luminosity relation, showing less spread than the “observed” values derived by Kudritzki et al. (1997). The positions of the Kudritzki et al. values in the diagram, compared to those of our models, again indicate rather large masses between 0.6 and 0.95 M_{\odot} , with a clear absence of CSPNs with masses below 0.6 M_{\odot} .

As explained before, to find so many very massive CSPNs is rather unexpected from the standpoint of current evolutionary theory, in view of their very high predicted evolutionary speeds.

4.2. The relations of the individual dynamical parameters v_{∞} and \dot{M}

To try to better understand the discrepancy found from the investigation of the wind momenta, we must compare the relations of the individual dynamical quantities involved (v_{∞} and \dot{M}), since these relations are not just a function of the stellar luminosity, as is the case for the “wind-momentum–luminosity relation”, they are also sensitively dependent on the stellar mass.

By doing so we find indeed that something must be seriously wrong. Figure 2 (upper panel) shows our predicted terminal velocities and the observed values. Figure 2 (lower panel) shows our predicted mass loss rates and those derived by Kudritzki et al. (1997) for their sample. Here a fundamental discrepancy immediately becomes obvious: whereas the positions of the observations in the diagram showing the terminal velocities cluster at rather small CSPN masses (between 0.5 and 0.6 M_{\odot}), their mass loss rates point to a majority of masses above 0.7 M_{\odot} .

A detailed look at the positions of individual CSPNs in the plots reveals even more alarming discrepancies. Take, for example, He 2-131. Its terminal velocity would indicate a mass of about 0.6 M_{\odot} (circle 1A in Figure 2 upper panel). But this mass is completely irreconcilable with its mass loss rate: it is found not at the position labelled 1A in Figure 2 (lower panel), but at 1B, with \dot{M} a factor of hundred higher, suggesting a mass of above 0.94 M_{\odot} ! The reverse is true for NGC 2392. Its terminal velocity points to a mass of about 0.9 M_{\odot} (circle 2A in Figure 2 upper panel), but its observed mass loss rate is much too small for this mass (circle 2B in Figure 2 lower panel), indicating a mass of approximately 0.6 M_{\odot} .

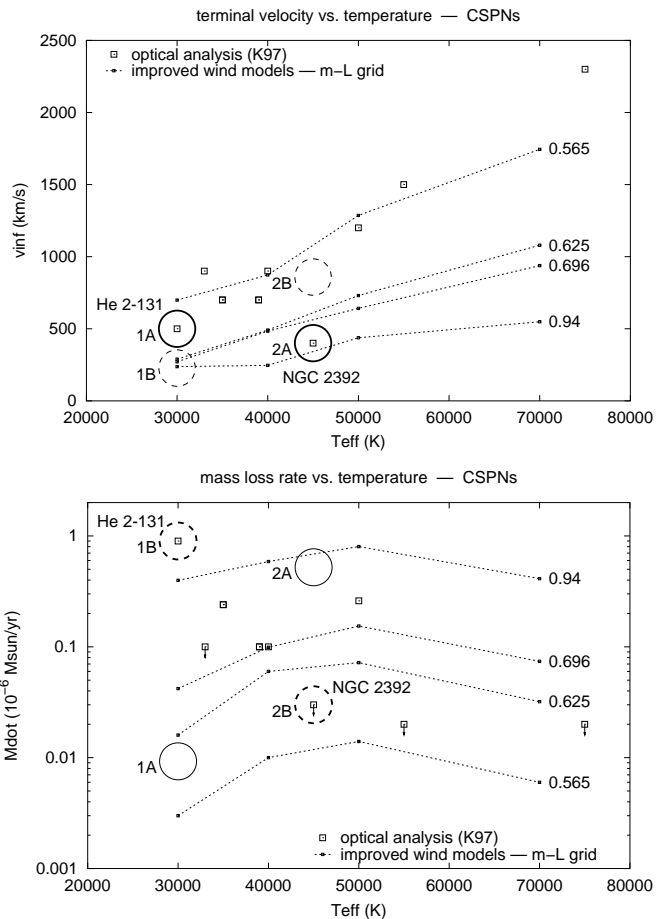


Fig. 2. Terminal velocities (upper panel) and mass-loss rates (lower panel) calculated for a grid of stars following post-AGB evolutionary tracks (dashed lines, masses in M_{\odot} labelled on the right) compared to observed values derived by Kudritzki et al. (1997) (squares). Note that the observed terminal velocities and mass-loss rates indicate different masses for the same objects (circles) – for a discussion see text.

If instead of the terminal velocities we take the mass loss rate determinations of Kudritzki et al. (1997) as basis for the discussion, then our calculations place these two stars at the positions labelled 1B and 2B in Figure 2 (upper panel), with terminal velocities differing by factors of 2 to 3. But this is clearly ruled out by the observations; v_{∞} is a directly measurable quantity!

Therefore, no matter how we look at these plots, we conclude that the analysis of Kudritzki et al. (1997) revealed mass loss rates which cannot be reconciled with the currently accepted post-AGB evolutionary tracks which the radiatively driven wind models shown have been based on. This is indeed a dilemma, because on the one hand the error in the determination of the Q -values in the analysis of Kudritzki et al. is much too small to account for the large differences in the mass loss rates necessary to explain our findings above; and on the other hand, the differences between the mass-loss rates given by Kudritzki et al. and those following from consistent wind dynamics (with the same stellar parameters) are more than an order of magnitude larger than the systematic uncertainty of

our method. *We are thus dealing with a real physical problem and not merely a minor detail of the modelling procedure.*

So far we have used from the UV spectra of the CSPNs only one bit of information: the observed terminal velocity v_∞ . Now we will try to clarify the situation by fitting the full UV spectra with the new atmospheric models. In this way the wind theory will provide us with stellar parameters derived independently of the post-AGB evolution theory, and in case we are successful by fitting the spectra consistently with the dynamical parameters we might have the chance to decide whether the reason for this discrepancy lies with the evolutionary tracks on the one hand or the analysis by Kudritzki et al. (1997) on the other.

5. Consistent UV analysis of the CSPNs He 2-131 and NGC 2392

We will start with a detailed description of the two puzzling cases we have been faced with above.

Figure 3 (top left) shows the synthetic UV spectrum of the model corresponding to position 1A in Figure 2. It is clearly incompatible with the observed spectrum² of He 2-131 (middle), since its mass loss rate and due to that its luminosity is obviously too small, as evidenced by the presence of mostly purely photospheric lines, hardly affected by the unincisive thin wind. The theory of radiation-driven winds offers a solution: this CSPN must have a much larger luminosity, because L is the major factor determining the mass loss rate. We have calculated a series of models with increasing luminosity – and therefore increasing mass loss rate – (at the same time adjusting the mass to keep the terminal velocity at its observed value) to verify if one of these models could reproduce the numerous strongly wind-contaminated iron lines observed especially between 1500 and 1700 Å. Indeed, a more luminous model, able to sustain the high mass loss rate of model 1B in Figure 2, produces a convincing fit – see Figure 3, bottom left. The parameters of this model are given in Table 1.

The situation is reversed with NGC 2392. The synthetic spectrum of model 2A in Figure 2 is incompatible with the observed UV spectrum (Figure 3, right top and middle, respectively), since it produces many strongly wind-contaminated lines, which are not observed; the star produces almost exclusively photospheric lines! Again the problem can be attributed to the luminosity, which is too high in this case. Decreasing the luminosity and thus the mass loss rate yields a model which is quite well in agreement with the observed spectrum (Figure 3, bottom right). The stellar parameters of this model are also given in Table 1.

In summary, the new model atmospheres produce a good fit to all the observable features in the UV spectrum. We remark at this point that our error in the stellar mass is very small ($\leq 0.1 M_\odot$) due to the sensitive dependence on the predicted v_∞

² Note that here and in the following, the observed spectra are contaminated by interstellar Lyman- α absorption. We have not attempted to include this in our models, since the affected region has no bearing on our conclusions. Neither are other interstellar lines included in the modelling procedure.

and the small error received from determining this value from the observed spectrum ($\leq 10\%$). Furthermore, we note that our predicted values of v_∞ are in agreement within 10% with the observed values in the case of massive O stars (cf. Hoffmann and Pauldrach 2001). Thus, a possible internal error leaves no margin for a larger uncertainty in the deduced masses.

What can we conclude from the derived stellar parameters? Let us consider first the weak-winded CSPN, NGC 2392. We determine a T_{eff} of 40000 K from the ionization equilibrium of Fe ions in the stellar UV spectrum, similar to the value obtained from the ionization equilibrium of He I and He II (absorption lines in the optical stellar spectrum).³ The very low terminal wind velocity of 400 km s⁻¹, together with the low luminosity (needed to adjust the predicted mass loss rate so that the predicted and observed spectra are in good agreement) lead us to adopt a small radius. Using this radius ($1.5 R_\odot$) and v_∞ we get a stellar mass of only $0.41 M_\odot$, a value much smaller than obtained if we assume the classical post-AGB mass–luminosity relation – a high mass of $0.9 M_\odot$ was the result found by Kudritzki et al. (1997).

Note that the radius $1.5 R_\odot$ and mass $0.41 M_\odot$ of this CSPN correspond to $\log g = 3.7$, in good agreement with the $\log g$ derived earlier from the NLTE plane-parallel analysis of the optical stellar spectrum.

In the case of the central star of He 2-131 the terminal velocity of 500 km s⁻¹ (and $T_{\text{eff}} = 33000$ K) would appear to suggest, according to the classical post-AGB mass–luminosity relation (cf. Figure 2 upper panel), a stellar mass of about $0.6 M_\odot$. However, the wind features observed in the UV spectrum forced us to increase the stellar R and thus L , which in turn increased \dot{M} until a good fit was obtained. From the corresponding large radius – $5.5 R_\odot$ – and v_∞ we derive a stellar mass of $1.39 M_\odot$, a value very close to the Chandrasekhar mass limit for white dwarfs! Thus, in this case the resulting mass is even more extreme than the value of $0.9 M_\odot$ obtained by Kudritzki et al. (1997).

6. Consistent UV analysis of 7 additional CSPNs

In a similar fashion as for the two objects described in detail in the previous section, we have computed hydrodynamical models that reproduce the observed UV spectra of the 7 other CSPNs of our sample. The spectra are plotted in Figure 4, the resulting parameters are listed in Table 1.

We would like to remark on two points in this context. The first is that the observed spectrum of IC 4637 (not shown) is very noisy. Our parameters given for this particular star are therefore not of the same quality as those of the other objects, and should thus be seen more as a hydrodynamic consistency

³ We do not want to hide the fact that this central star has an anomalously high He II Zanstra temperature of about 70000 K and an even higher energy-balance temperature (Méndez et al. 1992), but we have carefully verified that both the visual and especially the UV stellar features are decidedly incompatible with such high temperatures. This discrepancy is at present unresolved. Apparently an additional source of He-ionizing photons is needed in this case. For the moment we ignore this, and perform the analysis using the information about T_{eff} derived from the stellar spectrum.

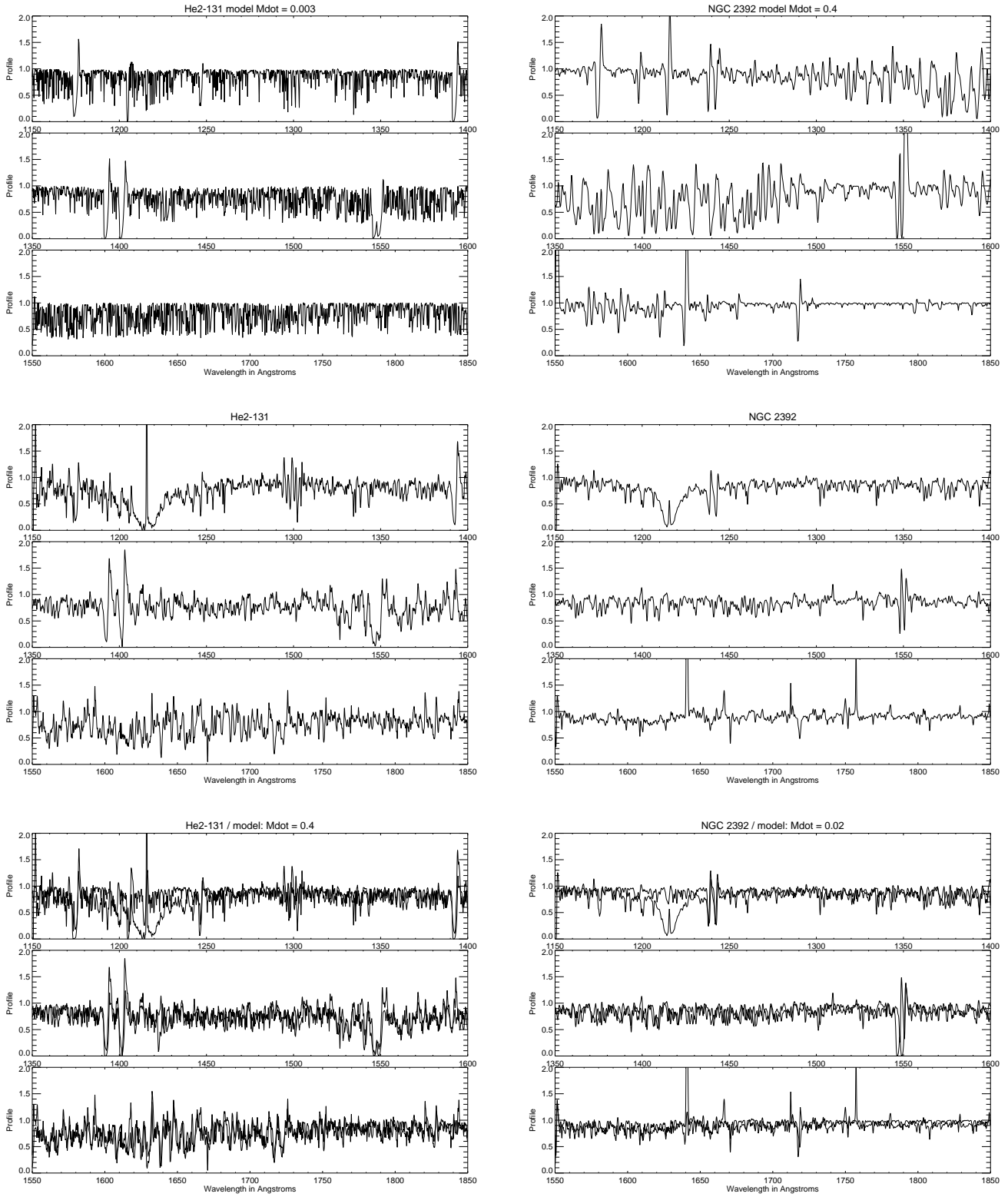


Fig. 3. (Left) Top: Synthetic spectrum of model 1A for He 2-131 (see text). This is incompatible with the observed IUE spectrum (middle). A model with a significantly enhanced luminosity which gives a higher mass loss rate, reproduces the distinctive features in the UV spectrum much better (bottom, overplotted with the observed spectrum to better show the similarity). (Right) Top: Synthetic spectrum of model 2A for NGC 2392. Again, this is incompatible with the observed IUE spectrum (middle). In this case, however, the luminosity (L) and thus the mass loss rate is much too high, whereas a model with a lower luminosity reproduces the observed spectrum (bottom).

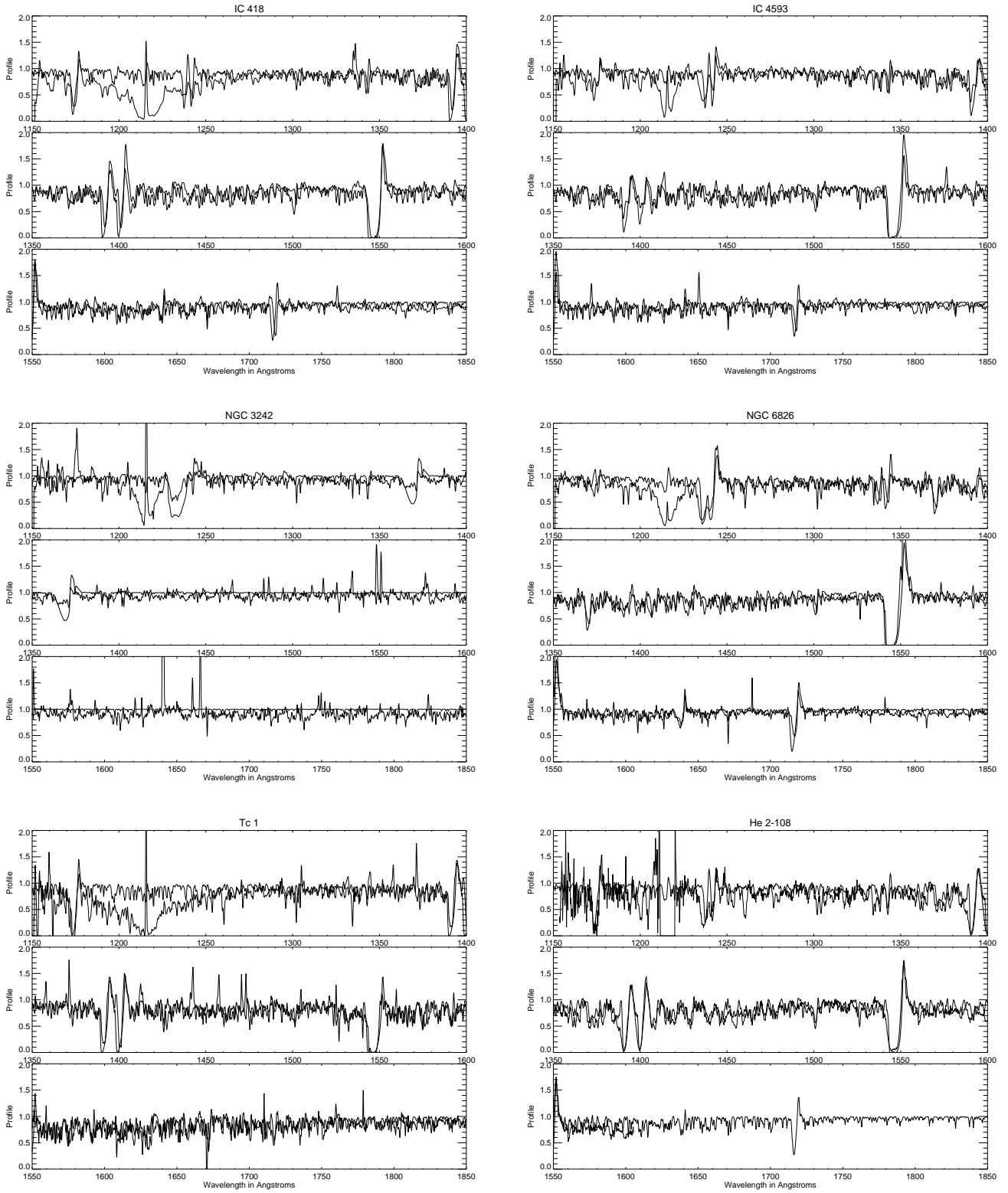


Fig. 4. Synthetic UV spectra from consistent atmospherical models for the other 6 CSPNs of our sample, compared to the observed UV spectra: IC 418 and IC 4593 (*top*), NGC 3242 and NGC 6826 (*middle*), and Tc 1 and He 2-108 (*bottom*).

check to the values derived by Kudritzki et al. (1997), than as resulting from a detailed spectral fit.

The second is that the UV spectra of IC 418 and He 2-108 are very similar, and we therefore derive similar parameters for these two stars, as the same model obviously fits both spectra equally well.

Concerning the elemental composition, we have adopted the Helium abundances from Kudritzki et al. (1997). For the other elements, we have assumed a solar abundance pattern, justified by the good fit to the observed UV spectra. A minor discrepancy is seen in NGC 2392, which the optical spectrum would indicate to be N-rich and C-deficient, a result also reflected in the UV spectrum (for example, both the observed C III and C IV lines are weaker than those of the model). However, the influence of this on the hydrodynamics is small, since C and N are not major contributors to the line force (Pauldrach 1987) and the sum of C, N, and O would remain constant if these abundances were the result of the CNO-process.

7. Interpretation of CSPN winds

Table 1 shows the result of applying the method and UV analysis to the nine CSPNs of our sample.

First of all, these results are, in a broad sense, encouraging. We have not found any object with decidedly impossible masses and luminosities (for example, we could have derived masses and luminosities typical of massive Pop. I stars: certainly that would have been quite embarrassing, but it did not happen). However, a closer look shows that we are in a very unexpected situation.

Figure 5 shows the relation between stellar mass and luminosity obtained from our model atmosphere analyses, in comparison with the mass–luminosity relation of the evolutionary tracks, represented by the values from Kudritzki et al. (1997). From the viewpoint of current stellar evolutionary calculations this plot is somewhat unsettling: there is a very large spread in masses, between 0.4 and $1.4 M_{\odot}$, and the derived masses and luminosities do not agree with the classical post-AGB mass–luminosity relation. Most CSPNs are underluminous for their mass (or too massive for their luminosities).

In Figure 6 we show again the wind-momentum–luminosity relation for both massive hot stars and CSPNs, but this time based on the parameters derived in our analysis. Our new parameters give wind momenta of the right order of magnitude and within the expected luminosity range (there may be still too many CSPNs at $\log L/L_{\odot} > 4$, but not so many as in Kudritzki et al. 1997). The CSPNs are found along the extrapolation of the wind-momentum–luminosity relation defined by the massive hot stars, and the CSPNs show a smaller dispersion, i.e., a tighter correlation of wind-momentum with luminosity, than was the case in Kudritzki et al. (1997). None of these facts is surprising, because our derived parameters are now based on the wind theory; of course the theory, consistently applied, will not produce any departure from its own predictions! However, the really significant fact is that we could produce a very convincing fit simultaneously to a multitude of diagnostic features in the CSPN UV spectra. There was no guarantee a priori that such a good overall fit was possible, and this is the main rea-

son why we think that it is not easy to simply argue “the wind models must be wrong”. Instead, it is very likely that the theory and the models as an approach to it are correct since the experiment in the form of a comparison of observed and synthetic UV spectra was successful.

More importantly, the results obtained for NGC 2392 and NGC 3242 rule out the possibility that our method simply systematically overestimates the stellar masses: for these two stars we derive masses that lie below those deduced by Kudritzki et al. (1997). In the extreme case of NGC 2392, any systematic overestimate of the mass would require this star to have a mass even below $0.4 M_{\odot}$. If there is any physical effect at work whose neglect results in a systematic error in the analysis, it would need to be such that it can lead to an over- as well as an underestimate of the masses, despite reproducing nearly perfectly the observed UV spectra. Our current knowledge of stellar winds does not provide us with any mechanism able to do this.

If we drop the *assumption* made by Kudritzki et al. that the stars obey the theoretical post-AGB mass–luminosity relation, and instead scale their mass loss rates to our radii⁴ – keeping \dot{Q} , the real observational quantity, fixed – then their wind momenta match ours to within about a factor of two. Furthermore, their sample with the radii thus scaled now also shows a much tighter correlation of the wind momentum to luminosity than before (see Figure 6). This indicates that **two independent procedures** to obtain the mass loss rates – one based on optical (Kudritzki et al.), the other based on UV wind-sensitive line profiles (our models) – **have given consistent results**. In other words, the problem cannot be attributed exclusively to the observational data used by Kudritzki et al. (1997) to estimate the mass loss rates. It is not a problem of the optical mass loss rate determinations per se, but a consequence of the *radii* assumed in that analysis.

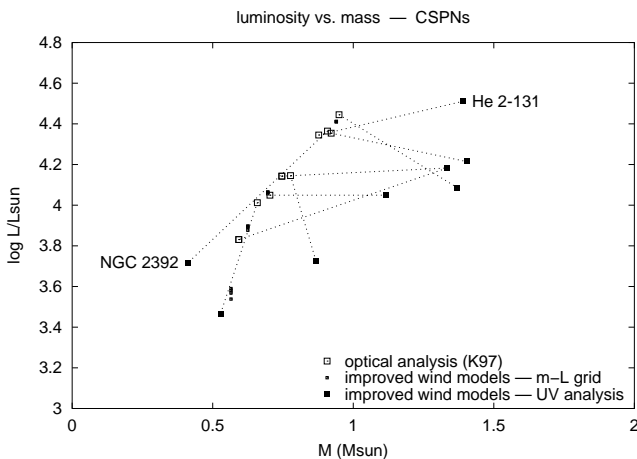
If we believe both, the current evolutionary theory and the luminosities and masses we have determined from the atmospheric models, then most of our CSPNs have not followed a classical post-AGB evolution. We find many stars near the Chandrasekhar limit for white dwarfs. They do not obey the core-mass–luminosity relation (being underluminous for their mass) and this indicates that their internal structure must be different. The special case of NGC 2392 is also remarkable: with such a small mass it cannot be a post-AGB star, and we would be forced to consider alternative evolutionary histories, involving probably a binary system merged immediately after the first visit to the red giant branch. A few similar cases of low-mass CSPNs have been noted in the past: EGB 5 and PHL 932, see Méndez et al. (1988a, 1988b). What makes NGC 2392 a more troublesome case is the additional fact that kinematically it is a rather young PN, while numerical simulations of binary merging lead to expect no visible nebulae around them, or at most very old ones, like EGB 5 and PHL 932.

If we reject such drastic departures from the classical post-AGB evolutionary picture, still assuming the evolutionary calculations to be correct, then we would need to conclude that

⁴ Additionally allowing for their different effective temperatures by requiring that the observed visual flux ($\sim R^2 T_{\text{eff}}$) stay constant.

Table 1. Parameters of nine CSPNs derived from our analysis of the UV spectra using our model atmospheres, compared to the values found by Kudritzki et al. 1997.

Object	T_{eff} (K)	R (R_{\odot})	$\log \frac{L}{L_{\odot}}$	M (M_{\odot})	$\log g$ (cgs)	\dot{M} ($10^{-6} M_{\odot}/\text{yr}$)	v_{∞} (km/s)
our models							
NGC 2392	40000	1.5	3.7	0.41	3.70	0.018	420
NGC 3242	75000	0.3	3.5	0.53	5.15	0.004	2400
(IC 4637	55000	0.8	3.7	0.87	4.57	0.019	1500)
IC 4593	40000	2.2	4.0	1.11	3.80	0.062	850
He 2-108	39000	2.7	4.2	1.33	3.70	0.072	800
IC 418	39000	2.7	4.2	1.33	3.70	0.072	800
Tc 1	35000	3.0	4.1	1.37	3.62	0.021	900
He 2-131	33000	5.5	4.5	1.39	3.10	0.35	450
NGC 6826	44000	2.2	4.2	1.40	3.90	0.18	1200
Kudritzki et al. 1997							
NGC 2392	45000	2.5	4.4	0.91	3.6	≤ 0.03	400
NGC 3242	75000	0.6	4.0	0.66	4.7	≤ 0.02	2300
IC 4637	55000	1.3	4.1	0.78	4.1	≤ 0.02	1500
IC 4593	40000	2.2	4.0	0.70	3.6	0.1	900
He 2-108	35000	3.2	4.1	0.75	3.3	0.24	700
IC 418	37000	3.5	4.3	0.89	3.3	0.26	700
Tc 1	33000	5.1	4.4	0.95	3.0	≤ 0.1	900
He 2-131	30000	5.5	4.3	0.88	2.9	0.9	500
NGC 6826	50000	2.0	4.4	0.92	3.8	0.26	1200

**Fig. 5.** Luminosity vs. mass for the evolutionary tracks (open squares) compared to the observed quantities determined with our method (filled squares). Although the luminosities deduced from the UV spectra lie in the expected range, a much larger spread in the masses (from 0.4 to 1.4 M_{\odot}) is obtained. The relation between CSPN mass and luminosity deviates severely from that taken from the theory of post-AGB evolution. Of course the latter is followed by the open squares and dots, because in that case it had been assumed from the start.

our models, while adequate for massive O supergiants, are a failure for stars of similar surface temperature and gravity in another evolutionary status, and produce good fits to the CSPN UV spectra only by a surprising and misleading coincidence. Considering the successes of radiatively-driven wind theory, however, we regard this conclusion as highly improbable. We must therefore contemplate the possibility that our current knowledge of stellar evolution might be incomplete.

8. Spectroscopic distances and white dwarf masses

Facing this surprising situation, we ask if there is any way of further verifying the CSPN masses and luminosities we determined. One possible way is to calculate the spectroscopic distances and verify if they agree with the rest of the available evidence. Another way, since we expect CSPNs to become white dwarfs, is to look into what is currently known about the white dwarf mass distribution and into the recent results on asteroseismology of pre-white dwarfs.

Having all the basic stellar parameters it is easy to calculate the spectroscopic distances, following, for example, the method described in Méndez et al. (1992), which uses the stellar mass, $\log g$, monochromatic model atmosphere flux at visual wavelength, and dereddened apparent visual magnitude.

Table 2 shows these quantities and the resulting distances. They are not too different from the earlier spectroscopic distances by Méndez et al. (1988b, 1992), except for the effect of the different stellar masses we are using now. NGC 2392 gets a smaller distance and He 2-131 a larger one because the new mass is smaller and larger, respectively, than before.

Now we want to discuss systematically how these spectroscopic distances compare with individual PN distances derived from other methods. We disregard all the statistical distances published by many authors because they are too uncertain for a case-by-case discussion. We consider in turn trigonometric parallaxes, distances derived from visual companions to the central stars, cluster distances, extinction distances, and expansion distances.

Table 2. Computed spectroscopic distances of our sample stars and the quantities used to derive them. (See text.)

Object	Mass (M_{\odot})	$\log g$ (cgs)	F_{\star}	V	c	distance (kpc)	$-\log F(\text{H}\beta)$	M_{β}
NGC 2392	0.41	3.70	7.48	10.53	0.16	1.67	10.29	0.5
NGC 3242	0.53	5.15	14.69	12.10	0.09	1.10	9.80	0.3
IC 4637	0.87	4.57	10.64	12.47	1.10	1.01	11.24	1.6
IC 4593	1.12	3.80	7.69	11.27	0.12	3.63	10.55	-0.5
He 2-108	1.33	3.70	7.49	12.82	0.40	6.76	11.41	-0.4
IC 418	1.33	3.70	7.49	10.00	0.32	2.00	9.62	-2.0
Tc 1	1.37	3.62	6.38	11.38	0.36	3.73	10.66	-0.8
He 2-131	1.39	3.10	6.26	10.50	0.14	5.62	10.16	-2.4
NGC 6826	1.40	3.90	8.61	10.69	0.04	3.18	9.97	-1.4

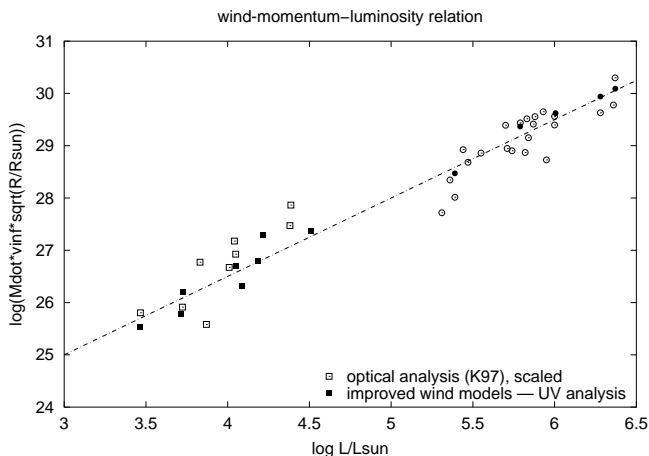


Fig. 6. The wind-momentum–luminosity relation for CSPNs (lower left) based on our values determined from the UV spectra (filled squares). The open squares are the values from Kudritzki et al. (1997) scaled to our determined radii, thus eliminating the need for an a-priori assumption for the radii, as was done by Kudritzki et al. (see text). Compared to Figure 1 the result is striking: now there is good agreement between the optical and UV mass loss rate determinations.

8.1. Trigonometric parallaxes

There is no overlap with the sample we are analyzing here. However, it is possible to compare trigonometric versus other spectroscopic parallaxes. Some ground-based trigonometric parallaxes are listed by Harris et al. (1997). We consider only those objects with reliable parallaxes larger than 2 milli-arc-seconds, i.e., with distances below 500 pc: NGC 6853, NGC 7293, S 216. Their distances compare very well with the spectroscopic distances of Napiwotzki (1999).

The Hipparcos parallaxes again do not overlap with our sample, but again it is possible to compare with other spectroscopic parallaxes. Here there is some disagreement, especially in the case of PHL 932 and (marginally) A 36. The parallax for NGC 1360 is too uncertain, but Pottasch and Acker (1998) show convincingly that the Hipparcos distances of PHL 932 and A 36 require higher surface gravities than indicated by the spectroscopic analysis *if we assume a central star mass of $0.6 M_{\odot}$* . One way to reduce the discrepancy is to reduce the mass of the central star; so in fact we could

argue that Hipparcos has confirmed the conclusion that the central star of PHL 932 must have a very low mass, below $0.3 M_{\odot}$, and cannot be a post-AGB star (Méndez et al. 1988a). Napiwotzki (1999) has repeated the spectroscopic analysis of PHL 932, using different models and spectrograms, and obtains atmospheric parameters marginally consistent with those of Méndez et al. (1988a). His surface gravity is somewhat higher, but not as high as required by the Hipparcos parallax, unless we reduce the central star mass to the rather implausible value of $0.1 M_{\odot}$. Therefore in the case of PHL 932 some degree of contradiction remains. Would somebody please remeasure this parallax? Nowadays it can probably be done from the ground with adequate CCD techniques.

8.2. Distances derived from visual companions to the CSPNs

Again no overlap; but Ciardullo et al. (1999) assign a distance of 2.4 kpc to NGC 1535, in good agreement with the spectroscopic distance of 2.0 kpc in Méndez et al. (1992).

8.3. Cluster distances

Again no overlap. The only object we can mention here is the central star of the PN in the globular cluster M 15, where the spectroscopic distance is in excellent agreement with the cluster distance, see McCarthy et al. (1997).

8.4. Extinction distances

Here finally we find some objects in common with our sample. Martin (1994) concludes that the extinction distance of He 2-131 (about 700 pc), although substantially smaller, does not necessarily invalidate our distance, in view of the high Galactic latitude of this PN. The same point was made earlier by Maciel (1985): given its high latitude, this object at a distance of 700 pc would be some 180 pc below the Galactic plane, which is not very different from the halfthickness of the Galactic absorbing layer. As a consequence, the extinction distance should be taken as a lower limit to the true distance. The same can be argued about Tc 1, with an extinction distance of 600 pc, although Martin considers this case more of a con-

tradition with the spectroscopic distance. For another of our objects (He 2-108) again there is no conflict.

Martin's best case of a contradiction is IC 2448, with an extinction distance of 840 pc and a spectroscopic distance of about 3 kpc. Unfortunately IC 2448 is not in the sample we are studying here; we do not know if a revised spectral analysis would reduce its spectroscopic distance somewhat. In any case, we think that one isolated discrepant case does not have too much weight, given the existence of many other cases showing agreement, because the isolated discrepancy can always be attributed to accidental fine structure in the interstellar dust distribution.

8.5. Expansion distances

Again no overlap with our sample, but since we mentioned IC 2448 in the previous subsection, we should add that there is a recent expansion distance estimate for this PN by Palen et al. (2002). Their result is 1.4 kpc, apparently in better agreement with the extinction distance. Here we would like to sound a word of caution: a point which was made already some time ago by Steffen et al. (1997) and again by Schönberner (2001). The outer rim of a PN is defined by a shock front, the temporal displacement of which is not given by a material velocity and is not easily derivable from the Doppler splitting of the strongest PN emission lines. Hydrodynamic modelling indicates that frequently the Doppler splitting is smaller than the linear velocity of expansion in the plane of the sky. The assumption that both are equal can easily lead to systematically too small expansion distances, perhaps by a factor as large as 2. For that reason we think that some more work is needed on the interpretation of the angular expansion of PNs.

8.6. Summary on distances

The amount of information is too small to extract any solid conclusion. The independent evidence would seem to provide support to several spectroscopic distances, but there are a few discrepant cases that need to be resolved.

Since we are primarily interested in testing the validity of the theory of post-AGB evolution, a few more comments are relevant. An interesting consequence of the extinction distances is that they produce several central stars with extremely low luminosities, which cannot be post-AGB stars (see Martin 1994). Therefore we may still have a severe problem with the classical interpretation of several *other* CSPNs as post-AGB stars; similar to what we found for NGC 2392.

In this situation we need more and better independent distance determinations, good enough to convince everybody. For the moment, we find no compelling reason to reject the spectroscopic distances, although we understand that some of them are taken with skepticism. But we would expect the spectroscopic distances, if based on an inadequate physical theory, to fail all together in a very systematic way; not just a few of them wrong and all the others OK. And so we still expect that the few conflicting cases may be resolved in favor of the spectroscopic distances when more evidence is added.

8.7. The constraints from the PN luminosity function

There is another verification we can undertake, based on the behavior of extragalactic PNs. They show a very characteristic luminosity function (PNLF), with a well-defined limiting brightness, which has been successfully used for extragalactic distance determinations (see, e.g., Jacoby and Ciardullo 1993, Jacoby 1997). We can try to verify if our spectroscopic distances produce any overluminous PN; that would be a nice argument supporting a smaller spectroscopic distance in that case.

Now one complication is that for extragalactic work the PNLF is built using the normally very bright nebular emission [O III] $\lambda 5007$. Very low-excitation PNs do not contribute to the bright end of the $\lambda 5007$ PNLF. But it turns out that some of our central stars belong to low-excitation PNs, implying that the flux in $\lambda 5007$ does not provide any useful limit. For that reason we have decided to do the test using a recombination line, namely H β . The problem is now that we do not have too much observational information about the limiting H β flux in other galaxies: the only well-observed case is the LMC. But we can try to supplement the observational LMC limit by a limit obtained from numerical simulations of the PNLF: see Méndez and Soffner (1997). Their Figure 6 shows the observed H β LMC PNLF, compared with a simulated PNLF. Allowing for a somewhat larger sample size in our Galaxy (see the effect of increasing the sample size in Figure 10 of Méndez and Soffner), we can estimate that the brightest PNs in our Galaxy should have an absolute H β magnitude of about -2.3 (the relation between observed H β flux and H β apparent magnitude is traditionally defined as $m_\beta = -2.5 \log F_\beta - 13.74$).

The resulting absolute H β magnitudes we derive using our spectroscopic distances are listed in Table 2. There is only one case at the limit: He 2-131, with $M_\beta = -2.4$. All the other distances produce weaker absolute H β magnitudes. Again we find no strong reason to reject our spectroscopic distances, although He 2-131 is admittedly at the very limit of acceptability.

9. Masses of white dwarfs and pre-white dwarfs

Probably the most severe conflict we have is the large number of very massive CSPNs, in view of the known mass distribution of white dwarfs, with a well-defined maximum at about $0.6 M_\odot$. Although this could be used to argue against the credibility of our analysis, we would like to point to the existence of some recent results involving very massive pre-white dwarfs and white dwarfs. Most interesting is a report by Kawaler (2001) who finds a wide range of pulsation periods among H-deficient CSPNs, which he tentatively interprets as due to a correspondingly large range of masses, from 0.52 to $1.2 M_\odot$. This looks surprisingly similar to our result, based on a completely different observational technique applied to a completely different sample of central stars (our stars have H-rich atmospheres).

Another study worth mentioning is by Napiwotzki et al. (1999). They have determined masses for a sample of 46 hot DA white dwarfs selected from the Extreme UV Explorer (EUVE) and ROSAT Wide Field Camera bright source lists.

They find a peak mass of $0.59 M_{\odot}$, in agreement with many other studies, but find a non-negligible fraction of white dwarfs with masses in excess of $1 M_{\odot}$.

Yet another study by Silvestri et al. (2001), dealing with a sample of 41 white dwarfs in wide binary systems, finds a bimodal mass distribution with a second mass peak at $1.1 M_{\odot}$. They interpret this second peak, suspiciously close to twice the mass of the first peak, as the result of binary mergers.

Therefore, our mass distribution, with its probable dependence on very strong selection effects, is perhaps not as irreconcilable with the rest of the evidence as we could have thought initially.

The conflict with the post-AGB evolutionary speeds is not too important if we decide to accept a drastic departure from the relation between luminosity and mass. In this case new stellar structure and evolutionary calculations would be needed.

10. Conclusions and perspectives

We have applied our new model atmospheres, involving a much improved treatment of blocking and blanketing by all metal lines in the entire sub- and supersonically expanding atmosphere, to the analysis of a sample of 9 PN central stars. We have shown how the new models can produce an essentially perfect fit to a multitude of spectral features in the UV spectra of the CSPNs. The fits lead us to determine a set of stellar parameters including separate determinations of luminosity and mass, allowing for the first time a full test of the post-AGB evolutionary calculations. Surprisingly, we find drastic departures from the theoretical post-AGB mass–luminosity relation. We emphasize that this is a consequence of a drastic discrepancy between the mass-loss rates following from consistent wind dynamics with stellar parameters from the evolutionary tracks and those necessary to reproduce the observed spectra, which differ by up to a factor of 100 and thus indicate a real physical problem and not merely a minor detail of the modelling procedure.

The luminosities we derive for the stars of our sample lie in the expected range, but we find a much larger spread in the masses, from 0.4 to $1.4 M_{\odot}$. The resulting relation between CSPN mass and luminosity deviates severely from that given by the theory of post-AGB evolution.

For five out of the nine CSPNs of our sample we obtain masses near, *but not above*, the critical Chandrasekhar mass limit for white dwarfs. Despite our sample most probably being influenced by selection effects, this result nevertheless invites speculation about the role of a group of CSPNs as precursors to the white dwarfs believed to end up as Type Ia supernovae.

We cannot at the moment offer a clear-cut explanation to the discrepancy between radiation-driven wind theory confirmed by UV spectroscopy on the one hand and the theory of post-AGB stellar evolution on the other (in particular the fact that from the former we derive masses both larger and smaller than those predicted by the latter); however, we point out a number of other independent observational investigations (see section 8) that have also found a similarly large spread (up to $1.2 M_{\odot}$) in the CSPN/white-dwarf masses which cannot be explained by the classical post-AGB evolutionary theory.

Nevertheless, if we believe both, the current evolutionary theory and the luminosities and masses we have determined from the atmospheric models, then most of the CSPNs of our sample have not followed a classical post-AGB evolution.

Acknowledgements. We wish to thank our colleague Dr. R.-P. Kudritzki for helpful comments and discussions. This work was supported by the Sonderforschungsbereich 375 of the Deutsche Forschungsgemeinschaft and by the DLR under grant 50 OR 9909 2.

References

- Blöcker T., 1995, *A&A* 299, 755
 Ciardullo R., Bond H. E., Sipior M. S., et al., 1999, *AJ* 118, 488
 Harris H. C., Dahn C. C., Monet D. G., & Pier J. R., 1997, in *proc. IAU Symp.* 180, *Planetary Nebulae*, eds. H. J. Habing & H. J. G. L. M. Lamers, p. 40
 Haser S. M., 1995, PhD-Thesis
 Hoffmann T. L. & Pauldrach A. W. A., 2001, in *proc. IAU Symp.* 209, *Planetary Nebulae*, in press
 Jacoby G., 1997, in *proc. IAU Symp.* 180, *Planetary Nebulae*, eds. H. J. Habing & H. J. G. L. M. Lamers, p. 448
 Jacoby G. & Ciardullo R., 1993, in *proc. IAU Symp.* 155, *Planetary Nebulae*, eds. R. Weinberger & A. Acker, p. 503
 Kawaler S. D., 2001, *ASP Conf. Series* 226, p. 287
 Kudritzki R.-P., Méndez R. H., Puls J., & McCarthy J. K., 1997, in *proc. IAU Symp.* 180, *Planetary Nebulae*, eds. H. J. Habing & H. J. G. L. M. Lamers, p. 64
 Maciel W., 1985, *Rev. Mex. Astr. Astrof.* 10, 199
 Martin W., 1994, *A&A* 281, 526
 McCarthy J. K., Méndez R. H., Becker S., Butler K., & Kudritzki R.-P., 1997, in *proc. IAU Symp.* 180, *Planetary Nebulae*, eds. H. J. Habing & H. J. G. L. M. Lamers, p. 122
 Méndez R. H., Groth H. G., Husfeld D., Kudritzki R.-P., & Herrero A., 1988a, *A&A* 197, L25
 Méndez R. H., Kudritzki R.-P., Herrero A., Husfeld D., & Groth H. G., 1988b, *A&A* 190, 113
 Méndez R. H., Kudritzki R.-P., & Herrero A., 1992, *A&A* 260, 329
 Méndez R. H. & Soffner T., 1997, *A&A* 321, 898
 Napiwotzki R., 1999, *A&A* 350, 101
 Napiwotzki R., Green P. J., & Saffer R. A., 1999, *ApJ* 517, 399
 Palen S., Balick B., Hajian A. R., et al., 2002, *AJ* 123, 2666
 Pauldrach A. W. A., 1987, *A&A* 183, 295
 Pauldrach A. W. A., Puls J., Kudritzki R.-P., et al., 1988, *A&A* 207, 123
 Pauldrach A. W. A., Kudritzki R.-P., Puls J., et al., 1994, *A&A* 283, 525
 Pauldrach A. W. A., Hoffmann T. L., & Lennon M., 2001, *A&A* 375, 161
 Pauldrach A. W. A., Hoffmann T. L., Méndez R. H., 2001a, in *proc. IAU Symp.* 209, *Planetary Nebulae*, in press
 Pauldrach A. W. A., 2003, *Rev. Mod. Astron.* Vol. 16, 141–177
 Pauldrach A. W. A. & Hoffmann T. L., 2004, *A&A*, in prep.
 Pottasch S. R. & Acker A., 1998, *A&A* 329, L5
 Puls J., Kudritzki R.-P., Herrero A., et al., 1996, *A&A* 305, 171
 Schönberner D., 2001, in *proc. IAU Symp.* 209, *Planetary Nebulae*, in press
 Scuderi S., Panagia N., Stanghellini C., et al., 1998, *A&A* 332, 251
 Sellmaier F., Puls J., Kudritzki R.-P., et al., 1993, *A&A* 273, 533
 Silvestri N. M., Oswalt T. D., Wood M. A., et al., 2001, *ASP Conf. Series* 226, p. 246
 Steffen M., Schönberner D., Kifonidis K., & Stahlberg J., 1997, in *proc. IAU Symp.* 180, *Planetary Nebulae*, eds. H. J. Habing & H. J. G. L. M. Lamers, p. 368
 Tinkler C. M. & Lamers H. J. G. L. M., 2002, *A&A* 384, 987

List of Publications

- Hoffmann T. L., Pauldrach A. W. A., *Wind models for O-type stars*, in: Kwok S., Dopita M., Sutherland R. (eds.), Proc. IAU Symp. 209, ASP, p. 189 (2003)
- Hoffmann T. L., Pauldrach A. W. A., Puls J., *Wind models and synthetic UV spectra for O-type stars*, in: van der Hucht K. A., Herrero A., Esteban C. (eds.), Proc. IAU Symp. 212, ASP, p. 206 (2003)
- Mehlert D., Seitz S., Saglia R. P., Appenzeller I., Bender R., Fricke K. J., Hoffmann T. L., Hopp U., Kudritzki R.-P., Pauldrach A. W. A., *Gravitationally lensed high redshift galaxies in the field of 1E0657-56*, A&A 379, 96–106 (2001)
- Pauldrach A. W. A., Lennon M., Hoffmann T. L., Sellmaier F., Kudritzki R.-P., Puls J., *Realistic Models for Expanding Atmospheres*, in: Howarth I. (ed.), Proc. 2nd Boulder-Munich Workshop, PASPC 131, p. 258 (1998)
- Pauldrach A. W. A., Hoffmann T. L., Lennon M., *Radiation-driven winds of hot luminous stars. XIII. A description of NLTE line blocking and blanketing towards realistic models for expanding atmospheres*, A&A 375, 161–195 (2001)
- Pauldrach A. W. A., Hoffmann T. L., Méndez R. H., *Radiation driven atmospheres of O-type stars: constraints on the mass–luminosity relation of central stars of planetary nebulae*, in: Kwok S., Dopita M., Sutherland R. (eds.), Proc. IAU Symp. 209, ASP, p. 177 (2003)
- Pauldrach A. W. A., Hoffmann T. L., Méndez R. H., *Radiation-driven winds of hot luminous stars. XV. Constraints on the mass–luminosity relation of central stars of planetary nebulae*, A&A, in press (2004)
- Puls J., Repolust T., Hoffmann T., Jokuthy A., Venero R., *Advances in radiatively driven wind models*, in: van der Hucht K. A., Herrero A., Esteban C. (eds.), Proc. IAU Symp. 212, ASP, p. 61 (2003)
- Sauer D., Pauldrach A. W. A., Hoffmann T., Hillebrandt W., *Synthetic Spectra of Type Ia Supernovae at Early Epochs*, in: Marcaide J. M., Weiler K. W. (eds.), proc. IAU Colloquium 192, in press (2004)
- Sternberg A., Hoffmann T., Pauldrach A. W. A., *Ionizing Photon Emission Rates from O- and Early B-Type Stars and Clusters*, ApJ, in press (2003)

Curriculum Vitae

Tadziu Hoffmann

Personal Details

German, born 3 December 1968 in Windhoek, South West Africa

Education

Jan 1975 – Dec 1975 Grundschule Swakopmund (South West Africa)
Jan 1976 – Dec 1977 Freiherr-vom-Stein-Schule, Eppstein im Taunus (Germany)
Jan 1978 – Dec 1978 International School of Curitiba, Curitiba (Brazil)
Jan 1979 – Jun 1982 American School of Recife, Recife (Brazil)
Jul 1982 – Jun 1984 International Education Association, Belo Horizonte (Brazil)
Jul 1984 – May 1987 Gymnasiale Oberstufe, Hofheim am Taunus (Germany)

Military Service

Oct 1987 – Dec 1988 “Grundwehrdienst”, Gebirgsjägerbataillon 233, Mittenwald

University Education

Nov 1988 – Jul 1995 Study of Physics at the University of Munich

Career

Jan 1996 – date “Wissenschaftlicher Mitarbeiter” at the Institute for Astronomy and Astrophysics of the University of Munich

Acknowledgements

I would like to express my thanks to the many people who have helped make this thesis possible. First and foremost my parents, who have enabled me to be where I am now; my friends Tetsuo Yamamoto, Christoph Stadler, and Markus Schneider, for providing support and encouragement during my studies at the LMU; Rolf-Peter Kudritzki, ex-“chief” of the USM, for introducing me to the field of hot stars; Adi Pauldrach and Joachim Puls, the “core” of the Munich hot star group, to whom I owe most of my knowledge of stellar atmospheres, gained in numerous heated debates about radiation transfer and NLTE in general; Ilse Holzinger for dealing with the bureaucracy; and last but not least the interdisciplinary lunch group and all my colleagues who have made and make the USM such an inspiring place to work: (in alphabetical order) Jan Bernkopf, Keith Butler, Dijana Dominis, Niv Drory, Thomas Gehren, Philip Hultsch, Andreas Korn, Harald Lesch, Paco Najarro, André Nickel, Ralf Palsa, Peter Petrenz, Norbert Przybilla, Thomas Puzia, Johannes Reetz, Tamara Repolust, Arno Riffeser, Daniel Sauer, Florian Sellmaier, Uwe Springmann, Matthias Stehle, Michael Wegener, and of course all those I’ve forgotten to mention.